Three-dimensional ozone distribution based on assimilation of nadir-sounding UV-VIS satellite observations

van Peet, Jacob

DOI
10.4233/uuid:8062f124-6fb4-43fe-8bd6-c2122c872409

Publication date
2019

Document Version
Final published version

Citation (APA)
van Peet, J. (2019). *Three-dimensional ozone distribution based on assimilation of nadir-sounding UV-VIS satellite observations*. [Dissertation (TU Delft), Delft University of Technology]. https://doi.org/10.4233/uuid:8062f124-6fb4-43fe-8bd6-c2122c872409

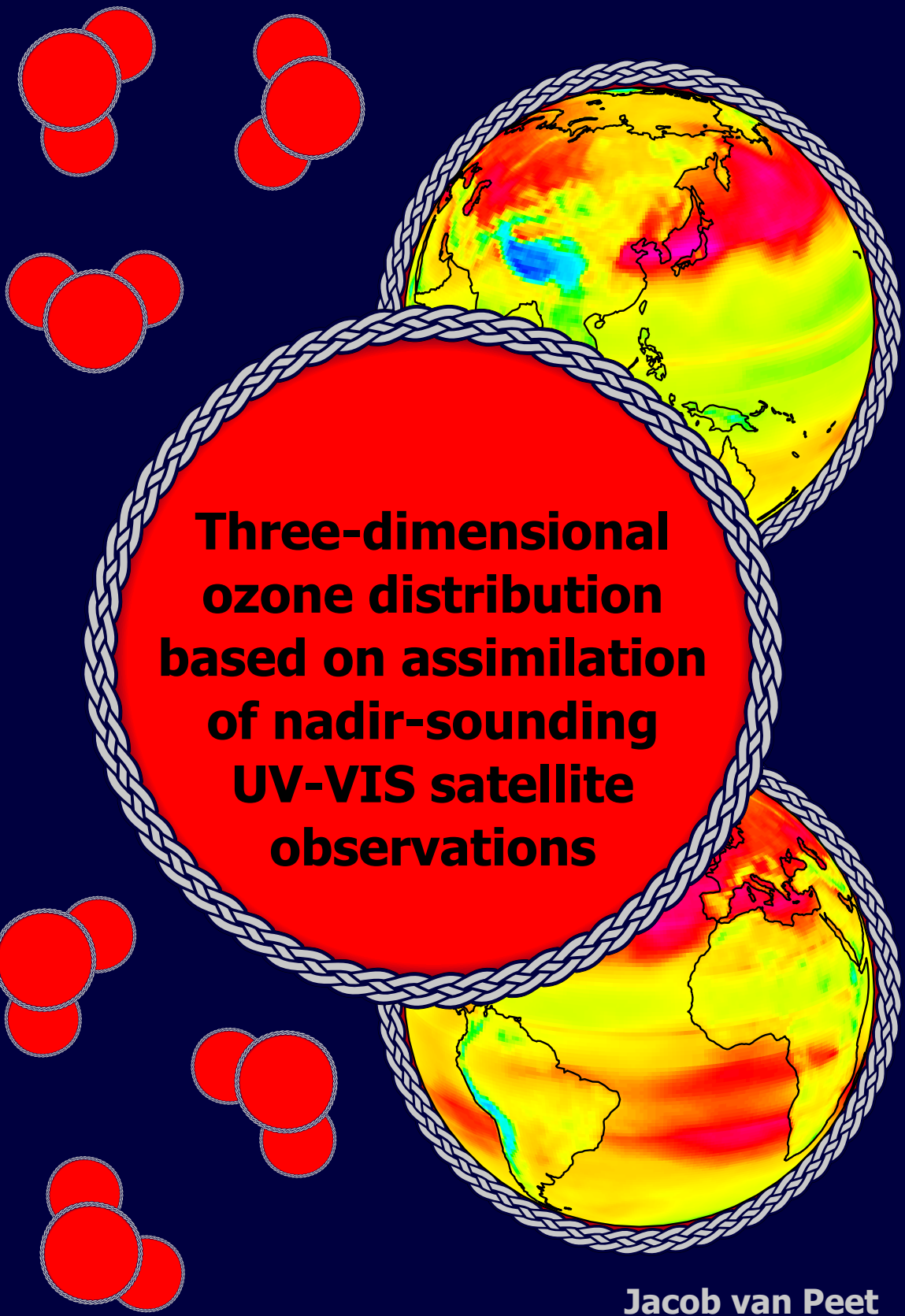

Three-dimensional ozone distribution based on assimilation of nadir-sounding UV-VIS satellite observations

Jacob van Peet

Three-dimensional ozone distribution based on assimilation of nadir-sounding UV-VIS satellite observations

Three-dimensional ozone distribution based on assimilation of nadir-sounding UV-VIS satellite observations

Dissertation

for the purpose of obtaining the degree of doctor
at Delft University of Technology,
by the authority of the Rector Magnificus prof.dr.ir. T.H.J.J. van der Hagen,
Chair of the Board for Doctorates,
to be defended publicly on Thursday, 14 March, 2019 at 15:00 o'clock

by

Jacob Cornelis Adriaan VAN PEET

Master of Science Physical Geography,
Utrecht University, The Netherlands,
Master of Science Physics and Astronomy,
Utrecht University, The Netherlands,
born in Ermelo, The Netherlands.

This dissertation has been approved by the promotors.

Composition of the doctoral committee:

Rector Magnificus	chairperson
Prof. dr. P. F. Levelt	Delft University of Technology. *promotor*
Prof. dr. R. J. van der A	Nanjing University of Information Science & Technology (NUIST), China. *promotor*
Independent members:	
Prof. dr. H. M. Kelder	Eindhoven University of Technology, The Netherlands
Prof. dr. G. de Leeuw	Finnish Meteorological Institute, Finland
dr. M. van Roozendael	Belgian Institute for Space Aeronomy, Belgium
Prof. dr. ir. W. W. J. Russchenberg	Delft University of Technology, The Netherlands
Prof. dr. A. P. Siebesma	Delft University of Technology, The Netherlands

TU Delft Delft University of Technology

Royal Netherlands Meteorological Institute *Ministry of Infrastructure and Water Management*

Keywords: *ozone, trace gas, satellite observation, data assimilation*

Printed by: *Ipskamp Printing, The Netherlands*

ISBN 978-94-6384-027-9
NUR 956

An electronic version of this dissertation is available at
http://repository.tudelft.nl/.

Contents

Summary

Ozone (0_3) directly and indirectly affects human health (depending on the altitude it is sometimes referred to as “good” or “bad” ozone) and has an important role in the temperature structure of the atmosphere. Because of the impact of ozone on air quality and climate change, the objective of this thesis is to improve our understanding of the global distribution of atmospheric ozone in space and time, not just in the stratosphere, but also in the troposphere, where it directly affects living organisms.

In this thesis, ozone is measured with satellite-based instruments that measure reflected solar light in the Ultra Violet - VISible (UV-VIS) wavelength range ($280 < \lambda < 330$ nm). In the UV-VIS, the absorption cross-section of ozone varies by several orders of magnitude, providing the altitude information for the ozone distribution. The ozone profiles are retrieved from the measured radiation with the optimal estimation technique. To make optimal use of the advantages of both observations and atmospheric models, they are combined using the Kalman filter data assimilation technique. The assimilation output consists of regular gridded 3D ozone fields without missing data at regular time intervals.

Ozone profiles retrieved from UV-VIS satellite measurements have a limited vertical sensitivity of an estimated 7–10 km in the stratosphere, and increasing values higher and lower in the atmosphere. In Chapter 2 we therefore check if the operationally retrieved ozone profiles by the Ozone ProfilE Retrieval Algorithm (OPERA) are capable of resolving the sharp ozone gradients that occur under ozone hole conditions. OPERA is used to retrieve ozone profiles for the period September-December 2008, which are validated against independent ozone sonde measurements from the Antarctic research station Neumayer. The results show that OPERA is capable of retrieving ozone profiles under difficult ozone hole circumstances, also if the a priori information is not representative for ozone hole conditions. A gridded dataset ($1° \times 1°$) was also created to study the development and breakup of the ozone hole during the 2008 ozone hole season. Between September-October, the region of maximum ozone depletion is between 100 and 50 hPa, while in November-December it is somewhat lower (between 100 and 70 hPa), with higher concentrations above. The ozone hole season ends with the inflow of ozone enriched air from above, eventually leading to the breakup of the ozone hole.

We extend the analysis of the retrieved ozone profiles to a global scale in Chapter 3. OPERA is tuned for optimal retrievals from both GOME and GOME-2 (on Metop-A), and the settings that differ from the operational retrievals (such as the number of layers and the way the detector pix-

els are combined) are described. The retrieved profiles are validated with ozone sondes from the World Ozone and Ultraviolet Radiation Data Centre (WOUDC), with collocation criteria that the sonde station should be inside the ground pixel footprint, the sonde should have reached at least 10 hPa and the time difference between satellite overpass and sonde launch should be less than 2 hr. The mean differences between the satellite instruments and the ozone sondes are between 0–10 % from the surface up to 10 hPa. The analyis of OPERA retrievals under ozone hole conditions was extended in altitude using lidar observations from the mid-latitude station in Río Gallegos (51° S, 69.3° W). OPERA is capable of retrieving correct ozone profiles over this station, even if the a priori is not representative of the air mass over the station due to the rotation of the polar vortex.

Measurements from GOME-2 and OMI are combined with the chemical transport model TM5 using a Kalman filter data assimilation technique in Chapter 4. Ozone profiles for the period 2008–2011 are retrieved with OPERA from GOME-2 measurements, while for OMI the operationally retrieved profiles are used. All information that is present in the retrievals (i.e. averaging kernels, covariance matrices and of course the profiles themselves), is used in the assimilation. The model covariance matrix is expensive to calculate, and is parameterized into a time dependent standard deviation field and a time independent correlation field. Biases between the two instruments are minimised by applying an ozone sonde based correction, which is applied to all measurements before they are assimilated. The uncertainty in the satellite measurements is assessed with a novel method, which does not depend on any ground based data. For a given wavelength, the radiance difference between two adjacent detector pixels is calculated and stored for a large number of measurements. The resulting distribution is assumed to be Gaussian, and the standard deviation of the fitted distribution is compared to the supplied measurement uncertainty. Biases with respect to ozone sondes for the simultaneous assimilation of GOME-2 and OMI observations vary between -5 % and +10 % between the surface and 100 hPa, and between -3 % and +3 % in the region between 100 and 10 hPa where both instruments are most sensitive.

The same GOME-2 and OMI data described in the previous paragraph were assimilated for 2008 in a high spatial resolution version of the assimilation algorithm to study tropospheric ozone (in this thesis the 0–6 km partial ozone column). The horizontal model resolution was upgraded by a factor of six, and to reduce computational cost, the vertical model resolution was reduced from 44 to 31 layers. At the same time, the meteorological data used in the model was upgraded from ECMWF's operational datastream to the ERA-Interim dataset. The derived tropospheric columns were validated with ozone sonde measurements. The difference between assimilated total columns from DOAS measurements and the 6 km to top of atmosphere partial column from the assimilated profiles showed a too large variation to be used reliably. Therefore, the directly integrated partial column between 0

and 6 km should be used instead. The median global bias is smaller for the assimilation model run than for the free model run, but the large variation makes it difficult to make definitive statements on a regional or local scale. Features such as enhanced ozone concentrations as a result of biomass burning and ozone rich air flowing from Asia over the Pacific are more clear in the assimilated results than in the free model run.

For future tropospheric ozone research, it would be an advantage if the vertical resolution and sensitivity of OPERA in the troposphere could be increased. This might be possible by extending the wavelength range used in the retrieval with the Huggins or Chappuis bands, or by including measurements from the thermal infrared. The uncertainties in the spectral measurements of different instruments can be derived using the new, in-flight method described in Chapter 4. In that case, all retrievals have consistently derived uncertainty levels, which is an advantage when the retrievals are assimilated into the chemical transport model TM5. Other TM5-related settings might also be updated, such as the parameterized ozone chemistry and the climatology used to nudge the model towards an equilibrium state. With these updates, the assimilation algorithm might be extended with other instruments such as IASI and the SBUV instruments, to create a long term time series that will span nearly 50 years. New polar-orbiting instruments such as TROPOMI, GOME-2 on Metop-C, Sentinel 5 and geostationary instruments such as Sentinel 4, TEMPO and GEMS can also be used to extend such a time-series further into the future.

Samenvatting

Ozon (0_3) heeft direct en indirect invloed op de menselijke gezondheid (afhankelijk van de hoogte wordt het soms "goede" of "slechte" ozon genoemd) en het speelt een belangrijke rol in het temperatuur verloop in de atmosfeer. Vanwege de invloed van ozon op luchtkwaliteit en klimaatverandering is het doel van dit proefschrift het verbeteren van ons begrip van de mondiale verdeling van ozon in tijd en ruimte, niet alleen in de stratosfeer, maar ook in de troposfeer, waar het een directe invloed heeft op levende organismen.

In dit proefschrift wordt ozon gemeten met instrumenten op satellieten die het gereflecteerde zonlicht meten in het ultraviolet en visuele (UV-VIS) golflengte bereik ($280 < \lambda < 330$ nm). In het UV-VIS varieert de mate van absorptie van ozon met enkele ordes van grootte, wat de hoogte informatie van de ozon verdeling verschaft. De ozon profielen worden uit de gemeten straling afgeleid met de optimal estimation techniek. Om optimaal gebruik te maken van de voordelen van zowel waarnemingen en atmosferische modellen, worden ze gecombineerd met het Kalman filter, een data assimilatie techniek. De assimilatie uitvoer bestaat uit een regelmatig 3D ozon veld op vaste tijdsintervallen zonder ontbrekende data.

Ozon profielen die worden afgeleid uit UV-VIS satelliet metingen hebben een beperkte gevoeligheid voor veranderingen in hoogte die wordt geschat op 7–10 km in de stratosfeer, met toenemende waardes hoger en lager in de atmosfeer. In Hoofdstuk 2 controleren we daarom of de operationeel afgeleide ozon profielen met het Ozone ProfilE Retrieval Algorithm (OPERA) in staat zijn om de scherpe ozon gradiënten weer te geven die voorkomen onder ozongat omstandigheden. OPERA wordt gebruikt voor het afleiden van ozon profielen in de periode September-December 2008, die worden gevalideerd met onafhankelijke ozon sonde metingen van het Antarctische onderzoeksstation Neumayer. De resultaten tonen aan dat OPERA in staat is tot het afleiden van ozon profielen onder moeilijke ozongat omstandigheden, ook als de a priori informatie niet representatief is voor ozongat omstandigheden. Er is ook een gegridde dataset ($1° \times 1°$) gemaakt om de ontwikkeling en het uiteenvallen van het ozongat te bestuderen tijdens het ozongat seizoen in 2008. Van September tot en met Oktober vindt de maximum ozon afbraak plaats op een hoogte tussen 100 en 50 hPa, terwijl het in November en December wat lager is (tussen 100 en 70 hPa), met hogere concentraties daarboven. Het ozongat seizoen eindigt met de instroom van ozon rijke lucht van bovenaf, wat uiteindelijk leidt tot het uiteenvallen van het ozongat.

We breiden de analyse van de afgeleide ozon profielen uit naar een mondiale schaal in Hoofdstuk 3. OPERA is hierbij ingesteld voor optimale re-

trievals van zowel GOME als GOME-2 (op Metop-A), en de instellingen die verschillen van de operationele retrievals (zoals het aantal lagen en de manier waarop de detector pixels worden gecombineerd) worden beschreven. De afgeleide profielen worden gevalideerd met ozon sondes van het World Ozone and Ultraviolet Radiation Data Centre (WOUDC), met als collocatie criteria dat het sonde station zich binnen de grondpixel bevindt, de sonde ten minste 10 hPa heeft bereikt en dat het tijdverschil tussen de overkomst van de satelliet en het oplaten van de sonde kleiner is dan 2 uur. De gemiddelde verschillen tussen de satelliet instrumenten en de ozon sondes liggen tussen 0–10 % op hoogtes tussen het oppervlak en 10 hPa. De analyse van de OPERA retrievals onder ozongat omstandigheden is in hoogte uitgebreid met de lidar waarnemingen van het gematigde breedtegraad station in Río Gallegos (51° S, 69.3° W). OPERA kan correcte ozon profielen retrieven boven dit station, zelfs als de a priori niet representatief is voor de lucht massa boven het station als gevolg van de rotatie van de polar vortex.

Metingen van GOME-2 en OMI zijn gecombineerd met het chemisch transport model TM5 door middel van een Kalman filter data assimilatie techniek in Hoofdstuk 4. Ozon profielen voor de periode 2008–2011 zijn afgeleid met OPERA van GOME-2 metingen, terwijl voor OMI de operationeel afgeleide profielen zijn gebruikt. Alle informatie die aanwezig is in de retrievals (averaging kernels, covariantie matrices en natuurlijk de profielen zelf), wordt gebruikt in de assimilatie. De model covariantie matrix is tijdsintensief om te berekenen, en is daarom geparameteriseerd in een tijdsafhankelijk standaard afwijking veld en een tijdsonafhankelijk correlatie veld. Afwijkingen tussen de twee instrumenten zijn geminimaliseerd door toepassing van een op ozon sondes gebaseerde correctie, die wordt toegepast op alle satelliet metingen voordat ze worden geassimileerd. De onzekerheid in de satelliet metingen wordt geëvalueerd met een nieuwe innovatieve methode die niet afhankelijk is van grond metingen. Voor een gegeven golflengte wordt het radiantie verschil tussen twee aangrenzende detector pixels berekend en opgeslagen voor een grote hoeveelheid metingen. Aangenomen wordt dat de uiteindelijke verdeling normaal verdeeld is, en de standaard afwijking van de gefitte verdeling wordt vergeleken met de meegeleverde meet onzekerheid. Afwijkingen met ozon sondes voor de gelijktijdige assimilatie van GOME-2 en OMI waarnemingen variëren tussen -5 % en +10 % op hoogtes tussen het oppervlak en 100 hPa, en tussen -3 % en +3 % op hoogtes tussen 100 en 10 hPa waar beide instrumenten het meest gevoelig zijn.

Dezelfde GOME-2 en OMI data uit de vorige paragraaf zijn geassimileerd voor het jaar 2008 met een hoge resolutie versie van het assimilatie algoritme om troposferisch ozon (in dit proefschrift de 0–6 km partiële ozon kolom) te bestuderen. De horizontale model resolutie is met een factor 6 opgewaardeerd, en om de rekentijd te beperken, is de verticale model resolutie teruggebracht van 44 naar 31 lagen. Tegelijkertijd is de meteorologische data die het model gebruikt opgewaardeerd van ECMWFs operationele

datastroom naar de ERA-Interim dataset. De afgeleide troposferische kolommen zijn gevalideerd met ozon sonde metingen. Het verschil tussen geassimileerde totale kolommen van DOAS metingen en de partiële kolom tussen 6 km en de top van de atmosfeer van de geassimileerde profielen vertoont een te grote variatie om betrouwbaar gebruikt te kunnen worden. In plaats daarvan wordt de direct geïntegreerde partiële kolom tussen 0 en 6 km gebruikt. De mediane mondiale afwijking is kleiner voor de geassimileerde ozon dan voor het vrije model, maar de grote variatie maakt het lastig om beslissende uitspraken te doen voor een regionale of lokale schaal. Kenmerkende elementen zoals verhoogde ozon concentraties ten gevolge van biomassa verbranding en ozon rijke lucht die vanuit Azië over de Stille Oceaan stroomt, zijn duidelijker in de geassimileerde resultaten dan in het vrije model.

Voor toekomstig troposferisch ozon onderzoek zou het voordelig zijn als de verticale resolutie en gevoeligheid van OPERA in de troposfeer verhoogd zouden kunnen worden. Dat is misschien mogelijk door het uitbreiden van het golflengte gebied dat in de retrieval gebruikt wordt met de Huggins of Chappuis banden, of door het gebruik van het thermisch infrarood. De onzekerheid in de spectrale metingen van de verschillende instrumenten kan, na lancering, bepaald worden met de nieuwe innovatieve methode uit Hoofdstuk 4. In dat geval hebben alle retrievals consistent afgeleide onzekerheids niveau's, wat voordelig is wanneer de retrievals in het chemisch transport model TM5 worden geassimileerd. Andere TM5-gerelateerde instellingen kunnen ook opgewaardeerd worden, zoals de geparameteriseerde ozon chemie en de klimatologie die gebruikt wordt om het model naar een evenwichtstoestand te sturen. Met deze updates kan het assimilatie algoritme uitgebreid worden met andere instrumenten zoals IASI en SBUV, om een lange tijdreeks te maken die bijna 50 jaar bestrijkt. Nieuwe instrumenten in een polaire baan, zoals TROPOMI, GOME-2 op Metop-C, Sentinel 5 en geostationaire instrumenten zoals Sentinel 4, TEMPO en GEMS kunnen ook worden gebruikt om zo'n tijdreeks in de toekomst verder uit te breiden.

1

Introduction

1.1. Background

Ozone (O_3) is a trace gas present in all layers of Earth's atmosphere. Despite its low abundance it has a significant role in the climate system and directly and indirectly affects human health, depending on the altitude. The atmosphere is divided into the stratosphere and the troposphere, based on the rate of change of the atmospheric temperature (see section 1.2.2). About 90 % of the atmosphere's ozone can be found in the stratosphere (the region with the maximum ozone concentration is called the ozone layer), the remainder is mostly found in the troposphere.

Stratospheric ozone is sometimes called "good" ozone, because it reduces the UV-B part (wavelengths below 315 nm) from the solar radiation. The World Health Organisation lists several detrimental effects of UV radiation on the human skin, eyes and immune system[1]. UV exposure increases ageing of the skin, high doses can cause sunburn, and prolonged exposure can cause various types of skin cancer of which melanoma is the most dangerous. In the eye, UV radiation can cause inflammations, cancer and blindness caused by cataracts. Too much UV-B radiation supresses the immune system and reduces the effectiveness of vaccinations. UV-B radiation can also negatively affect plant growth and photosynthesis, both for terrestrial plants and for phytoplankton[2]. Despite these negative effects, UV-B radiation is also healthy in small doses, since it has an essential role in the production of vitamin D.

Ozone in the troposphere is sometimes called "bad" ozone because it has direct and detrimental effects on human health[3,4]. It mostly affects the

[1] `http://www.who.int/uv/faq/uvhealtfac/en/index4.html`, retrieved 08-11-2017
[2] `https://earthobservatory.nasa.gov/Features/UVB/`, retrieved 08-11-2017
[3] `https://www.eea.europa.eu/publications/TOP08-98/page010.html`, retrieved 14-11-2017
[4] `https://www.epa.gov/ozone-pollution/health-effects-ozone-pollution`, retrieved

respiratory tract and the lungs, causing e.g. shortness of breath, coughing and a reduced lung function. Respiratory illnesses such as asthma and bronchitis are aggravated by exposure to ozone. Long-term exposure to ozone might increase the mortality rate due to respiratory illnesses. Ozone also negatively affects ecosystems and crop yield because it reduces photosynthesis and plant growth. Because plants react differently to exposure to ozone, the balance between species in an ecosystem may shift as well.

Apart from its direct and indirect effects on living organisms, ozone is also a greenhouse gas. It strongly absorbs solar radiation below 300 nm, which is why the temperature of the stratosphere is increasing with altitude. Therefore, understanding the ozone distribution is important for understanding the thermal structure of the atmosphere. Because of the important role ozone has in the temperature structure of the atmosphere it has been designated as one of the Essential Climate Variables (ECV) by the Global Climate Observing System (GCOS) of the World Meteorological Organisation (WMO) (WMO, 2016). An ECV is defined as a "physical, chemical or biological variable or a group of linked variables that critically contributes to the characterization of Earth's climate". With respect to atmospheric composition ECVs, it is stressed that information on the vertical distribution is essential for understanding, monitoring and modelling climate.

In the 1970s, important research was performed that improved our understanding of the atmospheric ozone distribution. Crutzen (1970) published an ozone destruction cycle involving nitrogen oxide radicals (NO_x) that explains the naturally observed 0_3 distribution (see Section 1.3.2). Molina and Rowland (1974) expressed their concern for the rising concentrations of chlorofluoromethanes (CFCs) and the effect that had on the destruction of stratospheric ozone. The first observations of extreme ozone depletion over the South Pole have been reported by the Japanese scientist S. Chubachi during the Quadrennial Ozone Symposium in 1984 in Halkidiki, Greece (Chubachi, 1985). Generally, the observations published a year later by (Farman et al., 1985) are considered to be the discovery of what became known as the ozone hole. For their work in atmospheric chemistry, particularly concerning the formation and decomposition of ozone, P.J. Crutzen, M.J. Molina and F.S. Rowland shared the Nobel prize for chemistry in 1995[5].

In 1987, the Montreal Protocol on Substances that Deplete the Ozone Layer was signed. The Montreal Protocol intends to control and reduce the production and use of ozone depleting substances. It was amended and adjusted on several occasions since it entered into force in 1989. The Montreal protocol and its amendments have been very successful in reducing the amount of ozone depleting substances (ODS, see Figure 1.1). In the figure, the concentration of each ODS is expressed as the amount of chlorine

14-11-2017

[5] https://www.nobelprize.org/nobel_prizes/chemistry/laureates/1995/, retrieved 13-11-2017

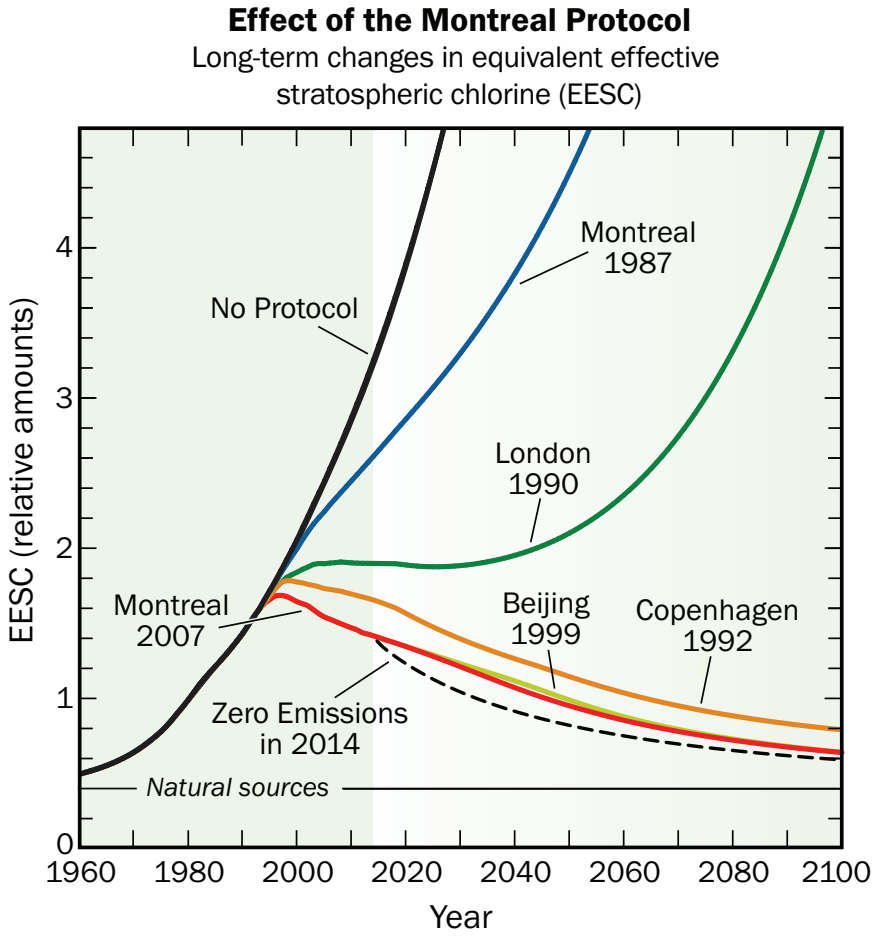

Figure 1.1: Effect of the Montreal Protocol and its subsequent amendments and adjustments on the (future) abundances of ODSs expressed in EESC (figure copied from Hegglin et al., 2015).

it would take to have the same ozone depleting effect. This hypothetical amount of chlorine is the equivalent effective stratospheric chlorine (EESC) for a particular ODS. Since 2009 it has been ratified by all 196 United Nations members.

The status of the ozone layer above the South Pole since 1970 is shown in Figure 1.2, where the mean total ozone for October are plotted based on the Multi Sensor Reanalysis (MSR; van der A et al., 2010, 2015). The MSR assimilates total ozone measurements from all available satellite instruments since 1970. The grey colour in the plots indicates the locations where the uncertainty of the derived ozone is too high.

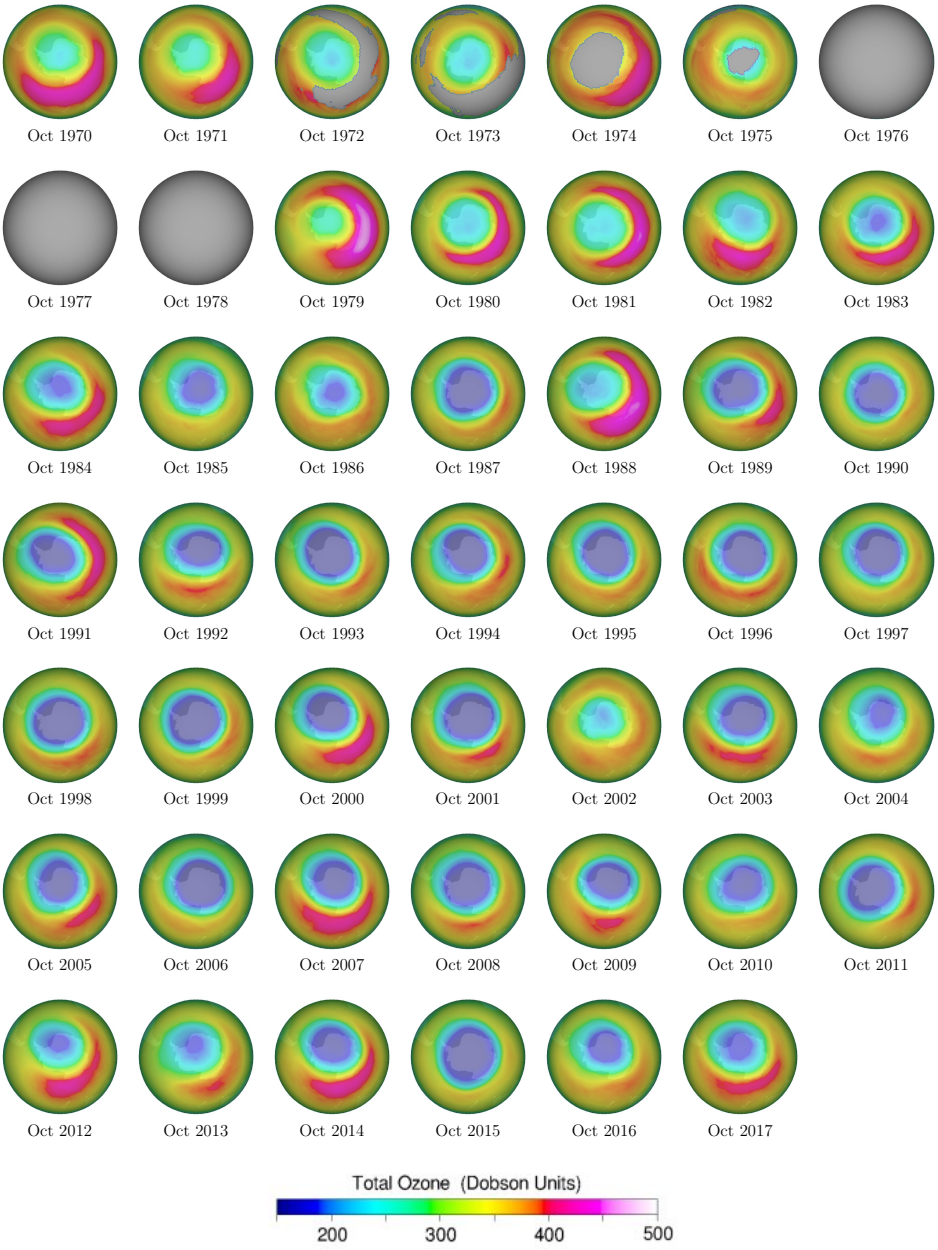

Figure 1.2: Averaged total ozone columns for the month October from the Multi Sensor Reanalysis. The grey colour in the plots indicates regions where the uncertainty of the derived ozone is too high.

1.2. Atmosphere

1.2.1. Composition

Planet Earth is covered with a thin layer of air called the atmosphere. Since the density of the atmosphere decreases continuously with higher altitude, there is no clear altitude where the atmosphere ends and outer space starts. A commonly used definition for the thickness of the atmosphere is 100 km, which is about 1.6 % of Earth's radius. However, this thin layer of air is essential for life on Earth: it filters ultra violet radiation and prevents the radiation from reaching the surface, the natural greenhouse effect warms the surface and the incident energy from the sun is redistributed over the surface of the Earth.

The atmosphere is composed of different gases. The amount of a gas can be given as the mixing ratio: the number of moles of that gas divided by the total number of moles of air. Assuming that the ideal gas law is valid in the atmosphere, the mixing ratio is equivalent to the volume mixing ratio (vmr): the volume of the gas divided by the volume of the air. The atmosphere consists mostly of nitrogen (78 %), oxygen (21 %), argon (0.93 %) and other trace gases such as carbon dioxide (400 parts per million by volume (ppmv)), methane (1.8 ppmv) and ozone (0–10 ppmv). These values are for dry air, the vmr of water vapour varies from a few ppmv to 0.04.

When the column density is given between the surface and the top of the atmosphere (TOA) it is usually referred to as the total column (density), the column density between other levels is called the partial column (density). The vertical column density can be expressed in Dobson units (DU), named after G.M.B. Dobson who made the first instrument to measure the total ozone column ($1\,\mathrm{DU} = 2.687 \times 10^{20}$ molecules m^{-2}).

1.2.2. Structure

The temperature of the atmosphere changes as a function of altitude. The rate at which the temperature changes is called the lapse rate (Γ), which is the negative value of the rate of change of temperature (T) as a function of altitude (z): $\Gamma = -\partial \mathrm{T} / \partial z$. The atmosphere is usually divided into layers based on sign changes of the lapse rate. From the surface of the Earth upwards, these layers are the troposphere, stratosphere, mesosphere and thermosphere. The regions between the layers where the lapse rate is close to 0, are called the tropopause, stratopause and mesopause respectively. The different "spheres" and "pauses" are indicated in Figure 1.3, which shows a schematic temperature profile based on the United States Standard Atmosphere (NOAA et al., 1976), and an ozone profile from the climatology by (McPeters et al., 2007). In this climatology, altitude is expressed as $z^* = 16 \times \log(1013 / P)$, where z^* is a number between 0 and 60 and P is the pressure at a given altitude, so each layer is approximately a km thick.

A widely used definition of the tropopause is based on the lapse rate (WMO, 1957): it is the lowest level at which the lapse rate decreases to $2^\circ\,\mathrm{C\,km^{-1}}$ or less, provided that the average lapse rate between this level and all higher levels within 2 km does not exceed $2^\circ\,\mathrm{C\,km^{-1}}$. Because it only depends on the lapse rate, this definition is often referred to as the lapse rate tropopause or the thermal tropopause. Other tropopause definitions have been used, based on the dynamical properties of the atmosphere or the gradient in the ozone concentration.

Because the atmospheric lapse rate in the troposphere is generally larger than the adiabatic lapse rate, the air is unstable and subject to turbulence and mixing. The lowest part of the troposphere, between the surface and 0.1 to 3 km where the influence of the surface on the atmosphere is largest, is called the planetary boundary layer. The thickness of the troposphere varies from approximately 7–8 km at the poles to 18 km around the equator.

UV light is absorbed by ozone, which causes an increase in temperature in the stratosphere with altitude. This results in a stable, stratified region of the atmosphere (hence the name stratosphere). The total mass of the atmosphere is about 5.2×10^{18} kg of which 99.9 % is contained within the combined troposphere and stratosphere. The troposphere contains almost all of the water in the atmosphere. The troposphere and stratosphere are the regions of the atmosphere that are most important from a climate and environmental point of view.

1.3. Ozone

1.3.1. Global distribution

McPeters et al. (2007) combined ozone measurements from the Stratospheric Aerosol and Gas Experiment II (SAGE II; 1988–2001), Microwave Limb Sounder (MLS; 1991–1999) with data from ozone sondes (1988–2002). An illustration of the resulting climatological ozone distribution for the months of April and October is given in Figure 1.4.

There are two important things to note from Figure 1.4 regarding the maximum ozone concentration: its altitude is highest in the tropics, and the largest values are found at higher latitudes. In the right panel of the plot the ozone hole (see section 1.3.2) is also clearly visible near the South Pole. The altitude of the maximum ozone concentration is highest in the tropics because most of the solar energy is absorbed in that region. The heating results in turbulent motion, pushing the air upwards. The chemical reactions that produce ozone (see sections 1.3.2 and 1.3.3) all require light, so one might expect that most ozone can be found in the tropics. However, this is not the case because stratospheric air is transported away from the tropics towards the poles in a process known as the Brewer-Dobson circulation. The Brewer-Dobson circulation results from tropospheric waves propagating up into the stratosphere, where they break and transfer energy

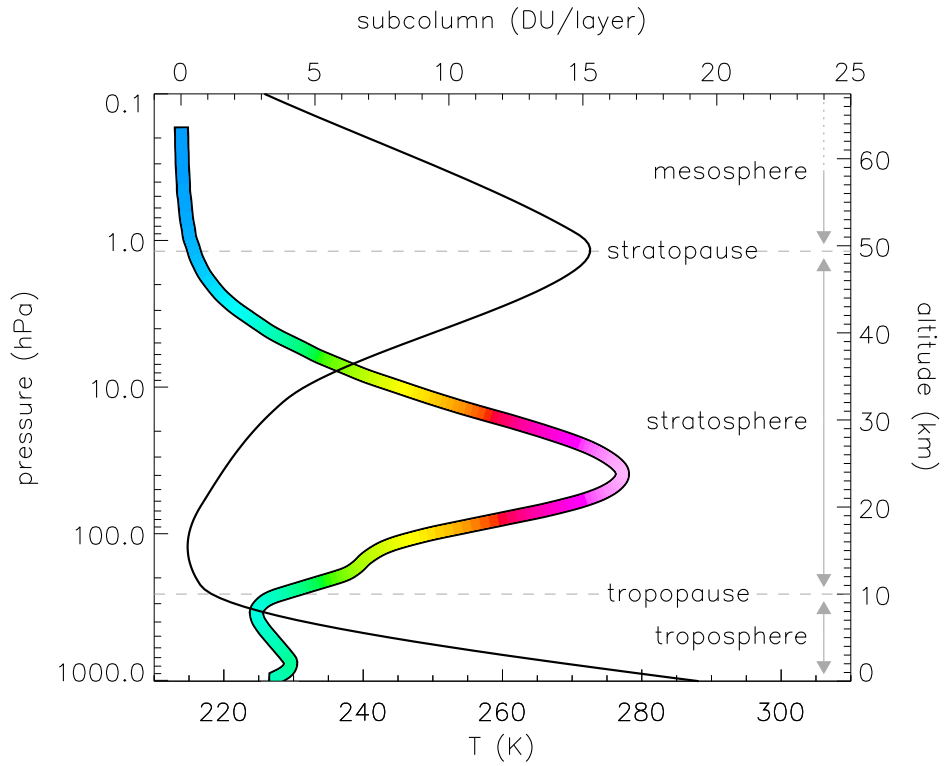

Figure 1.3: Schematic representation of the atmospheric structure. The solid line is a temperature profile based on the US Standard Atmosphere, with the corresponding values on the lower x-axis. To the right of the plot area, the atmospheric layers and transitions between them are also indicated. The colored band shows the ozone profile from the climatology by (McPeters et al., 2007) in DU layer^{-1} for June in the region between 40° and 50° North, with the corresponding values on the upper x-axis.

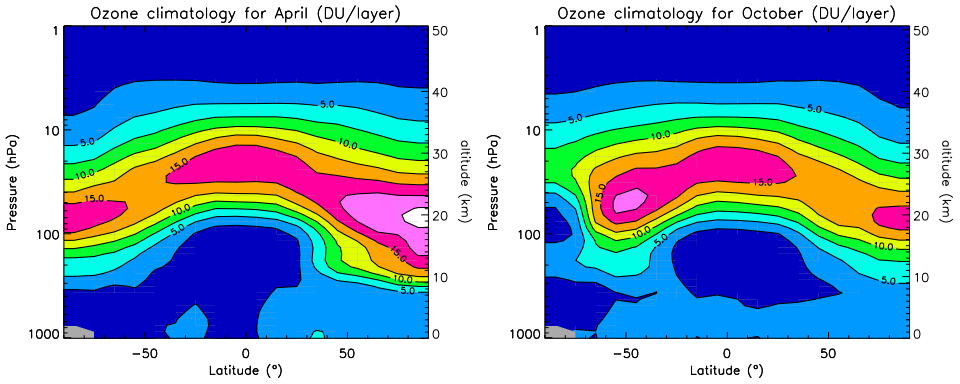

Figure 1.4: Ozone distribution from the climatology by McPeters et al. (2007) in DU layer^{-1} for April (left) and October (right).

and angular momentum. The conservation of angular momentum results in the poleward mass transport of the Brewer-Dobson circulation. The mass transport is strongest in the winter hemisphere, because the planetary (Rossby) waves contain more energy due to the larger temperature difference between the polar regions and the equator. The Brewer-Dobson circulation is stronger in the Northern hemisphere than in the Southern hemisphere due to the larger orography differences that influence the Rossby waves. A recent overview of the Brewer-Dobson circulation is given in Butchart (2014).

1.3.2. Stratospheric ozone chemistry

The production of ozone in the stratosphere can be qualitatively explained by the Chapman mechanism (see e.g. Chapman, 1929). This is a chain of chemical reactions involving oxygen, sunlight and other molecules (the reactions indicated in red in Figure 1.5). The first reaction (middle left in the plot) is the photodissociation of an oxygen molecule into two oxygen atoms by high energy photons with a wavelength of less than 240 nm. Since molecular oxygen is still abundant at these altitudes, the free O atoms quickly recombine with oxygen to form ozone. Here, M is an inert molecule, which is usually N_2 or O_2. The O_3 produced by this reaction can be converted back to molecular and atomic oxygen under the influence of light with a wavelength of 320 nm or smaller, or recombine with a free O atom to form O_2. These reactions have different reaction rates, and the steady state solution gives an O_3 profile of which the shape resembles the observed profile. However, the predicted concentrations are too high by a factor of two or more.

The missing reactions in the Chapman scheme are catalytic cycles: series of chemical reactions involving a catalyst. The catalyst reacts with the other reactants, but is not removed from the system. Therefore, the series of chemical reactions can run repeatedly, before the catalyst is removed by other processes. Two catalytic cycles form significant sinks for ozone and are required to bring the Chapman mechanism in accordance with the naturally observed O_3 distribution: one involving nitrogen oxide radicals (NO_x, marked I and highlighted in green in Figure 1.5), and a second one involving hydrogen oxide radicals (HO_x, marked II and highlighted in blue in Figure 1.5). The NO and OH that are involved in these two catalytic cycle are produced in the reactions of N_2O and H_2O with the excited O atom that results from the photodissociation of O_3 (top right in Figure 1.5).

N_2O (nitrous oxide or laughing gas) is formed in the troposphere, for the largest part due to natural processes (> 60 %) like nitrification and denitrification. The remainder is anthropogenic in origin and is produced in agriculture, fuel combustion and industry. N_2O has a lifetime of more than 100 years, so eventually it is transported up into the stratosphere. There it is oxidized by the high energy oxygen atom produced by the photodissociation of O_3 and forms nitric oxide (NO), which destroys O_3 in a catalytic cycle producing NO_2 (see e.g. Crutzen, 1970). Nitrogen dioxide (NO_2) can be

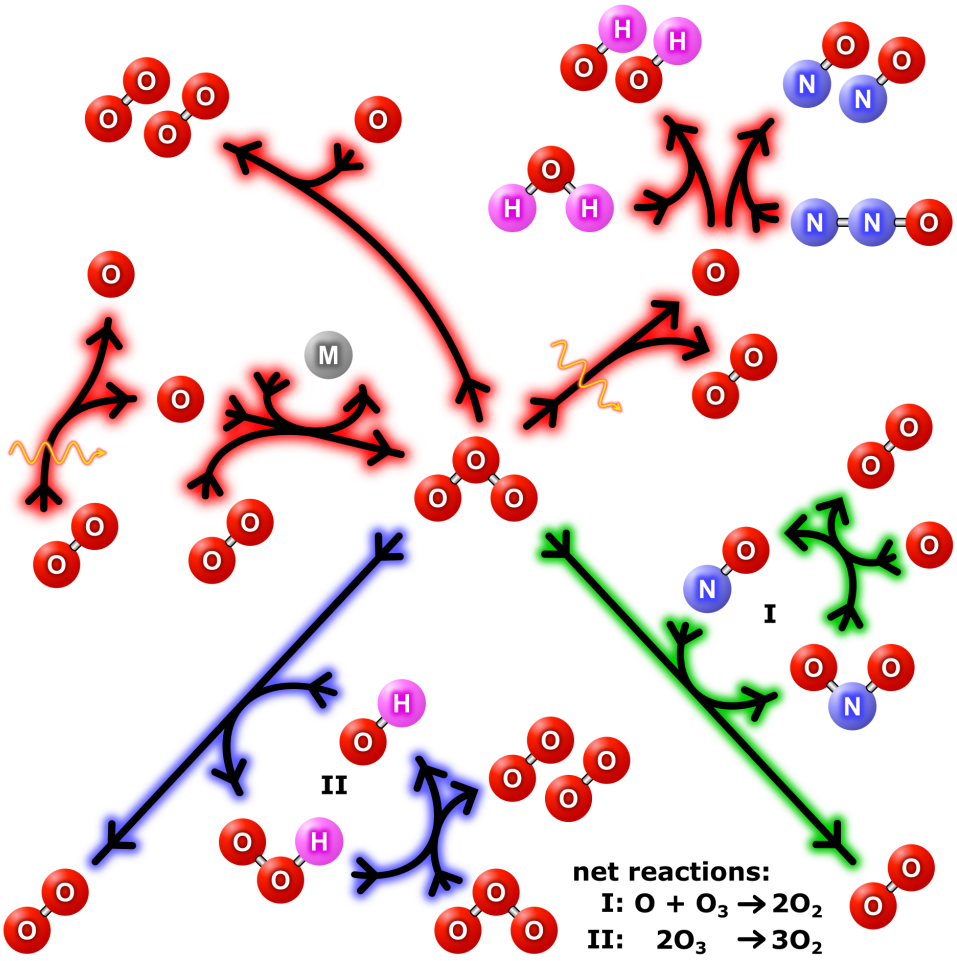

Figure 1.5: Natural occurring stratospheric ozone production and loss reactions. The Chapman mechanism is indicated by the red reactions. The photodissociation of O_2 (middle left) requires light with a wavelength of maximum 240 nm, while the photodissociation of O_3 (top right) requires light with a wavelength of maximum 320 nm. To bring the Chapman mechanism in agreement with naturally occurring ozone concentrations, two catalytic ozone destruction cycles (green and blue reactions) are required. The net reactions of these cycles are given in the lower right hand of the plot.

1

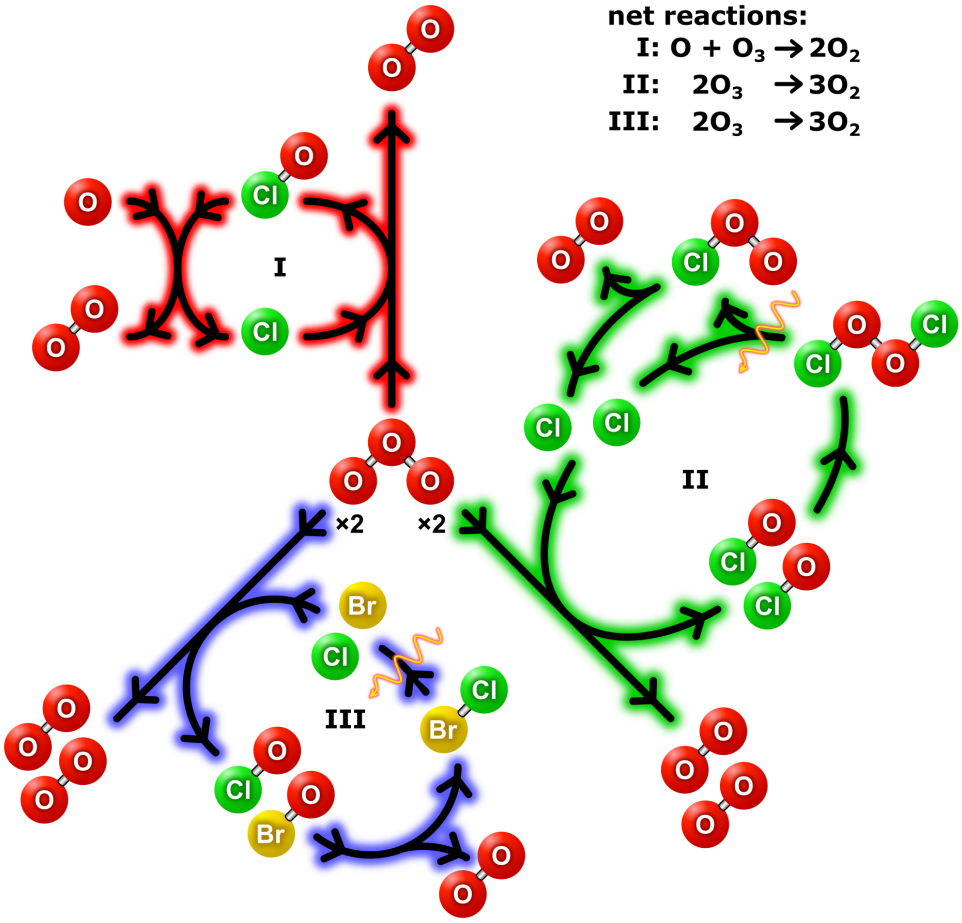

Figure 1.6: Catalytic ozone destruction cycles involved in the depletion of ozone layer. The photodissociation of ClOOCl in cycle II and BrCl in cycle III both require visible light. Because O is most abundant at low and mid-latitudes, cycle I is more important for those regions, while cycle II and III are more important for ozone loss at the poles. Note that the heterogeneous reactions on the surface of PSC particles (see equation 1.1) have not been plotted.

oxidized by OH and O_3 to form HNO_3 and N_2O_5, which serve as reservoirs for NO_x. Eventually, the catalytic cycle ends because of the transport of HNO_3 to the troposphere and subsequent removal by deposition.

In the second catalytic cycle, ozone reacts with the hydroxyl radical (OH) and forms the unstable and shortlived hydroperoxyl radical (HO_2). The hydroxyl radical is produced by the oxidization of water by the excited oxygen atom, which in turn is the result of the photo-dissociation of ozone.

The Chapman mechanism and the NO_x and HO_x related catalytic cycles give an ozone profile that resembles the natural occuring ozone distribution. However, other catalytic cycles involving halogen gases are required to explain the destruction of ozone around the globe. For the formation of the ozone hole during Antarctic springtime, heterogenous reactions on polar stratospheric clouds (PSCs) are also required (see below). Halogen gases such as chlorofluorocarbons (CFCs) are man-made gases for industrial purposes. They are stable gases with very long lifetimes (e.g. 100 years for CFC-12 (WMO, 2014)) and when they are emitted into the atmosphere they eventually reach the stratosphere. In the stratosphere, halogens are photodissociated resulting in Cl and Br radicals, which are key constituents of catalytic ozone destruction cycles shown in Figure 1.6.

These three catalytic cycles are responsible for the major part of stratospheric ozone loss, and they all require sunlight. The first cycle (see e.g. Molina and Rowland, 1974) requires the presence of free O atoms, which are most abundant at low and mid-latitudes. Therefore, this cycle is responsible for most ozone loss in the tropics and mid-latitudes, but near the poles, cycles II and III are more important for ozone loss.

Because most halogens are stable compounds with long lifetimes, they are present throughout the entire atmosphere in comparable concentrations. However, ozone loss is most severe over Antarctica because of a combination of unique properties. During austral winter, a strong polar vortex can develop around Antarctica. The polar vortex is a strong westerly circulation pattern that effectively isolates polar air from midlatitudes. Inside the polar vortex, temperatures reach values in wintertime that are low enough for polar stratospheric clouds (PSC) to form. PSCs are clouds containing ice particles that form in the stratosphere when the temperature drops below 197 K. On the surface of the PSCs a reaction between the reservoir species $ClNO_3$ and HCl of Cl can occur:

$$ClNO_3 + HCl \xrightarrow{PSC} Cl_2 + HNO_3 \tag{1.1}$$

During the Antarctic winter, Cl_2 concentrations continue to rise. At the same time, PSCs containing HNO_3 are removed from the stratosphere by sedimentation. When the light returns in spring, Cl_2 is photodissociated yielding 2 Cl atoms that can start the catalytic cycles described above. Since HNO_3 is removed by sedimentation of PSCs, the reservoir species $ClNO_3$ is not formed so the ozone destruction can continue till springtime temperatures have risen enough to prevent PSCs from forming.

1.3.3. Tropospheric ozone chemistry

Ozone occurs naturally in the troposphere, but concentrations have increased due to human activity. It can be transported from the stratosphere down to the troposphere in stratosphere-troposphere exchange events. Locally, ozone is produced primarily by reaction cycles involving carbon monoxide (CO), methane (CH_4) and other hydrocarbons (RH, where R is any organic group). These reaction cycles all require light and NO_x. The most important source sectors of these pollutants are transport and industry. The mixture of nitrogen oxides, ozone, aerosols and other pollutants is called smog (smog = smoke + fog) and usually the term photochemical smog is used for the reactions that produce particulate matter and ozone.

The first step in these reaction cycles is the oxidation with the hydroxyl radical (OH). OH plays an important role in the oxidizing capacity of the atmosphere and reacts with many natural and anthropogenic emitted gases. Because of the important role OH has in removing these gases from the atmosphere, it is often referred to as an "atmospheric detergent" (see e.g. Crutzen, 1986). The main source of OH in the troposphere is the photodissociation of O_3 by light with a wavelength between 300 and 320 nm (light with a shorter wavelength does not reach that far down into the atmosphere, and light with a longer wavelength does not have enough energy for photodissociation of O_3). In this reaction an excited oxygen atom is produced, which has enough energy to react with water to produce OH. The production of OH requires O_3, but oxidation of CO and CH_4 by OH also produces O_3, under circumstances with high concentrations of NO_x. It is interesting to note that chemical species such as OH and NO_x that deplete O_3 in the stratosphere might actually increase O_3 levels in the troposphere. This is due to the much lower concentrations of O and O_3 in the troposphere compared to the stratosphere.

1.4. Measurement principles

There are basically two options to measure ozone in the atmosphere: using in situ or remote sensing techniques. Note that this distinction does not assume anything on the location of measurement instruments. For example, an in situ instrument can be attached to a balloon or put on a plane to measure an ozone profile, while a remote sensing instrument can be located on the ground or attached to a satellite.

In situ techniques measure the ozone concentration of the local ambient air. The air is drawn into the instrument where the ozone concentration can be determined using for example, an electrical chemical cell or chemiluminescent reactions.

Remote sensing techniques operate on the principle of ozone absorbing or emitting electromagnetic radiation in various wavelength ranges.

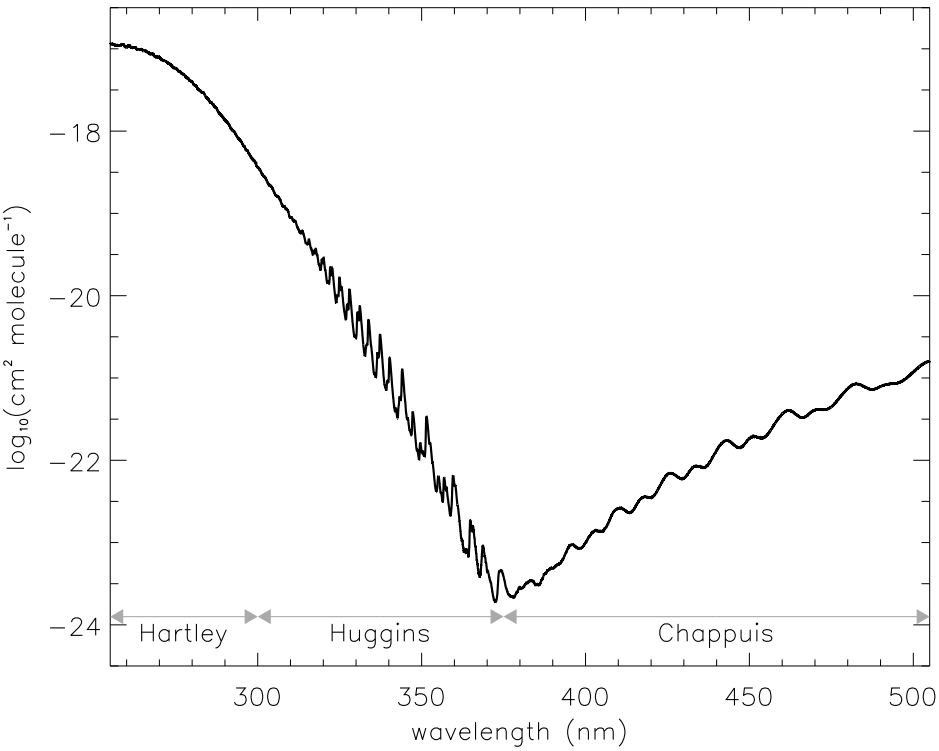

Figure 1.7: Ozone absorption cross-sections at 250K from the data by Brion et al. (1993, 1998); Daumont et al. (1992); Malicet et al. (1995). The wavelength ranges for the Hartley, Huggins and Chappuis absorption bands have been indicated.

In Figure 1.7, the absorption cross section (Brion et al., 1993, 1998; Daumont et al., 1992; Malicet et al., 1995) for ozone at 250 K has been plotted between 255 and 505 nm.

This wavelength range is usually divided into three absorption bands. The maximum absorption peak around 255 nm is called the Hartley absorption band, after the British scientist W.N. Hartley. The sharp absorption peaks between 300 and 375 nm are part of the Huggins band, named after the British astronomer W. Huggins. Finally, the broad absorption band between 375 and 650 nm is named after the French chemist J. Chappuis.

The atmosphere does not emit radiation in the Hartley, Huggins and Chappuis absorption bands because the temperature is too low (black body radiation at solar temperatures has a maximum emission at 500 nm, while at atmospheric temperatures it peaks around 10 μm). The radiation from these bands that is detected by satellite instruments is reflected solar light. The difference in absorption cross section in the Hartley-Huggins band between the maximum at 255 nm and the minimum near 375 nm is more than

6 orders of magnitude (at 255 nm, most of the solar radiation is absorbed by ozone, while at 375 nm, the atmosphere is mostly transparent for solar radiation). Due to this large difference and because of the sharp peaks in the Huggins bands, the absorption spectrum in this wavelength range contains information on the vertical ozone distribution. The Chappuis absorption band peaks around 600 nm, but is much weaker and had less pronounced absorption features than the Hartley-Huggins bands. Therefore, there is much less information on the ozone distribution present in radiation in the Chappuis band compared to the Hartley-Huggins bands. The Chappuis band is therefore mostly used to retrieve the ozone total column, or to enhance the information content of the retrieval in the troposphere (see e.g. Miles et al., 2015).

There are also a number of ozone emission lines in the thermal infrared (TIR, i.e. the wavelength range where the atmosphere emits radiation), most notably near 9.6 μm. At this wavelength, there's no reflected sunlight but the radiation is emitted by the ozone in the atmosphere itself. This emission line is used by TIR instruments, like IASI, to measure ozone.

1.5. Ground based observations

Ozone observations are routinely done from meteorological stations using a variety of instruments such as ozone sondes, lidar (LIght Detection And Ranging) and microwave. Ozone sondes are balloon-based instruments which are launched from the ground based station and drift upward through the atmosphere. During the flight, an ozone sonde measures the ozone concentration as it reacts with a chemical solution inside the sonde. In the entire altitude range (0–35 km) of the sonde, the response time of the sensor is about 20–30 s, and since the normal ascent velocity is about 5 m s^{-1}, the vertical resolution of ECC ozone sondes is about 100–150 m (Smit et al., 2007). Since an ozone sonde continuously samples the ambient air, it is classified as an in situ measurement. Ozone sonde measurements are collected in various databases, such as the general World Ozone and Ultraviolet Radiation Data Centre (WOUDC, `http://www.woudc.org`) and the Network for the Detection of Atmospheric Composition Change (NDACC, `http://www.ndsc.ncep.noaa.gov/`) or more focused on the tropical region such as the Southern Hemisphere ADditional OZonesondes (SHADOZ, `https://tropo.gsfc.nasa.gov/shadoz/`).

Lidar and microwave on the other hand are examples of active remote sensing instruments. Both emit radiation that is absorbed by ozone: an ozone lidar uses a UV-laser and microwave instrument obviously uses microwave radiation. Both lidar and microwave measurements can be obtained from the NDACC website mentioned above. In general, lidar profiles are accurate between about 15–50 km, with a vertical resolution varying between 1 km at 30 km altitude and 5 km at 40 km altitude (Steinbrecht et al., 2006). Microwave observations are used in the range between 20–60 km altitude, with a vertical resolution of 7–10 km (Steinbrecht et al., 2006). Lidar

measurements focused on tropospheric ozone are available for a number of North American stations from the Tropospheric Ozone Lidar Network (TOLNet, https://www-air.larc.nasa.gov/missions/TOLNet/).

A drawback of ground-based measurements is that it is impossible to obtain global coverage, since a measurement station is essentially a point source. In addition, the measurement stations are concentrated on the Northern Hemisphere in Europe and North America. The only way to obtain global coverage is to use satellite observations. Two obvious advantages of groundbased measurements are that they are cheap with respect to satellite missions, and the instruments are easily accessible for maintenance.

1.6. Satellite based observations

1.6.1. Total ozone

This thesis focuses on vertical profiles of ozone derived from satellite-based measurements. Although it is possible to integrate the profiles to obtain the total ozone column, usually total ozone is obtained by the differential optical absorption spectroscopy (DOAS) technique.

In a DOAS retrieval, only a small part of the UV-spectrum in the Huggins band around 330 nm is used to retrieve the total ozone column. First, the reflectivity (R) is calculated by dividing the Earth radiance spectrum ($I(\lambda)$) by the Solar spectrum ($F_0(\lambda)$)

$$R(\lambda) = \frac{I(\lambda)}{\mu_0 F_0(\lambda)} \tag{1.2}$$

here, μ_0 is the cosine of the solar zenith angle. The reflectivity can also be written as the reflectivity one would obtain if there was no ozone present ($R_0(\lambda)$), multiplied by an exponential decay function (i.e. the Lambert-Beer law)

$$R(\lambda) = R_0(\lambda) \exp(-N_s \sigma(\lambda)) \tag{1.3}$$

where $\sigma(\lambda)$ is the ozone cross sections and N_s is the average light path through the atmosphere (i.e. slant column density). Once the slant column density has been calculated, it is converted into the vertical column density by dividing it by the air mass factor (M, i.e. the path length divided by atmospheric height)

$$N_v = \frac{N_s}{M} \tag{1.4}$$

If the main research interest is total ozone, the DOAS retrieval technique has a number of advantages over retrieving and integrating a profile. For a DOAS retrieval, an absolute calibrated spectrum is not required since only the reflectivity is used. For determining the slant column density, no information on surface reflection or cloud and aerosol properties is required. These quantities are included in the air mass factor, which is usually calculated off-line and stored in look-up tables. Because no online radiative

transfer calculations are required during the retrieval, DOAS retrievals are much faster than profile retrievals.

DOAS retrievals of total columns are accurate to a few percent when compared to ground based measurements such as Brewer and Dobson spectrometers. The accuracy can be improved by using a direct fitting method instead of a differential fit as in the GODFIT algorithm (GOme Direct FITting). For example, the algorithm has been implemented in the operational GOME Data Processor version 5 (GDP5; Van Roozendael et al., 2012). An improved version of GODFIT has been used to derive a homogenized total ozone column dataset from the European satellite instruments GOME, GOME-2 (Metop-A; Munro et al., 2016) and SCIAMACHY (Lerot et al., 2014).

1.6.2. Ozone profiles

It is clear that the total ozone column does not provide a 3D distribution. As mentioned in section 1.1, the atmospheric essential climate variables require knowledge on the vertical distribution. The only feasible way to obtain the global, vertical ozone distribution is by observations through satellite instruments. There are a number of different techniques to obtain a trace gas profile from a satellite instrument. In the limb viewing geometry, the instrument measures scattered sunlight, and is pointing through the atmosphere, but not at the Earth. Limb measurements are only reliable in the stratosphere, and the vertical resolution is high, but the horizontal resolution is low. For example, for data version 2.2 of the microwave limb sounder onboard the AURA satellite, there are about 240 limb scans per orbit and the ozone profiles should only be used between 215 and 0.02 hPa (Froidevaux et al.). Occultation instruments look through the atmosphere at the Sun or other stars. The Global Ozone Monitoring by Occultation of Stars (GOMOS) instrument onboard ENVISAT has an altitude range from 5–15 km (night) or 15–25 km (day) up to the top of the atmosphere (120–150 km) with a vertical resolution of 1–1.7 km (Bertaux et al., 2010). A nadir looking instrument on the other hand, looks down from the satellite towards the Earth. The viewing geometry aside, satellite instruments make use of different wavelength bands such as the UV-VIS or infrared. For example, the GOME-2 and IASI instruments are both nadir looking instruments on the Metop series of satellites, but GOME-2 measures the UV-VIS spectrum, and IASI the thermal infrared. Once a spectrum has been measured, the vertical ozone distribution can be inferred from it. The nadir looking UV-VIS instruments measure from the surface up to an altitude of about 80 km, with a vertical resolution of about 7–15 km (Hoogen et al., 1999; Liu et al., 2010).

In general, for a measurement vector $\mathbf{y}$ and a vector describing the state of the atmosphere (i.e. the state vector) $\mathbf{x}$ we can write:

$$\mathbf{y} = F(\mathbf{x}) + \boldsymbol{\epsilon} \tag{1.5}$$

where F is the forward model containing all physics such as radiative trans-

fer, and $\boldsymbol{\epsilon}$ is the measurement noise. To obtain a solution to equation 1.5, one could construct a cost function and calculate $\mathbf{x}$, which minimises the cost function. Assuming that $\mathbf{x}$ and $\mathbf{y}$ have Gaussian probability density functions, the cost function is given by the least-squares method:

$$C = (\mathbf{y} - F(\mathbf{x}))^T \mathbf{S}_\epsilon^{-1} (\mathbf{y} - F(\mathbf{x})) \tag{1.6}$$

where $\mathbf{S}_\epsilon$ is the measurement error covariance matrix. However, the problem is often underdetermined (i.e. there are less measurements than unknowns) and if a solution to the cost function can be found, it is not unique. To prevent this, the solution is further constrained by adding a term to the cost function to include available a priori information. This procedure is known as optimal estimation (or finding the maximum a posteriori solution, see e.g. Rodgers, 2000), and the cost function becomes:

$$C = (\mathbf{y} - F(\mathbf{x}))^T \mathbf{S}_\epsilon^{-1} (\mathbf{y} - F(\mathbf{x})) + (\mathbf{x} - \mathbf{x}_a)^T \mathbf{S}_a^{-1} (\mathbf{x} - \mathbf{x}_a) \tag{1.7}$$

where $\mathbf{x}_a$ is the a priori profile and $\mathbf{S}_a$ is the a priori error covariance matrix. Finding a minimum for the cost function yields the retrieved profile $\hat{\mathbf{x}}$ and its associated covariance matrix $\hat{\mathbf{S}}$ (see Chapter 3). The same equations can be found if the retrieval problem is viewed from a Bayesian point of view.

Another method to make the least-squares cost function better behaved is by regularization. Several regularisation techniques are developed by Tikhonov, Twomey and Phillips in the early 1960's. In regularization, some form of the norm of $\mathbf{x}$ is added to the least-squares solution of equation 1.6: $\lambda (\mathbf{x} - \mathbf{x}_0)^T \mathbf{L} (\mathbf{x} - \mathbf{x}_0)$. Here, λ is a regularization factor that weighs the relative contribution of the least-squares solution and the norm, and $\mathbf{L}$ is the regularization matrix. The vector $\mathbf{x}_0$ might be set to the a priori profile or even to $\mathbf{0}$. Similarly, the regularization matrix might be set to the unit matrix or the inverse of the a priori covariance matrix $\mathbf{S}_a$. Note that the optimal estimation method is a special form of regularisation, where $\lambda = 1$, $\mathbf{x}_0 = \mathbf{x}_a$ and $\mathbf{L} = \mathbf{S}_a^{-1}$. Regularization has been applied to ozone profile retrieval from the GOME instrument by (Hasekamp and Landgraf, 2001). They used $\mathbf{x}_0 = \mathbf{0}$ and $\mathbf{L} = \mathbf{I}$, and determined the value of λ by plotting the norm of $\mathbf{x}$ versus the norm of the least-squares solution. The resulting curve depends on the value of the regularization factor and shows a typical L-shape, and the optimal value for the regularization factor is in the corner between the vertical and horizontal parts of the curve.

A cost function is not required when retrieving ozone profiles using neural networks. A neural network consists of layers of interconnected processing nodes called neurons. The signal between two neurons is determined by the weights assigned to the neurons. These weights are tuned in the training phase of the network, where matching input and output data are offered to the network. After the training phase, the network can be applied to new data not present in the training dataset. In neural network retrievals, the

training dataset is selected by the algorithm developer and should at least consist of collocated datasets of radiances and ozone profiles (e.g. obtained by ozone sondes). Auxiliary data such as geolocation coordinates and observation angles can also be added to the training dataset. Neural network retrievals have been applied to GOME data to obtain ozone profiles (see e.g. Iapaolo et al., 2007) and to OMI (Levelt et al., 2006) data with a focus on tropospheric columns (see e.g. Di Noia et al., 2013).

The main advantage of neural network retrievals is that it is much faster than for example optimal estimation techniques because no complicated radiative transfer equations are needed. However, designing and training the network may require some time. Since a neural network does not have an explicit physical basis, the quality of the retrieval depends on the size of the training dataset and the design of the network. For situations not in the training dataset, the neural network might yield unexpected results.

In this thesis, we use the optimal estimation approach to retrieve ozone profiles from UV-VIS satellite instruments. Optimal estimation is used in a number of operational ozone profile retrieval algorithms. It provides an uncertainty estimate of the retrieved profile (i.e. the covariance matrix) and information on the vertical smoothing of the measurement (i.e. the averaging kernel). Both the covariance matrix and the averaging kernel are used in the assimilation of the observations in the chemical transport model. Choices such as which value to use for the regularization factor are not required, and in contrast with neural networks, optimal estimation has a clear physical basis.

Satellite based instruments are the most practical way to obtain the global coverage required to measure the ozone distribution of the atmosphere. The instruments that are used in this thesis measure the reflected solar light in the UV-VIS range of the spectrum. These instruments are all onboard satellites that orbit the Earth in a sun-synchronous orbit. A sun-synchronous orbit is a near polar orbit (i.e. it nearly passes over the poles) and has the advantage that the local equator crossing time is the same for each orbit. Since the UV-VIS satellite instruments require reflected sunlight, they can only measure during the day-side of their orbit.

Atmospheric models, on the other hand, can give a global coverage of ozone at regular intervals (typically at 0, 6, 12 and 18 hours UTC). They generally also have a higher vertical resolution than satellite measurements of ozone. But models tend to settle on an equilibrium state, which might differ from the true ozone distribution.

Satellite measurements and atmospheric models can be combined using data assimilation (DA). Simply put, DA is about finding a weighted mean between measurements and model results. In this thesis, a Kalman filter is used to combine measurements from GOME-2 and OMI with the chemical transport model TM5. The mathematics of the assimilation algorithm is given in Chapter 4, and the principles are shown in Figure 1.8. On the

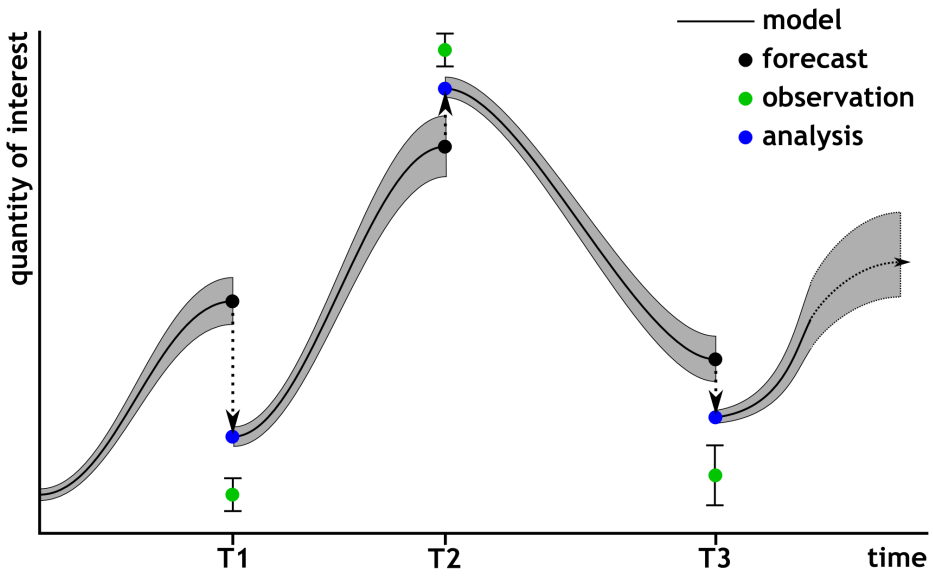

Figure 1.8: A schematic plot of the Kalman filter.

y-axis we see the quantity of interest, in this case ozone, while the x-axis depicts time. The black solid line indicates the model output, and the grey area around it is the model uncertainty. The green circles with error bars represent the observations, while the black circles represent the model output at the time of the observation (known as the forecast). The Kalman filter equations calculate a new ozone value and uncertainty at the time of the observation (known as the analysis). The analysis is then used to continue the model calculations. Note that the uncertainty of the analysis is smaller than either that of the forecast or the observation.

There are two important statistics that can be used as a measure for the performance of the assimilation. The first is the observation (green circle) minus forecast (black circle), also known as the OmF. The second is the observation (green circle) minus analysis (analysis), also known as the OmA. The OmF is a measure of how well the model performs if no data would be assimilated, while the OmA is a measure of how well the assimilation results are pulled towards the observations and therefore if the model and observation uncertainty are characterized correctly. Because the assimilation value is adjusted in the direction of the observation, the OmF should be larger than the OmA, as has been indicated Figure 1.8.

1.6.3. Tropospheric ozone

The tropospheric ozone column is the amount of ozone from the surface up to the tropopause. However, close to the tropopause an influx of stratospheric air with higher ozone concentrations into the troposphere might

occur. We will focus on the ozone concentrations in the lower part of the troposphere, since this has the highest impact on living organisms. Therefore, the tropospheric column that is used in this thesis is defined as the partial column from the surface up to 6 km. Tropospheric ozone can be determined by a number of satellite based methods such as nadir-limb matching (e.g. van der A, 2001; Ebojie et al., 2014), the empirically corrected tropospheric ozone residual method (Fishman and Balok, 1999; Fishman et al., 2003), a residual method based on assimilated ozone profiles (Chapter 5 of this thesis; de Laat et al., 2009) and the convective cloud differential method (Ziemke et al., 1998).

Tropical tropospheric columns can be determined using the convective-cloud-differential method (Ziemke et al., 1998). In this method, cloudy retrievals are used to obtain the above cloud ozone column, while total columns are retrieved from cloud free pixels. The resulting difference is a measure for the tropospheric ozone column below the cloud top (approximately 200 hPa in the tropics). Recently, this method has been applied to European satellite measurements to study the trends in a 20 year long time series (Heue et al., 2016).

Global tropospheric columns cannot be derived using the convective-cloud-differential method because the cloud top height outside the tropics varies too much. Direct integration of the retrieved UV-VIS ozone profiles up to the tropopause might seem an alternative, but a drawback to this approach is that UV-VIS instruments are not very sensitive to the height of ozone in the troposphere and lower stratosphere. Therefore, information on the ozone in the troposphere and stratosphere is mixed, leading to smoothed ozone profiles. This can be seen from the averaging kernels (see Figure 3.1). To restore the height information of ozone, assimilated ozone profiles can be used because information from the retrieved ozone profiles, averaging kernels and chemical transport model are combined.

On the other hand, the sensitivity and information content of UV-VIS instruments is higher in the stratosphere. The VIS radiation used in a DOAS total column retrieval penetrates deeper into the atmosphere than the UV radiation used in profile retrievals. Therefore, DOAS can be used to determine very accurate total columns. To make maximum use of the information content in both DOAS and UV-VIS retrievals, the UV-VIS stratospheric column can be subtracted from the DOAS total column. In this residual method, the remainder is taken as the tropospheric column. For spatial and temporal gridded data, the assimilated total columns can be used instead of DOAS columns directly (de Laat et al., 2009).

In this thesis (Chapter 5), assimilated ozone profiles will be used to determine the ozone column between the surface (i.e. mean sea level) and 6 km. The top level is chosen to minimise contamination of the ozone signal with stratospheric air. Ozone measurements for the year 2008 from GOME-2 and OMI are assimilated simultaneously into the chemical transport model TM5. We will compare a residual method and direct integration of the as-

similated ozone fields up to the 6 km level. In the residual method, the stratospheric assimilated columns will be subtracted from the total ozone columns from de Multi Sensor Reanalysis (MSR, van der A et al., 2010, 2015). The residual and the direct integrated ozone columns are both compared to ozone sonde measurements. The residual ozone columns show a too large variation to be used reliably, so the direct integrated columns should be used instead.

1.7. Research objectives

Ozone is an important trace gas in the atmosphere, that can both protect and harm the biosphere, depending on the altitude. Ozone is also a greenhouse gas and its vertical distribution is an important factor in explaining the temperature gradient of the atmosphere. In other words, ozone is a key parameter in Earth's climate system. This thesis has the research objective to improve our understanding of the global distribution of atmospheric ozone in space and time, not just in the stratosphere, but also in the troposphere, where it directly affects living organisms.

For a correct description of the ozone distribution in the atmosphere, measurements are required. Ground-based measurements are not uniformly spread over the globe, and it is not feasible to cover the whole surface of the Earth with measurement equipment. Satellite-based measurements are therefore a better option to obtain global coverage. In this thesis, only ozone profiles retrieved from measurements by nadir looking UV-VIS instruments are used. These kind of measurements usually have a vertical resolution of a few kilometres or more.

In Chapter 2, we investigate if the resolution of ozone profiles retrieved using nadir looking UV-VIS instruments is sufficient to observe gradients in the vertical ozone distribution occurring during ozone hole conditions, when ozone concentrations around the ozone maximum are severely depleted. GOME-2 ozone profiles that are retrieved operationally with the Ozone ProfilE Retrieval Algorithm (OPERA) are validated in space and time against ozone sondes from the Antarctic research station Neumayer under specific ozone depletion conditions.

Chapter 3 extends the analysis of OPERA ozone profiles to a global scale. The algorithm is tuned for optimal performance with both GOME and GOME-2 instruments. The OPERA algorithm can be applied to observations of multiple instruments with uniform retrieval settings to obtain a long term time series of ozone. The performance of the updated algorithm under ozone hole conditions is investigated using observations of the lidar at the observing station in Río Gallegos on the Southern tip of South America.

In Chapter 4, GOME-2 and operational OMI ozone profile retrievals are combined with the chemical transport model TM5 using a Kalman filter.

The output has been validated against ozone sondes. Compared to the assimilation of measurements from each of these instruments separately, the combined assimilation strongly reduces the bias in the altitude region where both instruments are most sensitive. The algorithm is used to derive a four year time series of assimilated ozone profiles, that can be used to study ozone dynamics in space and time.

In Chapter 5, the horizontal resolution of the assimilation algorithm described in the previous chapter is increased from 3° × 2° to 1° × 1° (longitude × latitude). The increased resolution is required to derive tropospheric columns from the assimilated ozone profiles. To prevent stratospheric pollution of the tropospheric ozone signal, the column from the surface up to 6 km is used as the tropospheric column. The column above 6 km is subtracted from the total columns from a multi sensor reanalysis. Both types of tropospheric ozone columns, obtained from the direct calculation and from the residual method, are validated against columns derived from ozone sonde measurements.

References

Bertaux, J. L., Kyrölä, E., Fussen, D., Hauchecorne, A., Dalaudier, F., Sofieva, V., Tamminen, J., Vanhellemont, F., Fanton d'Andon, O., Barrot, G., Mangin, A., Blanot, L., Lebrun, J. C., Pérot, K., Fehr, T., Saavedra, L., Leppelmeier, G. W., and Fraisse, R.: Global ozone monitoring by occultation of stars: an overview of GOMOS measurements on ENVISAT, Atmospheric Chemistry and Physics, 10, 12 091–12 148, doi: 10.5194/acp-10-12091-2010, 2010.

Brion, J., Chakir, A., Daumont, D., Malicet, J., and Parisse, C.: High-resolution laboratory absorption cross section of O_3. Temperature effect, Chemical Physics Letters, 213, 610–612, doi:10.1016/0009-2614(93)89169-I, 1993.

Brion, J., Chakir, A., Charbonnier, J., Daumont, D., Parisse, C., and Malicet, J.: Absorption Spectra Measurements for the Ozone Molecule in the 350–830 nm Region, Journal of Atmospheric Chemistry, 30, 291–299, 1998.

Butchart, N.: The Brewer-Dobson circulation, Reviews of Geophysics, 52, 157–184, doi:10.1002/2013RG000448, 2014.

Chapman, S.: A theory of upper-atmospheric ozone, Memoirs of the Royal Meteorological Society, 3, URL https://www.rmets.org/publications/classic-papers, 1929.

Chubachi, S.: A Special Ozone Observation at Syowa Station, Antarctica from February 1982 to January 1983, in: Atmospheric Ozone, edited by Zerefos, C. S. and Ghazi, A., pp. 285–289, Springer Netherlands, Dordrecht, 1985.

Crutzen, P. J.: The influence of nitrogen oxides on the atmospheric ozone content, Quarterly Journal of the Royal Meteorological Society, 96, 320–325, doi:10.1002/qj.49709640815, 1970.

Crutzen, P. J.: Is the detergent of the atmosphere decreasing? – Importance of methane for the OH radical concentration and atmospheric photochemistry, Report EUR 10492 EN, Commission of the European Communities, URL https://publications.europa.eu/en/publication-detail/-/publication/99c7dbe1-e543-4bfb-9547-a808ecf9581c#, 1986.

Daumont, D., Brion, J., Charbonnier, J., and Malicet, J.: Ozone UV spectroscopy. I - Absorption cross-sections at room temperature, Journal of Atmospheric Chemistry, 15, 145–155, 1992.

de Laat, A. T. J., van der A, R. J., and van Weele, M.: Evaluation of tropospheric ozone columns derived from assimilated GOME ozone profile

observations, Atmospheric Chemistry and Physics, 9, 8105–8120, doi: 10.5194/acp-9-8105-2009, 2009.

Di Noia, A., Sellitto, P., Del Frate, F., and de Laat, J.: Global tropospheric ozone column retrievals from OMI data by means of neural networks, Atmospheric Measurement Techniques, 6, 895–915, doi: 10.5194/amt-6-895-2013, 2013.

Ebojie, F., von Savigny, C., Ladstätter-Weißenmayer, A., Rozanov, A., Weber, M., Eichmann, K.-U.., Bötel, S., Rahpoe, N., Bovensmann, H., and Burrows, J. P.: Tropospheric column amount of ozone retrieved from SCIAMACHY limb–nadir-matching observations, Atmospheric Measurement Techniques, 7, 2073–2096, doi:10.5194/amt-7-2073-2014, 2014.

Farman, J. C., Gardiner, B. G., and Shanklin, J. D.: Large losses of total ozone in Antarctica reveal seasonal ClO_x/NO_x interaction, Nature, 315, 207–210, doi:10.1038/315207a0, 1985.

Fishman, J. and Balok, A. E.: Calculation of daily tropospheric ozone residuals using TOMS and empirically improved SBUV measurements: Application to an ozone pollution episode over the eastern United States, Journal of Geophysical Research (Atmospheres), 104, 30 319–30 340, doi: 10.1029/1999JD900875, 1999.

Fishman, J., Wozniak, A. E., and Creilson, J. K.: Global distribution of tropospheric ozone from satellite measurements using the empirically corrected tropospheric ozone residual technique: Identification of the regional aspects of air pollution, Atmospheric Chemistry and Physics, 3, 893–907, doi:10.5194/acp-3-893-2003, 2003.

Froidevaux, L., Jiang, Y. B., Lambert, A., Livesey, N. J., Read, W. G., Waters, J. W., Browell, E. V., Hair, J. W., Avery, M. A., McGee, T. J., Twigg, L. W., Sumnicht, G. K., Jucks, K. W., Margitan, J. J., Sen, B., Stachnik, R. A., Toon, G. C., Bernath, P. F., Boone, C. D., Walker, K. A., Filipiak, M. J., Harwood, R. S., Fuller, R. A., Manney, G. L., Schwartz, M. J., Daffer, W. H., Drouin, B. J., Cofield, R. E., Cuddy, D. T., Jarnot, R. F., Knosp, B. W., Perun, V. S., Snyder, W. V., Stek, P. C., Thurstans, R. P., and Wagner, P. A.: Validation of Aura Microwave Limb Sounder stratospheric ozone measurements, Journal of Geophysical Research (Atmospheres), 113, doi:10.1029/2007JD008771.

Hasekamp, O. P. and Landgraf, J.: Ozone profile retrieval from backscattered ultraviolet radiances: The inverse problem solved by regularization, Journal of Geophysical Research, 106, 8077–8088, doi:10.1029/2000JD900692, 2001.

Hegglin, M. I., Fahey, D. W., McFarland, M., Montzka, S. A., and Nash, E. R.: Twenty Questions and Answers About the Ozone Layer: 2014 Update,

Scientific Assesment of Ozone Depletion: 2014, World Meterological Organization, Geneva, Switzerland, 2015.

Heue, K.-P., Coldewey-Egbers, M., Delcloo, A., Lerot, C., Loyola, D., Valks, P., and van Roozendael, M.: Trends of tropical tropospheric ozone from 20 years of European satellite measurements and perspectives for the Sentinel-5 Precursor, Atmospheric Measurement Techniques, 9, 5037–5051, doi:10.5194/amt-9-5037-2016, 2016.

Hoogen, R., Rozanov, V. V., and Burrows, J. P.: Ozone profiles from GOME satellite data: Algorithm description and first validation, Journal of Geophysical Research, 104, 8263–8280, doi:10.1029/1998JD100093, 1999.

Iapaolo, M., Godin-Beekmann, S., Del Frate, F., Casadio, S., Petitdidier, M., McDermid, I. S., Leblanc, T., Swart, D., Meijer, Y., Hansen, G., and Stebel, K.: Gome ozone profiles retrieved by neural network techniques: A global validation with lidar measurements, Journal of Quantitative Spectroscopy and Radiative Transfer, 107, 105–119, doi:https://doi.org/10.1016/j.jqsrt.2007.02.015, 2007.

Lerot, C., Van Roozendael, M., Spurr, R., Loyola, D., Coldewey-Egbers, M., Kochenova, S., van Gent, J., Koukouli, M., Balis, D., Lambert, J.-C., Granville, J., and Zehner, C.: Homogenized total ozone data records from the European sensors GOME/ERS-2, SCIAMACHY/Envisat, and GOME-2/MetOp-A, Journal of Geophysical Research (Atmospheres), 119, 1639–1662, doi:10.1002/2013JD020831, 2014.

Levelt, P. F., van den Oord, G. H. J., Dobber, M. R., Malkki, A., Visser, H., de Vries, J., Stammes, P., Lundell, J. O. V., and Saari, H.: The Ozone Monitoring Instrument, IEEE Transactions on Geoscience and Remote Sensing, 44, 1093–1101, doi:10.1109/TGRS.2006.872333, 2006.

Liu, X., Bhartia, P. K., Chance, K., Spurr, R. J. D., and Kurosu, T. P.: Ozone profile retrievals from the Ozone Monitoring Instrument, Atmospheric Chemistry and Physics, 10, 2521–2537, doi:10.5194/acp-10-2521-2010, 2010.

Malicet, J., Daumont, D., Charbonnier, J., Parisse, C., Chakir, A., and Brion, J.: Ozone UV spectroscopy. II - Absorption Cross-Sections and Temperature Dependence, Journal of Atmospheric Chemistry, 21, 263–273, doi:10.1007/BF00696758, 1995.

McPeters, R. D., Labow, G. J., and Logan, J. A.: Ozone climatological profiles for satellite retrieval algorithms, Journal of Geophysical Research (Atmospheres), 112, D05 308, doi:10.1029/2005JD006823, 2007.

Miles, G. M., Siddans, R., Kerridge, B. J., Latter, B. G., and Richards, N. A. D.: Tropospheric ozone and ozone profiles retrieved from GOME-2

and their validation, Atmospheric Measurement Techniques, 8, 385–398, doi:10.5194/amt-8-385-2015, 2015.

Molina, M. J. and Rowland, F. S.: Stratospheric sink for chlorofluoromethanes: chlorine atom-catalysed destruction of ozone, Nature, 249, 810–812, doi:10.1038/249810a0, 1974.

Munro, R., Lang, R., Klaes, D., Poli, G., Retscher, C., Lindstrot, R., Huckle, R., Lacan, A., Grzegorski, M., Holdak, A., Kokhanovsky, A., Livschitz, J., and Eisinger, M.: The GOME-2 instrument on the Metop series of satellites: instrument design, calibration, and level 1 data processing - an overview, Atmospheric Measurement Techniques, 9, 1279–1301, doi: 10.5194/amt-9-1279-2016, 2016.

NOAA, NASA, and USAF: U.S. Standard Atmosphere 1976, Report nr. NOAA-S/T 76-1562, U.S. Government Printing Office, Washington D.C., USA, 1976.

Rodgers, C. D.: Inverse methods for atmospheric sounding, vol. Vol. 2 of *Series on Atmospheric, Oceanic and Planetary Physics*, World Scientific Publishing, Singapore, 2008 edn., 2000.

Smit, H. G. J., Straeter, W., Johnson, B. J., J., O. S., Davies, J., W., T. D., Hoegger, B., Stubi, R., Schmidlin, F. J., Northam, T., Thompson, A. M., Witte, J. C., Boyd, I., and Posny, F.: Assessment of the performance of ECC-ozonesondes under quasi-flight conditions in the environmental simulation chamber: Insights from the Juelich Ozone Sonde Intercomparison Experiment (JOSIE), Journal of Geophysical Research (Atmospheres), 112, doi:10.1029/2006JD007308, 2007.

Steinbrecht, W., Claude, H., Schönenborn, F., McDermid, I. S., Leblanc, T., Godin, S., Song, T., Swart, D. P. J., Meijer, Y. J., Bodeker, G. E., Connor, B. J., Kämpfer, N., Hocke, K., Calisesi, Y., N., S., de la Noë, J., Parrish, A. D., Boyd, I. S., Brühl, C., Steil, B., Giorgetta, M. A., Manzini, E., Thomason, L. W., Zawodny, J. M., McCormick, M. P., Russell, J. M., Bhartia, P. K., Stolarski, R. S., and Hollandsworth-Frith, S. M.: Long-term evolution of upper stratospheric ozone at selected stations of the Network for the Detection of Stratospheric Change (NDSC), Journal of Geophysical Research (Atmospheres), 111, doi:10.1029/2005JD006454, 2006.

van der A, R. J.: Improved ozone profile retrieval from combined nadir/limb observations of SCIAMACHY, Journal of Geophysical Research (Atmospheres), 106, 14 583–14 594, doi:10.1029/2001JD900089, 2001.

van der A, R. J., Allaart, M. A. F., and Eskes, H. J.: Multi sensor reanalysis of total ozone, Atmospheric Chemistry and Physics, 10, 11 277–11 294, doi:10.5194/acp-10-11277-2010, 2010.

van der A, R. J., Allaart, M. A. F., and Eskes, H. J.: Extended and refined multi sensor reanalysis of total ozone for the period 1970-2012, Atmospheric Measurement Techniques, 8, 3021–3035, doi:10.5194/amt-8-3021-2015, 2015.

Van Roozendael, M., Spurr, R., Loyola, D., Lerot, C., Balis, D., Lambert, J.-C., Zimmer, W., van Gent, J., van Geffen, J., Koukouli, M., Granville, J., Doicu, A., Fayt, C., and Zehner, C.: Sixteen years of GOME/ERS-2 total ozone data: The new direct-fitting GOME Data Processor (GDP) version 5 - Algorithm description, Journal of Geophysical Research (Atmospheres), 117, doi:10.1029/2011JD016471, 2012.

WMO: Commission For Aerology (CAe), abridged final report of the second session, Report nr. WMO - No. 65. RP. 27, Secretariat of the World Meteorological Organization, Geneva, Switzerland, 1957.

WMO: Scientific Assessment of Ozone Depletion: 2014, Global Ozone Research and Monitoring Project–Report No. 55, World Meteorological Organization, Geneva, Switzerland, 2014.

WMO: The global observing system for climate: implementation needs, Report nr. GCOS-200, Geneva, Switzerland, 2016.

Ziemke, J. R., S., C., and K., B. P.: Two new methods for deriving tropospheric column ozone from TOMS measurements: Assimilated UARS MLS/HALOE and convective-cloud differential techniques, Journal of Geophysical Research (Atmospheres), 103, 22 115–22 127, doi:10.1029/98JD01567, 1998.

2

Height resolved ozone hole structure as observed by the Global Ozone Monitoring Experiment-2

We present Global Ozone Monitoring Experiment-2 (GOME-2) ozone profiles that were operationally retrieved with the KNMI Ozone ProfilE Retrieval Algorithm (OPERA) algorithm for the period September-December 2008. It is shown that it is possible to accurately measure the vertical distribution of stratospheric ozone for Antarctic ozone hole conditions from spectra measured at ultraviolet wavelengths from a nadir viewing instrument. Comparisons with ozone sonde observations from the Neumayer station at the Antarctic coast show a good agreement for various ozone profile shapes representing different phases of the annual recurring ozone hole cycle. A preliminary analysis of the three-dimensional structure of the ozone hole shows for example that at the vortex edges ozone rich mid-latitude middle and upper stratospheric layers can be found over ozone depleted lower stratospheric 'ozone hole' layers. These Antarctic ozone profile observations combined with the daily global coverage of GOME-2 enables the monitoring of the three-dimensional structure of the ozone hole on a daily basis.

This chapter has been published in Geophysical Review Letters as van Peet et al. (2009).

2.1. Introduction

The launch of the Global Ozone Monitoring Experiment (GOME) on board of the European Remote Sensing 2 satellite in April 1995 started a new era of measuring earth-reflected solar radiation with relatively high spectral resolution for UltraViolet and VISible wavelengths (UV-VIS). A number of studies have shown that it is possible to retrieve ozone profiles from these UV-VIS spectral observations (e.g. Chance et al., 1997; Munro et al., 1998). Over the years, various research groups have developed ozone profile retrieval algorithms for spectral UV-VIS measurements, and identified and improved upon various errors due to calibration issues, retrieval methodology and parameter uncertainties (e.g. Hoogen et al., 1999; Hasekamp and Landgraf, 2001; van der A et al., 2002; Liu et al., 2005). Meijer et al. (2006) provide an evaluation of nine different GOME ozone profile retrieval algorithms available at the time. They concluded that stratospheric ozone profiles can be determined quite well, but that accurately measuring tropospheric ozone remains a challenge due to inadequate instrument calibration and the weak signal for tropospheric ozone information. These retrievals are expected to improve considerably for instruments like the Ozone Monitoring Instrument (OMI) and Global Ozone Monitoring Experiment-2 (GOME-2) due to smaller ground pixels, a better characterization of the instrument spectral response (slit) function and an improved polarization correction, which were major limitations for GOME (van der A et al., 2002; Schutgens and Stammes, 2003). Liu et al. (2005) showed nevertheless that GOME ozone retrievals can provide realistic and valuable tropospheric ozone information for tropical and mid-latitude locations.

A common feature of UV-VIS ozone profiles is their limited vertical resolution, estimated typically at 7–15 km (e.g. Hoogen et al., 1999; Liu et al., 2005), with a considerable amount of vertical smoothing. As a consequence, small scale vertical ozone features cannot be observed. This has important implications for both tropospheric and lower stratospheric ozone observations, which frequently show large ozone variations with a small vertical extent and sharp ozone gradients which cannot be resolved in UV-VIS ozone profiles. In particular, the Antarctic ozone hole provides a challenge as the thickness of ozone depleted layers in the ozone hole is typically about 5 km - the ozone hole is located between 12 to 20 km altitude - and sharp ozone changes occur at the upper and lower edges of the ozone hole. An additional problem for Antarctic ozone profile retrievals is the difficulty in discriminating snow/ice surfaces and middle/high level clouds, which can cause large retrieval errors in the retrieved ozone profiles. Therefore, until now little emphasis has been put on assessing the quality of Arctic and especially Antarctic UV-VIS ozone profiles (Meijer et al., 2006; de Clercq and Lambert, 2007). With the launch of various instruments with improved instrumentation and spatial resolution since 2002 (SCanning Imaging Absorption spectroMeter for Atmospheric CartograpHY, OMI, GOME-2), it is expected that the retrievals from these instruments will result in improved

knowledge about the vertical distribution for the Antarctic ozone hole.

The GOME-2 instrument (Callies et al., 2000), launched on 19 October 2006 onboard Metop-A, flies in a sun-synchronous polar orbit with an equator crossing time of 09:30 hrs (local solar time). GOME-2 is a nadir looking cross-track scanning spectrometer. The instrument measures backscattered solar light from the Earth's atmosphere between 240–790 nm in four channels with a relatively high spectral resolution (0.2–0.4 nm). In its normal mode, the instrument has an almost global daily coverage with a cross-track swath width of 1920 km which is split up in ground pixels with a horizontal resolution of 80 × 40 km between 307–790 nm but with 640 × 40 km below 307 nm due to much weaker signals. The measurements from GOME-2 are especially suitable for retrieval of the total column and vertical profiles of atmospheric ozone (which is one of the essential climate variables (Mason, 2003)), and other key atmospheric trace gases, such as NO_2, SO_2, BrO and formaldehyde. GOME-2 has been measuring ozone profiles from January 2007 onwards, providing daily coverage of the Antarctic ozone hole area during the entire 2008 ozone hole season. The operational retrieval algorithm for GOME-2 ozone profiles is the Ozone ProfilE Retrieval Algorithm (OPERA) algorithm [van der A et al. (2002); van Oss and de Haan (2004); and *Mijling et al.* [2008], "Preparing for GOME-2 ozone profile retrievals: improving the profile retrieval algorithm using GOME data", *in preparation*], which will be described in the next section.

We explore one season of GOME-2 ozone profiles under Antarctic ozone hole conditions to investigate the current status and quality of GOME-2 ozone profile observations, and demonstrate the effect of improvements that have been made to the OPERA algorithm over the last couple of years. We investigate how well the ozone profile retrievals from GOME-2 UV-VIS measurements can capture the vertical distribution of ozone during Antarctic ozone hole conditions and discuss the use of these observations for monitoring the 3-D structure of the Antarctic ozone hole on a daily basis.

2.2. OPERA

Ozone profile retrieval algorithms from UV spectra use the fact that the absorption cross section of ozone decreases steeply with wavelengths between 270–340 nm. Scattered sunlight detected by the satellite at short wavelengths experiences strong absorption by ozone and therefore has only travelled the top layers of the atmosphere: it only carries information on the ozone distribution in these layers. With increasing wavelengths, photons also carry ozone information from lower layers. Ozone absorption structures in the Huggins bands are temperature dependent, providing additional information for tropospheric ozone retrievals (Chance et al., 1997). Above 340 nm the spectra is more transparent and used to extract information on surface reflection and cloud parameters. Retrieving ozone profiles from this information is an underconstrained inverse problem: there are more parameters describing the profile than there are independent pieces

of information available in the spectrum.

OPERA is an algorithm that solves this problem using the optimal estimation method (e.g. Rodgers, 2000), which includes a priori information to stabilize the inversion. The state vector consists of the atmospheric parameters that are fitted, in this case 40 layers of ozone and the albedo. The albedo can be the cloud albedo or the surface albedo; when the cloud fraction is larger than 0.20, the cloud albedo is used. Optimal estimation requires a priori information (including error covariance) for the state vector elements and the derivatives of the measurement to the state. The a priori information is taken from the ozone climatology of (McPeters et al., 2007). The derivatives of the measurement to the state vector (i.e. weighting functions) are calculated with the radiative transfer model LidortA (van Oss and Spurr, 2002 a). Since this model does not include polarisation, the derivatives are corrected afterwards, for the neglect of polarisation, using pre-calculated look-up tables. The radiative transfer model uses the cross sections from Daumont et al. (1992); Malicet et al. (1995); Brion et al. (1998) and meteorological information from ECMWF. The optimal estimation method is applied iteratively until convergence is reached. The convergence criteria for the retrieval are based on the magnitude of the state update and the deviation between measured and simulated radiances. The retrieval of ozone profiles is currently done using ground pixels of 640×40 km.

2.3. Intercomparison of ozone profiles

For validation of the GOME-2 ozone profiles we use data from the ozone balloon sounding program conducted at the Antartic research station Neumayer (8.26° W and 70.65° S) which has been operational since 1992, with ozone profiles obtained weekly. During the development of the ozone hole, the sounding frequency is increased to three times a week. All measurements were made using an ECC 6A type ozone sonde. These measurements are available at the World Ozone and Ultraviolet Radiation Data Centre database (http://www.woudc.org/index_e.html).

The Neumayer station was selected since it is located near the edge of the Antarctic polar vortex and here we expect to observe some interesting variability in the ozone concentration associated with the vortex dynamics. In addition, the Neumayer station is the only Antarctic station that makes its measurements publicly available within a few days after observation.

We only compare ozone sonde data and satellite data when the following three criteria have been fullfilled. First, the Neumayer Station should be located inside the satellite footprint. Second, within a footprint, the distance between Neumayer and the pixel centre should not exceed 300 km, the typical length scale of lower stratospheric ozone variations (Sparling et al., 2006). Third, the launch of the sonde and the overpass of the satellite should be within 12 hours of each other. In total 37 collocations were found for the period September - December 2008, some of which are collocations of one sonde with multiple GOME-2 overpasses.

The sonde profile is convolved with the averaging kernel ($\mathbf{A}$, defined as the sensitivity of the retrieval $\hat{\mathbf{x}}$ to the true state $\mathbf{x}$) and the a priori profile ($\mathbf{x_a}$) of the satellite observation, according to the equation $\hat{\mathbf{x}} = \mathbf{x}_a + \mathbf{A}(\mathbf{x} - \mathbf{x}_a) + \boldsymbol{\epsilon}$ (e.g. Rodgers, 2000, chapter 3), where $\boldsymbol{\epsilon}$ is the measurement error. Replacing $\mathbf{x}$ by the sonde observation, $\hat{\mathbf{x}}$ gives us the retrieved sonde profile, which is smoothed in the same way as if it would have been observed by GOME-2, and can therefore be compared to the actual retrieved ozone profile. Both original and convolved sondes are used in the intercomparison with the GOME-2 profiles (see figure 2.1).

With the collocation criteria described above it is possible for multiple collocations to occur on the same day if the GOME-2 pixels overlap. We therefore have gridded the data to 1° × 1° using an area weighted averaging. The gridded dataset is used in constructing plots of time series (see figure 2.2) and cross-cutting views of the atmosphere (see figure 2.3).

2.4. Results

In figure 2.1 we show a comparison between sonde and satellite profiles representing various stages in the ozone hole life cycle with very different ozone profile shapes. As an indication of the quality of the retrievals we include the mean and standard deviation of the differences beteween all retrieved GOME-2 profiles (in the period September-Decembder 2008) and the convolved sonde profiles. We see that the ozone profiles compare very well, even when the a priori information does not resemble ozone hole conditions. Note that the retrieved profiles are also in good agreement with the sonde profiles at high solar zenith angles.

The results of the profile comparison give confidence in the retrieval algorithm. Therefore, we made a time series of the gridded dataset over the Neumayer Station. It is plotted in figure 2.2, starting at 1 September 2008 and continuing up to 31 December 2008. The time series shows the development and breakup of the ozone hole. The double peaked ozone profile that was visible in the collocations in figure 2.1 is also visible in the time series. The region of maximum ozone depletion is located between 100 and 50 hPa between 16 September and 25 October 2008 and between 100 and 70 hPa afterwards. Around 26 October, air masses with elevated ozone concentrations start to appear between 50 and 20 hPa altitude and a few days later the concentrations suddenly drop by approximately a factor of two. This behavior recurs a couple of times in the rest of the time series. The air masses with elevated ozone concentration slowly descend during the latter half of the ozone hole period. This downward movement replenishes part of the ozone depleted air in the Antarctic ozone hole, eventually leading to its disappearance (Sato et al., 2009). The variability in ozone concentrations can be explained by the dynamics of the ozone hole. Neumayer is located near the edge of Antarctica and usually also close to the edge of the ozone hole. The ozone hole is, at any given moment, generally not circular symmetric, and due to Rossby wave propagation the edges of the ozone hole

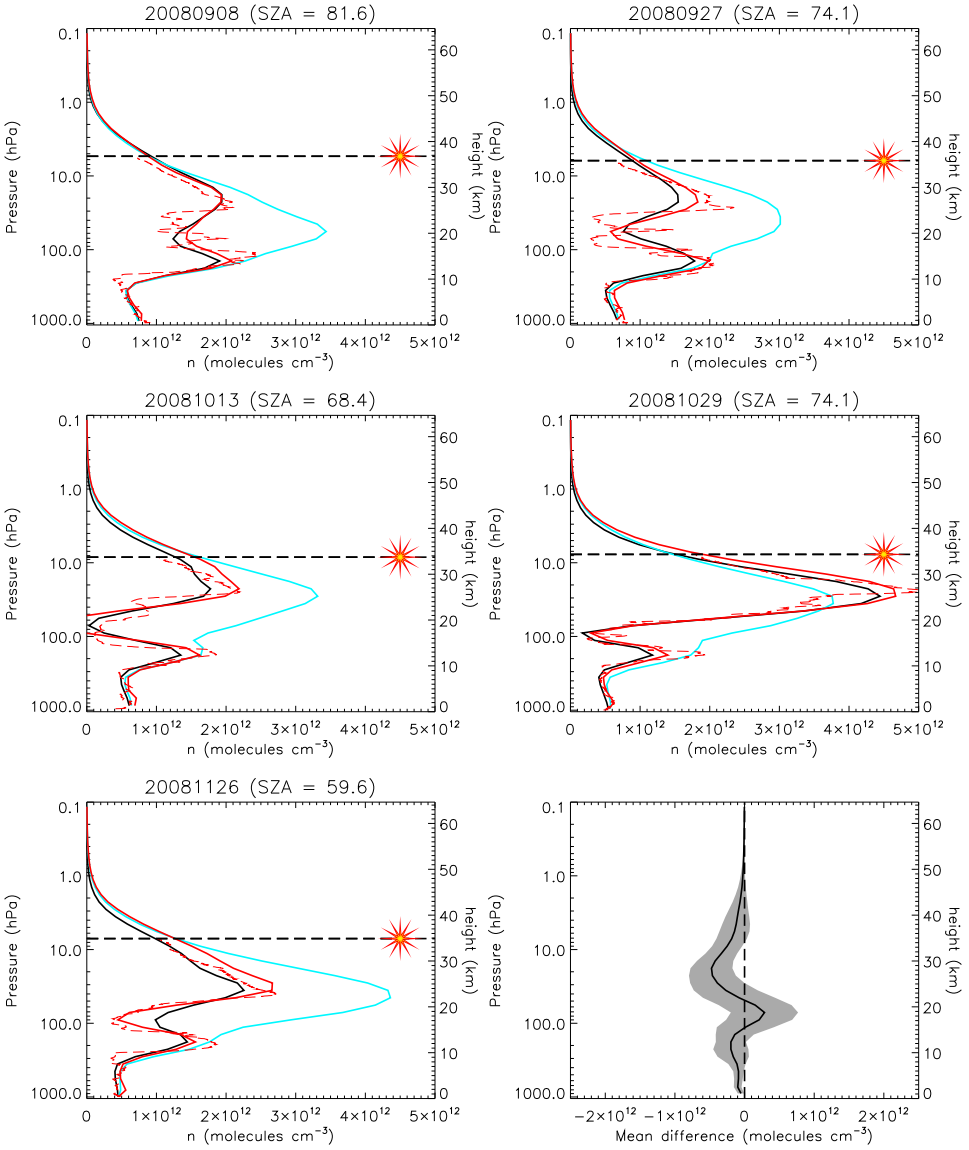

Figure 2.1: Ozone profiles (number density n in molecules cm^{-3}) for the Neumayer Station using original, non-gridded data. The black line is the GOME-2 profile, the solid red line is the sonde profile convolved with the a priori profile and the averaging kernel (see section 2.3), the dotted red line is the original sonde profile and the blue line is the a priori profile. Above the sonde burst level (indicated by the horizontal dotted line) the sonde profile is set equal to the a priori. The date and solar zenith angle (SZA) are indicated above each plot. The bottom right plot shows the mean difference (GOME-2 - sonde) of all collocations in the period September - December 2008 (black line) and the 1σ error (grey area).

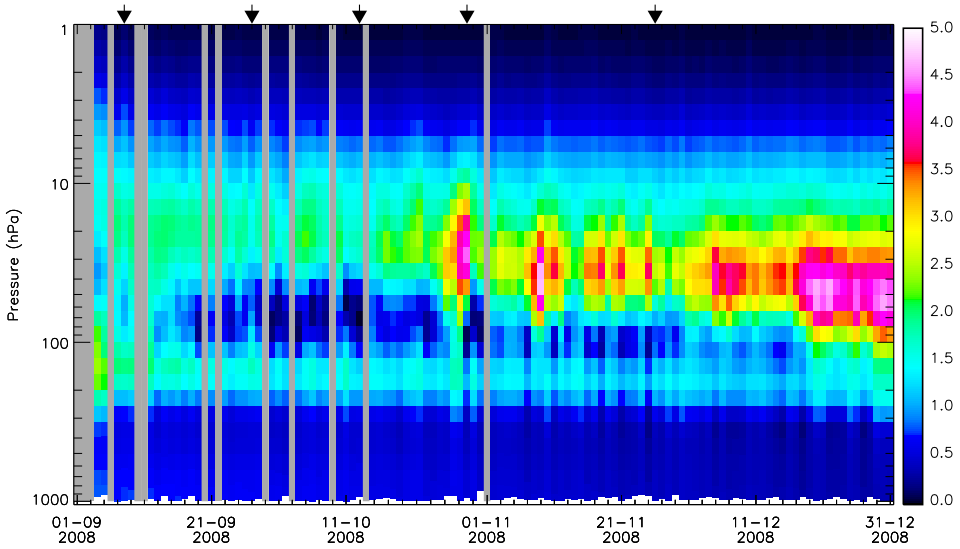

Figure 2.2: Time series of the ozone concentration over the Neumayer Station. Arrows along the top indicate the locations of the profiles in figure 2.1. Grey areas indicate missing data. Concentrations are given in 10^{12} molecules cm^{-3}.

slowly rotate around Antarctica. As a result, the Neumayer station is located either inside or outside the Antarctic vortex depending on the shape and rotation of the ozone hole edge.

Note the persistence of the region with low ozone concentrations between 100 and 70 hPa after approximately 29 October 2008. Clearly the ozone depleted air from inside the vortex is flowing under ozone rich air at higher altitudes. This interesting dynamical feature might be obscured by the traditional ozone hole definition, which is based on the total ozone column. The ozone rich air compensates the ozone depleted air in the total column, thereby giving the impression that the ozone hole is smaller than it actually is.

The maximum ozone depletion occured around the beginning of October. For 13 October 2008, the middle left plot of figure 2.1 gives the collocation of GOME-2 with a sonde launched from the Neumayer Station. To get a better impression of the global behavior of the ozone concentration around the time of maximum ozone depletion, we made North-South and East-West cross sections of the atmosphere (see figure 2.3), centered on Neumayer.

In the North-South cross section, the ozone hole can be seen very clearly at latitudes poleward of 60° S. The minimum ozone concentration is reached around 70 hPa with slightly higher concentrations above and below it. The East-West cross section shows a region of high ozone concentration from 90° E crossing the date line to 80° W. This coincides with a region of increased total ozone columns (that were integrated from the ozone profile

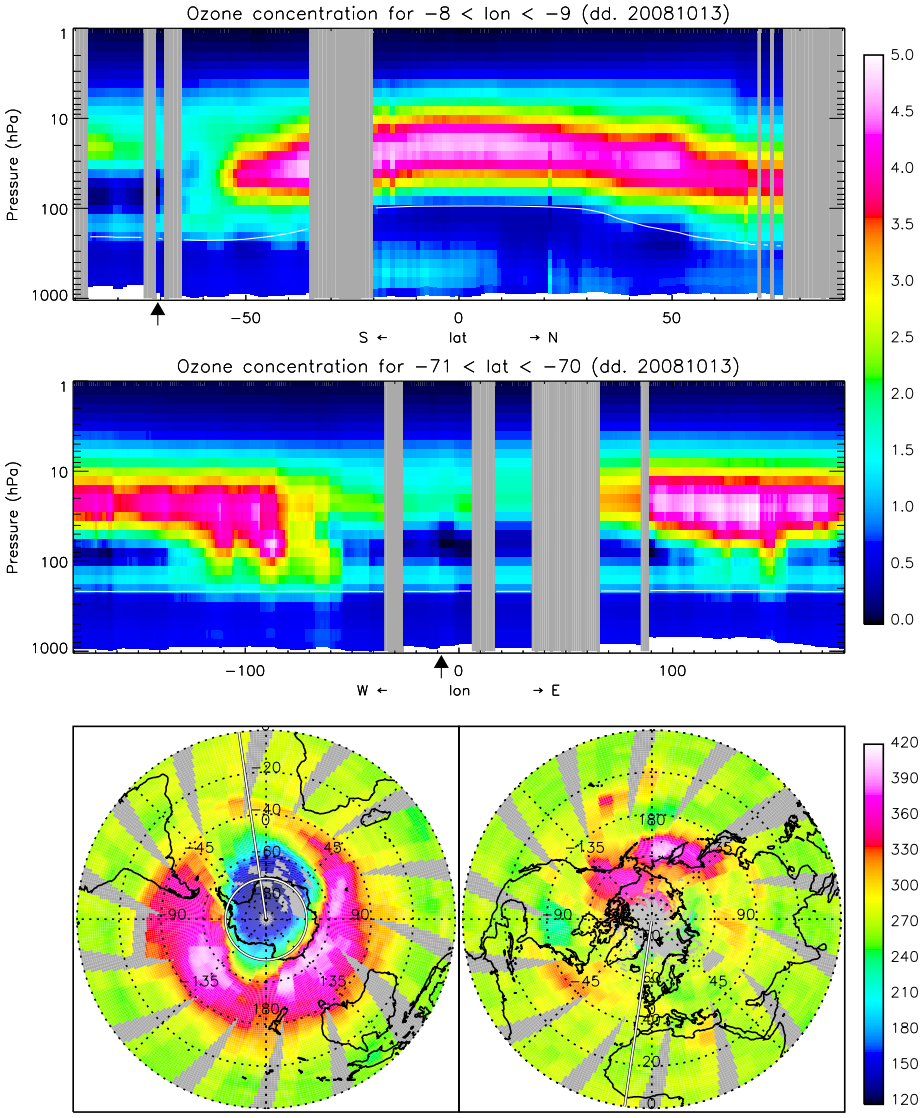

Figure 2.3: North-South (top) and East-West (middle) cross sections of the atmosphere (in molecules cm^{-3}) for 13 October 2008. Grey areas indicate missing data. In the top plot we show the ozone cross section for constant longitude (8.26° W) with the South Pole to the left and the North Pole to the right. The middle plot shows the cross section for constant latitude (70.65° S) with 180° W to the left and 180° E to the right. In both plots, the location of Neumayer is indicated by the arrows and the thermal tropopause (based on the climatology) has been indicated by a white line for reference. The bottom plots show GOME-2 total ozone columns integrated from the ozone profile retrievals (in DU) for the Southern Hemisphere (left) and the Northern Hemisphere (right) and the exact location of the cross sections.

retrievals) as can be seen in the bottom left plot. Below this ozone rich air, there is the region of maximum depletion, interrupted by a couple of ozone rich intrusions from above.

2.5. Discussion and Conclusions

The first GOME-2 ozone profiles for Antarctic ozone hole conditions are presented. The algorithm OPERA is capable of retrieving the ozone profile in good agreement with ozone sonde measurements in this region. The time series shows that we are capable of monitoring the three dimensional structure of the ozone hole on a day-to-day basis. One interesting observation is the presence of ozone depleted laminae below the ozone maximum at the edge of the Antarctic vortex, possibly caused by a combination of lower stratospheric vortex dynamics and middle and upper stratospheric transport of ozone rich air from mid-latitudes. Since the ozone hole definition is based on total ozone columns, this might affect the derived size of the ozone hole. Future research will investigate in more detail how the standard ozone hole definition relates to an ozone hole area based on the GOME-2 ozone profiles.

One of the Essential Climate Variables (ECV) that is defined in the Global Climate Observing System programme (Mason, 2003) on atmospheric composition is ozone. We have demonstrated that we are able to monitor the ozone concentration in 4D, that is in both space and time. The retrieved profiles can be used in an assimilation process, thereby satisfying the requirement of global coverage for the ECVs.

Since the GOME-2 instrument series will continue flying until about 2020, the expected recovery of the ozone hole can be monitored. In addition, the daily three dimensional coverage of the ozone hole opens new exciting possibilities to study Antarctic vortex dynamics, transport processes and evaluating climate models that include stratospheric chemistry.

Acknowledgements. The authors want to thank EUMETSAT for providing the GOME-2 data and the World Ozone and Ultraviolet Radiation Data Centre data archive (`http://www.woudc.org/index_e.html`) for providing access to the ozone sonde data.

References

Brion, J., Chakir, A., Charbonnier, J., Daumont, D., Parisse, C., and Malicet, J.: Absorption Spectra Measurements for the Ozone Molecule in the 350–830 nm Region, Journal of Atmospheric Chemistry, 30, 291–299, 1998.

Callies, J., Corpaccioli, E., Eisinger, M., Hahne, A., and Lefebvre, A.: GOME-2 – Metop's Second-Generation Sensor for Operational Ozone Monitoring, ESA bulletin, 102, 28–36, 2000.

Chance, K. V., Burrows, J. P., Perner, D., and Schneider, W.: Satellite measurements of atmospheric ozone profiles, including tropospheric ozone, from ultraviolet/visible measurements in the nadir geometry : a potential method to retrieve tropospheric ozone, Journal of Quantitative Spectroscopy and Radiative Transfer, 57, 467–476, doi:10.1016/S0022-4073(96)00157-4, 1997.

Daumont, D., Brion, J., Charbonnier, J., and Malicet, J.: Ozone UV spectroscopy. I - Absorption cross-sections at room temperature, Journal of Atmospheric Chemistry, 15, 145–155, 1992.

de Clercq, C. and Lambert, J.-C.: CHEOPS-GOME, geophysical information content and validation of ERS-2 GOME ozone profile data records, ESA technical note TN-IASB-GOME1-CHEOPS-01-1/B, 2007.

Hasekamp, O. P. and Landgraf, J.: Ozone profile retrieval from backscattered ultraviolet radiances: The inverse problem solved by regularization, Journal of Geophysical Research, 106, 8077–8088, doi:10.1029/2000JD900692, 2001.

Hoogen, R., Rozanov, V. V., and Burrows, J. P.: Ozone profiles from GOME satellite data: Algorithm description and first validation, Journal of Geophysical Research, 104, 8263–8280, doi:10.1029/1998JD100093, 1999.

Liu, X., Chance, K., Sioris, C. E., Spurr, R. J. D., Kurosu, T. P., Martin, R. V., and Newchurch, M. J.: Ozone profile and tropospheric ozone retrievals from the Global Ozone Monitoring Experiment: Algorithm description and validation, Journal of Geophysical Research (Atmospheres), 110, 20 307–+, doi:10.1029/2005JD006240, 2005.

Malicet, J., Daumont, D., Charbonnier, J., Parisse, C., Chakir, A., and Brion, J.: Ozone UV spectroscopy. II - Absorption Cross-Sections and Temperature Dependence, Journal of Atmospheric Chemistry, 21, 263–273, doi:10.1007/BF00696758, 1995.

Mason, P. J., ed.: The second report on the adequacy of the global observing systems for climate in support of the UNFCCC, GCOS, report nr.: GCOS-82 (WMO/TD-No.1143), 2003.

McPeters, R. D., Labow, G. J., and Logan, J. A.: Ozone climatological profiles for satellite retrieval algorithms, Journal of Geophysical Research (Atmospheres), 112, D05 308, doi:10.1029/2005JD006823, 2007.

Meijer, Y. J., Swart, D. P. J., Baier, F., Bhartia, P. K., Bodeker, G. E., Casadio, S., Chance, K., Del Frate, F., Erbertseder, T., Felder, M. D., Flynn, L. E., Godin-Beekmann, S., Hansen, G., Hasekamp, O. P., Kaifel, A., Kelder, H. M., Kerridge, B. J., Lambert, J.-C., Landgraf, J., Latter, B., Liu, X., McDermid, I. S., Pachepsky, Y., Rozanov, V., Siddans, R., Tellmann, S., van der A, R. J., van Oss, R. F., Weber, M., and Zehner, C.: Evaluation of Global Ozone Monitoring Experiment (GOME) ozone profiles from nine different algorithms, Journal of Geophysical Research (Atmospheres), 111, 21 306–+, doi:10.1029/2005JD006778, 2006.

Munro, R., Siddans, R., Reburn, W. J., and Kerridge, B. J.: Direct measurement of tropospheric ozone distributions from space, Nature, 392, 168–171, doi:10.1038/32392, 1998.

Rodgers, C. D.: Inverse methods for atmospheric sounding, vol. Vol. 2 of *Series on Atmospheric, Oceanic and Planetary Physics*, World Scientific Publishing, Singapore, 2008 edn., 2000.

Sato, K., Tomikawa, Y., Hashida, G., Yamanouchi, T., Nakajima, H., and Sugita, T.: Longitudinally-dependent ozone increasse in the Antarctic polar vortex revealed by balloon and satellite observations, Journal of the Atmospheric Sciences - Early Online Releases, doi:10.1175/2008JAS2904.1, 2009.

Schutgens, N. A. J. and Stammes, P.: A novel approach to the polarization correction of spaceborne spectrometers, Journal of Geophysical Research, doi:10.1029/2002JD002736, 2003.

Sparling, L. C., Wei, J. C., and Avallone, L. M.: Estimating the impact of small-scale variability in satellite measurement validation, Journal of Geophysical Research (Atmospheres), 111, D20310, doi:10.1029/2005JD006943, 2006.

van der A, R. J., van Oss, R. F., Piters, A. J. M., Fortuin, J. P. F., Meijer, Y. J., and Kelder, H. M.: Ozone profile retrieval from recalibrated Global Ozone Monitoring Experiment data, Journal of Geophysical Research (Atmospheres), 107, 4239–+, doi:10.1029/2001JD000696, 2002.

van Oss, R. F. and de Haan, J. F.: Algorithm Theoretical Basis Document for OPERA, issue 1.1, CHEOPS/KNMI/ATBD/001/17-20, 2004.

van Oss, R. F. and Spurr, R. J. D.: Fast and accurate 4 and 6 stream linearized discrete ordinate radiative transfer models for ozone profile retrieval, Journal of Quantitative Spectroscopy and Radiative Transfer, 75, 177–220, doi:10.1016/S0022-4073(01)00246-1, 2002 a.

van Peet, J. C. A., van der A, R. J., de Laat, A. T. J., Tuinder, O. N. E., König-Langlo, G., and Wittig, J.: Height resolved ozone hole structure as observed by the Global Ozone Monitoring Experiment-2, Geophysical Research Letters, 36, L11 816, doi:10.1029/2009GL038603, 2009.

3

Ozone ProfilE Retrieval Algorithm (OPERA) for nadir-looking satellite instruments in the UV–VIS

For the retrieval of the vertical distribution of ozone in the atmosphere the Ozone ProfilE Retrieval Algorithm (OPERA) has been further developed. The new version (1.26) of OPERA is capable of retrieving ozone profiles from UV–VIS observations of most nadir-looking satellite instruments like GOME, SCIAMACHY, OMI and GOME-2. The setup of OPERA is described and results are presented for GOME and GOME-2 observations. The retrieved ozone profiles are globally compared to ozone sondes for the years 1997 and 2008. Relative differences between GOME/GOME-2 and ozone sondes are within the limits as specified by the user requirements from the Climate Change Initiative (CCI) programme of ESA (20 % in the troposphere, 15 % in the stratosphere). To demonstrate the performance of the algorithm under extreme circumstances, the 2009 Antarctic ozone hole season was investigated in more detail using GOME-2 ozone profiles and lidar data, which showed an unusual persistence of the vortex over the Río Gallegos observing station (51° S 69.3° W). By applying OPERA to multiple instruments, a time series of ozone profiles from 1996 to 2013 from a single robust algorithm can be created.

This chapter has been published in Atmospheric Measurement Techniques as van Peet et al. (2014).

3.1. Introduction

Ozone is an important trace gas in the Earth's atmosphere. Whereas ozone in the stratosphere is essential to protect life from harmful UV radiation, ozone in the troposphere is considered to be a pollutant. At the same time ozone is a climate-forcing gas, and is therefore listed as one of the essential climate variables (ECV) by GCOS WMO (`http://gcos.wmo.int`, see e.g. 2010). Vertical information on the distribution of ozone is required for the study of climate change, numerical weather forecasts, air quality and UV index.

The most accurate method to measure the vertical ozone concentration is by means of balloon-borne ozone sondes, but these have two drawbacks. First, they only reach as high as about 30 km. Second, it is impossible to obtain global coverage using sondes. These problems can be partly overcome by using satellite-based measurements. In 1957 the first algorithm was described for calculating the energy in the incident radiation at a satellite-based detector measuring backscattered solar light (Singer and Wentworth, 1957). A few years later Twomey (1961) showed how to actually retrieve the ozone concentration from the incident radiation at the detector.

The first satellite instrument designed to measure the vertical distribution of ozone was the backscatter ultraviolet (BUV) spectrometer instrument on NIMBUS 4, which was launched in 1970. It was followed by the solar backscatter ultraviolet (SBUV) on NIMBUS 7 in 1978 and the SBUV/2 family aboard the NOAA satellites from 1985 onwards. A complete description of the retrieval algorithm for the (S)BUV instruments can be found in Bhartia et al. (1996).

In April 1995 the Global Ozone Monitoring Experiment (GOME) instrument was launched aboard the second European Remote Sensing satellite (ERS-2) (Burrows et al., 1999). GOME was the first of a new series of instruments with an increased wavelength range and higher spectral resolution with respect to the (S)BUV instruments. Other instruments followed, e.g. the SCanning Imaging Absorption spectroMeter for Atmospheric CartograpHY (SCIAMACHY; see Bovensmann et al., 1999), which was launched aboard ENVISAT in 2002; the Ozone Monitoring Instrument (OMI; see Levelt et al., 2006), launched in 2004 aboard Aura; and GOME-2 (Callies et al., 2000), launched in 2006 aboard the first of EUMETSAT's Metop series.

The development of the Ozone ProfilE Retrieval Algorithm (OPERA) started as a retrieval algorithm for GOME data (van der A et al., 2002). In this version, the forward radiative transfer model (RTM) MODTRAN (Anderson et al., 1995; Berk et al., 1989) was used. Ozone cross sections were derived from the high-resolution transmission molecular database 1996 (HITRAN96). The Ring effect was accounted for, but polarisation was neglected. The a priori information was taken from the Fortuin and Kelder climatology (Fortuin and Kelder, 1998). Clouds were modelled by assuming a higher surface albedo.

The OPERA version (1.03) used in the ozone profile retrieval algorithm re-

view paper by Meijer et al. (2006) included improvements to the wavelength calibration, polarisation sensitivity correction and degradation correction. The MODTRAN radiative transfer model was replaced by the LIDORT-A RTM (van Oss and Spurr, 2002 a). Cloud properties were calculated using the Fast Retrieval Scheme for Clouds from the Oxygen A band (FRESCO; Koelemeijer et al., 2001).

Mijling et al. (2010) studied the convergence statistics of OPERA (v. 1.0.9) for GOME in order to improve the profile retrieval. They identified certain geographical regions where OPERA has problems in converging, such as the South Atlantic Anomaly region and above deserts. The effect of input data, such as ozone cross sections, and climatology on the retrieval were also investigated. It was found that in applying these adaptations, the number of non-convergent retrievals was reduced from 10.7 to 2.1 %, and the mean number of iteration steps from 5.1 to 3.8.

In this article, we will describe, for the first time, OPERA version 1.26 applied to the retrieval of GOME and GOME-2 profiles. A different version of OPERA has been used operationally since 2007 within the O3MSAF of EUMETSAT (`http://o3msaf.fmi.fi/index.html`) for GOME-2 profile retrieval which has been validated using ozone sondes, lidar and microwave instruments (Delcloo and Kins, 2009). That version performs well under challenging circumstances such as the Antarctic ozone hole (van Peet et al., 2009). The OPERA version described here is not limited to GOME-2, however, but is also applicable to GOME and the retrieval of SCIAMACHY and OMI data is under development. Because OPERA can be applied to different instruments, it is used in the development of an algorithm to produce a 15-year-long time series of ozone profiles from GOME, SCIAMACHY, GOME-2 and OMI within the ozone project of ESA's Climate Change Initiative (CCI) programme (`http://www.esa-ozone-cci.org/`). Within this project, a comparison is made (Keppens, 2013) between OPERA and the retrieval scheme developed at the Rutherford Appleton Laboratory (Miles, 2013).

In Sect. 3.2 we give a description of GOME and GOME-2. In Sect. 3.3 we give a short overview of the theoretical background of OPERA and the changes with respect to other versions. In Sect. 3.4 we will show the results for an intercomparison of GOME and GOME-2 retrievals with ozone sondes. Finally, in Sect. 3.5 we will show how well OPERA is capable of capturing the dynamics of the Antarctic ozone hole during the 2009 season.

3.2. Instrument description

3.2.1. GOME

In April 1995 the Global Ozone Monitoring Experiment (GOME) was launched aboard the second European Remote Sensing satellite (ERS-2) (Burrows et al., 1999). One of the major changes with respect to the (S)BUV instruments was the wavelength range and the higher spectral resolution.

Table 3.1: Relative measurement noise in the level 1 data.

λ	260	280	300	320	340
GOME	5 %	5 %	1 %	< 1 %	< 1 %
GOME-2	25 %	25 %	5 %	< 1 %	< 1 %

Retrieval algorithms based on optimal estimation (see, for example, Rodgers, 2000) for GOME were developed by, for example, Munro et al. (1998), Hoogen et al. (1999), Hasekamp and Landgraf (2001), van der A et al. (2002) and Liu et al. (2005). No official ESA ozone profile product exists for GOME, but a comprehensive intercomparison of different GOME retrieval algorithms was done by Meijer et al. (2006).

GOME is a nadir viewing instrument that measures the backscattered radiation from the atmosphere between 240 and 790 nm at a resolution of 0.2–2.4 nm. GOME uses a scanning mirror with a period of 4.5 s in the forward scan direction and 1.5 s in the backward scan direction.

Because OPERA uses the part of the spectrum between 265 and 330 nm, only parts of GOME channels 1 (237 to 307 nm) and 2 (312 to 406 nm) are used. In order to achieve a sufficient signal-to-noise ratio, part of channel 1 (channel 1a) is read out every 12 s (two forward and two backward scans), while the other part of channel 1 (channel 1b) and channel 2 are read out every 1.5 s. Table 3.1 gives the relative measurement noise as reported in the level 1 data for a few selected wavelengths. More information on how the different channels are combined is given in Sect. 3.4.2.

3.2.2. GOME-2

The successor of GOME was GOME-2 (Callies et al., 2000), launched in 2006 aboard the first satellite in EUMETSAT's Metop satellite series. The experience gained in the operation of GOME led to a significant number of changes, but the overall concept remained the same. GOME-2 measures backscattered solar light from the Earth's atmosphere between 250 and 790 nm in four channels with a relatively high spectral resolution (0.2–0.4 nm).

GOME-2 uses a scanning mirror similar to GOME; a forward scan takes 4.5 s and the backward scan takes 1.5 s. In the normal mode, a forward scan corresponds to 40 km × 1920 km, which yields an almost global daily coverage. Channel 1a has an integration time of 1.5 s, corresponding to three ground pixels in a forward scan with a size of 40 km × 640 km. Bands 1b/2b have an integration time of 0.1875 s, corresponding to 24 ground pixels in a forward scan with a size of 40 km × 80 km. Table 3.1 gives the relative measurement noise as reported in the level 1 data for a few selected wavelengths. More information on how the different channels are combined is given in Sect. 3.4.3.

3.3. Algorithm description

3.3.1. Retrieval theory

The retrieval theory and notation used is based on Rodgers (2000). The state of the atmosphere can be represented by the state vector $\mathbf{x}$, which, in version 1.26 of OPERA, consists of the layers of the ozone profile, the albedo (see Sect. 3.3.2) and an additive offset (see Sect. 3.3.2). The measurement vector is given by $\mathbf{y}$. The relation between $\mathbf{x}$ and $\mathbf{y}$ is given by $\mathbf{y} = \mathbf{F}(\mathbf{x})$, where $\mathbf{F}$ is the forward model. This problem is generally underconstrained. Following the maximum a posteriori approach (Rodgers, 2000), the solution to $\mathbf{y} = \mathbf{F}(\mathbf{x})$ is given by

$$\hat{\mathbf{x}} = \mathbf{x}_a + \mathbf{A}\,(\mathbf{x}_t - \mathbf{x}_a) \tag{3.1}$$

$$\hat{\mathbf{S}} = (\mathbf{I} - \mathbf{A})\,\mathbf{S}_a \tag{3.2}$$

$$\mathbf{A} = \mathbf{S}_a\mathbf{K}^T\left(\mathbf{K}\mathbf{S}_a\mathbf{K}^T + \mathbf{S}_\epsilon\right)^{-1}\mathbf{K} \tag{3.3}$$

where $\hat{\mathbf{x}}$ is the retrieved state vector, $\mathbf{x}_a$ is the a priori, $\mathbf{A}$ is the averaging kernel, $\mathbf{x}_t$ is the "true" state of the atmosphere, $\hat{\mathbf{S}}$ is the retrieved covariance matrix, $\mathbf{I}$ is the identity matrix, $\mathbf{S}_a$ is the a priori covariance matrix, $\mathbf{K}$ is the weighting function matrix and $\mathbf{S}_\epsilon$ is the measurement covariance matrix. In OPERA, the measurement is the ratio of the radiance over the irradiance. The radiance and irradiance (and the errors) are taken from the level 1 data and used to calculate the measurement error according to error propagation theory. $\mathbf{S}_\epsilon$ is a diagonal matrix, with the measurement errors squared on the diagonal.

The averaging kernel can also be written as $\mathbf{A} = \partial\hat{\mathbf{x}}/\partial\mathbf{x}_t$ and gives the sensitivity of the retrieval to the true state of the atmosphere. The trace of $\mathbf{A}$ gives the degrees of freedom for the signal (DFS). When the DFS is high, the retrieval has learned more from the measurement than in the case of a low DFS, when most of the information in the retrieval will depend on the a priori. The total DFS can be regarded as the total number of independent pieces of information in the retrieved profile. The rows of $\mathbf{A}$ indicate how the true profile is smoothed out over the layers in the retrieval and are therefore also called smoothing functions. Ideally, the smoothing functions peak at the corresponding level and the half-width is a measure for the vertical resolution of the retrieval.

The covariance matrices include information on the uncertainty of $\mathbf{x}$. The diagonal elements are the variances of the corresponding elements in the retrieved profile. The off-diagonal elements give the correlations between layers.

3.3.2. Configuration

The Ozone ProfilE Retrieval Algorithm (OPERA) has many configurable parameters. The most important ones are listed in Table 3.2 and their settings are explained in more detail in the following sections.

Table 3.2: Some parameters of OPERA, a short description and the setting used in OPERA version 1.26.

Parameter	Description	Setting in OPERA
radiative transfer model	– LIDORT-A (van Oss and Spurr, 2002 a) – LABOS (used in the operational OMI retrieval algorithm; see e.g. Kroon et al., 2011)	LIDORT-A (see Sect. 3.3.2)
number of streams in the RTM	– LIDORT-A: four or six streams – LABOS: multiple of 2	six
Raman scattering	on or off	off
window bands	variable wavelength windows to use in the retrieval. Can be set independent from the instrument channels.	265 to 330 nm.
pressure grid	configurable levels which can be adapted "on the fly" to match surface pressure and cloud-top pressure	see Table 3.3
O_3 cross section	temperature parameterised cross sections by – Bass and Paur (1985) – Brion et al. (1993), Brion et al. (1998), Daumont et al. (1992) and Malicet et al. (1995); the polynomial expansion can be based on four or five temperatures.	the Brion, Daumont and Malicet cross-section database using five temperatures for the polynomial expansion (see Sect. 3.3.2)

(continued...)

Table 3.2: (continued...)

Parameter	Description	Setting in OPERA
temperature profile	– ECMWF operational – ERA-Interim reanalysis	ERA-Interim reanalysis (see Sect. 3.3.2)
O_3 climatology	– Fortuin and Kelder (Fortuin and Kelder, 1998) – TOMS-V8 (Bhartia and Wellemeyer, 2002) – McPeters, Labow and Logan (McPeters et al., 2007)	McPeters, Labow and Logan (see Sect. 3.3.2)
noise floor	systematic relative error of measured reflectance, added to measurement error	0.01 for GOME (level 1 data version 4.00), 0.00 for GOME-2 (level 1 data version 4.0)
additive offset	increase the modelled radiance at the short-wavelength end of the spectrum (see Sect. 3.3.2)	retrieved in optimal estimation
ATCT co-adding	combine measurements from different scan lines and wavelength channels	only activated for GOME-2 (see Sect. 3.4.3)
iteration/configuration	adjustable maximum number of iterations; convergence can be reached on relative cost function decrease, state vector update or both	maximum number of iterations is 10; convergence only checks on state vector update

Retrieval grid

The vertical resolution of retrieved nadir ozone profiles ranges between 7 and 15 km, depending on altitude, solar zenith angle and albedo (Hoogen et al., 1999; Liu et al., 2005; Meijer et al., 2006). A vertical resolution of 10 km or worse is achieved in the troposphere and upper stratosphere ($\geq$ 40 km), while values of 7 km have been reported for the middle stratosphere (at $\pm$ 25 km). The Nyquist criterion states that in order to be able to measure a certain resolution, the signal should be sampled at twice that resolution.

Another way to decide on the thickness of the retrieval layers is to check the DFS as a function of altitude. If the DFS remains constant when the altitude increases, the layers in that altitude range do not add information to the profile and can therefore be combined.

In Fig. 3.1, examples of the DFS of both a GOME and a GOME-2 observation over Europe are plotted as a function of altitude. The light-blue and red lines give the DFS for a high- resolution, 40-layer retrieval grid. The dark-blue and red lines give the same retrievals on the reduced 16-layer retrieval grid. At both low in the troposphere and high in the stratosphere, the DFS does not increase with height, which is an indication that these layers do not add information to the retrieved profile.

Above 60 km, the retrieved partial columns are practically zero, and therefore there appears hardly any reason to retrieve ozone above 60 km. However, for radiation balance in the radiative transfer model, the retrieval grid has been extended until 80 km (0.01 hPa).

The retrieval grid used here consists of 16 layers; an example for the DFS is given by the red line in Fig. 3.1. The altitudes of the layer boundaries are given in Table 3.3. The grid has two layers each 6 km thick from the surface up to 12 km; between 12 and 60 km the layers are 4 km thick, while above 60 km, two layers of 12 km each have been added for radiation balance in the radiative transfer model.

Ozone cross section

Several cross-section databases can be selected for use in OPERA. For OPERA version 1.26 the temperature parameterised cross sections of Brion, Daumont and Malicet have been used (Brion et al., 1993, 1998; Daumont et al., 1992; Malicet et al., 1995). Using the pressure grid defined in Table 3.3, ERA-Interim temperature profiles from the European Centre for Medium-Range Weather Forecasts (ECMWF; see Dee et al., 2011; Dragani, 2011) provide the temperature information for the ozone cross sections.

Clouds and surface albedo

For GOME and GOME-2, OPERA uses the FRESCO algorithm (Wang et al., 2008) to calculate the cloud-top pressure, cloud fraction and cloud albedo. FRESCO uses the surface albedo database by Koelemeijer et al. (2003), and the same values are used in OPERA.

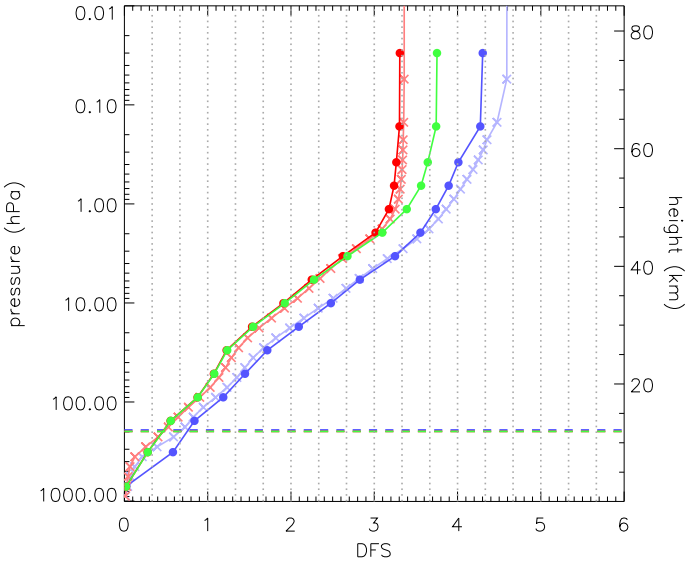

Figure 3.1: The cumulative DFS for a GOME observation on 26 May 1997 (blue) and for GOME-2 on 4 April 2008 (red) over Europe. The lines marked with crosses are the DFS for a high-resolution, 40-layer retrieval grid, while the lines marked with dots are the DFS for a retrieval on the 16-layer grid (see Table 3.3). The green line represents the same observation from GOME-2, but is retrieved without the additive offset. The horizontal dashed line is the thermal tropopause.

Table 3.3: The 16-layer pressure grid. Altitudes are given in kilometres and hectopascal for the lowest layer boundary. The surface pressure from the meteorology data ("PSURF") is used as the lowest boundary for layer 1. The top of atmosphere (TOA) is the top boundary of layer 16.

Layer	km	hPa	Layer	km	hPa
1	0	PSURF	10	40	4.27
2	6	446.05	11	44	2.47
3	12	196.35	12	48	1.43
4	16	113.63	13	52	0.83
5	20	65.75	14	56	0.48
6	24	38.05	15	60	0.28
7	28	22.02	16	72	0.05
8	32	12.74	TOA	84	0.01
9	36	7.37			

OPERA calculates two spectra: one for a completely cloudy case and one for a completely cloud-free case. The resulting spectrum is the average of these two, weighted by the cloud fraction. During the optimal estimation, either the surface albedo or the cloud albedo is included in the state vector and the other is held constant. The cloud fraction determines which option is used: if the cloud fraction is less than 0.2 (this value is configurable) the surface albedo is fitted and the cloud albedo is held constant. For cloud fractions larger than 0.2 the cloud albedo is fitted and the surface albedo is constant. By fitting an effective cloud fraction, the presence of aerosols is partly taken into account in the cloud retrieval. The error made with this procedure is smaller than when taking a (random) guess at the unknown aerosol distribution (confirmed by Boersma et al., 2004, for GOME NO_2 retrievals). If snow/ice is detected, only a cloud-free retrieval is done and the surface albedo is fitted.

Climatology

OPERA can use three different ozone climatologies as an a priori profile. These are the Fortuin and Kelder climatology (Fortuin and Kelder, 1998); the TOMS climatology (Bhartia and Wellemeyer, 2002); and the McPeters, Labow and Logan climatology (McPeters et al., 2007, MLL hereafter). Mijling et al. (2010) investigated the effect of these climatologies on the average number of iterations needed for convergence. The Fortuin and Kelder climatology is based on data from 1980 to 1991, which does not completely capture the Antarctic ozone depletion. The TOMS climatology requires an estimate of the total ozone column as an extra parameter in addition to latitude and time. It also requires an estimate of the error in the profile, which is not provided with the climatology. The MLL climatology was selected for the ozone profile retrievals in OPERA since it is more recent than the Fortuin and Kelder climatology and does not need estimates of the total column and error.

In an optimal estimation procedure, the full a priori covariance matrix is needed instead of only the error on the a priori profile. The MLL climatology does not include information on the covariance matrix, which therefore has to be constructed. For OPERA, this is done with an exponential decrease in pressure (see, for example, Hoogen et al., 1999; Meijer et al., 2006). The a priori covariance matrix ($\mathbf{S}_a$) off-diagonal elements depend on the diagonal elements as

$$\mathbf{S}_a(i,j) = \sqrt{\mathbf{S}_a(i,i)\mathbf{S}_a(j,j)}\,\mathrm{e}^{-\frac{|\log_{10}(P(i)/P(j))|}{l}} \tag{3.4}$$

where i and j are used to iterate over the layers of the a priori profile, $\mathbf{S}_a(i,i)$ are the variances taken from the climatology and $P(i)$ is the pressure. The variable l is the correlation length, which in OPERA is expressed in pressure decades and set to 0.3 (approximately 5 km).

Radiative transfer

OPERA can use two radiative transfer models, LABOS and LIDORT-A. The LABOS radiative transfer model was recently developed at the Royal Netherlands Meteorological Institute and is used for OMI profile retrievals (Kroon et al., 2011). Included in LABOS are an approximate treatment of rotational Raman scattering and a pseudo-spherical correction for direct sunlight. The assumption that the atmospheric layers are homogeneous holds only for multiple scattering. For single scattering, the atmospheric layers can be inhomogeneous. Further, weighting functions are calculated for specific altitudes in the atmosphere, namely at the interfaces between atmospheric layers and not for the atmospheric layers themselves.

LIDORT-A is an analytical solution for the radiative transfer equations, designed to be fast and accurate (van Oss and Spurr, 2002 a). While LABOS runs on any number of streams, LIDORT-A only runs on either four or six streams. However, a LABOS retrieval takes longer for a six-stream retrieval compared to LIDORT-A. It should be noted that for the best results LABOS should run on at least eight streams, which would take even longer.

Both RTMs have the option to include a full treatment of rotational Raman scattering, which increases the processing time by a factor of 2. The effect on the retrieved profiles is small, and therefore it has been decided not to activate the rotational Raman scattering in the retrieval in favour of speed.

The radiative transfer model LIDORT-A (van Oss and Spurr, 2002 a) is used to calculate the radiance at the top of the model atmosphere because it is faster than LABOS. In addition to the model atmosphere an initial ozone profile and geometrical parameters such as (solar) viewing angles should be provided to the RTM. Additional atmospheric data can be provided in the form of trace gas and aerosol databases.

South Atlantic Anomaly

The South Atlantic Anomaly (SAA) is the region of Earth where satellite orbits pass through the inner Van Allen radiation belt. The high-energy particles contained in the belt can cause spikes and noise in the measurements. The effects are especially notable in the short-wavelength end of the spectrum, where the signal levels are low.

In the version 1.26 of OPERA, an SAA filter is implemented which is a slightly adapted version of the filter described by Mijling et al. (2010), in which, starting at a reference wavelength of 290 nm and progressing towards shorter wavelengths, a measurement is discarded when the reflectance is more than the reflectance of the previous accepted wavelength plus 3 times the reflectance error. In addition to that filter, wavelengths with a reflectance lower than 85 % of the previous accepted wavelength are now discarded.

Using the filter adds successful retrievals in a region where otherwise no successful retrievals would be done. No special flags are raised to indicate whether the retrieval comes from the SAA region.

Calibration

GOME-2 suffers from degradation of the detector in much the same way as GOME and SCIAMACHY. The throughput of the detector is changing, most notably in the short-wavelength end of the spectrum. Because the light paths for the Earth and solar radiance are different, the instrument degradation does not cancel out in the radiance / irradiance ratio. For GOME corrections are supplied along with the level 1 data, but for GOME-2 no such data are supplied with the level 1 data.

As a result of the degradation of the detector, the modelled radiance by the RTM for a given "true" profile is on average lower than the measured radiance for wavelengths smaller than 300 nm. In order to correct for both degradation and the detector's calibration, an offset is included for band 1 in the forward model to increase the photon count. This "additive offset" is added to the state vector and fitted in the optimal estimation procedure.

With the addition of the wavelength independent additive offset (A0), the Sun-normalised radiance (SNR) is given by

$$\mathrm{SNR}(\lambda) = \frac{E(\lambda) + \mathrm{A0}}{I_0(\lambda)} \tag{3.5}$$

with E the simulated earth radiance, I_0 the solar irradiance and λ the wavelength. It is assumed that the wavelength is calibrated properly in the level 1 data, and no other checks are performed in OPERA.

Convergence

Optimal estimation is an iterative process, so a convergence criterion has to be set in order to prevent the algorithm from iterating indefinitely. The next step in the iteration of the state vector is given by Eq. (5.10) in Rodgers (2000):

$$\mathbf{x}_{i+1} = \mathbf{x}_a + \mathbf{S}_a \mathbf{K}_i^T \left(\mathbf{K}_i \mathbf{S}_a \mathbf{K}_i^T + \mathbf{S}_\epsilon\right)^{-1} \left[\mathbf{y} - \mathbf{F}\left(\mathbf{x}_i\right) + \mathbf{K}_i \left(\mathbf{x}_i - \mathbf{x}_a\right)\right] \tag{3.6}$$

The covariance matrix of the solution is calculated according to Eq. (3.2), and the gain matrix ($\mathbf{G}$) according to Eq. (5.15) in Rodgers (2000), using the same Jacobian ($\mathbf{K}_i$) as in the final iteration step. The gain matrix and Jacobian are used to calculate the averaging kernel matrix according to $\mathbf{A} = \mathbf{GK}$.

In OPERA version 1.26, the convergence criterion (calculated according to Eq. 5.29 in Rodgers, 2000) is based on the magnitude of the state vector update, and convergence has been reached when the relative change in the state vector is less than 2 %. A maximum of 10 iterations has been set before the retrieval is flagged as not converged. Since the average number of iterations is between 3.5 and 4.5, an upper limit of 10 iterations will only stop a small fraction of the retrievals. Out-of-bounds retrieval values and too high χ^2 values produce additional error flags.

3.4. Results

3.4.1. Methodology

Only converged ozone profile retrievals with solar zenith angle less than 80° have been used for a short validation study. The profiles produced by OPERA are compared to ECC-type ozone sondes (models Z and 6) that were obtained from the World Ozone and Ultraviolet Radiation Data Centre (WOUDC, 2011).

To be accepted for the validation, the sonde station should be inside the pixel footprint of the satellite instrument. The sondes are required to reach a minimum altitude of 10 hPa, and the time difference between sonde launch and satellite overpass should not be more than 2 h. When multiple collocations occur, only the collocation with the sonde that is closest in time to the satellite overpass is used. Therefore, each retrieval is validated against one sonde profile.

GOME profiles have been validated against sondes from 1997, while GOME-2 profiles have been validated against sondes from 2008. After applying the collocation criteria described above, 190 sondes from 25 stations worldwide (ranging from 1 to 48 sondes per station) were used for the validation of the GOME ozone retrievals, and 26 sonde stations with 564 sondes (ranging from 1 to 97 sondes per station) were used for the validation of GOME-2 profiles. The locations for the sonde stations that are used in the validation are given in Fig. 3.2.

The ozone profiles from sondes that are collocated with satellite measurements are interpolated to the pressure grid used in the ozone profile retrieval and converted to DU layer^{-1}. Above the sonde burst level, the interpolated sonde profile is extended with the retrieval a priori partial columns. The interpolated and extended sonde profile ($\mathbf{x}$) is then convolved with the averaging kernel ($\mathbf{A}$) and the a priori profile ($\mathbf{x}_a$) according to Eq. (3.1), with $\mathbf{x}_t$ replaced by the sonde profile $\mathbf{x}$. The resulting $\hat{\mathbf{x}}$ is the smoothed sonde profile as it would have been observed by the satellite instrument. This smoothed sonde profile is compared with the actual collocated satellite measurement. This procedure is followed for each sonde station separately, but also for three zonal regions: the Southern Hemisphere (−90 to −30° latitude), the tropics (−30 to 30° latitude) and the Northern Hemisphere (30 to 90° latitude).

3.4.2. GOME

For the validation of GOME we used all ozone sondes for 1997 from the WOUDC database that fulfil the collocation criteria explained in Sect. 3.4.1. The sonde locations are shown in Fig. 3.2.

The different integration times for channel 1a and the channels 1b and 2 result in different ground pixel sizes. One measurement from channel 1a covers an area at the surface of about 100 km × 960 km, and one forward scan measurement from channel 1b or 2 covers an area of 40km × 320 km.

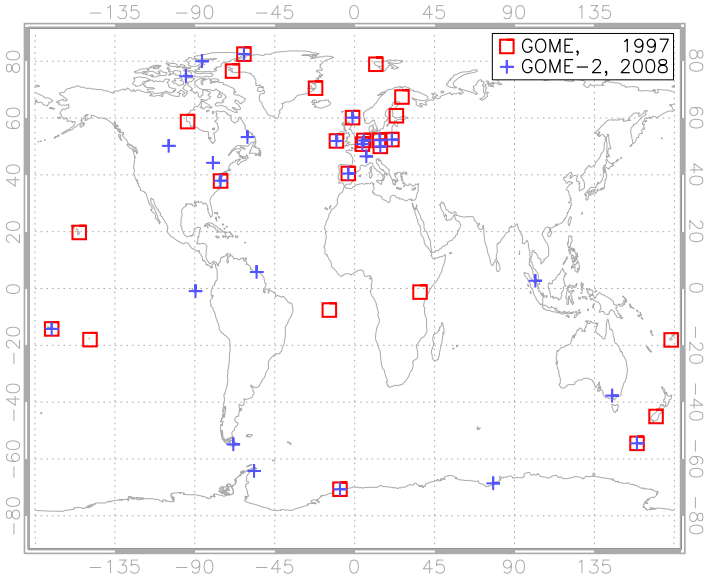

Figure 3.2: The locations of the ozone sonde stations used for the validation of GOME (1997, red squares) and GOME-2 (2008, blue crosses).

During one channel 1a integration time, the forward scans from channel 1b and 2 are read out six times. Each of these six channel 1b and 2 spectra is combined with the same overlapping channel 1a spectrum. The ground pixel size for the ozone profiles is therefore equal to the channel 1b and 2 ground pixel size.

Table 3.4 gives an overview of the validation results for GOME for the Southern Hemisphere (SH), the tropics (TR) and the Northern Hemisphere (NH). The global averages are given in the last column. On the first row the DFS are given for the GOME retrievals that collocate with the sonde measurements. The DFS is lowest in the tropics, indicating that more information in the profile is coming from the a priori. The number of iterations ("n_iter") needed for the retrieval to reach convergence is slightly higher in the tropics than for the other two regions.

The differences in DFS and number of iterations might be affected by the number of sondes used (the row with "n_sonde" in Table 3.4) for the validation. For the Southern Hemisphere and the tropics, far fewer sondes are available for the validation than for the Northern Hemisphere. The results in the global column are therefore biased towards the Northern Hemisphere results.

The final two rows in Table 3.4 give the total number of GOME pixels that were retrieved ("n_pix") and the percentage of converged pixels ("%"). The percentage of converged pixels is significantly lower for the Southern Hemisphere than for the tropics or the Northern Hemisphere. From Fig. 3.2

Table 3.4: GOME validation statistics. DFS represents degrees of freedom, n_iter the number of iterations, n_sonde the number of sondes, n_pix the total number of retrieved pixels, and % the percentage of converged retrievals. SH stands for Southern Hemisphere (−90 to −30°), TR tropics (−30 to 30°), and NH Northern Hemisphere (30 to 90°).

Latitude	SH	TR	NH	Global
DFS	4.16	3.62	4.31	4.20
n_iter	4.15	4.69	4.28	4.33
n_sonde	13	26	151	190
n_pix	546	570	3660	4776
converged (%)	72.2	97.5	99.3	96.0

it can be seen that the Southern Hemisphere is represented by three stations only, one of them being on the Antarctic continent. Since OPERA performs only a cloud-free retrieval over snow and ice, using an effective scene albedo, it has difficulties in discerning snow- and ice-covered surfaces from middle- and high-level clouds. This might be a reason why the percentage of converged retrievals is lower for the Southern Hemisphere.

Figure 3.3 gives mean relative differences of the collocations between sondes and GOME. The Southern Hemisphere, tropics and Northern Hemisphere are indicated by the blue, red and green lines respectively (solid lines are the retrieved values, and the dashed lines are the a priori). The error bars indicate the 95 % confidence interval around the means. For most of the altitude range, the retrievals perform better than the a priori compared with sondes.

The vertical dashed lines are accuracy levels for the troposphere and stratosphere defined in the user requirements of the ozone project of the ESA CCI programme (`http://www.esa-ozone-cci.org/`). For the short-term variability, an accuracy of 20 % is required in the troposphere, while a 15 % accuracy is required in the stratosphere. The GOME retrievals are well within the required accuracy levels for the whole height range covered by the ozone sondes. The slight deviation at the top for the atmosphere is not significant since only one or two sondes reach this altitude.

If the true profile (taken as the sonde profile here) is close to the a priori, Eq. (3.1) shows that the retrieved profile is also close to the a priori. Another aspect of the retrieval is that the a priori uncertainty is reduced according to Eq. (3.2). Figure 3.4 gives the mean of the relative error differences between the retrieval and the a priori. For the Northern and Southern Hemisphere, the mean relative error difference decreases from about −10 % near the surface to about −85 % at the top of the atmosphere. The tropics behave somewhat differently, starting at −40 % near the surface, increasing to about −15 % near 200 hPa and decreasing to −65 % near the top of the atmosphere. The mean relative error difference is smaller than zero for all latitude bands and for all altitudes, indicating that the retrieval performs as expected in reducing the a priori error.

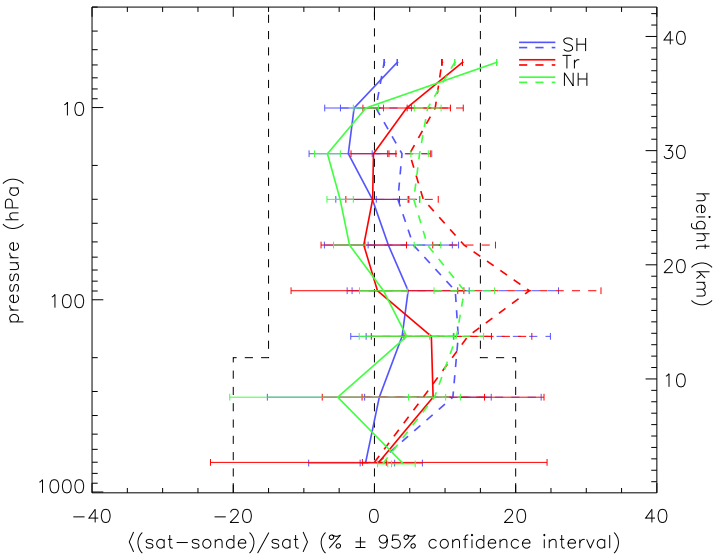

Figure 3.3: Mean of the relative differences per latitude band for GOME retrievals. Error bars indicate the 95 % confidence interval around the mean. The blue line gives the result for the Southern Hemisphere (SH), red for the tropics (Tr) and green for the Northern Hemisphere (NH) (solid for the retrieval, dashed for the a priori). The vertical dashed lines are accuracy levels for the troposphere and stratosphere defined in the ozone project of the ESA CCI programme.

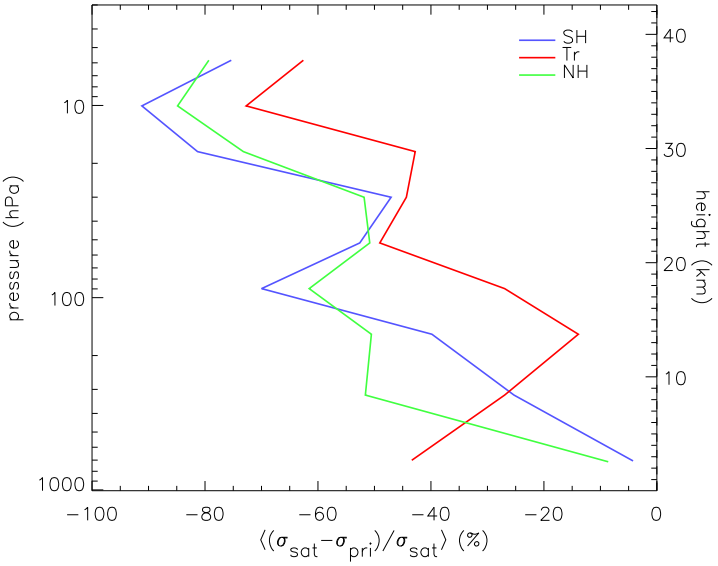

Figure 3.4: Mean of the relative error differences per latitude band for GOME retrievals and a priori. The blue line gives the result for the Southern Hemisphere (SH), red for the tropics (Tr) and green for the Northern Hemisphere (NH).

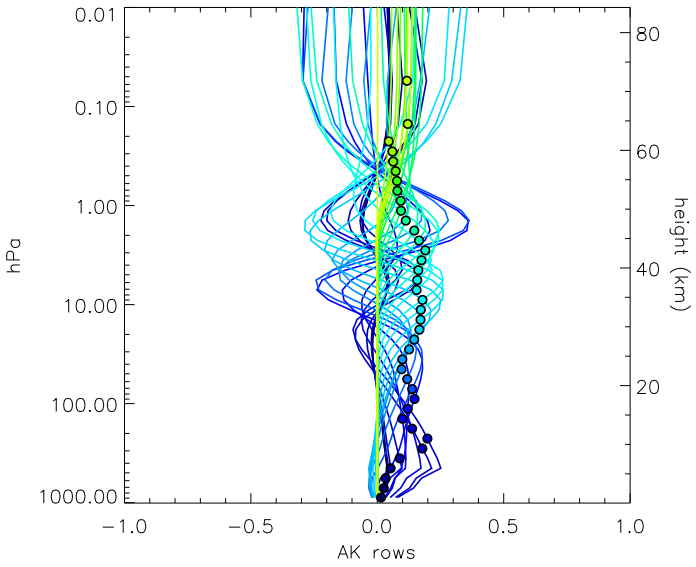

Figure 3.5: Averaging kernels for the 40-layer GOME retrieval over Europe that was also used in Fig. 3.1. The circles give the nominal altitude for the retrieval. The averaging kernels corresponding to the albedo and the additive offset have not been plotted.

Averaging kernels for the same pixel that was used to construct the DFS profiles for GOME in Fig. 3.1 are plotted in Figs. 3.5 and 3.6. The averaging kernel values at the nominal retrieval altitudes for the 40-layer retrieval are smaller than for the 16-layer retrieval. If the averaging kernel diagonal elements for the 40-layer retrieval are summed between the pressure levels of the 16-layer retrieval, the value is comparable to the corresponding diagonal element from the 16-layer retrieval.

In addition to the 16 ozone layers, there are two more state vector elements: the albedo (see Sect. 3.3.2) and the additive offset (see Sect. 3.3.2). Due to the selection of surface or cloud albedo in the state vector, the albedo distribution shows two peaks at 0.08 and 0.8 respectively. These values match the average albedo values for the surface and clouds and are observed in all zonal regions in all months.

In the GOME level 1 data the instrument degradation is taken into account in the correction data supplied with the level 1 data. Therefore, the additive offset is stable and rather low: the global 1997 mean is 0.3×10^9 photons with a standard deviation of 0.2×10^9 photons.

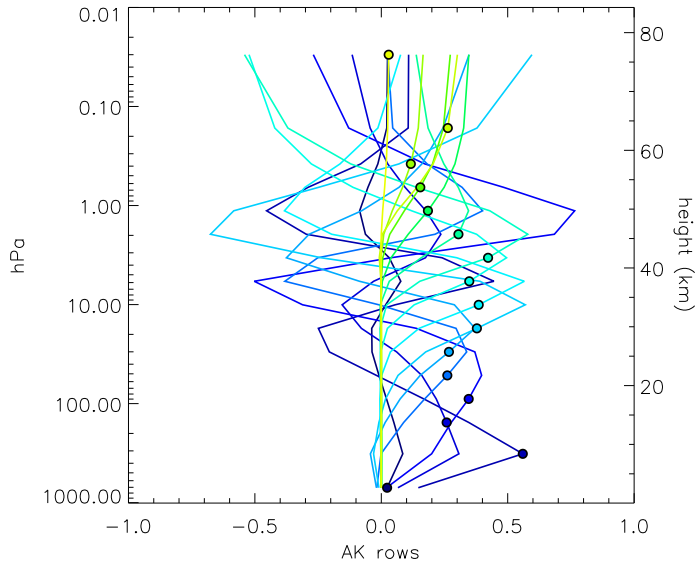

Figure 3.6: Averaging kernels for the 16-layer GOME retrieval over Europe that was also used for the blue line in Fig. 3.1. The circles give the nominal altitude for the retrieval. The averaging kernels corresponding to the albedo and the additive offset have not been plotted.

3.4.3. GOME-2

Horizontal correlation lengths of ozone in the atmosphere are 350 to 400 km in the lower stratosphere and 100 to 150 km in the middle and upper troposphere (Sparling et al., 2006). Using a pixel footprint that is much smaller than the correlation length leads to oversampling and higher computational cost. Therefore a compromise must be found between the different correlation lengths, the pixel size used in the retrieval and the computational cost.

There are three options to combine GOME-2 channel 1a spectra with channels 1b and 2b. The first option is to average the channels 1b and 2b spectra (0.1875 s integration time) until the total integration time is equal to the channel 1a integration time (1.5 s). The resulting spectrum can be combined with the channel 1a spectrum resulting in a ground pixel size of 40 km × 640 km (blue pixels in Fig. 3.7).

The second option is to combine each of the channel 1b/2b spectra within the channel 1a integration time with the channel 1a spectrum. This will result in eight ground pixels with a size of 40 km × 80 km (yellow pixels in Fig. 3.7).

The third option, called ATCT co-adding (along track, cross track), is different from the two options above in that it combines spectra from different forward scans, including channel 1a spectra. In Fig. 3.7, two different combinations are illustrated. The red borders give the ground pixel size when

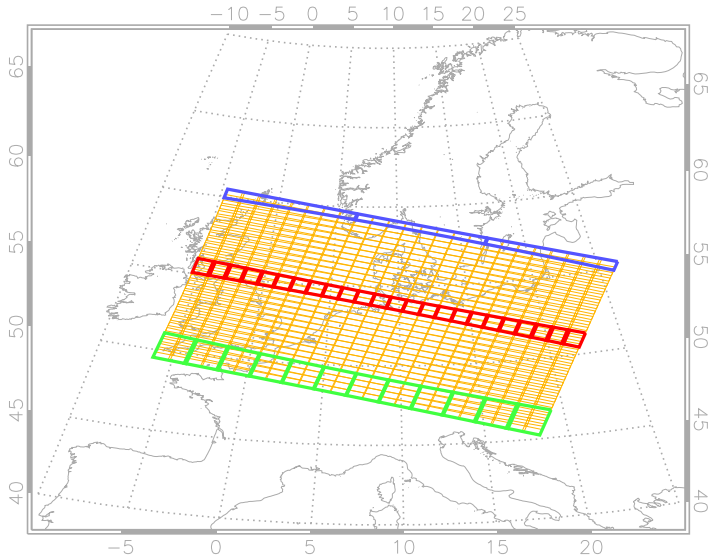

Figure 3.7: Blue grid: the average of eight spectra from channels 1b/2b, the result combined with the corresponding channel 1a spectrum. Yellow grid: separate combination of each channel 1b/2b spectrum with the overlapping channel 1a spectrum. Red grid: channel 1a spectrum and one 1b/2b spectrum from one forward scan combined with the next forward scan. Green grid: channel 1a spectrum and two 1b/2b spectra from one forward scan combined with the next three forward scans.

the channel 1b/2b spectra and the overlapping channel 1a spectrum in a forward scan are combined with the spectra from channel 1a and 1b/2b in the next forward scan. This results in ground pixels of approximately 80 km × 80 km. The green borders show the ground pixel size for a combination of two consecutive channel 1b/2b spectra with the overlapping channel 1a spectrum from a foward scan with the corresponding channel 1a and 1b/2b from the next three scan lines. This results in ground pixel sizes of approximately 160 km × 160 km.

Figures 3.8–3.10 show a comparison between the different methods of combining the measurements described above. In Fig. 3.8, the pixel size is approximately 40 km × 640 km, which is much larger than the correlation length in the upper troposphere in one direction. As a consequence, the details visible in Fig. 3.9 (pixel size 40 km × 80 km) are smoothed out. Processing all data at the same high resolution as in the middle plot is not feasible due to the high computational cost. Therefore, we combine two GOME-2 pixels cross track and four along track as in Fig. 3.10 (pixel size 160 km × 160 km), i.e. the green pixels in Fig. 3.7. At this resolution, the details from Fig. 3.9 are still visible and not completely smoothed out like in Fig. 3.8.

For the GOME-2 validation we used all available ozone sondes for 2008 from the WOUDC database complying with the collocation criteria explained in Sect. 3.4.1. The sonde locations are shown in Fig. 3.2.

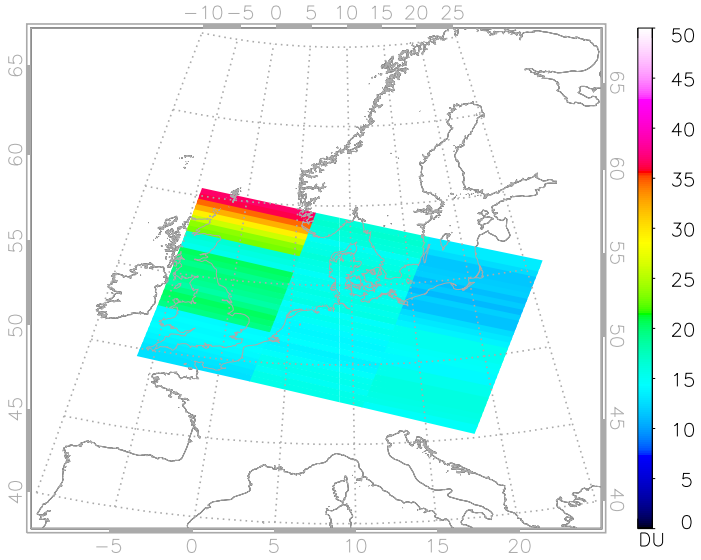

Figure 3.8: The partial ozone columns (DU) in the second layer of a retrieval (6 to 12 km) over Europe for the blue pixels that were illustrated in Fig. 3.7.

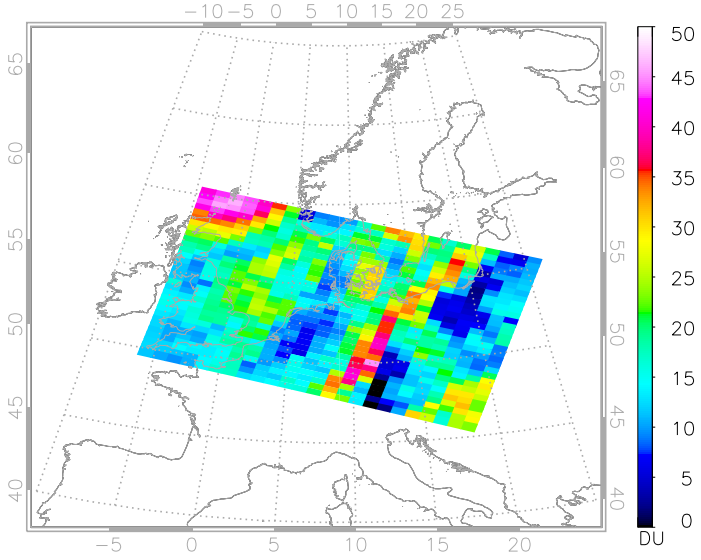

Figure 3.9: The partial ozone columns (DU) in the second layer of a retrieval (6 to 12 km) over Europe for the yellow pixels that were illustrated in Fig. 3.7.

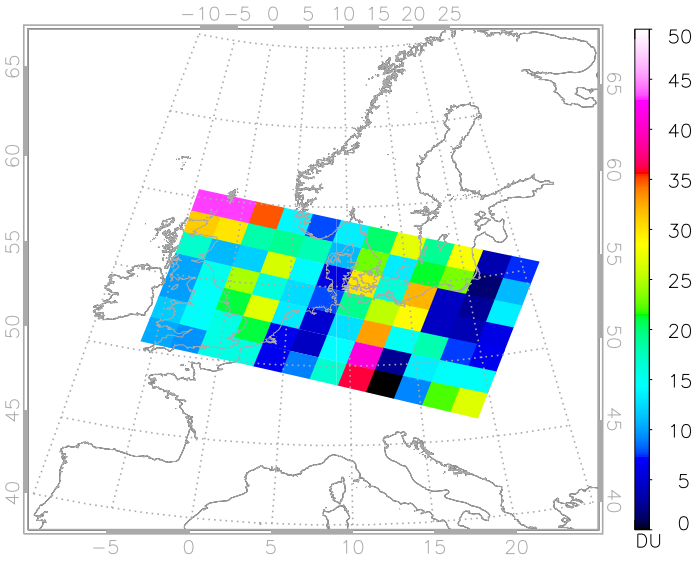

Figure 3.10: The partial ozone columns (DU) in the second layer of a retrieval (6 to 12 km) over Europe for the green pixels that were illustrated in Fig. 3.7.

Table 3.5 shows the validation data for GOME-2 in the same format as in Table 3.4. Although the differences in GOME-2 DFS between the Southern Hemisphere, tropics and Northern Hemisphere are similar to those of GOME, the absolute values for GOME-2 are lower than for GOME. This is caused by the different signal-to-noise ratios of the instruments. A smaller signal-to-noise ratio results in less information from the measurements and more information from the a priori. Table 3.6 gives the dependence of the DFS on the measurement noise. The DFS decreases with increasing measurement noise, which is the expected behaviour based on Eq. (3.3). It is assumed that the measurement errors are uncorrelated, so the measurement covariance matrix is a diagonal matrix. When a correlation between the measurements is introduced by setting the elements above and below the diagonal of the covariance matrix to 0.01 and 0.10 of the diagonal elements respectively, the mean DFS drops by 0.3 and 3 %.

The number of iterations is lower for GOME-2 than for GOME. If the error in the measurement is large, then the retrieval will remain close to the a priori and fewer iterations are needed before convergence is reached. Therefore it is probable that the lower DFS and number of iterations of GOME-2 with respect to GOME are caused by the same underlying mechanism.

The number of sondes used in the validation is larger for GOME-2 than for GOME, especially in the Southern and Northern Hemisphere. The number of retrieved pixels is much larger, due to the higher spatial resolution

Table 3.5: GOME-2 validation statistics for retrievals done on the green pixels in Fig. 3.7. Variables are the same as in Table 3.4.

Latitude	SH	TR	NH	Global
DFS	3.61	2.78	3.40	3.40
n_iter	3.85	3.53	3.55	3.59
n_sonde	92	32	440	564
n_pix	24 363	13 193	86 100	123 656
converged (%)	85.0	84.1	98.2	94.1

Table 3.6: GOME-2 DFS dependence on level 1 measurement error multiplied by "Factor". The values for factors 0 and ∞ are derived from Eq. (3.3) assuming that $\mathbf{S}_\epsilon$ is a diagonal matrix.

Factor	0	0.5	1.0	2.0	3.0	∞
DFS	16	4.28	3.62	2.85	2.44	0

of GOME-2.

The percentage of converged retrievals for GOME-2 with respect to GOME is higher in the Southern Hemisphere but lower in the tropics. The higher convergence in the Southern Hemisphere might be a consequence of the increased number of sonde stations for the validation of GOME-2 (six) with respect to GOME (three). There are more stations outside Antarctica, and
consequently fewer problems with snow and ice. On the other hand, it is unclear why the percentage of converged retrievals for the tropics is lower for GOME-2 than for GOME.

Figure 3.11 gives the mean relative differences for the validation of GOME-2. The retrieved values are similar to GOME, except for the second layer between 6 and 12 km. Here, GOME-2 significantly underestimates the sonde measurements in the Northern Hemisphere. In the tropics, the retrieved values for GOME-2 show a deviation comparable to that of GOME, but the bias is larger than for the a priori. The Southern and Northern Hemisphere show in general a better agreement up to 35 km between retrievals and sondes than between a priori and sondes.

In Fig. 3.12, a more detailed example for the mean relative differences in the Northern Hemisphere is given. Both the a priori and the retrieved profile were compared to the sonde profile and the sonde profile convolved with the averaging kernel. The differences with non-convolved sonde profiles are similar to the differences with the convolved sonde profiles. With the exception of the second layer of the retrieval, both perform better than the a priori. Note that the number of sondes above 10 hPa rapidly decreases.

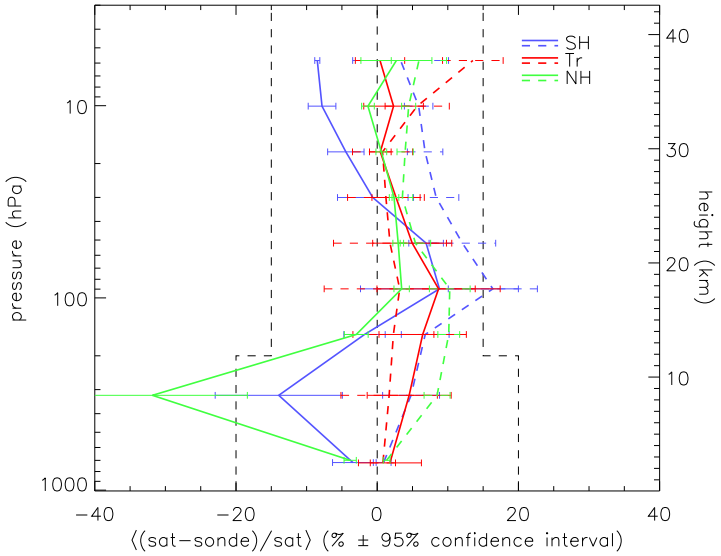

Figure 3.11: Mean of the relative differences per latitude band for GOME-2 retrievals. Error bars indicate the 95 % confidence interval around the mean. The blue line gives the result for the Southern Hemisphere (SH), red for the tropics (Tr) and green for the Northern Hemisphere (NH) (solid for the retrieval, dashed for the a priori). The vertical dashed lines are accuracy levels for the troposphere and stratosphere defined in the ozone project of the ESA CCI programme.

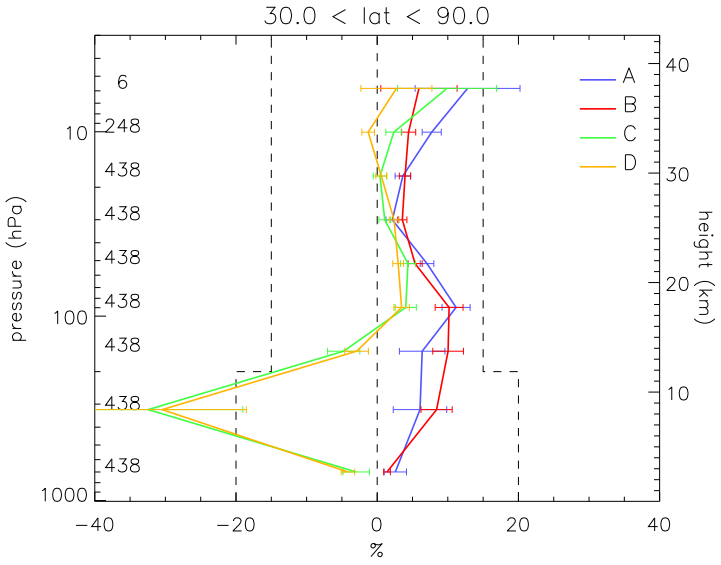

Figure 3.12: Mean of the relative differences for GOME-2 retrievals in the Northern Hemisphere. A is the mean of (apri-sonde)/apri, B is the mean of (apri-sonde_ak)/apri, C is the mean of (sat-sonde)/sat and D is the mean of (sat-sonde_ak)/sat, where “sat” is the retrieved profile, “apri” is the a priori profile, “sonde” is the sonde profile on the retrieval grid and “sonde_ak” is the sonde profile convolved with the averaging kernel. The differences with sonde_ak are also used in Fig. 3.11. The numbers on the left side of the plot indicate the number of collocations between GOME-2 and sondes for that layer.

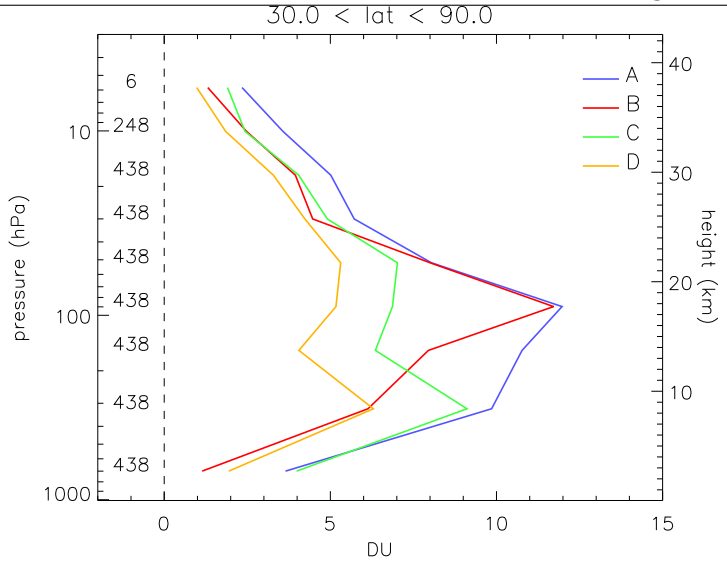

Figure 3.13: Root mean square (RMS) of the absolute differences for GOME-2 retrievals in the Northern Hemisphere. A is the RMS of apri-sonde, B is the RMS of apri-sonde_ak, C is the RMS of sat-sonde and D is the RMS of sat-sonde_ak, where “sat” is the retrieved profile, “apri” is the a priori profile, “sonde” is the sonde profile on the retrieval grid and “sonde_ak” is the sonde profile convolved with the averaging kernel. The numbers on the left side of the plot indicate the number of collocations between GOME-2 and sondes for that layer.

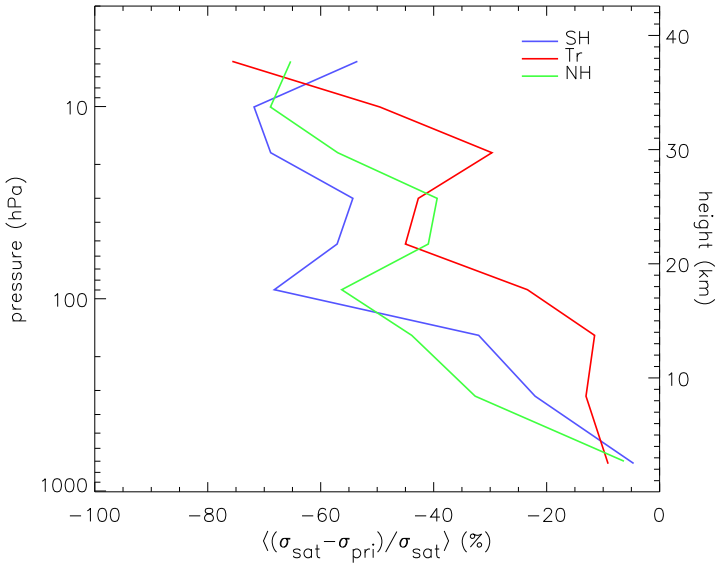

Figure 3.14: Mean of the relative error differences per latitude band for GOME-2 retrievals and a priori. The blue line gives the result for the Southern Hemisphere (SH), red for the tropics (Tr) and green for the Northern Hemisphere (NH).

In order to see how much of the actual variation is captured by the retrieval, the root-mean-square (RMS) differences are calculated and plotted in Fig. 3.13. The retrieval captures more of the actual variation than the a priori, both for the sonde profiles and sonde profiles convolved with the averaging kernel.

The mean relative errors of the retrieved profile and the a priori (see Fig. 3.14) are somewhat smaller for GOME-2 than for GOME. All three latitude bands start with relatively small error differences of the order of −5 to −10 % near the surface and decrease until about −65 % near the top of the atmosphere. Averaging kernels for the same pixel that was used to construct the DFS profiles for GOME-2 in Fig. 3.1 are plotted in Figs. 3.15 and 3.16.

The albedo state vector element for GOME-2 is very similar to GOME, but the additive offset is different in two aspects. The global mean additive offset for 2008 is larger than for GOME (1997): 1.1×10^9 photons with a standard deviation of 0.5×10^9 photons, because no calibration data have been supplied along with the GOME-2 level 1 data. The tropical region shows a bimodal distribution with peaks at 1.1×10^9 photons and 1.7×10^9 photons. The second peak is caused by two stations that are close to the South Atlantic Anomaly and which are used for the validation of GOME-2 (see Fig. 3.2). Since these two stations provided no data for 1997, they have not been used for the validation of GOME and the second peak is not observed in the GOME data. The additive offset for GOME-2 shows an increase from January until December 2008, with a maximum in June. This increase in additive offset is caused by the increased degradation of GOME-2.

Figure 3.17 gives a global map of the additive offset for 2 years (2007–2008) of GOME-2 data. Note that global coverage is not achieved, because retrievals were only done over areas where ozone sondes were available. It is clear that the SAA has a significantly higher mean additive offset than the rest of the Earth. Therefore the SAA has been treated as a separate region. Figure 3.17 shows the time series of the additive offset for the NH, Tr, SH and the SAA. All regions show an increasing trend for the additive offset, with the SAA being significantly higher.

As described in Sect. 3.3.2, GOME level 1 data are corrected for the instrument degradation, and therefore GOME does not show a trend in the additive offset. Since the same OPERA settings have been used for both GOME and GOME-2, the trend is most likely caused by instrument degradation.

The same GOME-2 data that were used in Figs. 3.1 and 3.16 were retrieved again without the additive offset. The green line in Fig. 3.1 shows the DFS profile, which is virtually the same as the retrieval with additive offset until an altitude of about 2 hPa (45 km). This is the same altitude above which the contribution of the true state to the retrieval starts to decrease. In the region above this altitude, the retrieval without additive offset gains about one third of a DFS compared to the retrieval including the additive

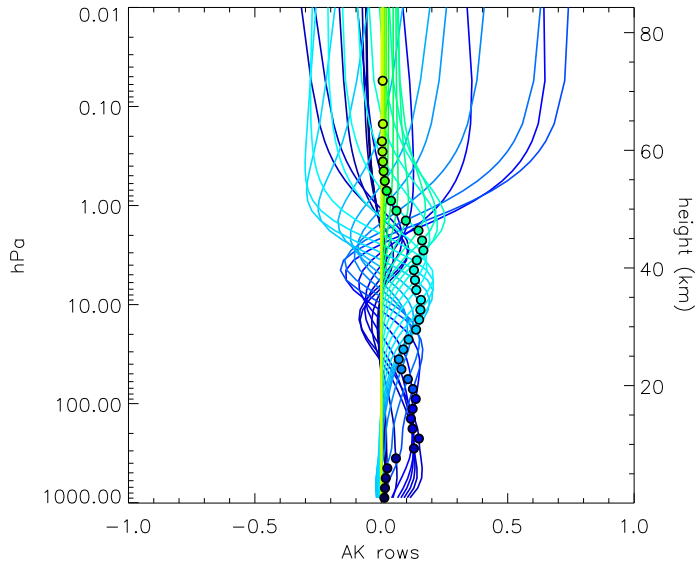

Figure 3.15: Averaging kernels for the 40-layer GOME-2 retrieval over Europe that was also used in Fig. 3.1. The circles give the nominal altitude for the retrieval. The averaging kernels corresponding to the albedo and the additive offset have not been plotted.

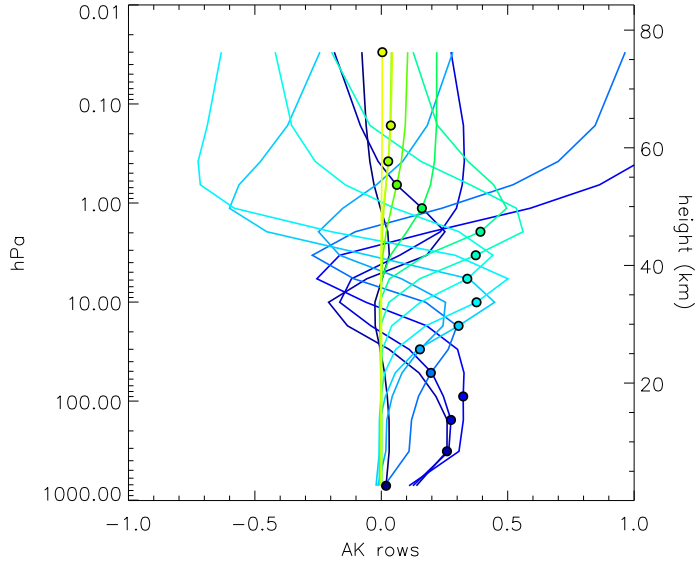

Figure 3.16: Averaging kernels for the 16-layer GOME-2 retrieval over Europe that was also used in Fig. 3.1. The circles give the nominal altitude for the retrieval. The averaging kernels corresponding to the albedo and the additive offset have not been plotted.

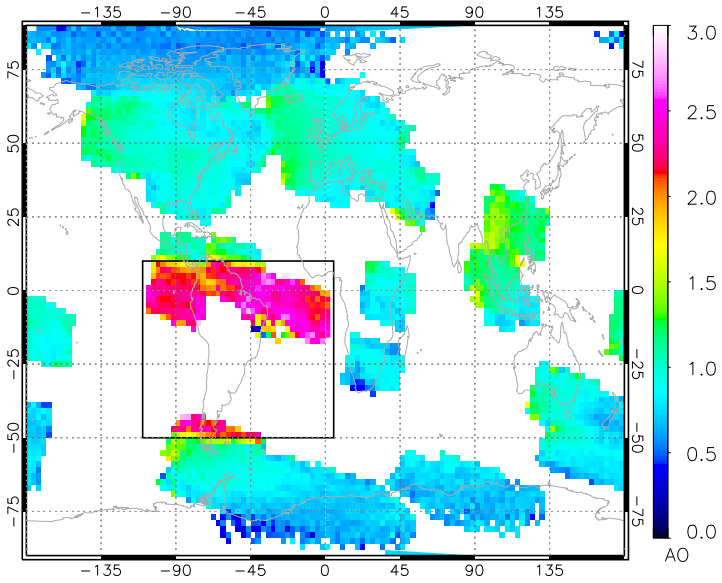

Figure 3.17: The mean of the additive offset (AO) for GOME-2 for 2007 and 2008 in $\times 10^9$ photons. The area indicated by the rectangle is affected by the South Atlantic Anomaly.

offset. Both retrievals level off above 0.3 hPa (60 km), indicating that no more information is present above that altitude. The averaging kernels for the retrieval without additive offset are very similar to the kernels of the retrieval with additive offset (see Fig. 3.16).

The additive offset has the largest effect in the region above 2 hPa, corresponding to the wavelength range of band 1. The validation results do not change significantly, but the global number of retrieved pixels that pass all quality criteria increases with 5.3 % when the additive offset is taken into account. The mean of the relative differences between the run with and the run without the additive offset is shown in Fig. 3.19.

Below 45 km, the retrieval is not very sensitive for the additive offset. The maximum difference is 2 %, with a standard deviation of the same order of magnitude. Above the 45 km, however, the difference increases to 25–30 %, with a standard deviation of 20 %.

Recent studies (e.g. Kyrölä et al., 2013; Gebhardt et al., 2014) show that the ozone trend over the last 20 years is of the order of a few percent per decade at altitudes over 20 km. Above 45 km, the observed trends are much smaller than the observed differences between the retrievals with and without the additive offset. For this altitude range it is possible that the trend will be (partly) masked by the additive offset. Below the 45 km, the trends larger than 2 % will not be masked by the additive offset.

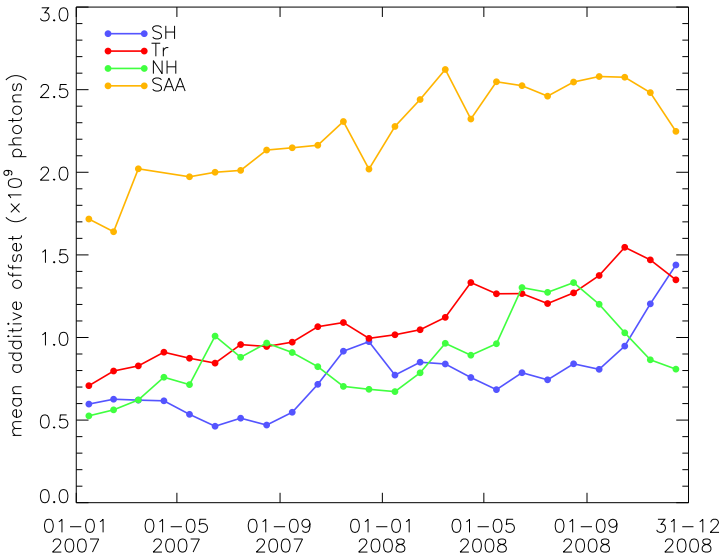

Figure 3.18: Time series of the monthly mean additive offset for GOME-2 for 2007 and 2008. The data for the South Atlantic Anomaly (SAA) time series are not included in the time series for the Southern Hemisphere (SH), tropics (Tr) or Northern Hemisphere (NH).

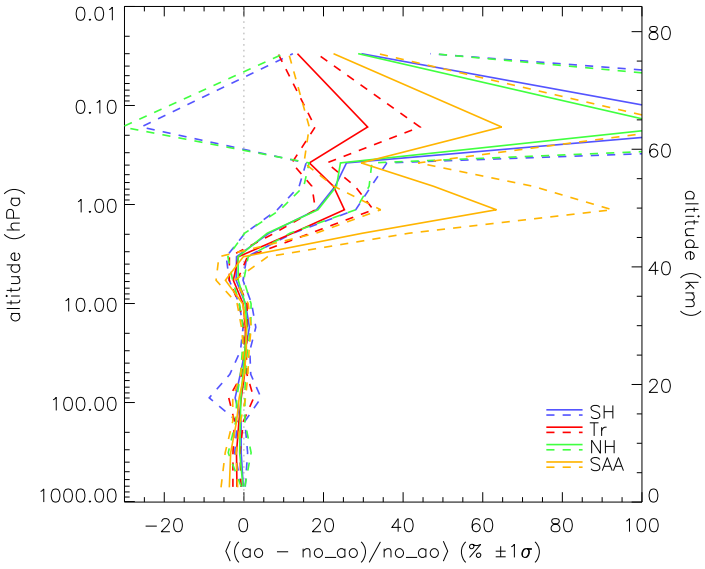

Figure 3.19: The mean of the relative differences between the retrieval with additive offset (AO) and without (no_AO). The blue line gives the result for the Southern Hemisphere (SH), red for the tropics (Tr) and green for the Northern Hemisphere (NH) (solid for the mean, dashed for the $\pm 1\sigma$ error). The South Atlantic Anomaly region (SAA; see Fig. 3.17) has been treated separately and is plotted in orange.

3.5. OPERA applied to the 2009 Antarctic ozone hole

In this section, we demonstrate the retrieval results by studying the Antarctic ozone hole in September, October, November and December 2009 as observed with GOME-2. For a period of three weeks in November 2009, the ozone hole showed an unusual persistence over the southern mid-latitude observing station in Río Gallegos (51° S, 69.3° W). During this period the a priori will be far from the true state of the atmosphere, which will be a challenge for OPERA. The lidar measurements made during the 2009 ozone hole season at this station (Wolfram et al., 2012) will be compared to GOME-2 ozone profile retrievals.

Van Peet et al. (2009) showed that GOME-2 is capable of studying the ozone hole dynamics in both space and time using ozone sondes from Neumayer Station. Using the lidar measurements from the Río Gallegos site enables us to extend the altitude range over which the GOME-2 measurements during ozone hole conditions can be validated. The ozone profiles are retrieved using the settings described in this article.

Note that Neumayer Station (70.65° S, 8.26° W) is located closer to the South Pole than the Río Gallegos observing station. As a consequence, the a priori for Neumayer Station will include vortex conditions, while the a priori for the Río Gallegos station will not. The vortex was present over Río Gallegos for a few consecutive weeks during November 2009 (de Laat et al., 2010). This is an interesting opportunity to study the performance of OPERA in situations where the a priori is very different than the actual ozone profile.

For the 2009 Antarctic ozone hole season we retrieved all GOME-2 data south of 45° S, and compared the GOME-2 retrievals to the lidar measurements from the Río Gallegos observing station. Due to the long integration times of the lidar (2.5 to 6 h), we selected those GOME-2 measurements that were closest in time to the centre of the integration time. The lidar operates at night, and time differences between the lidar and GOME-2 measurements vary between 6 and 11.5 h.

To make sure that the lidar and GOME-2 measure the same air mass, the assimilated total ozone columns from SCIAMACHY for both lidar measurement time and GOME-2 overpass time were compared. Measurements were not used if the difference was larger than 15 DU. The assimilated total ozone columns have been produced by the TM3DAM model Eskes et al. (2003) and the overpass data for Río Gallegos are freely available on `www.temis.nl`.

It is required for the lidar station to be within the GOME-2 pixel footprint, just as in the sonde validation. There are 25 lidar measurements available for the 2009 ozone hole season, and after applying the above collocation criteria, 18 were used for the validation.

The lidar profiles were interpolated to partial columns on the same pres-

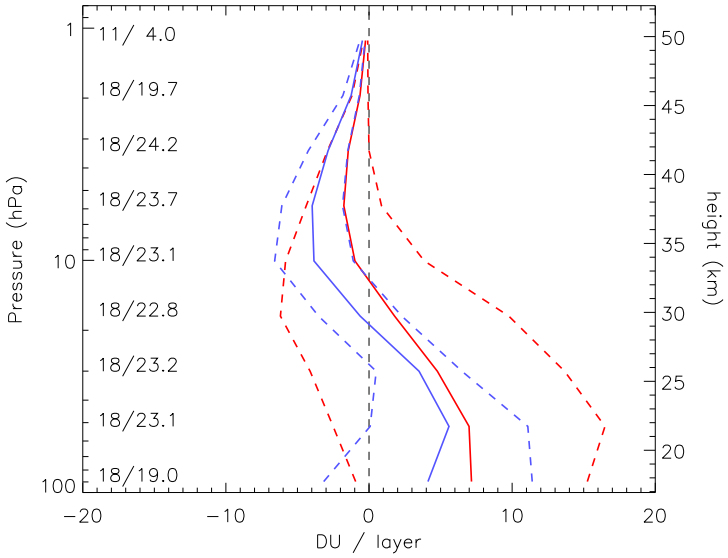

Figure 3.20: The mean of the differences between GOME-2 and the lidar at Río Gallegos (DU layer^{-1}) for the retrieval (blue) and the a priori (red). The solid line is the mean, and the dashed lines are the ± 1 standard deviations. The first number in the column on the left side is the number of collocations between GOME-2 and the lidar and the second number is the mean number of lidar layers averaged for that layer during interpolation.

sure grid that was used for the GOME-2 retrievals. Below 15 km and above 45 km (the lidar altitude range) the a priori partial columns were used to extend the lidar profile to cover the full GOME-2 retrieval range. The resulting lidar profiles were inserted into Eq. (3.1) as $\mathbf{x}_t$ and convolved with the averaging kernels. The mean differences with the GOME-2 profiles are shown in Fig. 3.20.

Between 100 and 20 hPa the absolute difference is positive, while above the 20 hPa it becomes negative. These deviations are larger than the theoretical error of the difference, and thus the bias is significant, but since it is only a few DU and because it changes from positive to negative, the effect on the total column will be small. Between 100 and 20 hPa the retrieval performs better than the a priori, while above the 20 hPa the a priori is somewhat closer to the lidar measurements than the retrieval.

As shown by Wolfram et al. (2012), the vortex passes over Río Gallegos a couple of times during the 2009 ozone hole season. The observations were grouped by their location being inside or outside the vortex to investigate whether the biases observed in Fig. 3.20 were affected by the vortex. The position of the vortex boundary was determined using the methodology described by Nash et al. (1996), applied on the 430 K potential temperature level from the ERA-Interim data (Dee et al., 2011; Dragani, 2011).

For 8 of the 18 collocations, the lidar at Río Gallegos was inside or close

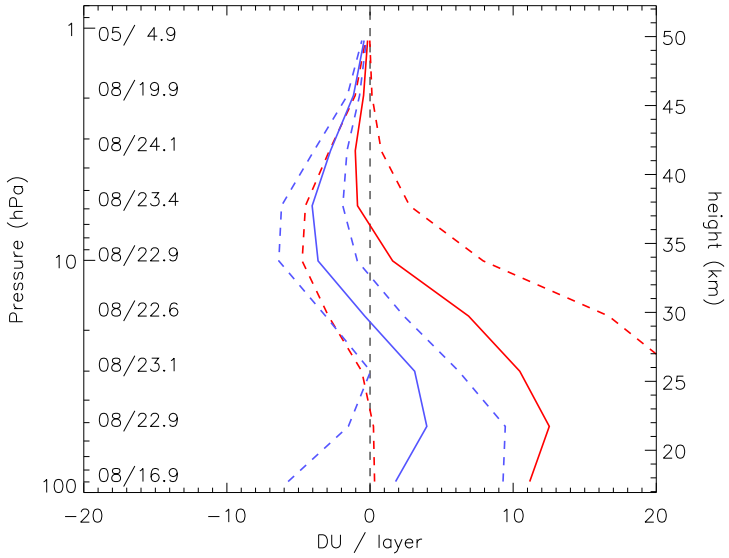

Figure 3.21: The mean of the absolute differences for collocations that occurred inside of, or close to, the vortex. The retrieval is plotted in blue and the a priori in red. The solid line is the mean, and the dashed lines are the ±1 standard deviations. The first number in the column on the left side is the number of collocations between GOME-2 and the lidar, and the second number is the mean number of lidar layers averaged for that layer during interpolation.

to the vortex; during the other it was outside of the vortex. The mean relative differences are plotted in Figures 3.21 and 3.22. There is little difference between these plots and the plot showing the mean of all differences (see Fig. 3.20). This is an indication that GOME-2 performs similarly inside and outside of the vortex.

However, the a priori behaves very differently when the position of the vortex with respect to Río Gallegos is taken into account. When Río Gallegos is inside of the vortex (Fig. 3.21), the a priori is far from the lidar measurements and shows a larger uncertainty compared to measurements made outside the vortex (Fig. 3.22). This difference is caused by the climatology, which at the latitude of Río Gallegos (51° S, 69.3° W) is not representative of the polar air present inside the vortex.

To investigate the temporal evolution of the vortex over Río Gallegos, all GOME-2 daily data were gridded onto a 1° × 1° grid, and a time series of these daily fields over the location of Río Gallegos is shown in Fig. 3.23.

The plot shows three episodes of stratospheric ozone depletion over Río Gallegos, indicated by the arrows at the top of the plot. At the end of September and the start of October, the vortex passes over Río Gallegos twice, but also rapidly disappears. Starting from the second week of November, a prolonged period is visible in which the vortex remains stationary over Río Gallegos. The three ozone-depleted periods are most visible in the two

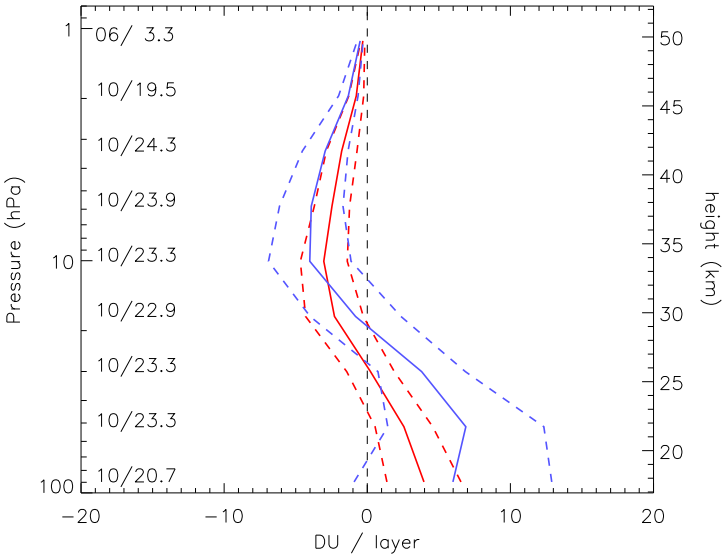

Figure 3.22: The mean of the absolute differences for collocations that occurred outside of the vortex boundary. The retrieval is plotted in blue and the a priori in red. The solid line is the mean, and the dashed lines are the ±1 standard deviations. The first number in the column on the left side is the number of collocations between GOME-2 and the lidar and the second number is the mean number of lidar layers averaged for that layer during interpolation.

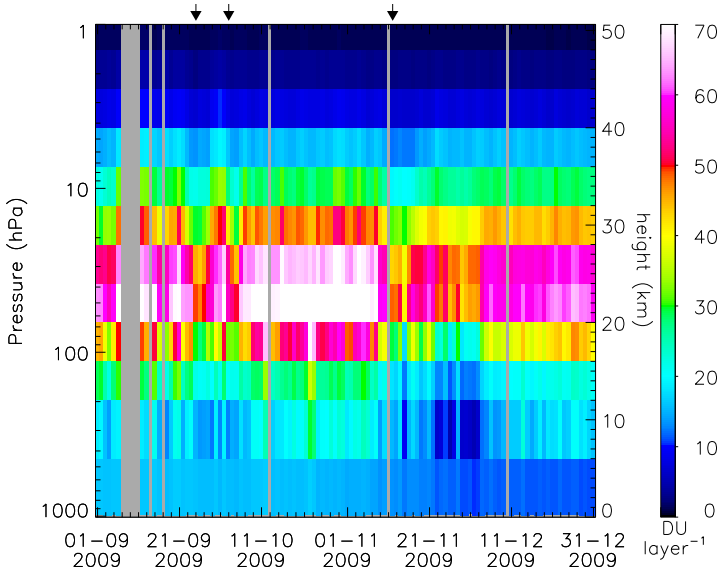

Figure 3.23: A time series of the gridded GOME-2 profiles (DU layer^{-1}) over Río Gallegos. The grey areas are missing GOME-2 data. The start of three episodes of ozone depletion are indicated by the arrows at the top of the plot.

layers with maximum ozone concentration between 20 and 28 km. In the layers directly above and below this region, ozone depletion is also visible, but it does not always coincide with the depletion between 20 and 28 km due to the dynamics of the vortex. At the end of the ozone hole season in December, a slow recovery of the ozone concentration is visible between 20 and 28 km.

In Fig. 3.24 the location of the vortex is plotted for 26 September 2009, when the vortex passed Río Gallegos for the first time. Figure 3.25 shows the location of the vortex for 13 November 2009 at the start of the three-week stationary period.

3.6. Conclusions

The Ozone ProfilE Retrieval Algorithm (OPERA) version 1.26 is described for the first time. OPERA can be applied to measurements from nadir-looking satellite instruments in the UV–VIS spectral region such as GOME and GOME-2. In this paper, profiles are retrieved on a 16-layer pressure grid using the cross sections from Brion et al. (1993, 1998), Daumont et al. (1992), and Malicet et al. (1995), a priori information from the McPeters, Labow and Logan climatology (McPeters et al., 2007), and the LIDORT-A radiative transfer model (van Oss and Spurr, 2002 a).

Ozone profiles from GOME and GOME-2 have been validated against ozone sondes from the World Ozone and Ultraviolet Radiation Data Centre WOUDC (2011). For GOME the ozone sondes from 1997 were used and for GOME-2 the ozone sondes from 2008. Validation results show that the mean deviation between sondes and satellite instruments are within the accuracy levels (20 % in the troposphere, 15 % in the stratosphere) for the troposphere and stratosphere defined in the user requirements of the ozone project of the ESA CCI programme (`http://www.esa-ozone-cci.org/`). The only exception is the layer between 6 and 12 km for GOME-2 between 30 and 90° N, which shows a mean deviation of approximately 30 %. The cause for this deviation is not yet known.

The Antarctic ozone hole season 2009 was investigated in more detail using the lidar measurements from the Río Gallegos observing station (51° S, 69.3° W). In November 2009, the vortex remained stationary over this station for three weeks, posing a challenge to the retrieval because the a priori does not include ozone depletion at this latitude and will be far from the true state of the atmosphere.

Below 20 hPa GOME-2 overestimates the ozone concentration compared to the lidar measurements with a few DU per layer. Between the 20 and 1 hPa the situation is reversed and GOME-2 underestimates the ozone concentration also with a few DU per layer compared to the lidar. Using all GOME-2 profiles over the Río Gallegos station, a time series of GOME-2 ozone profiles was constructed. This time series enables the study of highly variable ozone concentrations caused by the passage of the Antarctic polar vortex. Three notable ozone depletion episodes over Río Gallegos were ob-

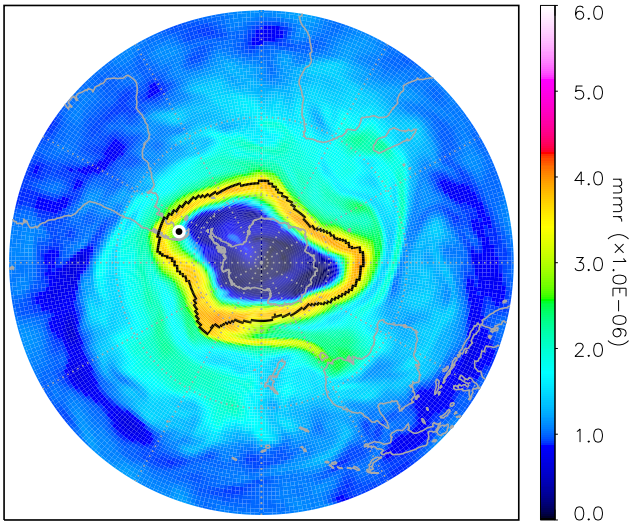

Figure 3.24: The vortex edge overplotted on top of the ERA-Interim ozone mass mixing ratio (mmr) at 430 K for 26 September 2009. The location of Río Gallegos is indicated by the black-in-white circle.

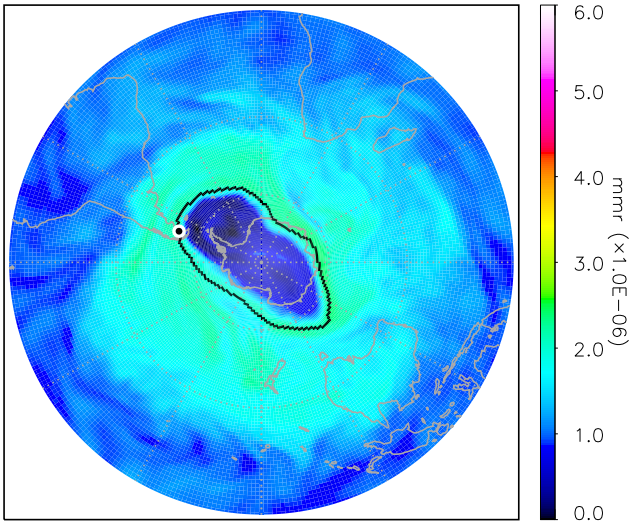

Figure 3.25: The vortex edge overplotted on top of the ERA-Interim ozone mass mixing ratio (mmr) at 430 K for 13 November 2009. The location of Río Gallegos is indicated by the black-in-white circle.

served: two short ones at the end of September and the start of October. The third episode started around the second week of November and lasted for three weeks. A closer inspection of the location of the vortex edge with respect to Río Gallegos showed that the station was inside the vortex for most of this period.

For the first time a single ozone profile retrieval algorithm can be applied to multiple nadir-looking UV–VIS instruments such as GOME and GOME-2. Therefore, OPERA is being used for the development of an algorithm that will be used to create a consistent multi-sensor time series of ozone profiles. Such a time series is important for the study of climate change.

Acknowledgements. The authors would like to thank all data contributors to the World Ozone and Ultraviolet Radiation Data Centre (WOUDC, `http://www.woudc.org/index_e.html`) for submitting their data to a public database and Environment Canada for hosting the database. The authors would also like to thank the referees for their valuable comments.

Edited by: J. Tamminen

References

Anderson, G. P., Kneizys, F. X., Chetwynd, J. H., Wang, J., Hoke, M. L., Rothman, L. S., Kimball, L. M., and McClatchey, R. A.: FASCODE/MODTRAN/LOWTRAN: Past/present/future, paper presented at 18th Annual Review Conference on Atmospheric Transmission Models, Hanscom Air Force Base, Mass., 6-8 June 1995., 1995.

Bass, A. and Paur, R.: The UV cross-sections of ozone: 1. Measurements in atmospheric ozone., in: Atmospheric Ozone: Proceedings of the quadrennial ozone symposium held in Halkidiki, Greece 3–7 September 1984, pp. 606–616, 1985.

Berk, A., Bernstein, L. S., and Robertson, D. C.: MODTRAN: A moderate resolution model for LOWTRAN-7, rep. GL-TR-89-0122, Geophys. Lab., Hanscom Air Force Base, Mass., 1989.

Bhartia, P. K. and Wellemeyer, C.: TOMS-V8 Total O3 Algorithm, in: OMI Algorithm Theoretical Basis Document Volume II, edited by Bhartia, P. K., 2002.

Bhartia, P. K., McPeters, R. D., Mateer, C. L., Flynn, L. E., and Wellemeyer, C.: Algorithm for the estimation of vertical ozone profiles from the backscattered ultraviolet technique, Journal of Geophysical Research, 101, 18 793–18 806, doi:10.1029/96JD01165, 1996.

Boersma, K. F., Eskes, H. J., and Brinksma, E. J.: Error analysis for tropospheric NO_2 retrieval from space, Journal of Geophysical Research (Atmospheres), 109, D04311, doi:10.1029/2003JD003962, 2004.

Bovensmann, H., Burrows, J. P., Buchwitz, M., Frerick, J., Noël, S., Rozanov, V. V., K. V. Chance, and Goede, A. P. H.: SCIAMACHY: Mission Objectives and Measurement Modes, Journal of Atmospheric Sciences, 56, 127–150, doi:10.1175/1520-0469(1999)056<0127:SMOAMM>2.0.CO;2, 1999.

Brion, J., Chakir, A., Daumont, D., Malicet, J., and Parisse, C.: High-resolution laboratory absorption cross section of O_3. Temperature effect, Chemical Physics Letters, 213, 610–612, doi:10.1016/0009-2614(93)89169-I, 1993.

Brion, J., Chakir, A., Charbonnier, J., Daumont, D., Parisse, C., and Malicet, J.: Absorption Spectra Measurements for the Ozone Molecule in the 350–830 nm Region, Journal of Atmospheric Chemistry, 30, 291–299, 1998.

Burrows, J. P., Weber, M., Buchwitz, M., Rozanov, V., Ladstätter-Weißenmayer, A., Richter, A., Debeek, R., Hoogen, R., Bramstedt, K.,

Eichmann, K.-U., Eisinger, M., and Perner, D.: The Global Ozone Monitoring Experiment (GOME): Mission Concept and First Scientific Results., Journal of Atmospheric Sciences, 56, 151–175, doi:10.1175/1520-0469(1999)056<0151:TGOMEG>2.0.CO;2, 1999.

Callies, J., Corpaccioli, E., Eisinger, M., Hahne, A., and Lefebvre, A.: GOME-2 – Metop's Second-Generation Sensor for Operational Ozone Monitoring, ESA bulletin, 102, 28–36, 2000.

Daumont, D., Brion, J., Charbonnier, J., and Malicet, J.: Ozone UV spectroscopy. I - Absorption cross-sections at room temperature, Journal of Atmospheric Chemistry, 15, 145–155, 1992.

de Laat, A. T. J., van der A, R. J., Allaart, M. A. F., van Weele, M., Benitez, G. C., Casiccia, C., Paes Leme, N. M., Quel, E., Salvador, J., and Wolfram, E.: Extreme sunbathing: Three weeks of small total O_3 columns and high UV radiation over the southern tip of South America during the 2009 Antarctic O_3 hole season, Geophysical Research Letters, 37, L14805, doi:10.1029/2010GL043699, 2010.

Dee, D. P., Uppala, S. M., Simmons, A. J., Berrisford, P., Poli, P., Kobayashi, S., Andrae, U., Balmaseda, M. A., Balsamo, G., Bauer, P., Bechtold, P., Beljaars, A. C. M., van de Berg, L., Bidlot, J., Bormann, N., Delsol, C., Dragani, R., Fuentes, M., Geer, A. J., Haimberger, L., Healy, S. B., Hersbach, H., Hólm, E. V., Isaksen, L., Kållberg, P., Köhler, M., Matricardi, M., McNally, A. P., Monge-Sanz, B. M., Morcrette, J.-J., Park, B.-K., Peubey, C., de Rosnay, P., Tavolato, C., Thépaut, J.-N., and Vitart, F.: The ERA-Interim reanalysis: configuration and performance of the data assimilation system, Quarterly Journal of the Royal Meteorological Society, 137, 553–597, doi:10.1002/qj.828, 2011.

Delcloo, A. and Kins, L.: O3MSAF validation report, see http://o3msaf.fmi.fi/, 2009.

Dragani, R.: On the quality of the ERA-Interim ozone reanalyses: comparisons with satellite data, Quarterly Journal of the Royal Meteorological Society, 137, 1312–1326, doi:10.1002/qj.821, 2011.

Eskes, H. J., Velthoven, P. F. J. V., Valks, P. J. M., and Kelder, H. M.: Assimilation of GOME total-ozone satellite observations in a three-dimensional tracer-transport model, Quarterly Journal of the Royal Meteorological Society, 129, 1663–1681, doi:10.1256/qj.02.14, 2003.

Fortuin, J. P. F. and Kelder, H.: An ozone climatology based on ozonesonde and satellite measurements, Journal of Geophysical Research, 103, 31 709–31 734, doi:10.1029/1998JD200008, 1998.

Gebhardt, C., Rozanov, A., Hommel, R., Weber, M., Bovensmann, H., Burrows, J. P., Degenstein, D., Froidevaux, L., and Thompson, A. M.:

Stratospheric ozone trends and variability as seen by SCIAMACHY from 2002 to 2012, Atmospheric Chemistry and Physics, 14, 831–846, doi: 10.5194/acp-14-831-2014, 2014.

Hasekamp, O. P. and Landgraf, J.: Ozone profile retrieval from backscattered ultraviolet radiances: The inverse problem solved by regularization, Journal of Geophysical Research, 106, 8077–8088, doi:10.1029/2000JD900692, 2001.

Hoogen, R., Rozanov, V. V., and Burrows, J. P.: Ozone profiles from GOME satellite data: Algorithm description and first validation, Journal of Geophysical Research, 104, 8263–8280, doi:10.1029/1998JD100093, 1999.

Keppens, A.: Round-Robin evaluation of nadir ozone profile retrievals: Methodology and application to MetOp-A GOME-2, Atmospheric Measurement Techniques, in preparation, 2013.

Koelemeijer, R. B. A., Stammes, P., Hovenier, J. W., and de Haan, J. F.: A fast method for retrieval of cloud parameters using oxygen a band measurements from the Global Ozone Monitoring Experiment, Journal of Geophysical Research, 106, 3475–3490, doi:10.1029/2000JD900657, 2001.

Koelemeijer, R. B. A., de Haan, J. F., and Stammes, P.: A database of spectral surface reflectivity in the range 335-772 nm derived from 5.5 years of GOME observations, Journal of Geophysical Research (Atmospheres), 108, 4070, doi:10.1029/2002JD002429, 2003.

Kroon, M., de Haan, J. F., Veefkind, J. P., Froidevaux, L., Wang, R., Kivi, R., and Hakkarainen, J. J.: Validation of Operational Ozone Profiles from the Ozone Monitoring Instrument, Journal of Geophysical Research (Atmospheres), 116, D18305, doi:10.1029/2010JD015100, 2011.

Kyrölä, E., Laine, M., Sofieva, V., Tamminen, J., Päivärinta, S.-M., Tukiainen, S., Zawodny, J., and Thomason, L.: Combined SAGE II-GOMOS ozone profile data set for 1984–2011 and trend analysis of the vertical distribution of ozone, Atmospheric Chemistry and Physics, 13, 10 645–10 658, doi:10.5194/acp-13-10645-2013, 2013.

Levelt, P. F., van den Oord, G. H. J., Dobber, M. R., Malkki, A., Visser, H., de Vries, J., Stammes, P., Lundell, J. O. V., and Saari, H.: The Ozone Monitoring Instrument, IEEE Transactions on Geoscience and Remote Sensing, 44, 1093–1101, doi:10.1109/TGRS.2006.872333, 2006.

Liu, X., Chance, K., Sioris, C. E., Spurr, R. J. D., Kurosu, T. P., Martin, R. V., and Newchurch, M. J.: Ozone profile and tropospheric ozone retrievals from the Global Ozone Monitoring Experiment: Algorithm description and validation, Journal of Geophysical Research (Atmospheres), 110, 20 307–+, doi:10.1029/2005JD006240, 2005.

Malicet, J., Daumont, D., Charbonnier, J., Parisse, C., Chakir, A., and Brion, J.: Ozone UV spectroscopy. II - Absorption Cross-Sections and Temperature Dependence, Journal of Atmospheric Chemistry, 21, 263–273, doi:10.1007/BF00696758, 1995.

McPeters, R. D., Labow, G. J., and Logan, J. A.: Ozone climatological profiles for satellite retrieval algorithms, Journal of Geophysical Research (Atmospheres), 112, D05 308, doi:10.1029/2005JD006823, 2007.

Meijer, Y. J., Swart, D. P. J., Baier, F., Bhartia, P. K., Bodeker, G. E., Casadio, S., Chance, K., Del Frate, F., Erbertseder, T., Felder, M. D., Flynn, L. E., Godin-Beekmann, S., Hansen, G., Hasekamp, O. P., Kaifel, A., Kelder, H. M., Kerridge, B. J., Lambert, J.-C., Landgraf, J., Latter, B., Liu, X., McDermid, I. S., Pachepsky, Y., Rozanov, V., Siddans, R., Tellmann, S., van der A, R. J., van Oss, R. F., Weber, M., and Zehner, C.: Evaluation of Global Ozone Monitoring Experiment (GOME) ozone profiles from nine different algorithms, Journal of Geophysical Research (Atmospheres), 111, 21 306–+, doi:10.1029/2005JD006778, 2006.

Mijling, B., Tuinder, O. N. E., van Oss, R. F., and van der A, R. J.: Improving ozone profile retrieval from spaceborne UV backscatter spectrometers using convergence behaviour diagnostics, Atmospheric Measurement Techniques, 3, 1555–1568, doi:10.5194/amt-3-1555-2010, 2010.

Miles, G.: Validation of GOME-2 tropospheric ozone profiles derived using optimal estimation, Atmospheric Measurement Techniques, submitted, 2013.

Munro, R., Siddans, R., Reburn, W. J., and Kerridge, B. J.: Direct measurement of tropospheric ozone distributions from space, Nature, 392, 168–171, doi:10.1038/32392, 1998.

Nash, E. R., Newman, P. A., Rosenfield, J. E., and Schoeberl, M. R.: An objective determination of the polar vortex using Ertel's potential vorticity, Journal of Geophysical Research, 101, 9471–9478, doi:10.1029/96JD00066, 1996.

Rodgers, C. D.: Inverse methods for atmospheric sounding, vol. Vol. 2 of *Series on Atmospheric, Oceanic and Planetary Physics*, World Scientific Publishing, Singapore, 2008 edn., 2000.

Singer, S. F. and Wentworth, R. C.: A method for the determination of the vertical ozone distribution from a satellite, Journal of Geophysical Research, 62, 299–308, doi:10.1029/JZ062i002p00299, 1957.

Sparling, L. C., Wei, J. C., and Avallone, L. M.: Estimating the impact of small-scale variability in satellite measurement validation, Journal of Geophysical Research (Atmospheres), 111, D20310, doi:10.1029/2005JD006943, 2006.

Twomey, S.: On the Deduction of the Vertical Distribution of Ozone by Ultraviolet Spectral Measurements from a Satellite, Journal of Geophysical Research, 66, 2153–2162, doi:10.1029/JZ066i007p02153, 1961.

van der A, R. J., van Oss, R. F., Piters, A. J. M., Fortuin, J. P. F., Meijer, Y. J., and Kelder, H. M.: Ozone profile retrieval from recalibrated Global Ozone Monitoring Experiment data, Journal of Geophysical Research (Atmospheres), 107, 4239–+, doi:10.1029/2001JD000696, 2002.

van Oss, R. F. and Spurr, R. J. D.: Fast and accurate 4 and 6 stream linearized discrete ordinate radiative transfer models for ozone profile retrieval, Journal of Quantitative Spectroscopy and Radiative Transfer, 75, 177–220, doi:10.1016/S0022-4073(01)00246-1, 2002 a.

van Peet, J. C. A., van der A, R. J., de Laat, A. T. J., Tuinder, O. N. E., König-Langlo, G., and Wittig, J.: Height resolved ozone hole structure as observed by the Global Ozone Monitoring Experiment-2, Geophysical Research Letters, 36, L11 816, doi:10.1029/2009GL038603, 2009.

van Peet, J. C. A., van der A, R. J., Tuinder, O. N. E., Wolfram, E., Salvador, J., Levelt, P. F., and Kelder, H. M.: Ozone ProfilE Retrieval Algorithm (OPERA) for nadir-looking satellite instruments in the UV–VIS, Atmospheric Measurement Techniques, 7, 859–876, doi:10.5194/amt-7-859-2014, 2014.

Wang, P., Stammes, P., van der A, R., Pinardi, G., and van Roozendael, M.: FRESCO+: an improved O_2 A-band cloud retrieval algorithm for tropospheric trace gas retrievals, Atmospheric Chemistry and Physics, 8, 6565–6576, doi:10.5194/acp-8-6565-2008, 2008.

WMO: Implementation plan for the global observing system for climate in support of the UNFCCC (2010 update), Report nr. GCOS-138, Geneva, Switzerland, 2010.

Wolfram, E. A., Salvador, J., Orte, F., D'Elia, R., Godin-Beekmann, S., Kuttippurath, J., Pazmiño, A., Goutail, F., Casiccia, C., Zamorano, F., Paes Leme, N., and Quel, E. J.: The unusual persistence of an ozone hole over a southern mid-latitude station during the Antarctic spring 2009: a multi-instrument study, Annales Geophysicae, 30, 1435–1449, doi:10.5194/angeo-30-1435-2012, 2012.

WOUDC: World Ozone and Ultraviolet Radiation Data Centre, Environment Canada, data retrieved 28-11-2011 from http://www.woudc.org/, 2011.

4

Simultaneous assimilation of ozone profiles from multiple UV-VIS satellite instruments

A three-dimensional global ozone distribution has been derived from assimilation of ozone profiles that were observed by satellites. By simultaneous assimilation of ozone profiles retrieved from the nadir looking satellite instruments Global Ozone Monitoring Experiment 2 (GOME-2) and Ozone Monitoring Instrument (OMI), which measure the atmosphere at different times of the day, the quality of the derived atmospheric ozone field has been improved. The assimilation is using an extended Kalman filter in which chemical transport model TM5 has been used for the forecast. The combined assimilation of both GOME-2 and OMI improves upon the assimilation results of a single sensor. The new assimilation system has been demonstrated by processing 4 years of data from 2008 to 2011. Validation of the assimilation output by comparison with sondes shows that biases vary between -5 % and +10 % between the surface and 100 hPa. The biases for the combined assimilation vary between -3 % and +3 % in the region between 100 and 10 hPa where GOME-2 and OMI are most sensitive. This is a strong improvement compared to direct retrievals of ozone profiles from satellite observations.

This chapter has been published in Atmospheric Chemistry and Physics as van Peet et al. (2018).

4.1. Introduction

Depending on the altitude, ozone in the Earth's atmosphere has different effects. In the stratosphere, ozone filters the harmful ultraviolet part from the incoming solar radiation, preventing it from reaching the surface. Near to the surface, ozone is a pollutant, which has negative effects on human health and can reduce crop yields. At the same time, ozone is a greenhouse gas with an important role in the temperature of the atmosphere.

Because of the important role ozone has in climate change, it has been designated as an essential climate variable (ECV) by the Global Climate Observing System (GCOS) of the World Meteorological Organization (WMO) (WMO, 2010). In the GCOS report, it is stressed that the full three-dimensional distribution of ozone is required.

The European Space Agency (ESA) has initiated the Climate Change Initiative (CCI) programme, which aims at long-term time series of satellite observations of the ECVs (http://cci.esa.int/). One of the subprogrammes is the Ozone CCI project (http://www.esa-ozone-cci.org/) that focuses on homogenized datasets of total ozone from different sensors (Lerot et al., 2014), stratospheric ozone distribution from limb and occultation observations (e.g. Sofieva et al., 2013) and the vertical ozone distribution from nadir observations (e.g. Miles et al., 2015). Long-term ozone datasets were also produced by the European Centre for Medium-Range Weather Forecasts (ECMWF) reanalyses such as ERA-40 (Uppala et al., 2005) and its successor ERA-Interim (Dee et al., 2011). Although primarily intended for improvement of the weather forecast, the assimilation of ozone is an integral part of theses reanalyses. ERA-40 is described in more detail in Dethof and Hólm (2004) and ERA-Interim in Dragani (2011). Total ozone column measurements from different satellite instruments were assimilated into a chemical transport model for the multi-sensor reanalysis (MSR) of ozone (van der A et al., 2010, 2015), spanning a 42 year period between 1970 and 2012.

Vertical ozone measurements from space-based ultraviolet (UV) instruments started with the Solar Backscatter Ultraviolet (SBUV) instruments from 1970 onwards on different satellites (e.g. Bhartia et al., 2013). Later, satellite instruments with higher resolution and increased spectral coverage were launched, for example Global Ozone Monitoring Experiment (GOME) onboard ERS-2 in 1995 (Burrows et al., 1999), SCanning Imaging Absorption spectroMeter for Atmospheric CHartographY (SCIAMACHY) onboard Envisat in 2002 (Bovensmann et al., 1999), Ozone Monitoring Instrument (OMI) onboard Aura in 2004 (Levelt et al., 2006) and Global Ozone Monitoring Experiment 2 (GOME-2) onboard Metop-A/B in 2006/2012 (Callies et al., 2000; Munro et al., 2016). Each location on Earth is typically observed once or twice a day by these satellites, so it is not possible to get global coverage at a specific time of the day. The retrieved ozone profiles from Ultraviolet-VISible (UV-VIS) nadir observations have a limited vertical resolution due to the smoothing effect in the retrieval (e.g. Rodgers, 1990).

The vertical resolution varies between 7 and 15 km (see Hoogen et al., 1999). To derive gridded 3D ozone distributions at fixed time intervals we use data assimilation, which combines the information present in the model and the observations, giving the optimal estimate of the ozone concentration. Either the retrieved ozone data, or the radiance data from the instrument can be assimilated into the model. Migliorini (2012) showed that both methods are equivalent. However, assimilating retrieved ozone data considerably simplifies the observation operator and reduces the number of measurements to assimilate. Since the measurement, averaging kernel and error covariance matrices are all used in our assimilation algorithm, all information gained from the retrieval is also present in the resulting assimilated model fields.

Two commonly used types of data assimilation are 4DVAR and (ensemble) Kalman filtering. For example, ozone profiles and total columns from different instruments (such as GOME) were assimilated using a 4DVAR assimilation scheme in the production of the ECMWF ERA-Interim reanalysis (see Dragani, 2011). The Belgian Assimilation System for Chemical ObsErvations (BASCOE, `http://bascoe.oma.be/`; Errera et al. (2008)) is a stratospheric 4DVAR data assimilation system for multiple chemical species including ozone and nitrogen dioxide. BASCOE is used in the Monitoring Atmospheric Composition and Climate Service (MACC) and Copernicus Atmosphere Monitoring Service (CAMS) projects for atmospheric services, the stratospheric ozone analyses from the MACC project are evaluated in Lefever et al. (2015). Recently, BASCOE has been coupled to the Integrated Forecast System of the ECMWF (Huijnen et al., 2016). 4DVAR is well suited to assimilate large amounts of observations, and the analysis provides a smooth field at the time of the assimilation. However, there are two disadvantages of 4DVAR with respect to Kalman filter techniques. First, 4DVAR requires the development and maintenance of an adjoint model, which is a complicated process. Second, 4DVAR does not produce a direct estimate of the uncertainty in the ozone field, although such an estimate can be derived using computationally expensive techniques.

The model covariance matrix is an integral and essential part of a Kalman filter, but it is difficult to derive and computationally expensive in the analysis calculation. Therefore, most Kalman filter implementations try to approximate the model covariance matrix. In the ensemble Kalman filter a selection of the ensemble members can be used to approximate the model covariance (see Evensen, 2003; Houtekamer and Zhang, 2016). Miyazaki et al. (2012) used an ensemble Kalman filter to assimilate different trace gas measurements from multiple satellite instruments into a chemical transport model.

In this research, we follow the Kalman filter approach described in Segers et al. (2005), where the model covariance matrix is parameterized into a time-dependent standard deviation field and a time-independent correlation field. The algorithm was updated and used by de Laat et al. (2009) to

subtract the assimilated stratospheric ozone column from the total column in order to obtain the tropospheric ozone column. We have implemented several major updates and improvements in the algorithm compared to the version of de Laat et al. (2009). We check the observational error characterization, redefine the model error growth and derive a new correlation matrix for the ozone field. The new algorithm is the first that simultaneously assimilates nadir ozone profiles from multiple high-spectral-resolution satellite instruments. We demonstrate the new algorithm by assimilating ozone profile observations from GOME-2 and OMI for the period 2008-2011 into the chemical transport model TM5 (e.g. Krol et al., 2005). To minimize the bias between the two instruments, we developed a bias correction based on ozone sondes to be applied to the observations before assimilation. A bias correction based on total column measurements from ground stations was earlier used for the MSR of total ozone (van der A et al., 2015). Since we assimilate ozone profiles we require an altitude dependent bias correction for which ozone soundings are selected.

In section 4.2 we briefly describe the ozone profile observations, and in section 4.3 the chemical transport model that we use for the data assimilation is described. Section 4.4 gives a short overview of the assimilation algorithm, section 4.5 describes the improvements applied to the assimilation algorithm and the results will be shown in section 4.6. In section 4.7 we demonstrate the performance of the assimilation algorithm over the Tibetan Plateau. A discussion of the results is given in section 4.8 and the conclusions are presented in section 4.9.

4.2. Observations

Data from the UV-VIS satellite instruments GOME-2 and OMI are available for the last 10 years.

GOME-2 (Callies et al., 2000; Munro et al., 2016) was launched onboard Metop-A in 2006. The instrument measures the solar light reflected by the Earth's atmosphere between 250 and 790 nm. For the retrievals used in this research, the radiance measurements are binned in the cross-track and along-track directions such that the ground pixels measure approximately 160 km × 160 km. The ozone profiles for GOME-2 are retrieved with the OPERA retrieval algorithm, hich is described in van Peet et al. (2014). We increased the number of layers in this study from 16 to 32 for more accurate radiative transfer model results.

OMI (Levelt et al., 2006) was launched onboard Aura in 2004. The instrument measures the solar light reflected by the Earth's atmosphere between 270 and 500 nm. One important difference between OMI and GOME-2 is that OMI does not use a scanning mirror like GOME-2, but a fixed 2D CCD detector. One dimension of the detector is used to cover the spectral range, the other is used to cover the cross-track direction. The ground pixels for the profiles retrieved from the UV-VIS spectrum measure approximately 13 km × 48 km in nadir. Note that only 1 in 5 scan lines are re-

trieved. The size of the ground pixels is increasing towards the edge of the swath. OMI has two UV channels that are used in ozone profile retrieval: UV1 and UV2. UV1 has 30 cross-track pixels, while UV2 has 60 cross-track pixels. The UV2 pixels are therefore averaged to coincide with the UV1 pixels. A description of the OMI ozone retrieval algorithm and validation results with respect to ground measurements and other satellite instruments can be found in Kroon et al. (2011).

The algorithms used to retrieve the ozone profiles from GOME-2 and OMI are both based on an optimal estimation technique. The state of the atmosphere is given by the state vector $\mathbf{x}$, while the measurement is given by the measurement vector $\mathbf{y}$ and error $\boldsymbol{\epsilon}$. These two vectors are related by the forward model $\mathbf{F}$ according to $\mathbf{y} = \mathbf{F}(\mathbf{x}) + \boldsymbol{\epsilon}$. Following the maximum a posteriori approach (Rodgers, 2000), the solution is given by

$$\hat{\mathbf{x}} = \mathbf{x}_a + \mathbf{A}\,(\mathbf{x}_t - \mathbf{x}_a) + \mathbf{G}\boldsymbol{\epsilon} \tag{4.1}$$

$$\hat{\mathbf{S}} = (\mathbf{I} - \mathbf{A})\,\mathbf{S}_a \tag{4.2}$$

$$\mathbf{A} = \mathbf{G}\mathbf{K} = \mathbf{S}_a\mathbf{K}^T\left(\mathbf{K}\mathbf{S}_a\mathbf{K}^T + \mathbf{S}_\epsilon\right)^{-1}\mathbf{K} \tag{4.3}$$

where $\hat{\mathbf{x}}$ is the retrieved state vector, $\mathbf{x}_a$ is the a priori state of the atmosphere, $\mathbf{A}$ is the averaging kernel, $\mathbf{x}_t$ is the "true" state of the atmosphere, $\mathbf{G}$ is the gain matrix ($\mathbf{S}_a\mathbf{K}^T\left(\mathbf{K}\mathbf{S}_a\mathbf{K}^T + \mathbf{S}_\epsilon\right)^{-1}$), $\mathbf{G}\boldsymbol{\epsilon}$ the retrieval noise, $\hat{\mathbf{S}}$ is the retrieved covariance matrix, $\mathbf{I}$ is the identity matrix, $\mathbf{S}_a$ is the a priori covariance matrix, $\mathbf{K}$ is the weighting function matrix or Jacobian (it gives the sensitivity of the forward model to the state vector) and $\mathbf{S}_\epsilon$ is the measurement covariance matrix.

The averaging kernel can also be written as $\mathbf{A} = \partial\hat{\mathbf{x}}/\partial\mathbf{x}_t$ and gives the sensitivity of the retrieval to the true state of the atmosphere. The trace of $\mathbf{A}$ gives the degrees of freedom for the signal (DFS). For the cloud-free retrievals over the ozone sonde stations used in this study, the mean DFS for GOME-2 is 5.0 and for OMI is 5.1. When the DFS is high, the retrieval has learned more from the measurement than in the case of a low DFS, when most of the information in the retrieval will depend on the a priori state. The total DFS can be regarded as the total number of independent pieces of information in the retrieved profile. The rows of $\mathbf{A}$ indicate how the true profile is smoothed out over the layers in the retrieval and are therefore also called smoothing functions. Ideally, the smoothing functions peak at the corresponding level and the half-width is a measure for the vertical resolution of the retrieval.

Because the sensitivity of the retrieval to the vertical ozone distribution is represented by the averaging kernel, it is important to include the averaging kernel in the assimilation algorithm. Together, the retrieved state vector, the averaging kernel and error covariance matrix represent all information gained from the retrieval (Migliorini, 2012).

4.3. Chemical transport model TM5

The model used in the assimilation is a global chemistry transport model called TM5 (Tracer Model, version 5), see Krol et al. (2005) for an extended description. The (tropospheric) chemistry of TM5 has been evaluated in Huijnen et al. (2010) and included into the integrated forecasting system of the ECMWF (Flemming et al., 2015).

In the current model setup used for the assimilation of the ozone profiles, TM5 runs globally with grid cells of 3° longitude × 2° latitude, on 45 pressure levels. The pressure levels are a subset of the 91-level pressure grid from the ECMWF. The meteorological data used to drive the TM5 tracer transport are taken from the ECMWF operational analysis fields, produced on these 91 pressure levels.

Above 230 hPa, ozone chemistry is parameterized according to the equations described by Cariolle and Teyssèdre (2007), using the parameters of version 2.1. In the troposphere, the ozone concentrations are nudged towards the Fortuin & Kelder climatology (Fortuin and Kelder, 1998), with a relaxation time that increases from 0 days at 230 hPa to 14 days at 500 hPa and lower. No other trace gasses are modelled in this setup, which makes this version of TM5 fast and computationally cheap. Ozone concentrations are prevented from following the model equilibrium state too closely by the frequent confrontation of the model with the observations during the assimilation process.

4.4. Assimilation algorithm

The assimilation algorithm uses a Kalman filter, and is described in Segers et al. (2005). The state vector $\mathbf{x_i}$ (i.e. the ozone distribution at time $t = i$) and the measurement vector $\mathbf{y_i}$ (i.e. the retrieved profiles at time $t = i$) are given by

$$\mathbf{x}_{i+1} = M(\mathbf{x}_i) + \mathbf{w}_i, \quad \mathbf{w}_i \sim N(\mathbf{0}, \mathbf{Q}_i) \tag{4.4}$$

$$\mathbf{y}_i = H(\mathbf{x}_i) + \mathbf{v}_i, \quad \mathbf{v}_i \sim N(\mathbf{0}, \mathbf{R}_i) \tag{4.5}$$

where M is the model that propagates the state vector in time. It has an associated uncertainty $\mathbf{w}$, which is assumed to be normally distributed with zero mean and covariance matrix $\mathbf{Q}$. The observation operator H, which includes the averaging kernel, gives the relation between $\mathbf{x}$ and $\mathbf{y}$. The uncertainty in $\mathbf{y}$ is given by $\mathbf{v}$, which is also assumed to have zero mean and covariance matrix $\mathbf{R}$ (which is identical to $\hat{\mathbf{S}}$ in the retrieval equations). In matrix notation, the propagation of the state vector and its covariance matrix ($\mathbf{P}$) are given by

$$\mathbf{x}_{i+1}^f = M\left(\mathbf{x}_i^a\right) \tag{4.6}$$

$$\mathbf{P}_{i+1}^f = \mathbf{M}\mathbf{P}_i^a\mathbf{M}^T + \mathbf{Q}_i \tag{4.7}$$

where $\mathbf{x}^f$ and $\mathbf{x}^a$ are the forecast and analysis state vectors, respectively, at time $t = i$, i.e. before and after assimilation of the observations. The

observations are assimilated according to:

$$\mathbf{x}_i^a = \mathbf{x}_i^f + \mathbf{K}_i \left(\mathbf{y}_i - H \left(\mathbf{x}_i^f \right) \right) \tag{4.8}$$

$$\mathbf{P}_i^a = \left(\mathbf{I} - \mathbf{K}_i \mathbf{H}_i \right) \mathbf{P}_i^f \tag{4.9}$$

$$\mathbf{K}_i = \mathbf{P}_i^f \mathbf{H}_i^T \left(\mathbf{H}_i \mathbf{P}_i^f \mathbf{H}_i^T + \mathbf{R}_i \right)^{-1} \tag{4.10}$$

where $\mathbf{K}$ is called the Kalman gain matrix, and the matrix $\mathbf{H}$ is the sensitivity of the observation operator with respect to the state.

The observation operator interpolates the model field to the observation location, converts the model units to the retrieval units and takes the smoothing of the satellite instruments into account by incorporating the averaging kernel. The model grid cells are $3 \times 2^\circ$ (longitude × latitude), much larger than the satellite ground pixels and therefore no horizontal interpolation is needed. The model profile, expressed DU/layer, is converted to the pressure levels of the retrieval grid by applying a simple linear interpolation in the ^{10}log(hPa) domain. For example, if the L2 profile layer overlaps with three model layers for 20, 100 and 30 %, the interpolated model partial column is $0.2 \times \mathrm{DU}_1 + 1.0 \times \mathrm{DU}_2 + 0.3 \times \mathrm{DU}_3$ (where DU_i is the partial column for layer i). Finally,the observation operator H is formed by applying the averaging kernel $\mathbf{A}$ to the difference between the state vector $\mathbf{x}$ and the a priori profile $\mathbf{y}_a$ used in the retrieval:

$$H(\mathbf{x}) = \mathbf{A} \left(\mathbf{BCx} - \mathbf{y}_a \right) \tag{4.11}$$

with $\mathbf{C}$ being the unit conversion (from the models kg gridcell^{-1} to the observations DU layer^{-1}), and $\mathbf{B}$ being the vertical interpolation. The sensitivity matrix $\mathbf{H}$ used in equations 4.9 and 4.10 is constructed as $\mathbf{H} = \mathbf{ABC}$.

In general, the number of elements in an ozone profile is much larger than the degrees of freedom (about 5 to 6). We can therefore reduce the number of data points per profile by taking the singular value decomposition of the $\mathbf{A}$, and only retain the vectors with a singular value larger than 0.1 (this is an absolute threshold and not relative to the maximum singular value). The profiles and matrices are transformed accordingly.

The computational cost of the assimilation algorithm can be further reduced by minimizing the size of the model covariance matrix $\mathbf{P}$. The TM5 model runs in the current setup on a horizontal grid of $2^\circ \times 3^\circ$ (latitude × longitude) on 44 layers, which makes the size of the covariance matrix $(475200)^2$ elements. A number of different approaches exist to minimize the size of the model covariance matrix. For example, in Eskes et al. (2003), the number of dimensions is reduced by only assimilating total columns, while the horizontal correlation depended only on the distance between the model grid cells. Here, we follow the approach described by Segers et al. (2005), by parameterizing the model covariance into a time-dependent standard deviation field and a constant correlation field. At each time step, the model's advection operator is applied to the standard deviation field. The

error growth (i.e. the addition of $\mathbf{Q}$ in equation 4.7) is modelled by a simple mathematical function, more details can be found in section 4.5.2. The model covariance matrix can now be calculated according to:

$$\mathbf{P} = \mathfrak{D}(\boldsymbol{\sigma})\,\mathbf{C}\mathfrak{D}(\boldsymbol{\sigma}) \tag{4.12}$$

with $\mathfrak{D}(\boldsymbol{\sigma})$ being a matrix with the values of the standard deviation $\boldsymbol{\sigma}$ on the diagonal and $\mathbf{C}$ the correlation matrix. The correlation matrix is calculated differently than in Segers et al. (2005), more details can be found in section 4.5.3.

Unfortunately, the $\left(\mathbf{H}_i\mathbf{P}_i^f\mathbf{H}_i^T + \mathbf{R}_i\right)$ matrix in the Kalman filter (equation 4.10) is badly conditioned, which makes the inversion sensitive to noise. Therefore, the eigenvalue decomposition of this matrix is calculated and the measurements are projected on the largest eigenvalues, which in total represent 98 % of the original trace of the matrix.

For the numerical stability of the assimilation algorithm, the difference between the observation and the model should not be too large. A filter is implemented that rejects the observation when the absolute difference between the observation and the model forecast is larger than 3 times the square root of the sum of the variance in the observation and the variance in the forecast:

$$\mathrm{abs}\left(\mathbf{y}_i - H\left(\mathbf{x}_i^f\right)\right) \geq 3\sqrt{\sigma_{y_i}^2 + \sigma_{x_i^f}^2} \tag{4.13}$$

with $\sigma_{\mathbf{y}}$ and $\sigma_{\mathbf{x}}^f$ the standard deviation of the observation $\mathbf{y}$ and the forecast $H(\mathbf{x}^f)$ for layer i, respectively. Note that this is done on a layer-by-layer basis, i.e. if in one layer the difference is too large, the whole observed profile is discarded.

Not all available ozone profiles can be assimilated into TM5 because the computational cost would be too high. Averaging retrievals on the model grid (sometimes called superobservations) was not possible because the assimilation algorithm described in this paper requires AKs and averaging AKs is not straightforward. Therefore 1 out of 3 GOME-2 profiles and 1 out of 31 OMI profiles are used. These numbers are chosen such that more or less the same number of observations are assimilated for each instrument, taking into account the decrease in available pixels due to the row anomaly in OMI. For OMI, the outermost pixels on each side of the swath are neglected, because of the large area of these pixels. Of the resulting retrievals, only cloud-free scenes (cloud fraction ≤ 0.2) are assimilated in order to get the maximum amount of information from the troposphere.

4.5. Improvements of the assimilation algorithm

The first version of our assimilation algorithm was described in Segers et al. (2005). They assimilated GOME ozone profiles for the year 2000. This dataset was extended to the period 1996–2001 by de Laat et al. (2009) who

derived tropospheric ozone for this period. The assimilated GOME observations in the previous algorithm version had a pixel size of 960 km × 100 km, much larger than the pixels in the current research. Since 2009, the assimilation algorithm has been further developed and improved for use with GOME-2. The improved resolution of GOME-2 and OMI ozone profiles and improved retrievals offer new possibilities, but also require adaptations in the data assimilation. It is the first time that ozone profiles from two nadir looking instruments, GOME-2 and OMI, are assimilated simultaneously. This has resulted in a significant number of updates and improvements to the assimilation algorithm compared to the version described in Segers et al. and de Laat et al. (2009), which are outlined in the following sections.

4.5.1. Observational error characterization

The covariance matrix of the observations that is used in the assimilation is composed of two components, the error on the spectral observations and the error of the a priori information. Since the spectral errors affect the assimilation results, they are first verified using the following method.

For a given wavelength, two adjacent detector pixels may have a radiance or reflectance difference that depends on the slope of the spectrum. Given enough samples, the standard deviation of the mean difference is a good indication of the noise at that particular wavelength. The relative difference D is calculated as

$$D = \frac{F(\lambda_1) - F(\lambda_2)}{0.5\,(F(\lambda_1) + F(\lambda_2))} \tag{4.14}$$

where F is the radiance and λ_1 the wavelength in detector pixel 1 and λ_2 the wavelength in the adjacent pixel. Because the standard deviation is sensitive to outliers, a Gaussian distribution is fitted to the data. The fitted standard deviation is multiplied with the spectrum and compared to the reported noise in the level-1 data.

For GOME-2, we checked 4 days in 2008: 15 March, 25 June, 26 September and 25 December. On December 10th, 2008 the band 1A/1B boundary was shifted from approximately 307 nm to 283 nm and the integration time in this wavelength range decreased from 1.5 s to 0.1875 s as was already the case for the rest of band 1B. Therefore, the data for the first 3 days are combined, while the data for 25 December is treated separately. The analysis was performed for different subsets, such as latitude, solar zenith angle and viewing angle, but results are shown for latitude only.

Figure 4.1 shows the resulting GOME-2 radiance spectra for all wavelengths. It should be noted that the these results are made using spectral data derived from the GOME Data Processor (GDP) version 5.3. The older version GDP 4 uses a different noise model, which yielded too large errors.

The wavelength grid for OMI varies with the location across the detector, so the error verification has been performed with a dependence on the cross-track position. An example radiance spectrum along with the uncertainties is shown in the left panel of Figure 4.2. There is a jump in the

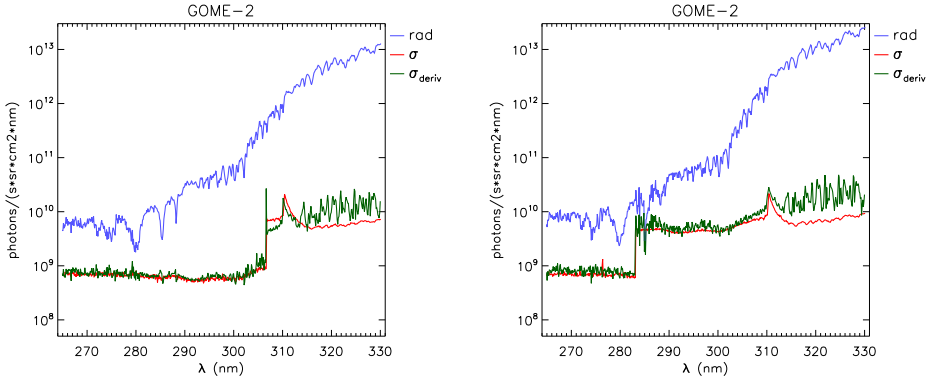

Figure 4.1: GOME-2 METOP-A radiance spectra calculated by OPERA: before (left) and after (right) the wavelength shift from 307 to 283 nm. The blue and red lines are the radiance and uncertainty that are used in OPERA. The green line shows the fitted standard deviations of the relative difference (see equation 4.14) multiplied by the radiance.

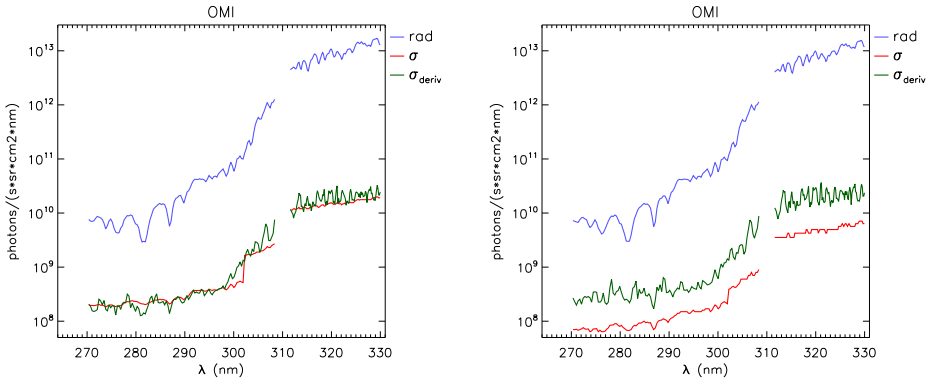

Figure 4.2: OMI radiance spectrum used in the retrieval, the area around 310 nm is not used. The blue and red lines are the radiance and uncertainty, respectively. The green line shows the fitted standard deviations of the relative difference (see equation 4.14) multiplied by the radiance. Left plot before the L0 to L1b processor update: date = 25-02-2006, lon = 145.2°, lat = −20.3°; right plot after the update: date = 5-2-2010, lon = 138.0°, lat = −28.0°.

spectral uncertainty (the red line) around 300 nm, which might be related to a change in the gain settings for the detector. For the selected pixel, the gain changes with a factor of 10 at 300 nm.

On February 1, 2010, a L0 to L1b processor update was implemented for OMI. The new processor version includes more detailed information on the row anomaly and a new noise calculation for the three channels UV1, UV2 and VIS. More information can be found on the following website: `http://projects.knmi.nl/omi/research/calibration/GDPS-History/GDPS_V113.html`. The new noise calculation was investigated by taking the radiance differences determined a few days after the update. The resulting

radiance spectra are given in the right panel of Figure 4.2. The uncertainties in the L1 observations after the L0 to L1b processor update are about a factor of 5 smaller than the uncertainties derived according to the method described above.

In general, the spectral uncertainties for GOME-2 show a good agreement with our fitted uncertainties and therefore we simply use the uncertainties provided with the observations. The spectral uncertainties for OMI show a good agreement with our fitted uncertainties before the processor update, but are too small afterwards. The consequences of these smaller uncertainties will be shown in section 4.6. Since we use the OMI observations as they are, we are not able to correct for the spectral uncertainties in the retrieval.

4.5.2. Model Error Growth

In section 4.4 we explained that using the full covariance propagation from the Kalman filter equations is too computationally intensive. Instead we parameterize the model covariance matrix into a time-dependent standard deviation field and a time-independent correlation field. The advection operator is applied to the standard deviation field, and the model error growth is modelled by applying a simple empirical relation.

In the previous version of the assimilation algorithm, the error growth for the total column was modelled by the function $e(t) = At^{1/3}$ (Eskes et al., 2003), with A being a fit parameter. The error for the total column was distributed over the layers in the profile, proportional to the partial columns in each layer (Segers et al., 2005). Deriving a similar relation on a layer-by-layer basis was not successful, because the error can grow unlimited using this error growth description. Especially during the polar night this might lead to unrealistic high error values.

Therefore, we use the following function

$$e(t) = \frac{at}{b + t} \tag{4.15}$$

where a and b are parameters which can be determined by fitting the observation minus forecast root mean square (RMS) as a function of time (see Eskes et al. (2003), figure 2). The parameter a is the maximum error of the model at a particular altitude. At $t = b$, the error is $0.5a$, therefore b is a measure of how fast the error grows after a measurement has been assimilated. The best results are obtained using $b = 2$ (days) and let the value of a vary over altitude. The values of a are determined by comparing the free model run (i.e. no assimilation) with all sondes for 2008. Because the model currently runs on a 3° × 2° (longitude × latitude) grid and the sonde observations are essentially point sources, these results include a representation error due to the grid-cell size of the model. The derived bias is therefore an overestimation of the real model error, and to prevent the model error from increasing too rapidly all collocations that are more than

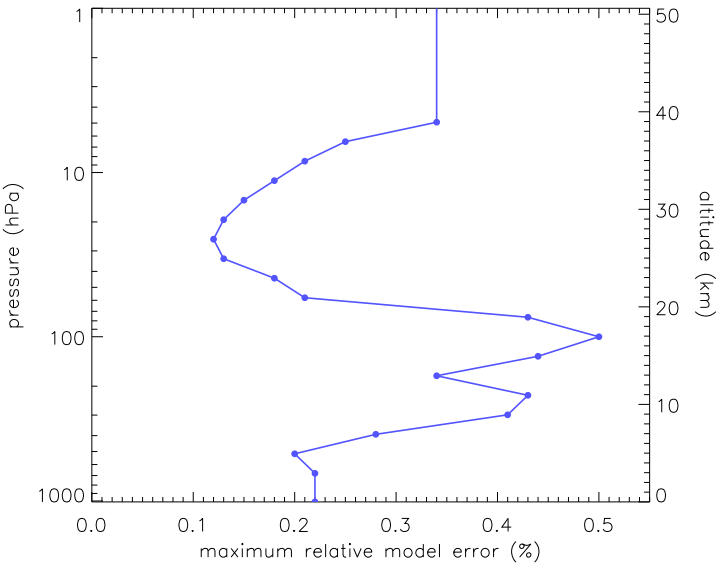

Figure 4.3: Maximum relative model error (a) as a fraction of the partial column at different altitudes.

$3\,\sigma$ from the mean are discarded. The RMS values of the resulting collocations are used as values for a, they are shown as relative values in Figure 4.3 for comparison over different altitudes. For the error of the layers above the maximum altitude of the sondes (about 5 hPa), a has been set to the same value as the last layer below the maximum altitude.

4.5.3. Model correlation matrix

In order to calculate the time-independent correlation field, we follow the National Meteorological Center's method (NMC-method) to determine the correlation in the model (see Parrish and Derber, 1992; Segers et al., 2005). Segers et al. (2005) used a reference run based on 6-hourly meteorological forecasts as the starting point for forecast runs that last 9 days and start at 12 UTC. After a spin-up period, 9 forecast fields per day are available which can be used to determine the correlation in ozone. Differences between the ozone concentration in these runs are due to the different meteorological inputs. Since the overpass frequency of GOME is 3 days, the forecast field from the run started 3 days before the current date was used to derive the correlations in the ozone field. This choice also best matched the correlation length found by Eskes et al. (2003), where total columns were assimilated instead of profiles.

We use a slightly different approach as Segers et al. (2005) because their method neglects uncertainties due to the chemistry parameterization. Also, the forecast lag of 3 days is not compatible with GOME-2 and OMI, which

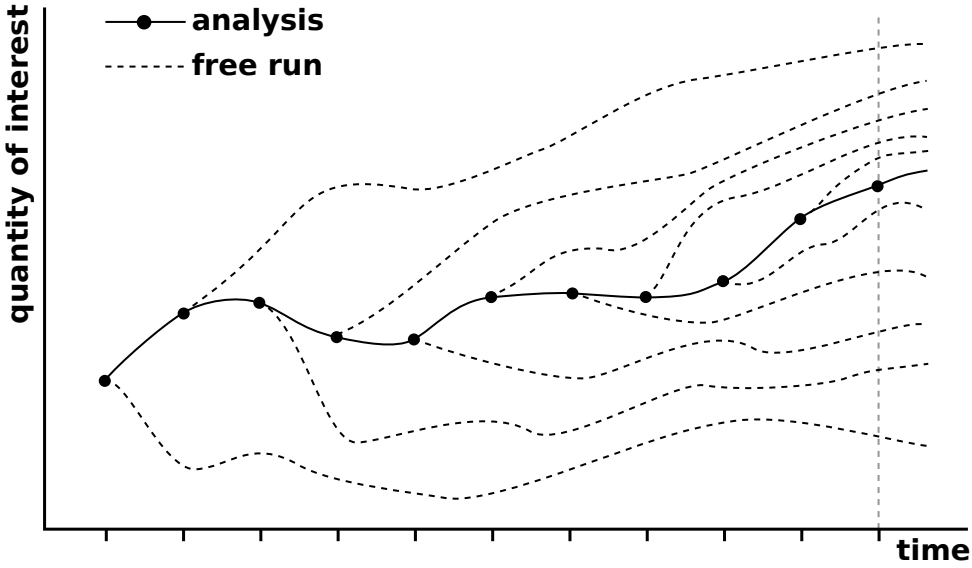

Figure 4.4: Determination of the TM5 correlation field. The solid line is an assimilation model run, the dashed lines are 10-day free model runs. After 10 days, there are 11 ozone fields for each given day which can be used to determine the correlations.

have daily global coverage. Our reference run is the result of the assimilation of profile observations for April 2008, which we consider the true state of the atmosphere. Using the analysis field at 0 UTC, a model run without assimilation (a free model run) is started for a duration of 10 days. After the first 10 days, there are 11 model fields for a given date at 12 UTC: 1 from the assimilation run and 10 from the free model runs (see Figure 4.4).

The difference between the assimilation and free model runs is used to determine the correlations between all pairs of grid cells in the vertical direction (constant location), in the East–West direction (constant latitude and altitude), and in the North–South direction (constant longitude and altitude). The correlations are determined as a function of the distance. Since the East–West distance between two grid cells is larger at the equator than near the poles, the East–West correlation also depends on the latitude. The calculated correlations as a function of distance are fitted with a Gaussian distribution (with correlations less than 0.01 set to zero). Both the calculated and fitted correlations are shown in Figure 4.5. The fitted correlations are used in subsequent model runs as the time-independent correlation field.

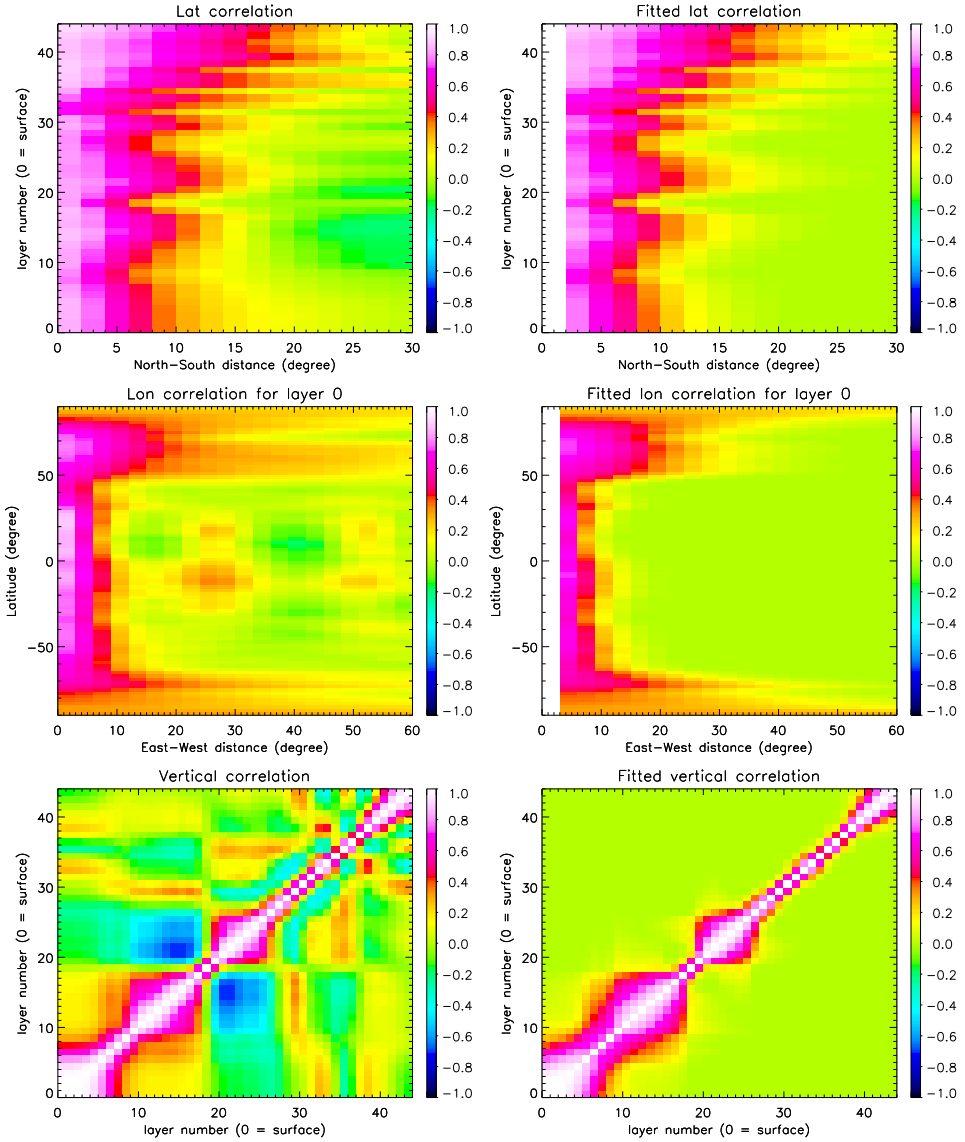

Figure 4.5: Calculated (left) and fitted (right) correlations for the latitudinal (top), surface layer longitudinal (middle) and vertical (bottom) directions.

4.5.4. Ozone profile error characterization and bias correction

The biases between two instruments should be as small as possible for a stable assimilation. Therefore, a bias correction as a function of solar zenith angle (SZA), viewing angle (VA) and time has been developed based on the results of the comparison with sondes. The bias correction factor is one minus the median of the relative deviation based on all collocated data in a given year. All observations in a given year are multiplied by this correction factor.

Figure 4.6 shows the global validation results for the 4 years of the assimilation period (2008–2011) of the GOME-2 and OMI profiles with ozone sondes downloaded from the World Ozone and Ultraviolet Radiation Data Centre (WOUDC, WMO/GAW, 2016). The validation methodology has been described in van Peet et al. (2014), and the main characteristics are the following. Only cloud-free (cloud fraction < 0.2) retrievals have been used, the sonde launch location should be located in the pixel footprint, and the satellite overpass time should be within 3 hours of sonde launch. When multiple retrievals collocate with the same sonde, only the one closest in time has been used. The collocated sonde profiles have been interpolated on the pressure grid of the retrievals and extended to the top of the atmosphere with the a priori profile above the burst level of the sonde. The interpolated and extended profiles are convolved with the averaging kernels in order to take the vertical sensitivity of the satellite instruments into account.

The bias of GOME-2 with respect to sondes varies between −1.1 and +1.7 DU (−7 and +7 %) between 100 and 10 hPa, while for altitudes below 100 hPa the bias is about −0.3 DU (−4 %). The bias of OMI varies between −4.5 and +2 DU (−8 and +15 %) between 100 and 10 hPa, while below 10 hPa the bias is positive with a maximum value of 4 DU (+27 %). The absolute biases cannot be compared directly because the layers of GOME-2 and OMI do not have the same thickness. Note that the remaining biases for the top layers in Figure 4.6 are not exactly zero for the corrected observations, because the figure is drawn for latitude bands, while the bias correction is made using SZA and VA bins and the number of sondes used in the comparison at that altitude is much smaller than at lower altitudes. For the validation of GOME-2, 1083 sondes were used, of which 10 reached the top level. For the validation of OMI, 776 sondes were used of which 33 reached the top level. Table 4.1 lists all stations and the number of sondes used in the validation and bias correction of the observations. The numbers in the station names refer to the WOUDC station identifiers.

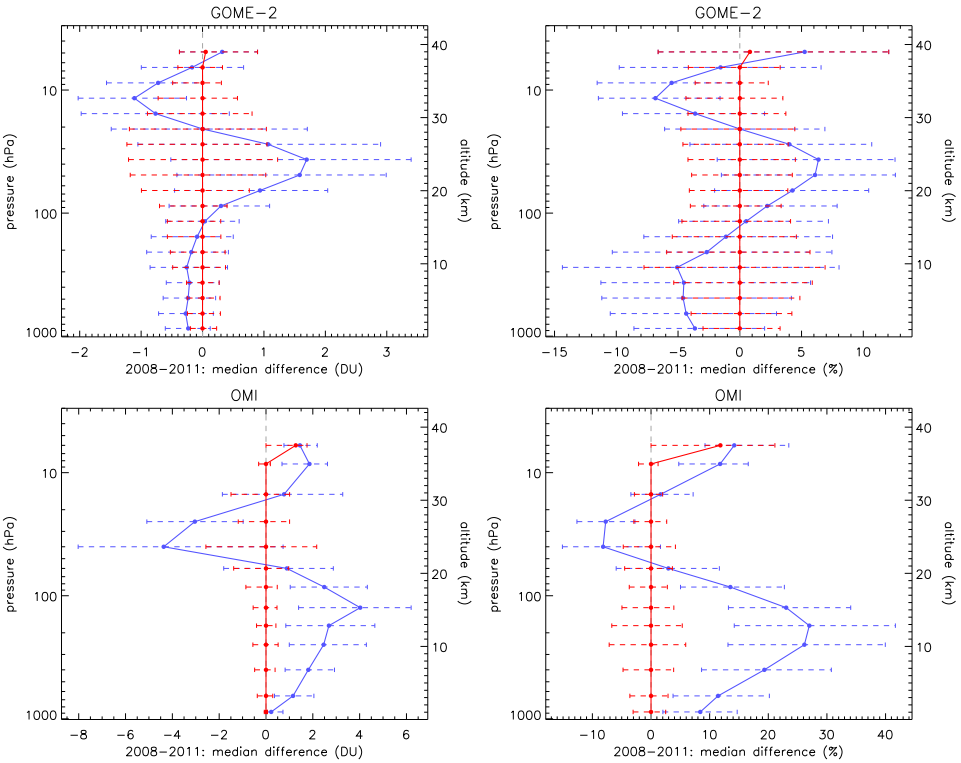

Figure 4.6: Global validation results for 2008–2011 for GOME-2 at the top and OMI at the bottom. The left column shows the median absolute differences, the right column shows the median relative differences. The blue line indicates the original observations, the red line the bias corrected observations that have been used as input for the assimilation. The error bars indicate the range between the 25 % and 75 % percentiles. Note that the x-axis scale is different for each plot.

Table 4.1: Stations used for the validation and bias correction of GOME-2 and OMI.

station	long.	lat.	# GOME-2	# OMI
stn_018_alert	-62.33	82.50	32	0
stn_021_edmonton	-114.11	53.55	0	4
stn_024_resolute	-94.97	74.71	27	1
stn_029_macquarie	158.94	-54.50	14	0
stn_043_lerwick	-1.19	60.14	31	26
stn_053_uccle	4.35	50.80	66	43
stn_055_vigna_di_valle	12.21	42.08	3	1
stn_076_goose_bay	-60.36	53.31	17	0
stn_089_ny_alesund	11.95	78.93	35	9

(continued...)

Table 4.1: (continued...)

station	lon	lat	# GOME-2	# OMI
stn_101_syowa	39.58	-69.01	0	4
stn_107_wallops_island	-75.47	37.93	28	23
stn_109_hilo	-155.04	19.43	34	0
stn_156_payerne	6.57	46.49	153	156
stn_174_lindenberg	14.12	52.21	30	36
stn_175_nairobi	36.80	-1.27	25	10
stn_191_samoa	-170.56	-14.23	42	3
stn_199_barrow	-156.60	71.30	12	14
stn_219_natal	-35.26	-5.49	0	27
stn_221_legionowo	20.97	52.40	39	33
stn_233_marambio	-56.62	-64.24	23	2
stn_242_praha	14.44	50.00	29	48
stn_256_lauder	169.68	-45.04	4	7
stn_308_madrid	-3.58	40.47	59	52
stn_315_eureka	-85.94	79.99	56	1
stn_316_debilt	5.18	52.10	40	29
stn_318_valentia	-10.25	51.93	37	19
stn_323_neumayer	-8.26	-70.65	63	11
stn_328_ascension	-14.42	-7.98	0	10
stn_330_hanoi	105.80	21.01	0	4
stn_336_isfahan	51.70	32.51	0	1
stn_338_bratts_lake	-104.70	50.20	24	37
stn_339_ushuaia	-68.31	-54.85	6	2
stn_344_hong_kong	114.17	22.31	4	28
stn_348_ankara	32.86	39.97	0	9
stn_394_broadmeadows	144.95	-37.69	36	29
stn_434_san_cristobal	-89.62	-0.92	1	0
stn_435_paramaribo	-55.21	5.81	33	0
stn_436_la_reunion	55.48	-21.06	20	11
stn_437_watukosek-java	112.60	-7.50	3	4
stn_438_suva_fiji	178.40	-18.13	6	3
stn_443_sepang_airport	101.70	2.73	6	0
stn_445_trinidad_head	-124.20	40.80	5	5
stn_450_davis	77.97	-68.58	5	12
stn_456_egbert	-79.78	44.23	22	13
stn_457_kelowna	-119.40	49.94	0	24
stn_466_maxaranguape	-35.26	-5.49	0	25
stn_477_heredia	-84.11	10.00	2	0
stn_494_alajuela	-84.21	9.98	11	0
		total	1083	776

4.6. Results and validation

We have assimilated GOME-2 (on Metop-A) and OMI ozone profiles for a period of 4 years between 2008 and 2011 using the Kalman filter algorithm described in the previous sections. In total, four model runs were performed: a 'free' model run without assimilation, a model run with assimilation of GOME-2 ozone profiles only, a model run with assimilation of OMI ozone profiles only and a model run with simultaneous assimilation of GOME-2 and OMI ozone profiles.

4.6.1. Altitude dependent OmF and OmA statistics

An important diagnostic of any assimilation system is the difference between the observations and the model (also known as innovations). In the following, we define the relative observation minus forecast (OmF) for layer i as:

$$\mathrm{OmF}_i = \frac{\left|\mathbf{y}_i - H\left(\mathbf{x}_i^f\right)\right|}{0.5\left(\mathbf{y}_i + H\left(\mathbf{x}_i^f\right)\right)} \tag{4.16}$$

with i the layer index, $\mathbf{y}$ the observed ozone profile, H the observation operator and $\mathbf{x}^f$ the forecast profile of the model (see section 4.4). The layers in the retrievals of GOME-2 and OMI have a different thickness, which makes the comparison of the OmF between the two instruments not straightforward. Therefore, both $\mathbf{y}$ and $H\left(\mathbf{x}^f\right)$ have been regridded to the same pressure levels before calculating the OmF. This new vertical grid is defined by levels at 0, 6 and 12 km followed by levels every 2 km up to 60 km, which are converted to hPa and correspond to surface pressure up to 0.28 hPa. The observation minus analysis (OmA) is defined in a similar way, but with $\mathbf{x}^f$ replaced with the analysis profile $\mathbf{x}^a$. Since the analysis field is a weighted average of the forecast model field and the observations, the OmA should be smaller than the OmF.

In Figure 4.7, the GOME-2 OmF and OmA from the model run with simultaneous assimilation of GOME-2 and OMI for four different layers have been plotted. The ozone sondes that were used in deriving the bias correction and the validation of the results were required to have reached at least 10 hPa. Therefore the selected layers in Figure 4.7 are the surface layer, the layer just below and above 10 hPa, and the top layer of the new pressure grid around 60 km (0.3 hPa). In Figure 4.8, the OmF and OmA for the same layers have been plotted for OMI. In the first year of the assimilation period, the surface layer OmF and OmA for GOME-2 are higher than those for OMI. At the end of 2008, after the wavelength shift between GOME-2 band 1A/1B, the situation is reversed and the OmF and OmA for GOME-2 are lower than those for OMI. The band 1A/1B wavelength shift is clearly present in the bottom layer of the GOME-2 OmF and OmA, which might be unexpected since the radiation from band 1A/1B does not reach the surface. But since the layers in an optimal estimation retrieval are related as described by the AK and covariance matrices, it is possible that the band

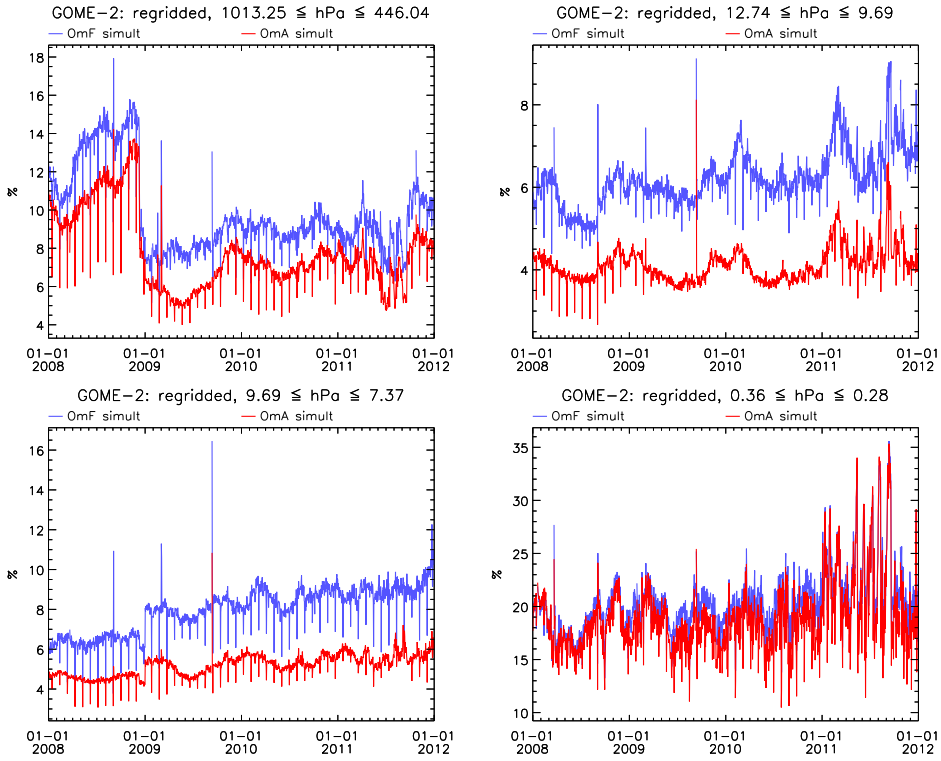

Figure 4.7: GOME-2 OmF (blue) and OmA (red) for the surface layer (top left), around 10 hPa (top right and bottom left) and around 0.3 hPa (bottom right). The OmF and OmA have been calculated for the regridded layers from the model run with simultaneous assimilation of GOME-2 and OMI.

1A/1B change affects the results in an altitude region where the radiation itself does not penetrate. The OMI data show a more pronounced yearly cycle than GOME-2. After the beginning of 2010, the OmF and OmA for both instruments are very similar for the summer months June, July and August, but the winter time values for OMI are higher. For the layer just below 10 hPa, the OmF and OmA for GOME-2 are about 1 percentage point higher than for OMI. For the layer just above 10 hPa, the OmF and OmA for GOME-2 start out lower than for OMI, but at the end of the assimilation period, the values are comparable. For the top layer, the OmF and OmA for GOME-2 are about 5 percentage point higher than for OMI . In general, the OmF is about 2–4 percentage point higher than the OmA, except for the top layer. There, the difference is in the order of 1 percentage point, but the values vary much more than lower in the atmosphere.

Both OmF and OmA for the GOME-2 assimilation run show regular decreases with a period of about 1 month. These decreases are caused by

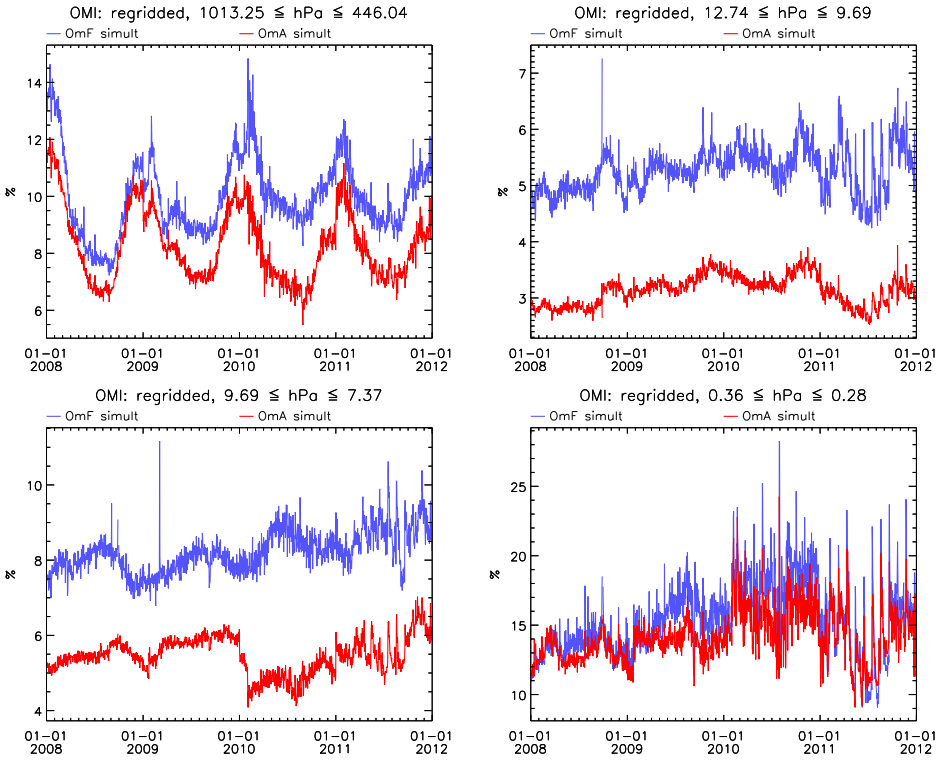

Figure 4.8: OMI OmF (blue) and OmA (red) for the surface layer (top left), around 10 hPa (top right and bottom left) and around 0.3 hPa (bottom right). The OmF and OmA have been calculated for the regridded layers from the model run with simultaneous assimilation of GOME-2 and OMI.

GOME-2 being operated in 'narrow-swath mode', when the swath is 320 km wide instead of 1920 km. For these narrow-swath observations, the model is closer to the retrieved profiles, causing a lower OmF/OmA. OMI also has a spatial zoom-in mode, which is activated about once a month, but these pixels are filtered out because they are too much influenced by the row anomaly and because the mapping between the UV-1 and UV-2 pixels change with respect to the normal mode. Peaks in the OmF and OmA for the GOME-2 assimilation, such as after an instrument test period between 7 and 12 September 2009, can be related to periods of missing data.

Sudden changes in the OmF and OmA are visible for some altitudes for both instruments at the start of some years. One example is in the layer just above the 10 hPa for GOME-2 at the start of 2009 or at the start of 2010 for OMI. The change for GOME-2 appears to coincide with the band 1A/1B shift, but it is really at the start of the year and not on December 10th, 2008. It is therefore unlikely that these two events are related. Since

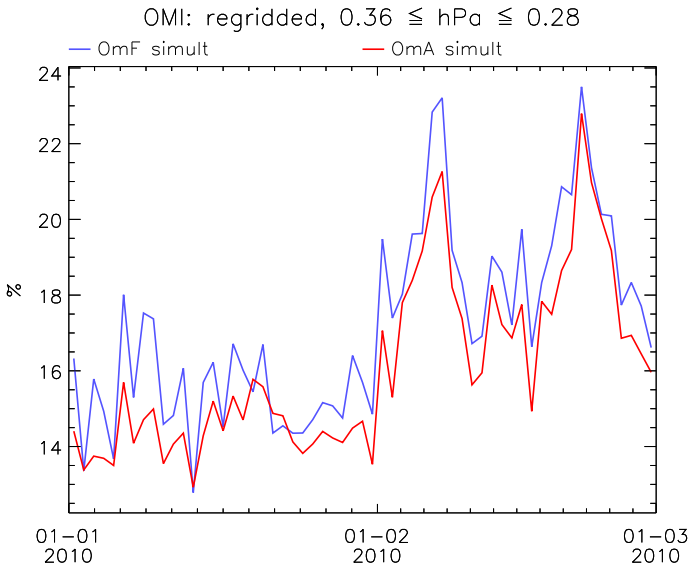

Figure 4.9: OMI OmF (blue) and OmA (red) for the layer around 0.3 hPa, zoomed in to a month before and after the L0 to L1b processor update. The OmF and OmA have been calculated for the regridded layers from the model run with simultaneous assimilation of GOME-2 and OMI.

there are no known instrumental or meteorological changes, the most likely cause is therefore the bias correction scheme for the observations, which changes its correction parameters at the start of each year.

Closer inspection of the OMI OmF and OmA change at the start of 2010 (see the lower left panel of Figure 4.8), shows that it actually consists of two steps: the first one at the start of the year and the second one a month later. That second step is also present in the lower right panel (the layer around 0.3 hPa), where the change is about 5 percentage point, but it is less clear due to the higher variability in the signal. Figure 4.9 shows the same data, but focused on the first two months of 2010. Both OmF and OmA increase by about 5 percentage point from one day to the next. The increase is even larger (and more clearly visible) in the data from the single instrument assimilation run for OMI.

Comparison of Figure 4.7 and Figure 4.8 shows that the OmF and OmA for one instrument might be larger than for the other, depending on the altitude. Which of the two instruments has a larger OmF or OmA value might also change over time. In other words, GOME-2 and OMI have a different sensitivity for different altitudes as represented by the averaging kernels. Assimilating the observations from these instruments simultaneously, increases the overall sensitivity of the assimilation.

Lower uncertainties in the spectra lead to lower uncertainties in the observations, which in its turn changes the balance between model and

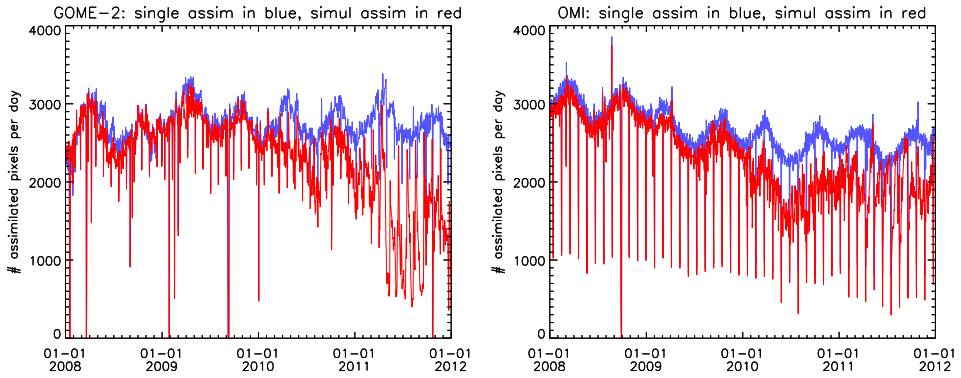

Figure 4.10: Number of assimilated observations from GOME-2 (left) and OMI (right). The blue lines represent the single instrument assimilation, the red lines the simultaneous assimilation.

observations in the Kalman filter and affects the innovations. Because the variance in the observation is lower, more pixels will be rejected by the OmF filter (see section 4.4 and Figure 4.10). Figure 4.10 shows the number of assimilated observations for both GOME-2 and OMI from the single and simultaneous instrument assimilation. In the single instrument assimilation runs, the model error is adapted to the new situation after the processor update and the total number of assimilated observations does not change. For the simultaneous assimilation, the assimilation results may be fluctuating between OMI and GOME-2 observations if a bias exists. This might result in higher assimilation errors. Therefore, the OmF filter (see section 4.4 and equation 4.13) rejects observations from both GOME-2 and OMI, even though only the uncertainties from one of the instruments (i.e. OMI) have changed.

4.6.2. Altitude independent OmF and OmA statistics

In order to show the geographical distribution of the OmF and OmA, the absolute values for each layer were quadratically added and the square root was taken from the result. These column-integrated OmF and OmA values were averaged on a daily basis for latitude bins with a size of 2°. In Figure 4.11, these column-integrated OmF and OmA are shown as function of latitude and time.

The highest values of the OmF and OmA are observed at high latitudes around the polar night. The GOME-2 band 1A/1B wavelength change is clearly visible, even though the plot shows OmF and OmA from the combined assimilation. Step changes in the OmA are visible at the start of each year, which coincides with an update of the bias correction parameters.

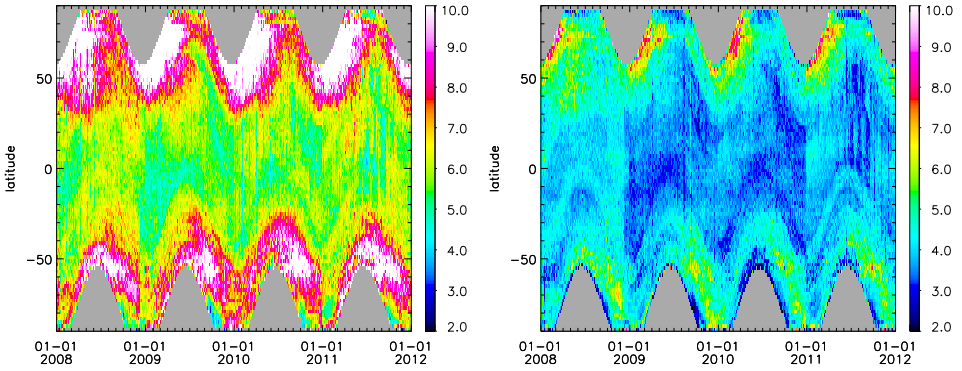

Figure 4.11: Mean OmF (left) and OmA (right) as a function of latitude (bin size 2°) and time (bin size 1 day) for the simultaneous assimilation of GOME-2 and OMI.

4.6.3. Expected and observed OmF

The OmF of the results should be consistent with the uncertainties of the observations and the model forecast. The expected OmF is based on the observation error and the forecast error and is the mean of the square root term in the right-hand side of equation 4.13 for all observations in a given layer. The observed OmF for each layer for the whole assimilation period on the other hand is the mean of the left-hand side of equation 4.13. In Figure 4.12, the observed OmF is plotted as a function of the expected OmF for the model runs with assimilation of GOME-2 only, with assimilation of OMI only, and for both instruments separate with the data taken from the model run with simultaneous assimilation.

Note that the pressure levels are those from the observations, not the regridded levels used in the calculation of the OmF and OmA above. The expected and observed OmF are close to the 1-to-1 line, which shows that the model error $\sigma_{\mathbf{x}f}$ is of the correct magnitude for the current observations. The expected and observed OmF are somewhat closer to the 1-to-1 line in the case of the simultaneous assimilation of GOME-2 and OMI than for the assimilation of each instrument independently. The model error that is used is therefore probably slightly better suited for the assimilation of multiple instruments simultaneously than for the assimilation of a single sensor.

4.6.4. Assimilation validation with sondes

The model output was validated against ozone sondes that were obtained from the World Ozone and Ultraviolet Radiation Data Centre (WOUDC, WMO/GAW, 2016), see Figure 4.13). This is the same ozone dataset as was used to derive the bias correction. Note, however, that many more observations are assimilated than were used deriving the bias correction, while all observations are corrected with the same factor. The assimilation

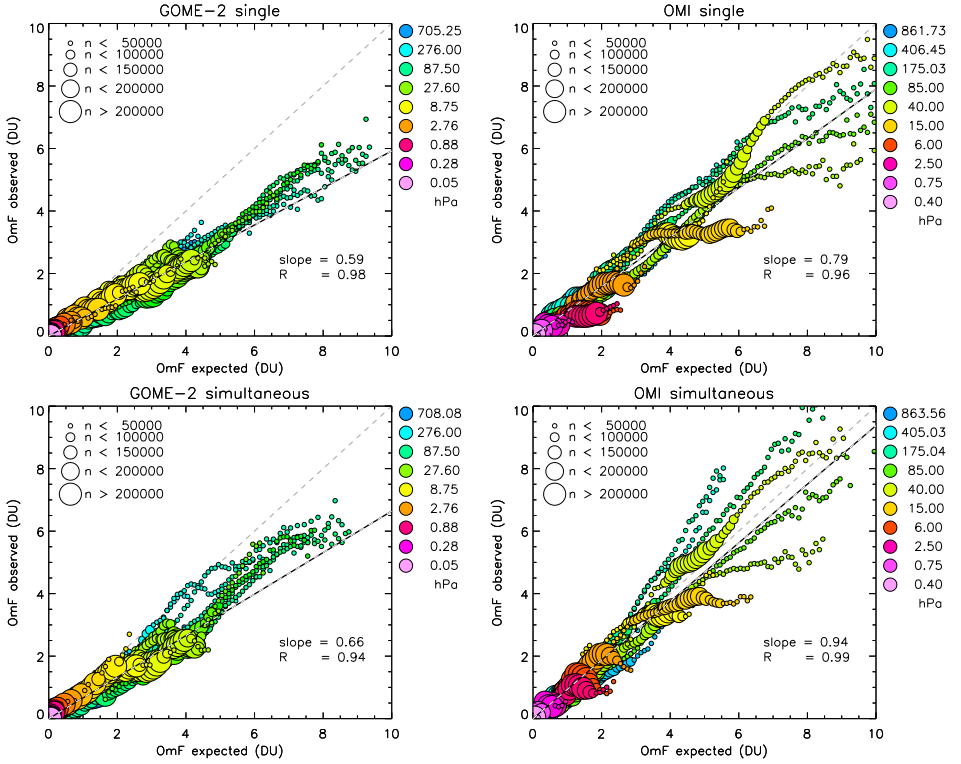

Figure 4.12: Observed vs. expected OmF. Top left: assimilation of GOME-2 only, top right: assimilation of OMI only. Bottom row: results from the simultaneous assimilation of both GOME-2 and OMI. Bottom left: GOME-2, bottom right: OMI. Colours indicate the pressure levels. Note that not all levels are plotted in the legend while all levels are plotted in the figure. The size of the circles gives the number of assimilated pixels (n) in that respective OmF-bin (bin-size = 0.2 DU). The slope for the fitted (dashed) line is given in the lower right corner of each panel, as is the correlation (R) between the expected and observed OmF.

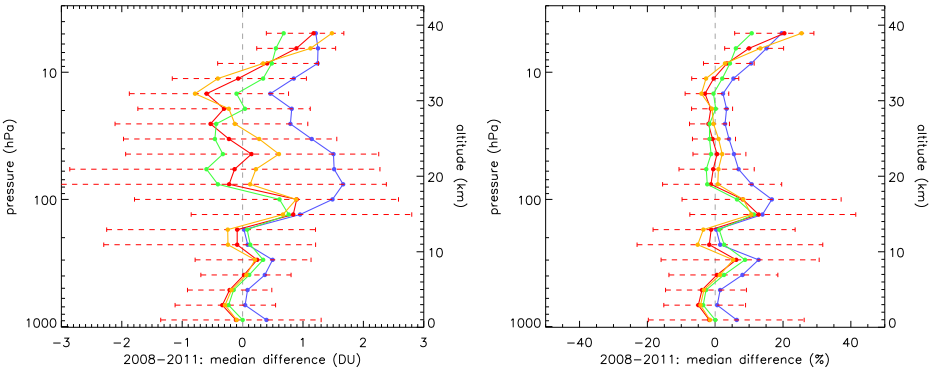

Figure 4.13: Validation of the model runs with ozone sondes for 2008-2011. Left: the median of the absolute difference in DU, right: the median of the relative differences. Blue: model run without assimilation, green: model run with assimilation of GOME-2 only, yellow: run with assimilation of OMI only, red: assimilation of both GOME-2 and OMI. The error bars are plotted for the simultaneous assimilation only, and range from the 25% to the 75% percentile.

model runs are significantly better than the free model run. This is especially true for the part of the atmosphere where GOME-2 and OMI are most sensitive to the ozone concentration, between 100 and 10 hPa. In this area, the model run with assimilation of GOME-2 only shows a negative bias with respect to the ozone sondes, while the assimilation of OMI shows a positive bias. The assimilation of both GOME-2 and OMI shows the smallest bias. The deviation in the differences are very similar for the four runs, which is why only the error bars for the simultaneous assimilation have been plotted in Figure 4.13. The 25–75 percentile differences are in the 20–55 percentage points range between 0 and 20 km and in the 10–20 percentage points range between 20 and 40 km.

In the troposphere, the assimilation also improves, but not as much as in the stratosphere. Note that in the troposphere the chemistry scheme is different than in the stratosphere (see section 4.3). The assimilation shows a deviation in the tropopause, between 200 and 100 hPa, although the L2 data do not show such large biases (see Figure 4.6). The vertical resolution of model and observation is different, therefore the ozone from the observation has to be redistributed over the model layers, a process which is included in the operator H. A small error in the redistribution of ozone in a region with a strong gradient in the concentration (such as the tropopause) will result in large uncertainties in the ozone concentration at this altitude. Above 10 hPa the assimilation shows increasing biases, and the difference with the free model run decreases. Although the L2 data also show an increasing bias above 10 hPa, it should be noted that the number of sondes reaching this altitude is limited with respect to the tropopause region between 200 and 100 hPa. Also, there is a representation error of the sonde with respect to the 3° longitude × 2° latitude model grid. Therefore it is not as straightforward to attribute this increase in bias to either model or observation error.

4.7. Case study

To demonstrate the performance of the assimilation algorithm we analysed the results for a day above the Tibetan Plateau (located between 30° N and 40° N), where a highly dynamical atmosphere exists. This makes it an interesting area to study atmospheric dynamics, and difficult for modelling so it can serve as a test case to see if the dynamics in the model are correctly implemented. On February 25th, 2008 a stratosphere–troposphere exchange event was observed in GOME-2 data (Chen et al., 2013), which can also be observed in the assimilation output. In Figure 4.14, ozone concentrations from the ERA-Interim reanalysis (Dee et al., 2011; Dragani, 2011) are plotted as contours over the ozone concentrations from the model runs with and without simultaneous assimilation of GOME-2 and OMI. There is a significantly better agreement between the two datasets north of 35° N at pressure levels between 70 and 10 hPa. Even though the GOME-2 and OMI instruments have limited sensitivity in the troposphere, the tropospheric ozone

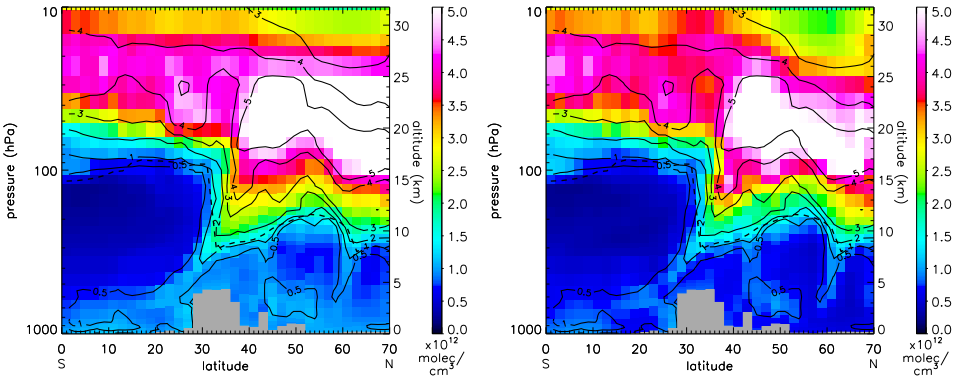

Figure 4.14: Two meridional cross sections over the Tibetan Plateau, located at 84.25° E on 25-02-2008, 6 UTC. The colours indicate the ozone concentration from the free model run (left) and the assimilation of both GOME-2 and OMI (right). The solid contours show the ozone concentrations from the ERA-Interim reanalysis. The dashed line shows the thermal tropopause.

concentrations of the ERA-Interim reanalysis and assimilated tropospheric ozone are in better agreement north of the Tibetan Plateau. There are also two stratosphere–troposphere exchanges (STE) visible, at 30° N and 60° N. These STEs are associated with strong jet-streams (perpendicular to the page) reaching wind speeds of up to 50 m/s at 250 hPa.

4.8. Discussion

When two instruments are assimilated simultaneously, their differences should be taken into account. For example, the algorithms used for the retrieval of GOME-2 and OMI ozone profiles both produce partial columns. However, the number of layers in the retrievals differ and the sensitivity of the retrieval is expressed by the averaging kernel. Both the different vertical resolution and the averaging kernel are incorporated into the observation operator H. Both instruments have different horizontal resolution, something which has not been taken into account in the current version of the assimilation algorithm. The measurement principle of GOME-2 (i.e. a cross-track scanning mirror) is different than that of OMI (i.e. a fixed 2D CCD detector). As a result, the ground pixel size of GOME-2 is constant, while that of OMI varies across the track. Therefore, the representation error of OMI will increase towards the edges of the swath. The effect of the changing OMI footprint size has not been investigated. To get an idea of the sub-grid-cell variation of the ozone concentration, we performed a small experiment where we assimilated the same observations (i.e. GOME-2 and OMI) into TM5 running on a 1° × 1° grid (as opposed to the standard 3° × 2° used in this article). The total column standard deviation of the six 1° × 1° grid cells covered by a single 3° × 2° grid cell is much smaller than

the error on the total column. Therefore, the representation error due to the large grid cells is not significant. A more thorough check on the instruments behaviour throughout time might have revealed the effect of the OMI L0 to L1b processor update sooner. The threshold of the parameter in the OmF filter might be made instrument and time-dependent in order to minimize the effect on the number of assimilated pixels.

Two different instruments can be biased with respect to each other. In order to minimize the bias, a bias correction scheme has been implemented with respect to ozone sondes. We used cloud-free observations (max. cloud fraction 0.20) for the bias correction in order to get a maximum amount of information from the troposphere. As a consequence, we could not use all available sondes in deriving the bias correction. Sudden changes in the bias correction parameters are visible at the start of the year, when the parameters are changed. To minimize these changes, it might be worthwhile to implement an interpolation scheme for the bias correction parameters similar as for the MSR data (see van der A et al., 2010, 2015).

The model can run a full chemistry scheme, but instead a parameterized chemistry scheme has been used in favour of speed. Another possibility to increase the accuracy of the model is to increase the horizontal resolution from the current 3° × 2° (long. × lat.) to 1° × 1° for example. However, in both cases it might be necessary to reduce the vertical resolution of the model to keep the computational cost at an acceptable level.

The model covariance matrix is also an expensive step in the assimilation algorithm. We have reduced the calculation cost by parameterizing it into a time-dependent error field and a time-independent correlation field. The data from April 2008 was used to derive the correlations, which were then used for the whole assimilation period. The assumption that the derived correlations are constant throughout time has not been tested.

4.9. Conclusions

An algorithm for the simultaneous assimilation of GOME-2 and OMI ozone profiles has been described. The algorithm uses a Kalman filter to assimilate the ozone profiles into the TM5 chemical transport model. Compared to previous versions, the algorithm is significantly updated. The observational error has been characterized using a newly developed in-flight calibration method. Since the Kalman filter equations are too expensive to calculate directly for the current setup, the model covariance matrix is divided into a time-dependent error field and a time-independent correlation field. The time evolution is applied to the error field only, while the correlation is assumed to be constant. The model error growth is modelled by a new function that prevents the error from increasing indefinitely, and the correlation field has been newly derived using the NMC method. Large biases between retrievals of the two instruments might destabilize the assimilation. To avoid this, a bias correction using global ozone sonde observations has been applied to the retrieved ozone profiles before assimilation.

Four model runs were performed spanning the years between 2008 and 2011: without assimilation, with assimilation of GOME-2 only, with assimilation of OMI profiles only and with simultaneous assimilation of both GOME-2 and OMI profiles. Depending on the altitude, the OmF and OmA for one instrument might be larger than the other, which might change in the course of time. Assimilating the observations from these instruments simultaneously, increases the overall sensitivity of the assimilation. Two notable instrumental effects are the band 1A/1B wavelength shift for GOME-2, which causes a significant decrease in OmF and OmA. For OMI, after the L0 to L1b processor update on 1 February 2010, the uncertainty in the observations is too small with respect to the method of in-flight validation of the uncertainties presented in this paper. This caused a decrease in the number of assimilated observations for both GOME-2 and OMI. The expected and observed OmF and OmA are more similar for the combined assimilation than for the separate assimilations. Validation with sondes from the WOUDC shows that the combined assimilation performs better than the single sensor assimilation in the region between 100 and 10 hPa where GOME-2 and OMI are most sensitive. The ozone concentrations in the troposphere are also affected by the assimilation, even though the instruments have limited sensitivity in that region. The biases of the assimilated ozone fields are smaller than those of the observations. The assimilated ozone fields are produced at regular time intervals and have no missing data. Despite the limited vertical resolution of GOME-2 and OMI, a case study of an STE over the Tibetan Plateau shows that the assimilation of ozone profiles can improve the ozone distribution in a highly dynamical region.

Data availability. OMI L2 ozone profiles are operationally retrieved and can be obtained from NASA's Goddard Earth Sciences (GES) Data and Information Services Centre (DISC) on-line archive at `https://aura.gesdisc.eosdis.nasa.gov/data/Aura_OMI_Level2/OMO3PR.003/`. GOME-2 L2 ozone profiles are specifically retrieved for this research and can be obtained by contacting the author. Although not used in this research, operationally retrieved GOME-2 ozone profiles can be retrieved from EUMETSATs ACSAF (`https://acsaf.org/index.html`), but note that a registration is required.

Competing interests. The authors declare that they have no conflict of interest.

Acknowledgements. The authors acknowledge all scientists and institutes who contributed their ozone sonde data to the World Ozone and Ultraviolet Radiation Data Centre (WOUDC, WMO/GAW, 2016), and the Meteorological Service of Canada for hosting this important public database. The authors would also like to thank Pepijn Veefkind for his comments in preparation of this paper. EUMETSAT is acknowledged for providing the GOME-2 L1 data and Olaf Tuinder and Robert van Versendaal for their help in the retrieval of the GOME-2 ozone profiles. The Dutch–Finnish OMI instrument is part of the NASA EOS Aura satellite payload. The OMI ozone profiles (OMO3PR, v003) were retrieved at NASA Goddard Earth Sciences Data and Information Services Center (GES DISC) and accessed from the local storage at the Royal Netherlands Meteorological Institute (KNMI). Part of this research has been funded by the Ozone_cci project (`http://www.esa-ozone-cci.org`), which is part of the Climate Change Initiative (CCI) programme of the European Space Agency (ESA).

References

Bhartia, P. K., McPeters, R. D., Flynn, L. E., Taylor, S., Kramarova, N. A., Frith, S., Fisher, B., and DeLand, M.: Solar Backscatter UV (SBUV) total ozone and profile algorithm, Atmospheric Measurement Techniques, 6, 2533–2548, doi:10.5194/amt-6-2533-2013, 2013.

Bovensmann, H., Burrows, J. P., Buchwitz, M., Frerick, J., Noël, S., Rozanov, V. V., K. V. Chance, and Goede, A. P. H.: SCIAMACHY: Mission Objectives and Measurement Modes, Journal of Atmospheric Sciences, 56, 127–150, doi:10.1175/1520-0469(1999)056<0127:SMOAMM>2.0.CO;2, 1999.

Burrows, J. P., Weber, M., Buchwitz, M., Rozanov, V., Ladstätter-Weißenmayer, A., Richter, A., Debeek, R., Hoogen, R., Bramstedt, K., Eichmann, K.-U., Eisinger, M., and Perner, D.: The Global Ozone Monitoring Experiment (GOME): Mission Concept and First Scientific Results., Journal of Atmospheric Sciences, 56, 151–175, doi:10.1175/1520-0469(1999)056<0151:TGOMEG>2.0.CO;2, 1999.

Callies, J., Corpaccioli, E., Eisinger, M., Hahne, A., and Lefebvre, A.: GOME-2 – Metop's Second-Generation Sensor for Operational Ozone Monitoring, ESA bulletin, 102, 28–36, 2000.

Cariolle, D. and Teyssèdre, H.: A revised linear ozone photochemistry parameterization for use in transport and general circulation models: multi-annual simulations, Atmospheric Chemistry and Physics, 7, 2183–2196, doi:10.5194/acp-7-2183-2007, 2007.

Chen, X., Añel, J. A., Su, Z., de la Torre, L., Kelder, H., van Peet, J. C. A., and Ma, Y.: The Deep Atmospheric Boundary Layer and Its Significance to the Stratosphere and Troposphere Exchange over the Tibetan Plateau, PLoS ONE, 8, e56 909, doi:10.1371/journal.pone.0056909, 2013.

de Laat, A. T. J., van der A, R. J., and van Weele, M.: Evaluation of tropospheric ozone columns derived from assimilated GOME ozone profile observations, Atmospheric Chemistry and Physics, 9, 8105–8120, doi:10.5194/acp-9-8105-2009, 2009.

Dee, D. P., Uppala, S. M., Simmons, A. J., Berrisford, P., Poli, P., Kobayashi, S., Andrae, U., Balmaseda, M. A., Balsamo, G., Bauer, P., Bechtold, P., Beljaars, A. C. M., van de Berg, L., Bidlot, J., Bormann, N., Delsol, C., Dragani, R., Fuentes, M., Geer, A. J., Haimberger, L., Healy, S. B., Hersbach, H., Hólm, E. V., Isaksen, L., Kållberg, P., Köhler, M., Matricardi, M., McNally, A. P., Monge-Sanz, B. M., Morcrette, J.-J., Park, B.-K., Peubey, C., de Rosnay, P., Tavolato, C., Thépaut, J.-N., and Vitart, F.: The ERA-Interim reanalysis: configuration and performance of the data assimilation system, Quarterly Journal of the Royal Meteorological Society, 137, 553–597, doi:10.1002/qj.828, 2011.

Dethof, A. and Hólm, E. V.: Ozone assimilation in the ERA-40 reanalysis project, Quarterly Journal of the Royal Meteorological Society, 130, 2851–2872, doi:10.1256/qj.03.196, 2004.

Dragani, R.: On the quality of the ERA-Interim ozone reanalyses: comparisons with satellite data, Quarterly Journal of the Royal Meteorological Society, 137, 1312–1326, doi:10.1002/qj.821, 2011.

Errera, Q., Daerden, F., Chabrillat, S., Lambert, J. C., Lahoz, W. A., Viscardy, S., Bonjean, S., and Fonteyn, D.: 4D-Var assimilation of MIPAS chemical observations: ozone and nitrogen dioxide analyses, Atmospheric Chemistry and Physics, 8, 6169–6187, doi:10.5194/acp-8-6169-2008, 2008.

Eskes, H. J., Velthoven, P. F. J. V., Valks, P. J. M., and Kelder, H. M.: Assimilation of GOME total-ozone satellite observations in a three-dimensional tracer-transport model, Quarterly Journal of the Royal Meteorological Society, 129, 1663–1681, doi:10.1256/qj.02.14, 2003.

Evensen, G.: The Ensemble Kalman Filter: theoretical formulation and practical implementation, Ocean Dynamics, 53, 343–367, doi:10.1007/s10236-003-0036-9, 2003.

Flemming, J., Huijnen, V., Arteta, J., Bechtold, P., Beljaars, A., Blechschmidt, A.-M., Diamantakis, M., Engelen, R. J., Gaudel, A., Inness, A., Jones, L., Josse, B., Katragkou, E., Marecal, V., Peuch, V.-H., Richter, A., Schultz, M. G., Stein, O., and Tsikerdekis, A.: Tropospheric chemistry in the Integrated Forecasting System of ECMWF, Geoscientific Model Development, 8, 975–1003, doi:10.5194/gmd-8-975-2015, 2015.

Fortuin, J. P. F. and Kelder, H.: An ozone climatology based on ozonesonde and satellite measurements, Journal of Geophysical Research, 103, 31 709–31 734, doi:10.1029/1998JD200008, 1998.

Hoogen, R., Rozanov, V. V., and Burrows, J. P.: Ozone profiles from GOME satellite data: Algorithm description and first validation, Journal of Geophysical Research, 104, 8263–8280, doi:10.1029/1998JD100093, 1999.

Houtekamer, P. L. and Zhang, F.: Review of the Ensemble Kalman Filter for Atmospheric Data Assimilation, Monthly Weather Review, 144, 4489–4532, doi:10.1175/MWR-D-15-0440.1, 2016.

Huijnen, V., Williams, J., van Weele, M., van Noije, T., Krol, M., Dentener, F., Segers, A., Houweling, S., Peters, W., de Laat, J., Boersma, F., Bergamaschi, P., van Velthoven, P., Le Sager, P., Eskes, H., Alkemade, F., Scheele, R., Nédélec, P., and Pätz, H.-W.: The global chemistry transport model TM5: description and valuation of the tropospheric chemistry version 3.0, Geoscientific Model Development, 3, 445–473, doi:10.5194/gmd-3-445-2010, 2010.

Huijnen, V., Flemming, J., Chabrillat, S., Errera, Q., Christophe, Y., Blechschmidt, A.-M., Richter, A., and Eskes, H.: C-IFS-CB05-BASCOE: stratospheric chemistry in the Integrated Forecasting System of ECMWF, Geoscientific Model Development, 9, 3071–3091, doi: 10.5194/gmd-9-3071-2016, 2016.

Krol, M., Houweling, S., Bregman, B., van den Broek, M., Segers, A., van Velthoven, P., Peters, W., Dentener, F., and Bergamaschi, P.: The two-way nested global chemistry-transport zoom model TM5: algorithm and applications, Atmospheric Chemistry and Physics, 5, 417–432, doi:10.5194/acp-5-417-2005, 2005.

Kroon, M., de Haan, J. F., Veefkind, J. P., Froidevaux, L., Wang, R., Kivi, R., and Hakkarainen, J. J.: Validation of Operational Ozone Profiles from the Ozone Monitoring Instrument, Journal of Geophysical Research (Atmospheres), 116, D18305, doi:10.1029/2010JD015100, 2011.

Lefever, K., van der A, R., Baier, F., Christophe, Y., Errera, Q., Eskes, H., Flemming, J., Inness, A., Jones, L., Lambert, J.-C., Langerock, B., Schultz, M. G., Stein, O., Wagner, A., and Chabrillat, S.: Copernicus stratospheric ozone service, 2009–2012: validation, system intercomparison and roles of input data sets, Atmospheric Chemistry and Physics, 15, 2269–2293, doi:10.5194/acp-15-2269-2015, 2015.

Lerot, C., Van Roozendael, M., Spurr, R., Loyola, D., Coldewey-Egbers, M., Kochenova, S., van Gent, J., Koukouli, M., Balis, D., Lambert, J.-C., Granville, J., and Zehner, C.: Homogenized total ozone data records from the European sensors GOME/ERS-2, SCIAMACHY/Envisat, and GOME-2/MetOp-A, Journal of Geophysical Research (Atmospheres), 119, 1639–1662, doi:10.1002/2013JD020831, 2014.

Levelt, P. F., van den Oord, G. H. J., Dobber, M. R., Malkki, A., Visser, H., de Vries, J., Stammes, P., Lundell, J. O. V., and Saari, H.: The Ozone Monitoring Instrument, IEEE Transactions on Geoscience and Remote Sensing, 44, 1093–1101, doi:10.1109/TGRS.2006.872333, 2006.

Migliorini, S.: On the Equivalence between Radiance and Retrieval Assimilation, Monthly Weather Review, 140, 258–265, doi:10.1175/MWR-D-10-05047.1, 2012.

Miles, G. M., Siddans, R., Kerridge, B. J., Latter, B. G., and Richards, N. A. D.: Tropospheric ozone and ozone profiles retrieved from GOME-2 and their validation, Atmospheric Measurement Techniques, 8, 385–398, doi:10.5194/amt-8-385-2015, 2015.

Miyazaki, K., Eskes, H. J., Sudo, K., Takigawa, M., van Weele, M., and Boersma, K. F.: Simultaneous assimilation of satellite NO_2, O_3, CO, and HNO_3 data for the analysis of tropospheric chemical composition and

emissions, Atmospheric Chemistry and Physics, 12, 9545–9579, doi:10.5194/acp-12-9545-2012, 2012.

Munro, R., Lang, R., Klaes, D., Poli, G., Retscher, C., Lindstrot, R., Huckle, R., Lacan, A., Grzegorski, M., Holdak, A., Kokhanovsky, A., Livschitz, J., and Eisinger, M.: The GOME-2 instrument on the Metop series of satellites: instrument design, calibration, and level 1 data processing - an overview, Atmospheric Measurement Techniques, 9, 1279–1301, doi:10.5194/amt-9-1279-2016, 2016.

Parrish, D. F. and Derber, J. C.: The National Meteorological Center's Spectral Statistical-Interpolation Analysis System, Monthly Weather Review, 120, 1747–1763, doi:10.1175/1520-0493(1992)120<1747:TNMCSS>2.0.CO;2, 1992.

Rodgers, C. D.: Characterization and error analysis of profiles retrieved from remote sounding measurements, Journal of Geophysical Research (Atmospheres), 95, 5587–5595, doi:10.1029/JD095iD05p05587, 1990.

Rodgers, C. D.: Inverse methods for atmospheric sounding, vol. Vol. 2 of *Series on Atmospheric, Oceanic and Planetary Physics*, World Scientific Publishing, Singapore, 2008 edn., 2000.

Segers, A. J., Eskes, H. J., van der A, R. J., van Oss, R. F., and van Velthoven, P. F. J.: Assimilation of GOME ozone profiles and a global chemistry-transport model using a Kalman filter with anisotropic covariance, Quarterly Journal of the Royal Meteorological Society, 131, 477–502, doi:10.1256/qj.04.92, 2005.

Sofieva, V. F., Rahpoe, N., Tamminen, J., Kyrölä, E., Kalakoski, N., Weber, M., Rozanov, A., von Savigny, C., Laeng, A., von Clarmann, T., Stiller, G., Lossow, S., Degenstein, D., Bourassa, A., Adams, C., Roth, C., Lloyd, N., Bernath, P., Hargreaves, R. J., Urban, J., Murtagh, D., Hauchecorne, A., Dalaudier, F., van Roozendael, M., Kalb, N., and Zehner, C.: Harmonized dataset of ozone profiles from satellite limb and occultation measurements, Earth System Science Data, 5, 349–363, doi:10.5194/essd-5-349-2013, 2013.

Uppala, S. M., Kållberg, P. W., Simmons, A. J., Andrae, U., Bechtold, V. D., Fiorino, M., Gibson, J. K., Haseler, J., Hernandez, A., Kelly, G. A., Li, X., Onogi, K., Saarinen, S., Sokka, N., Allan, R. P., Andersson, E., Arpe, K., Balmaseda, M. A., Beljaars, A. C. M., Van De Berg, L., Bidlot, J., Bormann, N., Caires, S., Chevallier, F., Dethof, A., Dragosavac, M., Fisher, M., Fuentes, M., Hagemann, S., Hólm, E., Hoskins, B. J., Isaksen, L., Janssen, P. A. E. M., Jenne, R., Mcnally, A. P., Mahfouf, J.-F., Morcrette, J.-J., Rayner, N. A., Saunders, R. W., Simon, P., Sterl, A., Trenberth, K. E., Untch, A., Vasiljevic, D., Viterbo, P., and Woollen, J.: The ERA-40 re-analysis, Quarterly Journal of the Royal Meteorological Society, 131, 2961–3012, doi:10.1256/qj.04.176, 2005.

van der A, R. J., Allaart, M. A. F., and Eskes, H. J.: Multi sensor reanalysis of total ozone, Atmospheric Chemistry and Physics, 10, 11 277–11 294, doi:10.5194/acp-10-11277-2010, 2010.

van der A, R. J., Allaart, M. A. F., and Eskes, H. J.: Extended and refined multi sensor reanalysis of total ozone for the period 1970-2012, Atmospheric Measurement Techniques, 8, 3021–3035, doi:10.5194/amt-8-3021-2015, 2015.

van Peet, J. C. A., van der A, R. J., Tuinder, O. N. E., Wolfram, E., Salvador, J., Levelt, P. F., and Kelder, H. M.: Ozone ProfilE Retrieval Algorithm (OPERA) for nadir-looking satellite instruments in the UV–VIS, Atmospheric Measurement Techniques, 7, 859–876, doi:10.5194/amt-7-859-2014, 2014.

van Peet, J. C. A., van der A, R. J., Kelder, H. M., and Levelt, P. F.: Simultaneous assimilation of ozone profiles from multiple UV-VIS satellite instruments, Atmospheric Chemistry and Physics, 18, 1685–1704, doi:10.5194/acp-18-1685-2018, 2018.

WMO: Implementation plan for the global observing system for climate in support of the UNFCCC (2010 update), Report nr. GCOS-138, Geneva, Switzerland, 2010.

WOUDC, WMO/GAW: WMO/GAW Ozone Monitoring Community, World Meteorological Organization- Global Atmosphere Watch Program (WMO-GAW)/World Ozone and Ultraviolet Radiation Data Centre (WOUDC) [Data]. Retrieved April 15, 2016, from http://woudc.org. A list of all contributors is available on the website., doi:10.14287/10000001, 2016.

5

Deriving tropospheric ozone from assimilated profiles

To derive global tropospheric O_3 columns from satellite observations, O_3 profiles retrieved from GOME-2A and OMI measurements were simultaneously assimilated into the TM5 global chemistry transport model for the year 2008. The horizontal model resolution has been increased by a factor of 6 for more accurate results, but to reduce computational cost, the number of model layers has been reduced from 44 to 31. The model ozone fields are used to derive tropospheric ozone, which is defined here as the partial column between mean sea level and 6 km altitude. Two methods for calculating the tropospheric columns from the free model run and assimilated O_3 fields are compared. In the first method, we calculate the residual between assimilated total columns and the partial model column between 6 km and the top of atmosphere. In the second method, we perform a direct integration of the assimilated O_3 fields between the surface and 6 km. The results are validated against tropospheric columns derived from ozone sonde measurements. It turned out that the residual method has a too large variation to be used reliably for the determination of tropospheric ozone, so the direct integration method has been used instead. The median global bias is smaller for the assimilated O_3 fields than for the free model run, but the large variation makes it difficult to make definitive statements on a regional or local scale. The monthly mean ozone fields show significant improvements and more detail when comparing the assimilated O_3 fields with the free model run, especially for features such as biomass burning enhanced O_3 concentrations and outflow of O_3 rich air from Asia over the Pacific.

This chapter is under review in Atmospheric Chemistry and Physics Discussions as van Peet and van der A (2019).

5.1. Introduction

Tropospheric ozone has direct and detrimental effects on human health (Beck et al., 1998; WHO, 2013). It mostly affects the respiratory tract and the lungs, causing e.g. shortness of breath, coughing and a reduced lung function. Respiratory illnesses such as asthma and bronchitis are aggravated by exposure to ozone. Long-term exposure to ozone might increase the mortality rate due to respiratory illnesses. Ozone also negatively affects ecosystems and crop yield because it reduces photosynthesis and plant growth (EPA, 2013). Because plants react differently to exposure to ozone, the balance between species in an ecosystem may shift as well. Monks et al. (2015) give an extensive review on tropospheric ozone and its precursors in relation to air quality and climate.

Apart from the direct and indirect effects on living organisms, ozone is also a greenhouse gas. It strongly absorbs solar radiation below 300 nm, which is why the temperature of the stratosphere is increasing with altitude. Therefore, understanding the ozone distribution is important for understanding the thermal structure of the atmosphere.

Ozone occurs naturally in the troposphere, but concentrations have increased due to human activity. Locally, ozone is produced primarily by reaction cycles involving carbon monoxide, methane and other hydrocarbons. The most important source sectors of these pollutants are transport and industry. Photodissociation of tropospheric ozone is the main source of OH, which has a major role in removing pollutants from the atmosphere. Ozone can also be transported from the stratosphere down to the troposphere in stratosphere-troposphere exchange events.

Because of the impact of (tropospheric) ozone on air quality and climate change, it has been designated as one of the Essential Climate Variables (ECV) by the Global Climate Observing System (GCOS) of the World Meteorological Organisation (WMO) (WMO, 2016). An ECV is defined as a "physical, chemical or biological variable or a group of linked variables that critically contributes to the characterization of Earth's climate". With respect to atmospheric composition ECVs, it is stressed that information on the vertical distribution is essential for understanding, monitoring and modelling climate. In the GCOS implementation plan (WMO, 2016), the target requirements for tropospheric ozone are a 4 h time resolution, a 20–50 km horizontal resolution and a 5 km vertical resolution. The required measurement uncertainty is 10–15 % and the measurement stability should be 2 % per decade.

The tropopause is the top of the troposphere, and a widely used definition is based only on the lapse rate (WMO, 1957): the tropopause is the lowest level at which the lapse rate decreases to 2° C km^{-1} or less, provided that the average lapse rate between this level and all higher levels within 2 km does not exceed 2° C km^{-1}. Because it only depends on the lapse rate, this definition is often referred to as the lapse rate tropopause (LRT) or the ther-

mal tropopause. Other tropopause definitions have been proposed, based on the dynamical properties of the atmosphere or the gradient in the ozone concentration. In general, the tropopause altitude is lowest at the poles (7–8 km) and highest around the equator (18 km).

The tropospheric ozone column is defined as the total ozone amount per unit area between the surface and the tropopause. However, near the tropopause, stratosphere-troposphere exchange of air may occur, which can lead to an under- or over-estimation of the lower tropospheric ozone column. Since the tropospheric ozone in the lower layers has the highest impact on living organisms, we will focus on the partial ozone column between the surface and 6 km above mean sea level. Because the top level is at a fixed altitude, it will be referred to as the fixed altitude top level (FAT) hereafter. The corresponding 0–6 km ozone partial column will be referred to as the FAT column.

Tropospheric ozone can be determined by a number of satellite based methods. In nadir-limb matching techniques, the integrated profile from a limb instrument is subtracted from the total column for the same air mass. Limb profiles and total columns can be obtained from the same instrument (e.g. SCIAMACHY; van der A, 2001; Ebojie et al., 2014), but also from different instruments on the same satellite (e.g. OMI total column and MLS limb profile; Ziemke et al., 2006). In Schoeberl et al. (2007), the horizontal resolution of the MLS limb profiles was increased by trajectory calculations before subtracting them from the OMI total columns. Tropospheric ozone columns were also derived from assimilated OMI total columns and MLS limb profiles by Stajner et al. (2008). Using only nadir observations, Fishman and Balok (1999); Fishman et al. (2003) combined Total Ozone Mapping Spectrometer (TOMS) total columns and Solar Backscattered Ultraviolet (SBUV) stratospheric profiles and determined tropospheric ozone with the empirically corrected tropospheric ozone residual method. Assimilated GOME profiles were subtracted from GOME/TOMS total columns by de Laat et al. (2009).

The methods mentioned above all use the UV-VIS range of the spectrum. There are also a number of ozone emission lines in the thermal infrared (i.e. the wavelength range where the atmosphere emits radiation, instead of reflecting solar light), most notably near 9.6 μm. This emission line can also be used by satellite instruments (e.g. IASI) to measure ozone.

In the tropics, the cloud top height is very stable at an altitude of approximately 200 hPa. Therefore, cloudy scenes can be used to obtain the above-cloud ozone column while the cloud-free scenes can be used to obtain total ozone columns. The difference between these two values is the ozone column below the cloud top. This convective-cloud-differential method (Ziemke et al., 1998) has recently been applied to European satellite measurements to study the trends in a 20 year time series and as a preparation for the TROPOMI mission (Heue et al., 2016).

Outside the tropics, the cloud top height varies too much to reliably ob-

tain ozone columns using the convective-cloud-differential method. Since UV-VIS instruments are not very sensitive to the height of tropospheric ozone, direct integration of UV-VIS ozone profiles does not provide a viable alternative either. The height information can be restored by using data assimilation, where information from ozone profiles, averaging kernels and the chemical transport model are combined. The sensitivity and information content of UV-VIS retrievals is higher in the stratosphere, therefore an alternative approach is to subtract stratospheric columns, derived from assimilated ozone profiles, from accurate total columns (for example from DOAS retrievals). The remainder is taken as the residual tropospheric column (de Laat et al., 2009).

In this paper, assimilated ozone profiles from the GOME-2 and OMI UV-VIS instruments will be used to derive tropospheric columns in two ways. One method is to integrate the assimilated ozone column up to the FAT, hereafter called the FAT column. The other method is to take the difference between the integrated assimilated profile from the FAT to the top of the atmosphere and the assimilated total ozone columns from the Multi Sensor Reanalysis (MSR; van der A et al., 2010, 2015), hereafter called the residual-FAT column.

5.2. Methodology

We use the ozone profiles from the UV-VIS instruments GOME-2 (Callies et al., 2000; Munro et al., 2016) and OMI (Levelt et al., 2006) that are described in van Peet et al. (2018). The ozone profiles from both instruments are retrieved with the optimal estimation technique. For GOME-2 the algorithm is described in van Peet et al. (2014), while the OMI algorithm is described in Kroon et al. (2011). The ozone profiles are assimilated into the global chemistry transport model TM5 (Tracer Model, version 5; e.g. Krol et al., 2005). Two major changes with respect to the settings used in van Peet et al. (2018) are an increased model resolution and a change from operational to ERA-Interim (Dee et al., 2011) meteorological fields that drive TM5. The ERA5 reanalysis data was not yet available for use in the TM5-version used in the assimilation.

To get more accurate assimilated ozone fields, the horizontal resolution of TM5 is increased from $3° \times 2°$ to $1° \times 1°$ (longitude × latitude). At the same time, the vertical resolution is decreased from 44 to 31 layers to reduce the computational cost. The original 44 layers are a subset from the vertical grid used by the European Centre for Medium-Range Weather Forecasts (ECWMF) operational data stream, while the new 31 layers are a subset from the vertical grid used for the ERA-Interim reanalysis. Below about 73 hPa (19 km), the layers are between 0.8 and 1.5 km thick, until about 54 km every other level is selected and the layer thickness increases from 3 to 5.5 km, and the top four levels are all selected. It is not expected that the reduction in vertical resolution affects the accuracy of the outcome, since the thickness of the model layers is still less than the estimated vertical

sensitivity of the retrievals, which is about 7–10 km in the stratosphere (Hoogen et al., 1999; Liu et al., 2010).

Like Segers et al. (2005), we assume that the correlation in the ozone distribution is constant in time, and that changes over time occur in the ozone standard deviation only. Therefore, the model covariance matrix is parameterised into a time independent correlation field and a time dependent uncertainty field. Due to the changes in resolution and meteorological fields, the correlation field had to be derived again according the same method as described in van Peet et al. (2018). No other changes have been made to the assimilation algorithm.

Since the horizontal resolution of the chemical transport model has been increased, the computational cost of the assimilation algorithm did also increase. In order to limit the total processing time only ozone profiles for the year 2008 were assimilated. TM5 was used for a free model run without assimilation of observations, and an assimilation model run with the simultaneous assimilation of both GOME-2 and OMI ozone profiles. For each model run, the FAT column was calculated by direct integration of the 0_3 fields, and the residual-FAT column was calculated using the Multi Sensor Reanalysis (MSR, van der A et al., 2010, 2015) total columns. The MSR is a long term (1970–2017) dataset of assimilated total columns from all available satellite measurements. The results are validated against ozone sondes downloaded from the public World Ozone and Ultraviolet Radiation Data Center (WOUDC, WMO/GAW, 2016) database. Since the model produces 0_3 fields with a 6 h interval at 0, 6, 12 and 18 hours UTC, the maximum difference between sonde launch and model field time is set to three hours. The sonde profile is compared to the model profile from the gridcell containing the sonde launch site, no interpolation of the model field to the sonde launch location is performed. In order for the ozone sondes to be used in the validation, it should have reached a minimum altitude of 10 hPa, and the integrated ozone profile should be between 100 and 550 DU.

5.3. Results

Figure 5.1 shows the monthly mean FAT columns for the year 2008. In general the free model, which is driven by the Cariolle chemistry parametrisations above 230 hPa, shows higher ozone values than the model with assimilated ozone. This is a known artifact of this parametrisation (Cariolle and Teyssèdre, 2007) without any further constraints to the model. Note that since the FAT has a fixed altitude with respect to sea level, elevated regions such as Antarctica or the Tibetan Plateau show a small tropospheric column. The Northern hemisphere has a higher FAT column than the Southern hemisphere, and a yearly cycle can be clearly seen in the plots. The high ozone concentrations in the Northern Hemisphere have various sources such as stratosphere-troposphere exchanges and anthropogenic emissions (Ziemke et al., 2011). An increase in ozone concentration is seen in the Southern Atlantic ocean for September, and between Africa

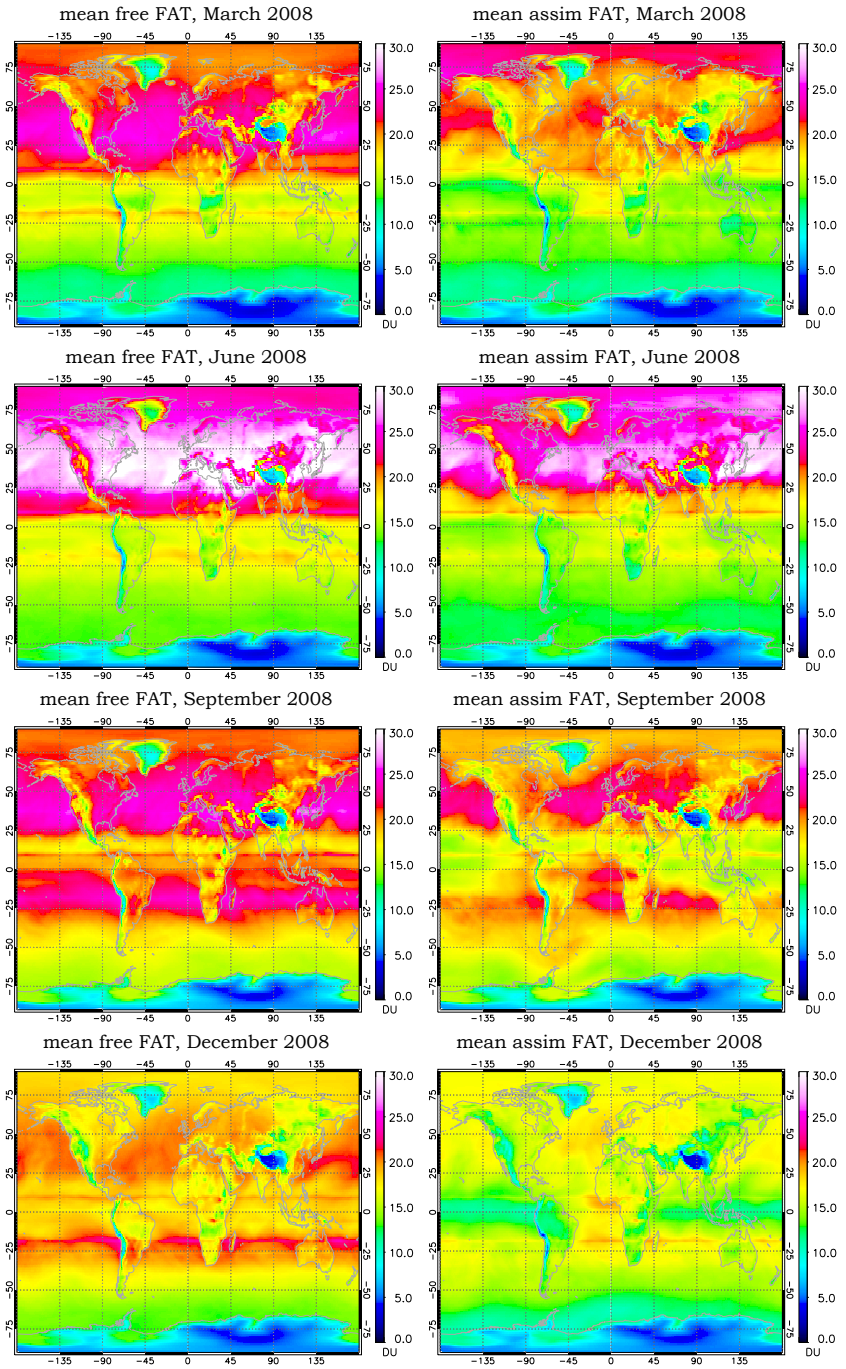

Figure 5.1: Monthly mean tropospheric O_3 fields. Left column: free model run, right column: assimilated O_3 fields. From top to bottom: March, June, September and December 2008.

and Australia in a zonal band around −25° latitude. This increase can be attributed to biomass burning, and coincides with the month of maximum NO2 concentration (an ozone precursor) in Africa (van der A et al., 2008). From March to September, transport of ozone rich air can be seen from Asia across the Pacific. Similar features in the yearly cycle of ozone are also observed in the tropospheric ozone climatology by Ziemke et al. (2011). This climatology is based on the residual of OMI total columns and MLS stratospheric columns (using the thermal tropopause definition), on a horizontal resolution of 5° × 5°. Two sharply defined narrow zonal features of elevated ozone concentrations can be seen at 10° and −20° latitude. These zonal features are also present in the free model run (left column in Figure 5.1), so they are not caused by the observations. Since the monthly mean (surface) pressure fields do not show a similar feature, it is unlikely that it is caused by the meteorological data that is used to drive the model. The most likely cause for these narrow zonal elevated ozone concentrations is therefore a model artefact. It should be noted that the difference is only a few DU, so these zonal features are not easily observed in total column maps.

In order to estimate the impact of the upgraded TM5 model resolution and meteorological data used to drive TM5, we validate the resulting tropospheric ozone columns with ozone sondes (from the surface up to approximately 30 km). Figure 5.2 shows absolute and relative biases for both the free model run and assimilated 0_3 fields. There is a significant improvement of the assimilated 0_3 fields over the free model run when compared to ozone sondes, with the exception of the UTLS (around 15 km). The sharp ozone gradients in this altitude range are not captured fully by the model and the satellite observations. These results are comparable to the TM5 model run used in van Peet et al. (2018, see their figure 13), where the same satellite data was assimilated into TM5, running on a coarser model resolution and with operational meteo data. In van Peet et al. (2018), the median bias for the tropospheric column is between -5 to 0 % for the period 2008–2011, while in the current research it is between -2 and 3 % for 2008 only.

In Figure 5.3, scatterplots of the FAT columns are shown for the free model run and the assimilated 0_3 fields and of the residual-FAT column for the assimilated 0_3 fields only. The data are grouped according to ozone sonde station. The free model run and assimilated 0_3 fields perform comparably and both have a higher correlation coefficient than the residual method (see Table 5.1). The residual method shows some negative columns, indicating that the stratospheric part of the assimilated profiles is larger than the total column from the MSR. Residual-FAT columns based on the free model run show even more negative values, so they are not shown in the figure. The residual method has a lower correlation coefficient and a higher uncertainty than the FAT columns of the free model run and assimilated 0_3 fields, and therefore will be omitted from the subsequent analysis.

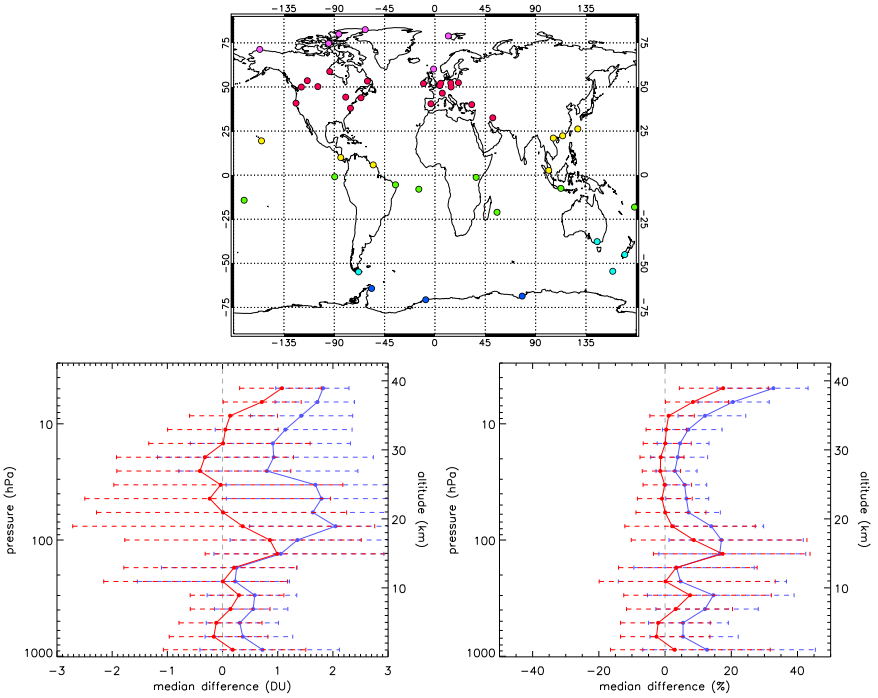

Figure 5.2: TM5 validation results with respect to sondes. The top plot shows the locations of all sondes used in the validation of the model. The color coding of the sondes is the same as in Figure 5.3. Bottom left: median absolute difference, bottom right: median relative difference. The blue line is the model run without assimilation, the red line is the model run with assimilation of GOME-2 and OMI.

We can see from Figure 5.2 that the bias with respect to sondes in the troposphere is smaller for the assimilated O_3 fields than for the free model run. Figure 5.3 and Table 5.1 show that the root mean square (rms) and correlation for the assimilated O_3 fields slightly improve compared to the free model run. To further investigate the variation between TM5 model results and sonde measurements, the rms and mean differences between the model and sonde FAT columns are plotted in Figure 5.4. The figure gives the RMS for all collocations (with a minimum of 10) per station as a function of latitude on the top left, and the mean difference on the top right. The green dots in the maps indicate stations where the absolute value of the rms (or mean) from the assimilated O_3 fields is smaller than for the free model run ($|\text{rms}_{\text{assim}}| < |\text{rms}_{\text{free}}|$ or $|\text{mean}_{\text{assim}}| < |\text{mean}_{\text{free}}|$). The red dots indicate stations where the reverse is true ($|\text{rms}_{\text{assim}}| > |\text{rms}_{\text{free}}|$ or $|\text{mean}_{\text{assim}}| > |\text{mean}_{\text{free}}|$). In the southern hemisphere (lat < -30), the assimilated O_3 fields show a smaller rms and a smaller absolute value of the mean for 4 and 5 out of 7 stations, respectively. In the tropics ($-30 \leq$ lat $<$ 30), the assimilated O_3 fields show a smaller rms and a smaller absolute

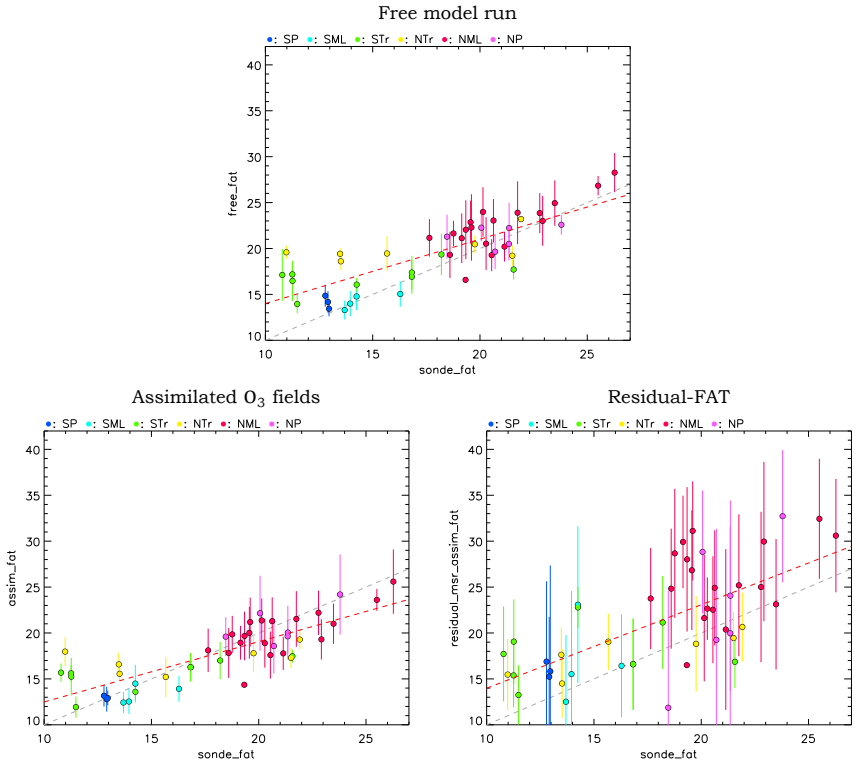

Figure 5.3: Scatterplots of tropospheric columns based on model output versus sonde measurements. The plot symbols are the median values of collocations grouped by station. The error bars indicate the 25–75 percentiles of the distribution. Top: free model run, bottom left: assimilated O_3 fields, bottom right: residual-FAT column for the assimilated O_3 fields. Colors indicate 30° latitude bands: SP = South Pole, SML = Southern MidLatitudes, STr = Southern TRopics, NTr = Northern TRopics, NML = Northern MidLatitudes, NP = North Pole. The grey dashed line is the 1:1-line and the red dashed line gives the best linear fit to the data, the fit parameters are listed in Table 5.1.

Table 5.1: Fit results of the scatterplots in Figure 5.3. The columns marked a and b are the linear fit parameters of the line $a + bx$, r is the linear Pearson correlation coefficient, rms is the root mean square between the values on both axes. The number of stations included in each plot is 48.

FAT column	a	b	r	rms
free	6.99	0.70	0.80	2.90
assim	5.92	0.66	0.82	2.38
residual assim	4.88	0.91	0.67	5.27

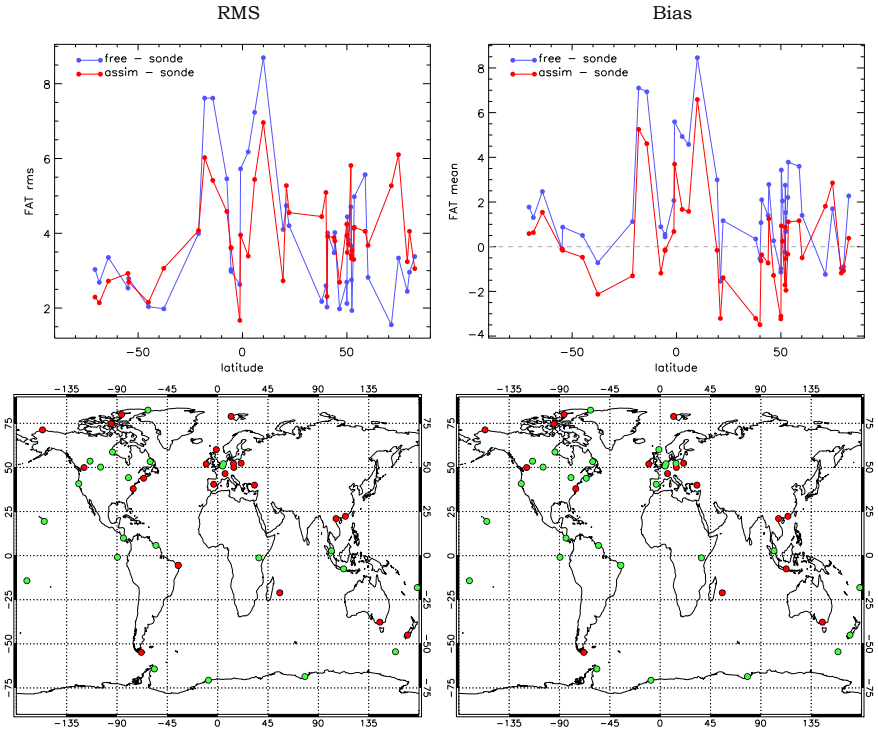

Figure 5.4: The FAT rms (top left) and mean (top right) per station as a function of latitude. The blue line gives the results for the free model run compared to sondes. The red line gives the results for the assimilated O_3 fields compared to sondes. Bottom left: green dots indicate stations where $|\text{rms}_{\text{assim}}| < |\text{rms}_{\text{free}}|$, red dots where $|\text{rms}_{\text{assim}}| > |\text{rms}_{\text{free}}|$. Bottom right: green dots indicate stations where $|\text{mean}_{\text{assim}}| < |\text{mean}_{\text{free}}|$, red dots where $|\text{mean}_{\text{assim}}| > |\text{mean}_{\text{free}}|$. Only results for stations with at least 10 collocations have been plotted.

value of the mean for 9 and 10 out of 14 stations, respectively. The assimilated O_3 fields perform better than the free model run for the majority of the tropical stations, but note that the rms and the absolute value of the mean are larger than at higher latitudes. In the northern hemisphere (lat $\geq$ 30), the assimilated O_3 fields show a smaller rms and a smaller absolute value of the mean for 9 and 13 out of 24 stations, respectively.

To study temporal variation, time series of monthly median global FAT-columns are shown in Figure 5.5. The free model run is closer to the sondes than the assimilated O_3 fields for January till May. The assimilated O_3 fields are closer to the sonde measurements than the free model run from June till December. For the lapse rate tropopause (not shown here), the assimilated O_3 fields are closer to the sonde data than the free model run throughout the year. Since in the troposphere the model is nudged towards an ozone climatology (Fortuin and Kelder, 1998), the climatological value for each collocation has been calculated and the monthly median is also

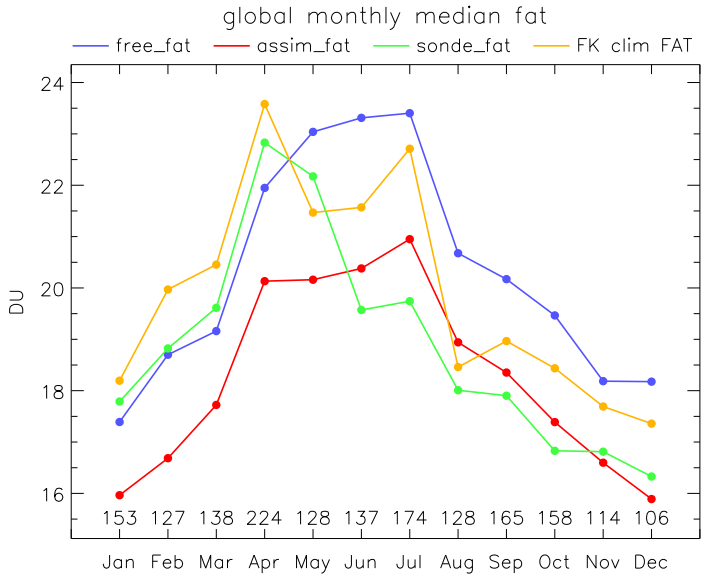

Figure 5.5: Time series of monthly median global FAT-columns. Blue line: free model run, red line: assimilated O_3 fields, green line: sonde data, yellow line: Fortuin and Kelder climatology. The numbers along the x-axis indicate the number of collocations between model and sondes.

shown in Figure 5.5. The free model run follows a similar pattern as the climatological values. It should be noted that the free model run and assimilated O_3 fields start with the same ozone concentrations. Due to the assimilation of observations they diverge quickly, and the monthly median values for January are not the same. The differences are very small, in the order of 2–3 DU, and close to the uncertainty.

As an example of the FAT-column variability throughout the year, Figure 5.6 shows time series for the free model run and assimilated O_3 fields, and for the sonde measurements over three different stations: the Antarctic station Neumayer (8.26° W, 70.56° S), the tropical station Hilo (155.04° W, 19.43° N) and the northern hemisphere station Lerwick (1.19° W, 60.14° N). For the Neumayer station, the free model run and assimilated O_3 fields give comparable results during the polar night. The decrease in the tropospheric column that is visible from October onwards is caused by solar radiation and NO_x induced O_3 destruction, not by the halogen induced destruction of the ozone hole (see e.g. Helmig et al., 2007). For the Hilo station, the assimilated O_3 fields shows systematically lower FAT columns than the free model run. The FAT columns from the assimilated O_3 fields are in better agreement with the sonde FAT columns than the free model run. For the Lerwick station, the free model run and assimilated O_3 fields show similar FAT columns, and the rms bias of the assimilated O_3 fields is larger than for the free model run. However, the absolute value of the mean bias is larger for the free model run than for the assimilated O_3 fields.

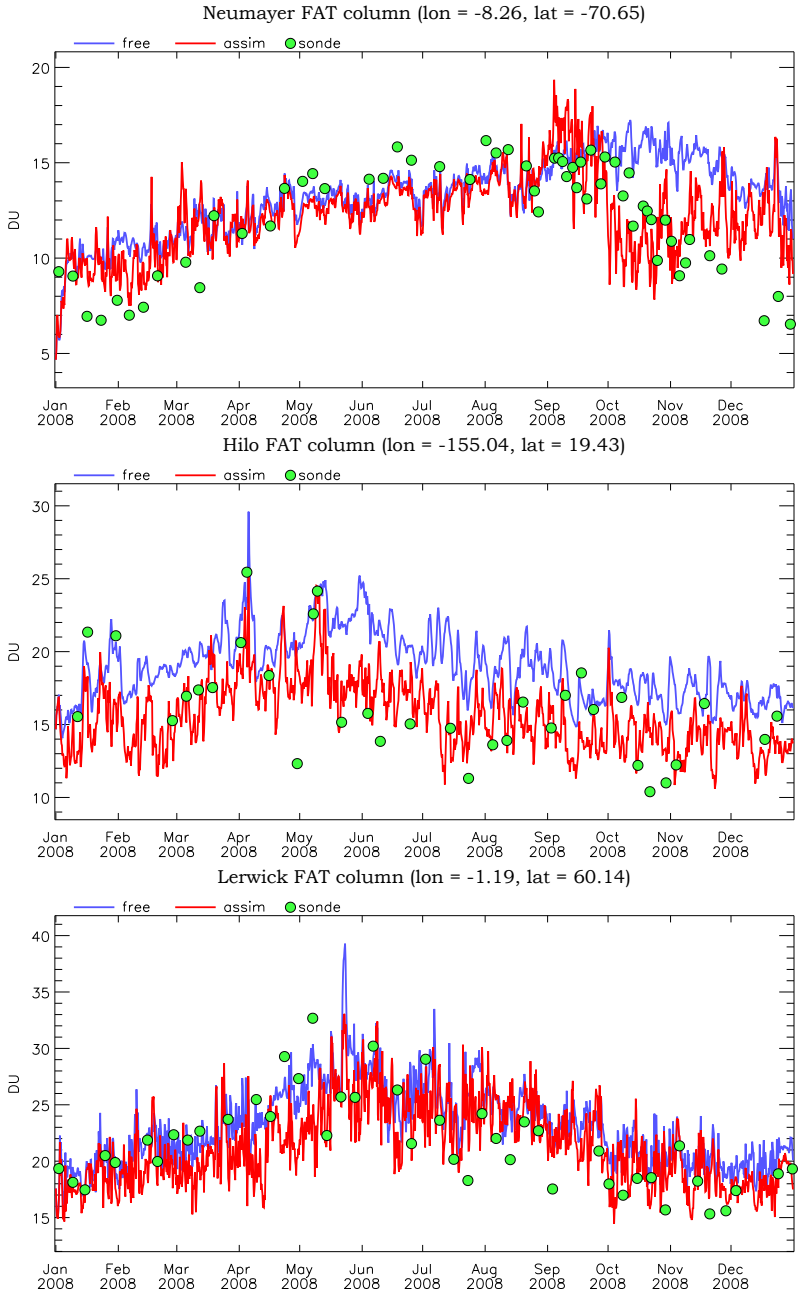

Figure 5.6: Three time series of collocated model output and ozone sonde measurements. From top to bottom: Neumayer, Hilo and Lerwick. The station coordinates have been indicated in the plot titles. Blue line: FAT-column from model run without assimilation, red line: FAT-column from model run with assimilation of GOME-2 and OMI measurements, green circles: ozone sonde measurements.

5.4. Discussion

Deriving tropospheric ozone from nadir looking UV-VIS instruments is a big challenge due to the limited sensitivity of these instruments in the troposphere. Since most of the radtion in the wavelength range between 280 and 330 nm is absorbed by the ozone layer, only a small part reaches the surface. Typical values for the Degree of Freedom for Signal (DFS, a measure for the number of independent pieces of information in the retrieval) of the tropospheric column are between ~0.5 at higher latitudes to ~1.2 in the tropics (Liu et al., 2005).

Both the DOAS total columns used in the MSR and the UV-VIS stratospheric partial columns from the retrievals used in this research are accurate measurements of the ozone concentration. The large variation in the residual-FAT column was therefore unexpected and we discuss the differences between both assimilation systems in some more detail. The MSR only assimilates total columns, which are distributed over the layers of the model proportionally to the subcolumn of that layer. The MSR-model uses the same parameterised ozone chemistry as the profile assimilation used in this research (Cariolle and Déqué, 1986; Cariolle and Teyssèdre, 2007), but with a more up-to-date version of the chemistry parameters (2.9 for the MSR, 2.1 for this research). However, since both assimilation systems are frequently updated with observations, it seems unlikely that the difference in parameterisation version plays a major role in the observed residual-FAT column variation. Also, data from all available total ozone satellite sensors is assimilated into the MSR instead of only the profiles from the two GOME-2 and OMI instruments that are assimilated into the current system. The observations are both bias corrected, the total columns with respect to Brewer-Dobson measurements and the profiles with respect to sondes. The MSR-model resolution is 0.5° × 0.5°, while the profile assimilation runs on 1° × 1°. The most extreme negative residuals are found for the Antarctic sonde stations, so high solar zenith angles may have some effect. However, since negative residuals are also found at lower latitudes, it cannot be the only explanation.

Since the residual-FAT column cannot be used reliably for determining the tropospheric ozone column, the directly integrated FAT columns from the assimilated 0_3 fields might offer an alternative. The global median difference with 0_3 sondes is clearly lower for the assimilated 0_3 fields than for the free model run (see Figure 5.2). However, this is not so clear from the scatterplots of the FAT columns grouped by station (see Figure 5.3). The spatial distribution is also much better for the assimilated 0_3 fields than for the free model run (see Figure 5.1). This can be seen in, for example, the outflow of ozone rich air from Asia over the Pacific and biomass burning enhanced 0_3 concentrations.

There are several potential explanations for the small improvements of the assimilation tropospheric ozone columns compared to the free model run. The reduced sensitivity in the troposphere of GOME-2 and OMI is

compensated for by incorporating the averaging kernel into the observation operator, and the tropospheric column is changed due to the assimilation. However, the tropospheric uncertainties of the observations might be too large to reduce the model uncertainties, so the improvement due to the assimilation only becomes clear when looking at the global median results.

The parameterised chemistry version that is being used is known to overestimate low latitude ozone in the troposphere (Cariolle and Teyssèdre, 2007). Below 230 hPa however, the model is nudged towards the climatology of Fortuin and Kelder (1998). Above 230 hPa the full Cariolle chemistry scheme is used, but two of the parameters in that scheme (i.e. the average volume mixing ratio and the overhead ozone column) are set to the climatological values.

Other possible factors contributing to the large variation in the FAT columns are the representation errors between the model and sondes and between model and observations. Since TM5 is running on a 1° × 1° horizontal grid, the model ozone concentrations are an average over the grid cell while the ozone sonde measurements are point sources. In mountainous regions, the altitude of the model grid cell might also not correspond to the altitude of the sonde station. The ground pixel size and location of the satellite observations might not coincide with the model grid cells either. For example, the footprint size of the GOME-2 measurements used in this research is about 160 × 160 km, which is larger than the model grid cells. The satellite instruments ground pixel centre determines in which model grid cell the pixel is assimilated.

Throughout the year, the FAT column from the assimilated 0_3 fields is smaller than the FAT column from the free model run (Figure 5.5). This is consistent with the validation results for the whole profile (Figure 5.2), and with the rms values between model and sondes in the scatterplots of Figure 5.3. The sonde FAT columns are closer to the free model run from January till May, but closer to the assimilated 0_3 fields from June till December. The reason for the "smallest bias" shift from the free model run to the assimilated 0_3 fields is unknown, but it should be stressed that the differences are small (in the order of 2–3 DU) and close to the uncertainty. If, instead of the FAT column, the column based on the lapse rate tropopause is used, such a "smallest bias" shift does not occur and the bias with respect to the assimilated 0_3 fields run is always smaller than for the free model run.

5.5. Conclusions

Ozone profiles retrieved from GOME-2A and OMI measurements were assimilated simultaneously into the TM5 global chemistry transport model for the year 2008. With respect to the model version used in van Peet et al. (2018, this thesis, Chapter 4), the horizontal resolution of TM5 is increased from 3° × 2° to 1° × 1° (longitude × latitude). At the same time, the vertical resolution is decreased from 44 to 31 layers to reduce the computa-

tional cost. The meteorological data used to drive the model has also been upgraded from the operational data stream from the ECMWF to the ERA-Interim data set. Due to the large variation in the residual-FAT columns in the current model setup, they can't be used reliably, and the direct integrated FAT columns should be used instead. The median global bias with respect to 0_3 sondes is smaller for the assimilated 0_3 fields than for the free model run. When the tropospheric 0_3 columns are grouped according to station, the root mean square of the median sonde columns and model output is smaller for the assimilated 0_3 fields than for the free model run. The rms for each station separately also shows an improvement for the majority of stations on the southern hemisphere and in the tropics. The absolute value of the bias is also smaller for the assimilated 0_3 fields than for the free model run for the majority of stations globally. The monthly median global FAT columns show a small bias with respect to ozone sonde measurements for the free model January till May, but from June till December, the assimilated 0_3 fields have the smallest biases with respect to ozone sondes. The monthly mean ozone fields show significant improvements and more detail when comparing the assimilated 0_3 fields with the free model run, especially for features such as biomass burning enhanced ozone concentrations and outflow of ozone rich air from Asia over the Pacific.

Data availability. OMI ozone profiles are operationally retrieved and can be obtained from NASA's Goddard Earth Sciences (GES) Data and Information Services Center (DISC) on-line archive at `https://aura.gesdisc.eosdis.nasa.gov/data/Aura_OMI_Level2/OMO3PR.003/`. GOME-2 ozone profiles are specifically retrieved for this research and can be obtained by contacting the author. Although not used in this research, operationally retrieved GOME-2 ozone profiles can be retrieved from EUMETSATs AC-SAF (`https://acsaf.org/index.html`), but note that a registration is required.

Author contributions. JvP has performed the calculations and analyses of the research and he wrote the paper with comments from RvdA. RvdA was involved in the conceptualization of the paper and had a supervising role.

Competing interests. The authors declare that they have no conflict of interest.

Acknowledgements. The authors acknowledge all scientists and institutes who contributed their ozone sonde data to the World Ozone and Ultraviolet Radiation Data Center (WOUDC, WMO/GAW, 2016), and the Meteorological Service of Canada for hosting this important public database. EUMETSAT is acknowledged for providing the GOME-2 L1 data and Olaf Tuinder and Robert van Versendaal for their help in the retrieval of the GOME-2 ozone profiles. The Dutch-Finnish OMI instrument is part of the NASA EOS Aura satellite payload. The OMI ozone profiles (OMO3PR, v003) were retrieved at NASA Goddard Earth Sciences Data and Information Services Center (GES DISC) and accessed from the local storage at the Royal Netherlands Meteorological Institute (KNMI). Part of this research has been funded by the Ozone_cci project (http://www.esa-ozone-cci.org), which is part of the Climate Change Initiative (CCI) program of the European Space Agency (ESA).

References

Beck, J. P., Krzyzanowski, M., and Koffi, B.: Tropospheric Ozone in the European Union - 'The Consolidated Report', Topic report no. 8/1998, European Environment Agency, URL https://www.eea.europa.eu/ds_resolveuid/5db5c3a7dec58df6efedccf980013b63, accessed online on 14-11-2017, 1998.

Callies, J., Corpaccioli, E., Eisinger, M., Hahne, A., and Lefebvre, A.: GOME-2 – Metop's Second-Generation Sensor for Operational Ozone Monitoring, ESA bulletin, 102, 28–36, 2000.

Cariolle, D. and Déqué, M.: Southern Hemisphere medium-scale waves and total ozone disturbances in a spectral general circulation model, Journal of Geophysical Research, 91, 10 825–10 846, doi:10.1029/JD091iD10p10825, 1986.

Cariolle, D. and Teyssèdre, H.: A revised linear ozone photochemistry parameterization for use in transport and general circulation models: multi-annual simulations, Atmospheric Chemistry and Physics, 7, 2183–2196, doi:10.5194/acp-7-2183-2007, 2007.

de Laat, A. T. J., van der A, R. J., and van Weele, M.: Evaluation of tropospheric ozone columns derived from assimilated GOME ozone profile observations, Atmospheric Chemistry and Physics, 9, 8105–8120, doi:10.5194/acp-9-8105-2009, 2009.

Dee, D. P., Uppala, S. M., Simmons, A. J., Berrisford, P., Poli, P., Kobayashi, S., Andrae, U., Balmaseda, M. A., Balsamo, G., Bauer, P., Bechtold, P., Beljaars, A. C. M., van de Berg, L., Bidlot, J., Bormann, N., Delsol, C., Dragani, R., Fuentes, M., Geer, A. J., Haimberger, L., Healy, S. B., Hersbach, H., Hólm, E. V., Isaksen, L., Kållberg, P., Köhler, M., Matricardi, M., McNally, A. P., Monge-Sanz, B. M., Morcrette, J.-J., Park, B.-K., Peubey, C., de Rosnay, P., Tavolato, C., Thépaut, J.-N., and Vitart, F.: The ERA-Interim reanalysis: configuration and performance of the data assimilation system, Quarterly Journal of the Royal Meteorological Society, 137, 553–597, doi:10.1002/qj.828, 2011.

Ebojie, F., von Savigny, C., Ladstätter-Weißenmayer, A., Rozanov, A., Weber, M., Eichmann, K.-U.., Bötel, S., Rahpoe, N., Bovensmann, H., and Burrows, J. P.: Tropospheric column amount of ozone retrieved from SCIAMACHY limb–nadir-matching observations, Atmospheric Measurement Techniques, 7, 2073–2096, doi:10.5194/amt-7-2073-2014, 2014.

EPA: Integrated Science Assessment (ISA) of Ozone and Related Photochemical Oxidants, Report EPA/600/R-10/076F, U.S. Environmental Protection Agency, Washington, DC, accessed online on 25-05-2018, 2013.

Fishman, J. and Balok, A. E.: Calculation of daily tropospheric ozone residuals using TOMS and empirically improved SBUV measurements: Application to an ozone pollution episode over the eastern United States, Journal of Geophysical Research (Atmospheres), 104, 30 319–30 340, doi:10.1029/1999JD900875, 1999.

Fishman, J., Wozniak, A. E., and Creilson, J. K.: Global distribution of tropospheric ozone from satellite measurements using the empirically corrected tropospheric ozone residual technique: Identification of the regional aspects of air pollution, Atmospheric Chemistry and Physics, 3, 893–907, doi:10.5194/acp-3-893-2003, 2003.

Fortuin, J. P. F. and Kelder, H.: An ozone climatology based on ozonesonde and satellite measurements, Journal of Geophysical Research, 103, 31 709–31 734, doi:10.1029/1998JD200008, 1998.

Helmig, D., Oltmans, S. J., Carlson, D., Lamarque, J.-F., Jones, A., Labuschagne, C., Anlauf, K., and Hayden, K.: A review of surface ozone in the polar regions, Atmospheric Environment, 41, 5138–5161, doi:10.1016/j.atmosenv.2006.09.053, 2007.

Heue, K.-P., Coldewey-Egbers, M., Delcloo, A., Lerot, C., Loyola, D., Valks, P., and van Roozendael, M.: Trends of tropical tropospheric ozone from 20 years of European satellite measurements and perspectives for the Sentinel-5 Precursor, Atmospheric Measurement Techniques, 9, 5037–5051, doi:10.5194/amt-9-5037-2016, 2016.

Hoogen, R., Rozanov, V. V., and Burrows, J. P.: Ozone profiles from GOME satellite data: Algorithm description and first validation, Journal of Geophysical Research, 104, 8263–8280, doi:10.1029/1998JD100093, 1999.

Krol, M., Houweling, S., Bregman, B., van den Broek, M., Segers, A., van Velthoven, P., Peters, W., Dentener, F., and Bergamaschi, P.: The two-way nested global chemistry-transport zoom model TM5: algorithm and applications, Atmospheric Chemistry and Physics, 5, 417–432, doi:10.5194/acp-5-417-2005, 2005.

Kroon, M., de Haan, J. F., Veefkind, J. P., Froidevaux, L., Wang, R., Kivi, R., and Hakkarainen, J. J.: Validation of Operational Ozone Profiles from the Ozone Monitoring Instrument, Journal of Geophysical Research (Atmospheres), 116, D18305, doi:10.1029/2010JD015100, 2011.

Levelt, P. F., van den Oord, G. H. J., Dobber, M. R., Malkki, A., Visser, H., de Vries, J., Stammes, P., Lundell, J. O. V., and Saari, H.: The Ozone Monitoring Instrument, IEEE Transactions on Geoscience and Remote Sensing, 44, 1093–1101, doi:10.1109/TGRS.2006.872333, 2006.

Liu, X., Chance, K., Sioris, C. E., Spurr, R. J. D., Kurosu, T. P., Martin, R. V., and Newchurch, M. J.: Ozone profile and tropospheric ozone retrievals from the Global Ozone Monitoring Experiment: Algorithm description and validation, Journal of Geophysical Research (Atmospheres), 110, 20 307–+, doi:10.1029/2005JD006240, 2005.

Liu, X., Bhartia, P. K., Chance, K., Spurr, R. J. D., and Kurosu, T. P.: Ozone profile retrievals from the Ozone Monitoring Instrument, Atmospheric Chemistry and Physics, 10, 2521–2537, doi:10.5194/acp-10-2521-2010, 2010.

Monks, P. S., Archibald, A. T., Colette, A., Cooper, O., Coyle, M., Derwent, R., Fowler, D., Granier, C., Law, K. S., Mills, G. E., Stevenson, D. S., Tarasova, O., Thouret, V., von Schneidemesser, E., Sommariva, R., Wild, O., and Williams, M. L.: Tropospheric ozone and its precursors from the urban to the global scale from air quality to short-lived climate forcer, Atmospheric Chemistry and Physics, 15, 8889–8973, doi:10.5194/acp-15-8889-2015, 2015.

Munro, R., Lang, R., Klaes, D., Poli, G., Retscher, C., Lindstrot, R., Huckle, R., Lacan, A., Grzegorski, M., Holdak, A., Kokhanovsky, A., Livschitz, J., and Eisinger, M.: The GOME-2 instrument on the Metop series of satellites: instrument design, calibration, and level 1 data processing - an overview, Atmospheric Measurement Techniques, 9, 1279–1301, doi:10.5194/amt-9-1279-2016, 2016.

Schoeberl, M. R., Ziemke, J. R., Bojkov, B., Livesey, N., Duncan, B., Strahan, S., Froidevaux, L., Kulawik, S., Bhartia, P. K., Chandra, S., Levelt,

P. F., Witte, J. C., Thompson, A. M., Cuevas, E., Redondas, A., Tarasick, D. W., Davies, J., Bodeker, G., Hansen, G., Johnson, B. J., Oltmans, S. J., VöMel, H., Allaart, M., Kelder, H., Newchurch, M., Godin-Beekmann, S., Ancellet, G., Claude, H., Andersen, S. B., Kyrö, E., Parrondos, M., Yela, M., Zablocki, G., Moore, D., Dier, H., von der Gathen, P., Viatte, P., Stübi, R., Calpini, B., Skrivankova, P., Dorokhov, V., de Backer, H., Schmidlin, F. J., Coetzee, G., Fujiwara, M., Thouret, V., Posny, F., Morris, G., Merrill, J., Leong, C. P., Koenig-Langlo, G., and Joseph, E.: A trajectory-based estimate of the tropospheric ozone column using the residual method, Journal of Geophysical Research (Atmospheres), 112, D24S49, doi:10.1029/2007JD008773, 2007.

Segers, A. J., Eskes, H. J., van der A, R. J., van Oss, R. F., and van Velthoven, P. F. J.: Assimilation of GOME ozone profiles and a global chemistry-transport model using a Kalman filter with anisotropic covariance, Quarterly Journal of the Royal Meteorological Society, 131, 477–502, doi:10.1256/qj.04.92, 2005.

Stajner, I., Wargan, K., Pawson, S., Hayashi, H., Chang, L., Hudman, R. C., Froidevaux, L., Livesey, N., Levelt, P. F., Thompson, A. M., Tarasick, D. W., Stübi, R., Andersen, S., Yela, M., KöNig-Langlo, G., Schmidlin, F. J., and Witte, J. C.: Assimilated ozone from EOS-Aura: Evaluation of the tropopause region and tropospheric columns, Journal of Geophysical Research (Atmospheres), 113, D16S32, doi:10.1029/2007JD008863, 2008.

van der A, R. J.: Improved ozone profile retrieval from combined nadir/limb observations of SCIAMACHY, Journal of Geophysical Research (Atmospheres), 106, 14 583–14 594, doi:10.1029/2001JD900089, 2001.

van der A, R. J., Eskes, H. J., Boersma, K. F., van Noije, T. P. C., Van Roozendael, M., De Smedt, I., Peters, D. H. M. U., and W., M. E.: Trends, seasonal variability and dominant NOx source derived from a ten year record of NO2 measured from space, Journal of Geophysical Research (Atmospheres), 113, D04 302, doi:10.1029/2007JD009021, 2008.

van der A, R. J., Allaart, M. A. F., and Eskes, H. J.: Multi sensor reanalysis of total ozone, Atmospheric Chemistry and Physics, 10, 11 277–11 294, doi:10.5194/acp-10-11277-2010, 2010.

van der A, R. J., Allaart, M. A. F., and Eskes, H. J.: Extended and refined multi sensor reanalysis of total ozone for the period 1970-2012, Atmospheric Measurement Techniques, 8, 3021–3035, doi:10.5194/amt-8-3021-2015, 2015.

van Peet, J. C. A. and van der A, R. J.: Deriving tropospheric ozone from assimilated profiles, Atmospheric Chemistry and Physics Discussions, 2019, 1–16, doi:10.5194/acp-2018-1280, 2019.

van Peet, J. C. A., van der A, R. J., Tuinder, O. N. E., Wolfram, E., Salvador, J., Levelt, P. F., and Kelder, H. M.: Ozone ProfilE Retrieval Algorithm (OPERA) for nadir-looking satellite instruments in the UV–VIS, Atmospheric Measurement Techniques, 7, 859–876, doi:10.5194/amt-7-859-2014, 2014.

van Peet, J. C. A., van der A, R. J., Kelder, H. M., and Levelt, P. F.: Simultaneous assimilation of ozone profiles from multiple UV-VIS satellite instruments, Atmospheric Chemistry and Physics, 18, 1685–1704, doi:10.5194/acp-18-1685-2018, 2018.

WHO: Review of evidence on health aspects of air pollution – REVIHAAP Project, Technical report, World Health Organisation – Regional Office for Europe, URL http://www.euro.who.int/__data/assets/pdf_file/0004/193108/REVIHAAP-Final-technical-report-final-version.pdf, accessed online on 25-05-2018, 2013.

WMO: Commission For Aerology (CAe), abridged final report of the second session, Report nr. WMO - No. 65. RP. 27, Secretariat of the World Meteorological Organization, Geneva, Switzerland, 1957.

WMO: The global observing system for climate: implementation needs, Report nr. GCOS-200, Geneva, Switzerland, 2016.

WOUDC, WMO/GAW: WMO/GAW Ozone Monitoring Community, World Meteorological Organization- Global Atmosphere Watch Program (WMO-GAW)/World Ozone and Ultraviolet Radiation Data Centre (WOUDC) [Data]. Retrieved April 15, 2016, from http://woudc.org. A list of all contributors is available on the website., doi:10.14287/10000001, 2016.

Ziemke, J. R., S., C., and K., B. P.: Two new methods for deriving tropospheric column ozone from TOMS measurements: Assimilated UARS MLS/HALOE and convective-cloud differential techniques, Journal of Geophysical Research (Atmospheres), 103, 22 115–22 127, doi:10.1029/98JD01567, 1998.

Ziemke, J. R., Chandra, S., Duncan, B. N., Froidevaux, L., Bhartia, P. K., Levelt, P. F., and Waters, J. W.: Tropospheric ozone determined from Aura OMI and MLS: Evaluation of measurements and comparison with the Global Modeling Initiative's Chemical Transport Model, Journal of Geophysical Research (Atmospheres), 111, D19 303, doi:10.1029/2006JD007089, 2006.

Ziemke, J. R., Chandra, S., Labow, G. J., Bhartia, P. K., Froidevaux, L., and Witte, J. C.: A global climatology of tropospheric and stratospheric ozone derived from Aura OMI and MLS measurements, Atmospheric Chemistry and Physics, 11, 9237–9251, doi:10.5194/acp-11-9237-2011, 2011.

6

Conclusions and Outlook

Ozone is a trace gas present throughout the Earth's atmosphere. Depending on the altitude where it is located, ozone can be considered "good" or "bad". The "good" ozone is found in the stratosphere where it blocks the UV-B radiation (defined as having a wavelength $\lambda < 315\,\mathrm{nm}$) present in solar light and prevents it from reaching the surface. UV-B radiation has several detrimental effects on human health and can negatively affect plant growth. The "bad" ozone is found in the troposphere, where it directly and adversely affects human health and ecosystem productivity. Since ozone strongly absorbs solar radiation, it also acts as a greenhouse gas and has a critical role in the temperature structure of the atmosphere. Therefore, ozone is an essential climate variable and its vertical distribution is essential for understanding, monitoring and modelling climate. Ozone can be measured in situ (for example with balloon borne sondes) or remotely (for example with satellite–based instruments). It is not feasible to obtain global coverage with in situ measurements, so satellite observations are required.

In this thesis, ozone profiles are obtained from nadir looking satellite instruments measuring the reflected solar light in the Hartley-Huggins absorption bands. The ozone profiles are retrieved using the optimal estimation technique (see e.g. Rodgers, 2000), which also provides information on the uncertainty (i.e. the covariance matrix) and the vertical smoothing of the retrieval (i.e. the averaging kernel). Satellite measurements do not give a global ozone field at every required time, but chemical transport models can. These models generally also have a higher vertical resolution than satellite based observations, but they tend to settle on an equilibrium state. Therefore, observations and model results are combined through data assimilation using a Kalman filter technique. Therefore, by combining observations and model output through data-assimilation techniques (like a Kalman filter), we can obtain an optimised description of the atmosphere.

The assimilated ozone fields are used to derive global partial columns

between mean sea level and 6 km altitude. In this altitude range, ozone directly affects living organisms, and the top level is low enough to prevent contamination of the signal with stratospheric air. The quality of the derived partial columns depends critically on the performance of the retrieval algorithm, the chemical transport model and the assimilation algorithm used to combine them. The current research is therefore focused largely on these three processes, in order to demonstrate the benefit of data assimilation in deriving tropospheric ozone columns.

6.1. Ozone profile retrieval under ozone hole conditions

Ozone profiles retrieved from UV-VIS satellite instruments have a limited vertical sensitivity. For example, the effective vertical resolution for ozone profiles using GOME is estimated at 7–9 km between 20–35 km altitude, increasing to 10 km or more above and below that altitude range (Hoogen et al., 1999; Meijer et al., 2006). Similar numbers are found for OMI: 7–11 km in the stratosphere, to 10–14 km in the troposphere (Liu et al., 2010).

Given this limited vertical resolution, and the requirement of 3D information for atmospheric ECVs, we investigated if the retrieval can capture sharp vertical gradients in an ozone profile. Since sharp vertical gradients are typically found under ozone hole conditions, we compared operationally retrieved ozone profiles from GOME-2 with ozone sonde measurements taken at the Antarctic research station Neumayer. The sonde profiles are convolved with the averaging kernel and a priori information (from the climatology by McPeters et al., 2007) before comparing them to collocated retrievals. Despite the rather large pixel footprint (640 × 40 km), and an a priori profile that does not contain detailed ozone hole information, the retrieval by the OPERA algorithm is capable of retrieving ozone profiles during ozone hole conditions. This is especially true for the 15–30 km altitude range, where ozone depletion is most severe. In a matter of days, the location of the Neumayer station can change from inside to outside of the polar vortex as a consequence of the rotation of the polar vortex. The resulting variations in ozone concentration are also captured well by the retrieval.

Next, we created a daily gridded dataset (1° × 1°) from the GOME-2 observations for the period September-December 2008. In the polar regions, the GOME-2 ground tracks overlap frequently and therefore the gridded dataset does not show too many gaps. The dataset can be used to study the development and breakup of the ozone hole. In September-October, the maximum ozone depletion is found in the altitude region between 100 and 50 hPa, while in November-December it is found between 100 and 70 hPa. We saw that the ozone depleted air inside the ozone hole is replenished with ozone rich air from above, eventually leading to the breakup of the ozone hole. There is a persistent region of ozone depleted air below air masses with elevated ozone concentrations during November-December (see Fig-

ures 2.2 and 2.3). The size of the ozone hole might therefore be larger than in the case of the traditional definition based on the total column being smaller than 220 DU.

OPERA is capable of retrieving ozone profiles under difficult circumstances during ozone hole conditions. Sharp vertical gradients in the ozone distribution are captured well by the retrieval. The resulting dataset can be used to improve our understanding of ozone hole dynamics in space and time, which in turn can improve UV index forecasts. People in high latitude regions can then take timely precautions if UV index will increase, which might happen on a timescale of days due to the rotation of the polar vortex.

6.2. Ozone profile retrieval on a global scale for multiple UV-VIS instruments

One of the advantages of a single retrieval algorithm for multiple instruments is that it can be used to create long term time series of retrieved ozone profiles with uniform settings. OPERA has been developed and validated as a retrieval algorithm for GOME (van der A et al., 2002; Meijer et al., 2006; Mijling et al., 2010), and since 2007 it is used operationally within the AC SAF project of EUMETSAT (`https://acsaf.org/`) for GOME-2 (flying on both the Metop-A and Metop-B satellites). It has been extensively validated since that time using ozone sonde, lidar and microwave instruments. In principle, OPERA can also be used for retrievals from the OMI instrument, and it has been used for SCIAMACHY ozone profile retrievals (Shah et al., 2018). Although OPERA has been applied to both GOME and GOME-2, the algorithm settings have not been optimised for simultaneous retrieval of both instruments. We therefore tuned the OPERA algorithm so that GOME and GOME-2 retrievals are done with uniform settings and validated the results against ozone sonde measurements.

The vertical resolution of the retrieval is an important parameter we investigated. In the operational version of OPERA, the number of layers was set to 40, evenly divided between surface and 0.001 hPa. Given a vertical resolution of 7–15 km (depending on the altitude), layers with a thickness of 4 km can be used in the stratosphere (with increasing thickness above and below) without loss of information. Above 0.28 hPa (60 km), there are only small amounts of ozone present, but the grid has been extended to 0.01 hPa (84 km) for radiation balance in the radiative transfer model. Therefore, we selected a vertical grid that is different from the operational grid and which has 16 layers between the surface and 0.01 hPa (84 km).

Different wavelength bands are combined for the spectrum that is used for the retrieval of the ozone profiles from GOME and GOME-2. These wavelength bands have different integration times, resulting in different ground pixel sizes. For GOME, the ground pixel size is approximately 40×320 km, while for GOME-2 measurements from different scanlines are combined, resulting in a ground pixel size of approximately 160×160 km.

Other important settings that can be configured in OPERA are: the ozone climatology that is used as a priori information, the ozone cross sections database, the way clouds and surface albedo are treated, the radiative transfer model, a South Atlantic anomaly filter and an additive offset that has been added to the state vector and which is in the optimal estimation procedure.

The retrieved ozone profiles have been validated against ozone sonde measurements obtained from the World Ozone and Ultraviolet Radiation Data Centre (WOUDC). The collocation criteria are: the sonde station should be inside the pixel footprint of the satellite instrument, the sondes have reached a minimum altitude of 10 hPa, and the time difference between sonde launch and satellite overpass should not be more than 2 h. The sonde profile is interpolated towards the retrieval pressure grid and extended with the a priori profile above the burst level. The interpolated and extended sonde profile is convolved with the averaging kernel to obtain a profile as it could have been observed by the satellite instrument. Finally, the smoothed profile is compared to the collocated satellite measurement.

One year of observations was compared to sonde measurements: 1997 for GOME and 2008 for GOME-2. For the 190 ozone sondes used in the validation of GOME measurements, the mean differences are between 0–10 % from the surface up to 10 hPa, and the mean DFS is 4.20. For the validation of GOME-2, 564 sondes were available globally. The mean differences are similar to those for GOME, except for the second layer between 6 and 12 km, where GOME-2 significantly underestimates the sonde measurements in the Northern Hemisphere. The mean DFS for the collocated profiles is 3.40, which is lower than for GOME, and which is caused by the different signal-to-noise ratio of the two instruments.

As shown in the previous section, OPERA is capable of retrieving ozone profiles under difficult Antarctic ozone hole conditions. Since that analysis was done using sondes only, we extended the altitude range by comparing the GOME-2 retrievals to lidar measurements during the 2009 ozone hole. These lidar measurements were taken at the mid-latitude station in Río Gallegos (51° S, 69.3° W). The polar vortex passes a number of times over this station during the 2009 ozone hole season (Wolfram et al., 2012), but the climatology used in the retrieval does not include ozone hole information at the latitude of Río Gallegos. The climatology is therefore representative for the air outside the vortex, but not for the air inside the vortex. The retrieved profile however, shows similar biases for the cases where the station is inside or outside the vortex.

We have shown that OPERA can be used to retrieve ozone profiles from multiple UV-VIS instruments such as GOME and GOME-2 on a global scale. Since OPERA can be used for different instruments, it can also be used to generate long term time series with uniform retrieval settings. If measurements from high spectral resolution instruments such as GOME and GOME-2 are combined with for example the SBUV measurements starting

in 1970 (Bhartia et al., 2013), a nearly 50 year long time series of ozone profiles may be produced. Such a long climate time series will improve our understanding of changing ozone concentrations over the past decades, as well as over the coming years due to the climate change.

6.3. Combining observations and model data

We have shown that OPERA is capable of retrieving ozone profiles from multiple UV-VIS satellite instruments. Retrieving ozone profiles for multiple instruments with the same algorithm has clear advantages for the generation of long term time series, but it is not always feasible. Due to implementation issues and time constraints, it is not always possible to (re-)process the observations with a single algorithm. For example, different instruments will have different overpass times, horizontal resolutions, vertical sensitivities and biases with respect to each other and to reference data (e.g. ozone sondes). In addition, satellite based instruments will typically observe a location on Earth only once or twice a day, so it will not be possible to get an ozone field with global coverage for a specific time of the day.

The output from a chemical transport model (CTM), on the other hand, is provided on a regular grid at fixed time intervals (e.g. 0, 6, 12 and 18 UTC). CTMs generally also have a higher vertical resolution than ozone retrievals from satellite instruments. Model results might settle on an equilibrium state which might not be representative for the true state of the atmosphere.

To combine ozone profile observations for the period 2008–2011 from GOME-2 (Munro et al., 2016) and OMI (Levelt et al., 2006) with the TM5 CTM (Krol et al., 2005), we used data assimilation, in our case a Kalman filter. The GOME-2 observations are retrieved with OPERA, while the operationally retrieved OMI ozone profiles use a different algorithm (Kroon et al., 2011). The GOME-2 profiles are retrieved on a pressure grid of 32 layers and have a ground pixel size of approximately 160×160 km. The OMI profiles are retrieved on a pressure grid of maximum 18 layers and have a ground pixel size of approximately 13 × 48 km in nadir, and increasing to the edge of the swath. GOME-2 has a mean DFS for cloud-free retrievals of 5.0, while for OMI the mean DFS is 5.1. The mean DFS for GOME-2 is about 1.5 points higher than the 3.4 reported in the previous section, due to the use of cloud free observations and a new version of the L1 data with a new error model.

The assimilation algorithm uses the observations, averaging kernels and covariance matrices, so all information present in the retrievals is also present in the assimilated ozone fields. This is equivalent to assimilating the radiances from the instrument directly (Migliorini, 2012), but simplifies the observation operator and reduces the number of measurements. In a Kalman filter, the model covariance matrix part is an integral part of the assimilation, but it is computationally expensive to calculate. We therefore used a similar solution as in Segers et al. (2005), and parameterise

the covariance matrix into a time dependent standard deviation field and a time independent correlation field. The differences between the observations are minimised by a bias correction based on ozone sondes, which is applied before assimilation. An observation minus forecast filter is implemented, which rejects observations if the absolute difference with the model forecast becomes too large. It is computationally intensive to assimilate all available observations, so 1 in 3 GOME-2 and 1 in 31 OMI retrievals are used. For OMI, due to their large area, the outermost pixels of each swath are neglected as well. The total number of assimilated observations between the two instruments is more or less the same. TM5 is running on a 3° × 2° (longitude × latitude) global grid with 44 layers ranging from the surface to the top of the atmosphere.

A novel method was developed to check the uncertainty levels of the level–1 measurements. It is assumed that for two adjacent detector pixels the radiance or reflectance difference depends on the slope of the spectrum. When enough data are collected, a Gaussian function can be fitted through the data and its standard deviation is a good approximation of the noise level at that particular wavelength. For GOME-2, this method yields the same results as the noise levels contained in the level–1 data files. For OMI, this method yields the same results as the level–1 data till February 2010, but larger values than in the level–1 data afterwards (see Figure 4.2). As a consequence, the number of assimilated pixels from both GOME-2 and OMI descreases when observations from both instruments are assimilated simultaneously (see Figure 4.10).

A new function containing an asymptotic limit on the maximum error was used for the model error growth. In a previous version of the assimilation algorithm this limit was not present, and the error could potentially grow too extreme values. This is especially true during the polar night, if there are no observations available to correct the model error field. The time independent model correlation matrix was updated as well, using a similar approach as in Segers et al. (2005).

GOME-2 and OMI are biased with respect to each other, so a bias correction based on ozone sonde data has been developed. The bias correction is based on the solar zenith angle, viewing angle and time and is applied to the observations before they are assimilated into TM5.

In total we performed four model runs for the period 2008–2011. A free model run without the assimilation of any data, a model run with the assimilation of only GOME-2 data, one with only OMI data and one with GOME-2 and OMI data simultaneously. Since the GOME-2 and OMI retrievals have a different vertical grid, the observation minus forecast (OmF) and observation minus analysis (OmA) were regridded to the same pressure grid to enable the direct comparison between the two instruments. Instrumental features that influence the uncertainty of the observations, can be seen in the OmF and OmA data at certain altitudes. For example, the band 1A/1B wavelength shift in the GOME-2 significantly reduces the

OmF and OmA for the surface layer (see Figure 4.7). After the L0/L1B processor update, the uncertainty of the OMI observations is much smaller than that of the GOME-2 observations. The model error can not adapt to the lower uncertainty in the OMI data, since it is constantly being reset by the higher GOME-2 observations. Therefore, the number of assimilated observations from both GOME-2 and OMI is significantly reduced when these instruments are assimilated simultaneously (see Figure 4.10).

The OmF and OmA values can be integrated over the profile and gridded so that the results can be used to study the variation of the OmF and OmA over latitude and time. The highest OmF and OmA values are found around the polar night. The GOME-2 band 1A/1B wavelength shift is clearly visible in the simultaneous assimilated data, as are changes due to updates in the bias correction parameters at the start of the year.

The assimilated 0_3 fields have a smaller bias than the free model run when compared to ozone sondes, especially between 100 and 10 hPa where GOME-2 and OMI are most sensitive to the ozone concentration. The simultaneous assimilation of GOME-2 and OMI shows a smaller bias than either of the single instrument assimilation runs. In the troposphere, the biases of the assimilation model runs are also smaller than the free model run, but the improvement is not as large as for the stratosphere. The assimilated ozone shows a bias of about 12 % between 100 and 200 hPa, but the observations do not show a similar deviation (see Figures 4.13 and 4.6). A case study over the Tibetan Plateau shows a better agreement between the assimilated ozone fields and the ERA-Interim dataset. The improvement is largest in the stratosphere, but is also clear in the troposphere around two stratosphere-troposphere exchange events.

For the first time, we simultaneously assimilated ozone profiles from multiple UV-VIS instruments to create a gridded dataset with a high temporal and spatial resolution. The assimilated ozone fields can be used to study dynamical features such as stratosphere-troposphere exchanges, or tropospheric ozone distribution. Assimilating observations from as many available UV-VIS instruments as possible (e.g. SBUV, GOME, GOME-2, OMI and SCIAMACHY) can create a nearly 50-year long climate time series, which will improve our understanding of past and future trends of atmospheric ozone concentrations.

6.4. Deriving tropospheric ozone

The data assimilation algorithm described in the previous section, has been used to determine tropospheric ozone on a high spatial and temporal resolution. The troposphere is the lowest layer of the Earth's atmosphere, which is topped by the tropopause. There are multiple definitions for the tropopause, which can be based on, for example, the lapse-rate or thermal tropopause (WMO, 1957), the dynamical properties of the atmosphere or the gradient in the ozone concentration. Near the tropopause stratosphere-troposphere exchange events can contaminate the upper-tropospheric ozone

concentration. Therefore, we focused our research on the partial ozone column between the surface and 6 km above mean sea level, which is the region were ozone has a direct impact on living organisms. The 0–6 km ozone partial column will be referred to as the fixed altitude top level (FAT) column hereafter. The FAT column can be calculated by direct integration of the model output or by the residual method, where the stratospheric part (from FAT to top of atmosphere) is subtracted from assimilated total columns.

We assimilated the same GOME-2 and OMI data for the year 2008 with a Kalman filter into the chemical transport model TM5. Two model runs were performed: a free model run without any assimilation of observations, and an assimilation model run with simultaneous assimilation of GOME-2 and OMI profiles. In view of the ozone correlation length of 100–150 km in the middle and upper troposphere (Sparling et al., 2006), the TM5 model setup of 3° × 2° (about 300 km × 200 km at the equator, longitude × latitude) might be too coarse when using the assimilated ozone fields to determine tropospheric ozone. We therefore increased the model resolution to 1° × 1° (longitude × latitude), and reduced the number of model layers from 44 to 31 to reduce computational cost. Due to the changes in horizontal and vertical resolution, the meteorological data that is used to drive TM5 was changed from the operational data stream to ERA-Interim data (Dee et al., 2011), and the time independent model correlation matrix was recalculated.

The FAT columns from both the free and assimilation model runs were validated with ozone sonde data from the WOUDC. Global monthly mean ozone FAT values show a clear yearly cycle and higher values in the Northern Hemisphere than in the Southern Hemisphere. Elevated ozone concentrations due to biomass burning can be seen between South America and Africa, and between Africa and Australia. Outflow of ozone rich air from Asia across the Pacific can also be observed. From the surface up to 5 hPa (40 km), the assimilated fields have a significantly lower median bias with respect to ozone sondes than the free model run. Around 100–200 hPa (around 15 km) the difference increases for both free and assimilation model runs, probably due to the sharp increase in ozone concentration in the lower stratosphere.

If the FAT columns are grouped per station and the model columns are plotted against the sonde columns, the assimilated and free FAT columns show a similar correlation. The root mean square of the model and sonde FAT columns for the assimilated ozone is lower than for the free model run. The residual FAT columns (i.e. the total MSR column minus the FAT-to-top-of-atmosphere partial column) show a lower correlation coefficient and a higher root mean square value than either free or assim FAT columns, so they have been omitted from further analysis. The tropics ($-30° \leq \text{lat} < -30°$) show larger root mean square and mean values for the difference between model and sonde than higher latitudes.

Time series of monthly median global FAT-columns show a small dif-

ference between the first and second half of 2008. During the first half, the free model run is closer to the sonde data, while for the second half, the assimilated ozone fields are closer to the sonde data. The reason for this "smallest bias shift" is unknown, but it should be noted that it is not present in the time series for the lapse rate tropopause (not shown). The free model run follows the same pattern as the climatological values. Although the free and assimilation model runs start with the same ozone concentrations, they diverge quickly due to the assimilation of observations and the monthly median values are not the same. The residual FAT columns show too large a variation to be used reliably, so the direct integrated FAT columns should be used instead. The monthly mean tropospheric ozone fields show significant improvements and more detail when comparing the assimilation results with the free model run, especially for features such as biomass burning enhanced ozone concentrations and outflow of ozone rich air from Asia over the Pacific.

6.5. Outlook

6.5.1. Improved tropospheric ozone based on observations

The Ozone ProfilE Retrieval Algorithm (OPERA) is being developed and maintained at the KNMI and has been used in this thesis to retrieve ozone profiles from GOME and GOME-2. An operational version is being used within EUMETSATs AC SAF (`https://acsaf.org/`) for ozone profile retrievals from GOME-2 (both on Metop-A and Metop-B). One of the future challenges is to improve the vertical resolution and sensitivity of OPERA in the troposphere. This is a difficult altitude, since the instruments look through the thick ozone layer and therefore the sensitivity is quite low. However, retrieval algorithms such as the Rutherford Appleton Laboratory (RAL) scheme (Miles et al., 2015) increase the sensitivity of the retrieval in the troposphere by adding information from the Huggins bands (wavelengths up to 336 nm, vs. 330 for OPERA).

Another possibility that might improve the sensitivity of the retrievals in the troposphere is a more synergistic approach, where measurements from completely different wavelength ranges (such as the UV-VIS and the TIR) are combined. For example, GOME-2 has been combined with measurements from the Infrared Atmospheric Sounding Interferometer (IASI; Cuesta et al., 2013), and OMI has been combined with measurements from the Tropospheric Emission Spectrometer (TES; Fu et al., 2013) and Atmospheric Infrared Sounder (AIRS; Fu et al., 2018). A different approach is to merge the ozone profiles after they have been retrieved. In the AURORA project (`http://www.aurora-copernicus.eu/`), this is achieved by a process called data fusion (e.g. Ceccherini et al., 2018). With data fusion, ozone profiles are first retrieved for the different wavelength ranges separately and merged in a later stage. Averaging kernels and covariance matrices are also merged into new matrices combining the information content of both wave-

length ranges. This leads to a higher DFS for the fused retrieval than for any of the retrievals separately. Within AURORA, a proof of principle is given for simulated measurements of the future Sentinel 4 and 5 satellites, but data fusion might also be applied to for example GOME-2 and IASI.

OPERA could potentially benefit from an increased wavelength range in the Huggins bands (Miles et al., 2015), or by adding the Chappuis band (Chance et al., 1997). Since at these wavelengths the radiation will penetrate the atmosphere and reach the surface, knowledge on the surface albedo and land usage is required. The calibration should also be consistent in the whole wavelength range, i.e. in all the different bands. OPERA might also be extended to incorporate the infrared part of the spectrum, which would require the implementation of a new radiative transfer model. The advantage of retrieving ozone profiles over such broad spectral range is that the retrieval is done consistently and an additional step such as data fusion is not required.

6.5.2. Improving the profile assimilation algorithm

The calibration of different wavelength ranges or instruments is often not done consistently, and biases will occur. One way to reduce the dependence on on-ground calibration data is to determine the L1 uncertainty levels with the in-flight method described in Section 4.5.1. Using that method, the uncertainty of all observations is derived consistently, which will reduce the probability of unexpected errors when the data is assimilated. Remaining biases between the assimilated observations should be reduced by applying a (sonde based) bias correction to the data before assimilation.

In this thesis, ozone profiles are assimilated into the chemical transport model TM5. Due to computational constraints, it is not possible to assimilate all available observations into the chemical transport model TM5, so a selection must be made. The data fusion method mentioned in the previous section might be used to combine retrievals into super-observations, thereby utilising as much information as possible, while limiting the computational cost.

The current profile assimilation version of TM5 was forked from the main code in order to optimise it for speed. One of the adaptations was to remove all chemistry in favour of the parameterised chemistry of Cariolle and Teyssèdre (2007), using the parameters of version 2.1. According to the release notes of this version of the parameters, a known issue is an overestimation of the tropospheric ozone concentration at low latitudes. An obvious improvement would be to update the parameters to a more recent version. For example, the MSR uses parameter version 2.9.

Another issue with the current version of the profile assimilation version of TM5 is that the model is nudged towards the climatology of Fortuin and Kelder (1998). This is obviously much older than the time span of the current research (2008–2011), so a more up to date climatology such as the one by McPeters et al. (2007) might yield better results. The McPeters

et al. (2007) climatology has a better representation of ozone hole conditions than the Fortuin and Kelder (1998) climatology, and is also used for the GOME-2 retrievals in this thesis. An updated version of the climatology can be found in McPeters and Labow (2012).

Instead of a climatology, a different dataset could be used to nudge TM5. For example, the MSR by van der A et al. (2010, 2015) is already used in the main version of TM5. However, it should be noted that the MSR is tuned for accuracy of the total columns, so the vertical distribution might be unreliable.

Some of the observed features in the assimilated ozone fields might be due to the errors of the model. If the model errors are too small with respect to those of the observations, the model is drawn too strongly towards its equilibrium state. The small zonal bands with elevated tropospheric ozone (see Figure 5.1) are probably due to a model artefact.

These possible model issues might be improved in the latest version of TM5 (called TM5-MP), which is also optimised to run in parallel on multiple cores to increase speed. The improved performance of the main TM5 model could become important if the resolution of the profile assimilation version has to be increased even further to for example $0.5° \times 0.5°$ or $0.25° \times 0.25°$. Porting the assimilation algorithm to the latest version of TM5 is highly advisable, and will require less work than implementing the latest features in the profile assimilation version.

6.5.3. Improved tropospheric ozone from assimilated profiles

One of the issues in determining the tropospheric column was the large variation in the residual FAT column, i.e. the difference between the MSR total column and the FAT-to-top-of-atmosphere partial column. The assimilation has a small bias with respect to sondes, with the exception of the region around 15 km, where the difference between the assimilated ozone profiles minus sonde measurements is about 18 %. There are also differences between the current profile assimilation and the MSR. The total columns in the MSR are bias corrected with respect to Brewer-Dobson measurements, not with sondes. The parameterised chemistry of Cariolle and Teyssèdre (2007) is used in both systems, but the MSR uses a more recent version of the parameters. The most extreme negative residuals are found for the Antarctic sonde stations, so high solar zenith angles may have some effect. It is therefore too early to definitively discard the residual FAT column using MSR total columns, and the issues mentioned above should be fixed first.

6.5.4. Climate time series of assimilated ozone profiles

An updated version of the profile retrieval and assimilation algorithms could be used to generate a long term time series of assimilated ozone profiles. Since OPERA can retrieve ozone profiles from GOME, GOME-2, SCIAMACHY and OMI, it is an obvious option as retrieval algorithm for such a long climate time series. As an alternative, the L2 data from the Copernicus

Climate Change Service Ozone (C3S Ozone) project might be used instead. Within that project, ozone profiles from GOME, SCIAMACHY, GOME-2 (Metop-A and Metop-B) and OMI are retrieved with the algorithm described by Miles et al. (2015). The assimilation algorithm is not limited to UV-VIS retrieval from the instruments mentioned above, other instruments such as IASI might be assimilated as well.

The BUV and SBUV instruments have been measuring ozone profiles since 1970, albeit at a lower spectral resolution than GOME and later instruments. The most recent version (v8.6) of the retrieval algorithm has been described by (Bhartia et al., 2013). If the observations from the SBUV and GOME type instruments are combined, a nearly 50 year long climate time series of satellite based ozone profiles may be produced.

The observations of ozone will be continued, both from polar orbiting and geostationary satellites. For example, the Metop-C satellite (carrying another GOME-2) is scheduled for launch in September 2018. So with a design lifetime of 5 years, the GOME-2 observations will continue until at least 2023. Starting in 2021, EUMETSAT Polar System - Second Generation (EPS-SG) series of satellites will be launched to cover the 2021–2040 period. The A-type satellites (Metop-SG 1A, 2A and 3A) will carry the Sentinel-5 instruments that measure the reflected solar light from the ultra violet (UV) to the short wave infrared (SWIR), which can be used to determine ozone concentrations. To reduce the gap between the EOS AURA (carrying OMI) satellite and the Sentinel-5 satellite, and as a complement to the Metop satellites (carrying GOME-2), the Sentinel-5 precursor satellite was launched successfully on October 13th, 2017. It has a single instrument payload, consisting of the TROPOMI instrument (Veefkind et al., 2012). TROPOMI has an unprecedented horizontal resolution of 7×7 km in nadir, enabling detailed measurements of ozone and other atmospheric constituents.

Ozone measurements will also become available from geostationary instruments such as the planned European Sentinel-4 (ESA, 2017), American TEMPO (Zoogman et al., 2017) and Korean GEMS instruments. Simulated Sentinel-4 ozone profiles have already been assimilated in the AURORA project (`http://www.aurora-copernicus.eu/`), which is part of the European Union's HORIZON 2020 programme. To be launched in the coming years, these geostationary instruments measure ozone from a fixed location relative to Earth, with a high time resolution of 1 hour between successive observations. A drawback is that these instruments do not provide global coverage, but only regional coverage over Europe, the USA and South-East Asia respectively. Due to the very high time resolution of these instruments, it is possible to study the diurnal cycle of ozone and the observations can also be used to validate the assimilated ozone fields.

Ozone profile observations from satellite based instruments were started in the 1970s with the BUV and SBUV instruments, and will continue till at least 2040 with the Sentinel-5 instruments. Assimilation of such a long

observation record into a chemical transport model such as TM5, will produce a high temporal and spatial resolution gridded dataset. Such an assimilated dataset can be used to increase our understanding of ozone in a changing climate, and improve climate predictions for the future.

References

Bhartia, P. K., McPeters, R. D., Flynn, L. E., Taylor, S., Kramarova, N. A., Frith, S., Fisher, B., and DeLand, M.: Solar Backscatter UV (SBUV) total ozone and profile algorithm, Atmospheric Measurement Techniques, 6, 2533–2548, doi:10.5194/amt-6-2533-2013, 2013.

Cariolle, D. and Teyssèdre, H.: A revised linear ozone photochemistry parameterization for use in transport and general circulation models: multi-annual simulations, Atmospheric Chemistry and Physics, 7, 2183–2196, doi:10.5194/acp-7-2183-2007, 2007.

Ceccherini, S., Carli, B., Tirelli, C., Zoppetti, N., Del Bianco, S., Cortesi, U., Kujanpää, J., and Dragani, R.: Importance of interpolation and coincidence errors in data fusion, Atmospheric Measurement Techniques, 11, 1009–1017, doi:10.5194/amt-11-1009-2018, 2018.

Chance, K. V., Burrows, J. P., Perner, D., and Schneider, W.: Satellite measurements of atmospheric ozone profiles, including tropospheric ozone, from ultraviolet/visible measurements in the nadir geometry : a potential method to retrieve tropospheric ozone, Journal of Quantitative Spectroscopy and Radiative Transfer, 57, 467–476, doi:10.1016/S0022-4073(96)00157-4, 1997.

Cuesta, J., Eremenko, M., Liu, X., Dufour, G., Cai, Z., Höpfner, M., von Clarmann, T., Sellitto, P., Foret, G., Gaubert, B., Beekmann, M., Orphal, J., Chance, K., Spurr, R., and Flaud, J.-M.: Satellite observation of lowermost tropospheric ozone by multispectral synergism of IASI thermal infrared and GOME-2 ultraviolet measurements over Europe, Atmospheric Chemistry and Physics, 13, 9675–9693, doi:10.5194/acp-13-9675-2013, 2013.

Dee, D. P., Uppala, S. M., Simmons, A. J., Berrisford, P., Poli, P., Kobayashi, S., Andrae, U., Balmaseda, M. A., Balsamo, G., Bauer, P., Bechtold, P., Beljaars, A. C. M., van de Berg, L., Bidlot, J., Bormann, N., Delsol, C., Dragani, R., Fuentes, M., Geer, A. J., Haimberger, L., Healy, S. B., Hersbach, H., Hólm, E. V., Isaksen, L., Kållberg, P., Köhler, M., Matricardi, M., McNally, A. P., Monge-Sanz, B. M., Morcrette, J.-J., Park, B.-K., Peubey, C., de Rosnay, P., Tavolato, C., Thépaut, J.-N., and Vitart, F.: The ERA-Interim reanalysis: configuration and performance of the data assimilation system, Quarterly Journal of the Royal Meteorological Society, 137, 553–597, doi:10.1002/qj.828, 2011.

ESA: SENTINEL-4, ESA's Geostationary Atmospheric Mission for Copernicus Operational Services, Report SP-1334 2nd. ed., URL `https://esamultimedia.esa.int/multimedia/publications/SP-1334/SP-1334.pdf`, 2017.

Fortuin, J. P. F. and Kelder, H.: An ozone climatology based on ozonesonde and satellite measurements, Journal of Geophysical Research, 103, 31 709–31 734, doi:10.1029/1998JD200008, 1998.

Fu, D., Worden, J. R., Liu, X., Kulawik, S. S., Bowman, K. W., and Natraj, V.: Characterization of ozone profiles derived from Aura TES and OMI radiances, Atmospheric Chemistry and Physics, 13, 3445–3462, doi:10.5194/acp-13-3445-2013, 2013.

Fu, D., Kulawik, S. S., Miyazaki, K., Bowman, K. W., Worden, J. R., Eldering, A., Livesey, N. J., Teixeira, J., Irion, F. W., Herman, R. L., Osterman, G. B., Liu, X., Levelt, P. F., Thompson, A. M., and Luo, M.: Retrievals of Tropospheric Ozone Profiles from the Synergic Observation of AIRS and OMI: Methodology and Validation, Atmospheric Measurement Techniques Discussions, 2018, 1–27, doi:10.5194/amt-2018-138, 2018.

Hoogen, R., Rozanov, V. V., and Burrows, J. P.: Ozone profiles from GOME satellite data: Algorithm description and first validation, Journal of Geophysical Research, 104, 8263–8280, doi:10.1029/1998JD100093, 1999.

Krol, M., Houweling, S., Bregman, B., van den Broek, M., Segers, A., van Velthoven, P., Peters, W., Dentener, F., and Bergamaschi, P.: The two-way nested global chemistry-transport zoom model TM5: algorithm and applications, Atmospheric Chemistry and Physics, 5, 417–432, doi:10.5194/acp-5-417-2005, 2005.

Kroon, M., de Haan, J. F., Veefkind, J. P., Froidevaux, L., Wang, R., Kivi, R., and Hakkarainen, J. J.: Validation of Operational Ozone Profiles from the Ozone Monitoring Instrument, Journal of Geophysical Research (Atmospheres), 116, D18305, doi:10.1029/2010JD015100, 2011.

Levelt, P. F., van den Oord, G. H. J., Dobber, M. R., Malkki, A., Visser, H., de Vries, J., Stammes, P., Lundell, J. O. V., and Saari, H.: The Ozone Monitoring Instrument, IEEE Transactions on Geoscience and Remote Sensing, 44, 1093–1101, doi:10.1109/TGRS.2006.872333, 2006.

Liu, X., Bhartia, P. K., Chance, K., Spurr, R. J. D., and Kurosu, T. P.: Ozone profile retrievals from the Ozone Monitoring Instrument, Atmospheric Chemistry and Physics, 10, 2521–2537, doi:10.5194/acp-10-2521-2010, 2010.

McPeters, R. D. and Labow, G. J.: Climatology 2011: An MLS and sonde derived ozone climatology for satellite retrieval algorithms, Journal of Geophysical Research (Atmospheres), 117, doi:10.1029/2011JD017006, 2012.

McPeters, R. D., Labow, G. J., and Logan, J. A.: Ozone climatological profiles for satellite retrieval algorithms, Journal of Geophysical Research (Atmospheres), 112, D05 308, doi:10.1029/2005JD006823, 2007.

Meijer, Y. J., Swart, D. P. J., Baier, F., Bhartia, P. K., Bodeker, G. E., Casadio, S., Chance, K., Del Frate, F., Erbertseder, T., Felder, M. D., Flynn, L. E., Godin-Beekmann, S., Hansen, G., Hasekamp, O. P., Kaifel, A., Kelder, H. M., Kerridge, B. J., Lambert, J.-C., Landgraf, J., Latter, B., Liu, X., McDermid, I. S., Pachepsky, Y., Rozanov, V., Siddans, R., Tellmann, S., van der A, R. J., van Oss, R. F., Weber, M., and Zehner, C.: Evaluation of Global Ozone Monitoring Experiment (GOME) ozone profiles from nine different algorithms, Journal of Geophysical Research (Atmospheres), 111, 21 306–+, doi:10.1029/2005JD006778, 2006.

Migliorini, S.: On the Equivalence between Radiance and Retrieval Assimilation, Monthly Weather Review, 140, 258–265, doi:10.1175/MWR-D-10-05047.1, 2012.

Mijling, B., Tuinder, O. N. E., van Oss, R. F., and van der A, R. J.: Improving ozone profile retrieval from spaceborne UV backscatter spectrometers using convergence behaviour diagnostics, Atmospheric Measurement Techniques, 3, 1555–1568, doi:10.5194/amt-3-1555-2010, 2010.

Miles, G. M., Siddans, R., Kerridge, B. J., Latter, B. G., and Richards, N. A. D.: Tropospheric ozone and ozone profiles retrieved from GOME-2 and their validation, Atmospheric Measurement Techniques, 8, 385–398, doi:10.5194/amt-8-385-2015, 2015.

Munro, R., Lang, R., Klaes, D., Poli, G., Retscher, C., Lindstrot, R., Huckle, R., Lacan, A., Grzegorski, M., Holdak, A., Kokhanovsky, A., Livschitz, J., and Eisinger, M.: The GOME-2 instrument on the Metop series of satellites: instrument design, calibration, and level 1 data processing - an overview, Atmospheric Measurement Techniques, 9, 1279–1301, doi:10.5194/amt-9-1279-2016, 2016.

Rodgers, C. D.: Inverse methods for atmospheric sounding, vol. Vol. 2 of *Series on Atmospheric, Oceanic and Planetary Physics*, World Scientific Publishing, Singapore, 2008 edn., 2000.

Segers, A. J., Eskes, H. J., van der A, R. J., van Oss, R. F., and van Velthoven, P. F. J.: Assimilation of GOME ozone profiles and a global chemistry-transport model using a Kalman filter with anisotropic covariance, Quarterly Journal of the Royal Meteorological Society, 131, 477–502, doi:10.1256/qj.04.92, 2005.

Shah, S., Tuinder, O. N. E., van Peet, J. C. A., de Laat, A. T. J., and Stammes, P.: Evaluation of SCIAMACHY Level-1 data versions using nadir ozone profile retrievals in the period 2003–2011, Atmospheric Measurement Techniques, 11, 2345–2360, doi:10.5194/amt-11-2345-2018, 2018.

Sparling, L. C., Wei, J. C., and Avallone, L. M.: Estimating the impact of small-scale variability in satellite measurement validation, Journal

of Geophysical Research (Atmospheres), 111, D20310, doi:10.1029/2005JD006943, 2006.

van der A, R. J., van Oss, R. F., Piters, A. J. M., Fortuin, J. P. F., Meijer, Y. J., and Kelder, H. M.: Ozone profile retrieval from recalibrated Global Ozone Monitoring Experiment data, Journal of Geophysical Research (Atmospheres), 107, 4239–+, doi:10.1029/2001JD000696, 2002.

van der A, R. J., Allaart, M. A. F., and Eskes, H. J.: Multi sensor reanalysis of total ozone, Atmospheric Chemistry and Physics, 10, 11 277–11 294, doi:10.5194/acp-10-11277-2010, 2010.

van der A, R. J., Allaart, M. A. F., and Eskes, H. J.: Extended and refined multi sensor reanalysis of total ozone for the period 1970-2012, Atmospheric Measurement Techniques, 8, 3021–3035, doi:10.5194/amt-8-3021-2015, 2015.

Veefkind, J. P., Aben, I., McMullan, K., Förster, H., de Vries, J., Otter, G., Claas, J., Eskes, H. J., de Haan, J. F., Kleipool, Q., van Weele, M., Hasekamp, O., Hoogeveen, R., Landgraf, J., Snel, R., Tol, P., Ingmann, P., Voors, R., Kruizinga, B., Vink, R., Visser, H., and Levelt, P. F.: TROPOMI on the ESA Sentinel-5 Precursor: A GMES mission for global observations of the atmospheric composition for climate, air quality and ozone layer applications, Remote Sensing of Environment, 120, 70–83, doi:10.1016/j.rse.2011.09.027, 2012.

WMO: Commission For Aerology (CAe), abridged final report of the second session, Report nr. WMO - No. 65. RP. 27, Secretariat of the World Meteorological Organization, Geneva, Switzerland, 1957.

Wolfram, E. A., Salvador, J., Orte, F., D'Elia, R., Godin-Beekmann, S., Kuttippurath, J., Pazmiño, A., Goutail, F., Casiccia, C., Zamorano, F., Paes Leme, N., and Quel, E. J.: The unusual persistence of an ozone hole over a southern mid-latitude station during the Antarctic spring 2009: a multi-instrument study, Annales Geophysicae, 30, 1435–1449, doi:10.5194/angeo-30-1435-2012, 2012.

Zoogman, P., Liu, X., Suleiman, R. M., Pennington, W. F., Flittner, D. E., Al-Saadi, J. A., Hilton, B. B., Nicks, D. K., Newchurch, M. J., Carr, J. L., Janz, S. J., Andraschko, M. R., Arola, A., Baker, B. D., Canova, B. P., Chan Miller, C., Cohen, R. C., Davis, J. E., Dussault, M. E., Edwards, D. P., Fishman, J., Ghulam, A., González Abad, G., Grutter, M., Herman, J. R., Houck, J., Jacob, D. J., Joiner, J., Kerridge, B. J., Kim, J., Krotkov, N. A., Lamsal, L., Li, C., Lindfors, A., Martin, R. V., McElroy, C. T., McLinden, C., Natraj, V., Neil, D. O., Nowlan, C. R., O'Sullivan, E. J., Palmer, P. I., Pierce, R. B., Pippin, M. R., Saiz-Lopez, A., Spurr, R. J. D., Szykman, J. J., Torres, O., Veefkind, J. P., Veihelmann, B., Wang, H., Wang, J., and Chance, K.: Tropospheric emissions: Monitoring of pollution (TEMPO),

Journal of Quantitative Spectroscopy and Radiative Transfer, 186, 17–39, doi:10.1016/j.jqsrt.2016.05.008, 2017.

Acknowledgements

First of all, I would like to thank Hennie Kelder and Ronald van der A for giving me the opportunity to start working at KNMI in 2008. Although I was appointed as a scientific researcher, and not as a PhD student, we agreed from the start that I would eventually combine my work into a dissertation.

And now, after two appointments of five years, that intention has finally been fullfilled. That would not have been possible without my promotor Pieternel Levelt, whose handwritten and subsequently photographed comments were sometimes hard to decipher, but helped to improve the first drafts of my thesis.

I would also like to thank Gerrit de Leeuw, Michel van Roozendael, Herman Russchenberg and Pier Siebesma, for accepting the invitation to join my doctoral committee.

Special thanks to my office mate for more than 10 years Marc Allaart, with whom I share an interest in history and archaeology. He also pointed me to the BBC television quiz QI, and because of him I've started watching snooker. His help with various Linux related problems has been invaluable.

I would like to thank Jos de Laat for answering all my questions on TM5 and meteorology, Olaf Tuinder for answering many questions ("vraagje") on OPERA, Robert van Versendaal for his help in processing the GOME-2 ozone profiles I used in the last two chapters of my thesis and Jieying Ding for patiently answering my questions on all kinds of publishing issues in the final months before my thesis defence.

Many thanks to all my colleagues who have answered my questions and shown an interest in my life and work, unfortunately I can not list all of you.

Over the years, I've supplied pets to a number of colleagues: Piet Stammes (chickens and kittens), Jos de Laat (chickens and a kitten for a friend of his), Maurits Kooremans (kittens) and Ping Wang (kitten). I hope they've brought joy to your life and wil continue to do so for a very long time.

Curriculum Vitæ

Jacob Cornelis Adriaan van Peet

1-5-1979 Born in Ermelo, The Netherlands.

Education

1997	Highschool diploma, Christelijk College Groevenbeek, Ermelo, The Netherlands
2002	M.Sc. Physical Geography, Utrecht University, Utrecht, The Netherlands
2006	M.Sc. Physics and Astronomy, Utrecht University, Utrecht, The Netherlands
2019	PhD. Atmospheric Remote Sensing, Faculty of Civil Engineering & Geosciences, Delft University of Technology, Delft, The Netherlands
	Thesis: Three-dimensional ozone distribution based on assimilation of nadir-sounding UV-VIS satellite observations
	Promotor: Prof. dr. P. F. Levelt
	Promotor: Prof. dr. R. J. van der A

Training

2010	ESA Earth Observation Summer School on Earth System Monitoring and modelling
2015	The programming language Python & Numerical Python

Work

1997 – 2006	during my university education, various teaching assistent positions at Utrecht University
2006 – 2008	OGD (`https://ogd.nl/`), various IT projects
2008 – 2018	KNMI (`https://www.knmi.nl/`), ozone profile retrieval and data assimilation
2018 – present	VU (`https://www.vu.nl/`), methane emissions using data assimilation

List of Publications

Chen, X., Añel, J. A., Su, Z., de la Torre, L., Kelder, H., **van Peet, J. C. A.**, and Ma, Y.: The Deep Atmospheric Boundary Layer and Its Significance to the Stratosphere and Troposphere Exchange over the Tibetan Plateau, PLoS ONE, 8, e56 909, doi:10.1371/journal.pone.0056909, 2013.

Cortesi, U., Ceccherini, S., Del Bianco, S., Gai, M., Tirelli, C., Zoppetti, N., Barbara, F., Bonazountas, M., Argyridis, A., Bós, A., Loenen, E., Arola, A., Kujanpää, J., Lipponen, A., Wandji Nyamsi, W., Van der A, R., **Van Peet, Jacob**, Tuinder, O., Farruggia, V., Masini, A., Simeone, E., Dragani, R., Keppens, A., Lambert, J., Van Roozendael, M., Lerot, C., Yu, H., and Verberne, K.: Advanced Ultraviolet Radiation and Ozone Retrieval for Applications (AURORA): A Project Overview, Atmosphere, 9, doi:10.3390/atmos9110454, 2018.

Keppens, A., Lambert, J.-C., Granville, J., Miles, G., Siddans, R., **van Peet, J. C. A.**, van der A, R. J., Hubert, D., Verhoelst, T., Delcloo, A., Godin-Beekmann, S., Kivi, R., Stübi, R., and Zehner, C.: Round-robin evaluation of nadir ozone profile retrievals: methodology and application to MetOp-A GOME-2, Atmospheric Measurement Techniques, 8, 2093–2120, doi:10.5194/amt-8-2093-2015, 2015.

Keppens, A., Lambert, J.-C., Granville, J., Hubert, D., Verhoelst, T., Compernolle, S., Latter, B., Kerridge, B., Siddans, R., Boynard, A., Hadji-Lazaro, J., Clerbaux, C., Wespes, C., Hurtmans, D. R., Coheur, P.-F., **van Peet, J. C. A.**, van der A, R. J., Garane, K., Koukouli, M. E., Balis, D. S., Delcloo, A., Kivi, R., Stübi, R., Godin-Beekmann, S., Van Roozendael, M., and Zehner, C.: Quality assessment of the Ozone_cci Climate Research Data Package (release 2017) – Part 2: Ground-based validation of nadir ozone profile data products, Atmospheric Measurement Techniques, 11, 3769–3800, doi:10.5194/amt-11-3769-2018, 2018.

Mielonen, T., de Haan, J. F., **van Peet, J. C. A.**, Eremenko, M., and Veefkind, J. P.: Towards the retrieval of tropospheric ozone with the Ozone Monitoring Instrument (OMI), Atmospheric Measurement Techniques, 8, 671–687, doi:10.5194/amt-8-671-2015, 2015.

Shah, S., Tuinder, O. N. E., **van Peet, J. C. A.**, de Laat, A. T. J., and Stammes, P.: Evaluation of SCIAMACHY Level-1 data versions using nadir ozone profile retrievals in the period 2003–2011, Atmospheric Measurement Techniques, 11, 2345–2360, doi:10.5194/amt-11-2345-2018, 2018.

van Peet, J. C. A. and van der A, R. J.: Deriving tropospheric ozone from assimilated profiles, Atmospheric Chemistry and Physics Discussions, 2019, 1–16, doi:10.5194/acp-2018-1280, 2019.

van Peet, J. C. A., Costantini, E., Méndez, M., Paerels, F. B. S., and Cottam, J.: Properties of the ionised plasma in the vicinity of the neutron-star X-ray binary EXO 0748-676, Astronomy and Astrophysics, 497, 805–813, doi:10.1051/0004-6361/200811181, 2009a.

van Peet, J. C. A., van der A, R. J., de Laat, A. T. J., Tuinder, O. N. E., König-Langlo, G., and Wittig, J.: Height resolved ozone hole structure as observed by the Global Ozone Monitoring Experiment-2, Geophysical Research Letters, 36, L11 816, doi:10.1029/2009GL038603, 2009b.

van Peet, J. C. A., van der A, R. J., Tuinder, O. N. E., Wolfram, E., Salvador, J., Levelt, P. F., and Kelder, H. M.: Ozone ProfilE Retrieval Algorithm (OPERA) for nadir-looking satellite instruments in the UV–VIS, Atmospheric Measurement Techniques, 7, 859–876, doi:10.5194/amt-7-859-2014, 2014.

van Peet, J. C. A., van der A, R. J., Kelder, H. M., and Levelt, P. F.: Simultaneous assimilation of ozone profiles from multiple UV-VIS satellite instruments, Atmospheric Chemistry and Physics, 18, 1685–1704, doi:10.5194/acp-18-1685-2018, 2018.